INFORMATION TO USERS

This manuscript has been reproduced from the microfilm master. UMI films the text directly from the original or copy submitted. Thus, some thesis and dissertation copies are in typewriter face, while others may be from any type of computer printer.

The quality of this reproduction is dependent upon the quality of the copy submitted. Broken or indistinct print, colored or poor quality illustrations and photographs, print bleedthrough, substandard margins, and improper alignment can adversely affect reproduction.

In the unlikely event that the author did not send UMI a complete manuscript and there are missing pages, these will be noted. Also, if unauthorized copyright material had to be removed, a note will indicate the deletion.

Oversize materials (e.g., maps, drawings, charts) are reproduced by sectioning the original, beginning at the upper left-hand corner and continuing from left to right in equal sections with small overlaps.

Photographs included in the original manuscript have been reproduced xerographically in this copy. Higher quality 6" x 9" black and white photographic prints are available for any photographs or illustrations appearing in this copy for an additional charge. Contact UMI directly to order.

ProQuest Information and Learning
300 North Zeeb Road, Ann Arbor, MI 48106-1346 USA
800-521-0600

UNIVERSITY OF CALIFORNIA

Los Angeles

Nonlinear Order Reduction and Control of Dissipative Partial Differential Equation Systems: Methods and Applications to Transport-Reaction Processes and Fluid Flows

A thesis submitted in partial satisfaction of the requirements for the degree Doctor of Philosophy in Chemical Engineering

by

Antonios Armaou

2001

UMI Number: 3024091

Bell & Howell Information and Learning Company
300 North Zeeb Road
P.O. Box 1346
Ann Arbor, MI 48106-1346

The thesis of Antonios Armaou is approved.

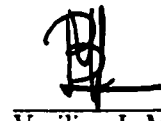

Vasilios I. Manousiouthakis

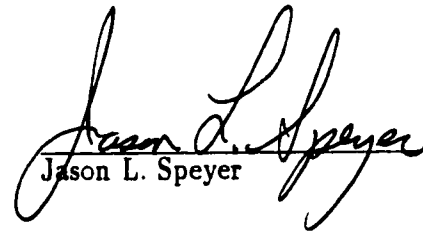

Jason L. Speyer

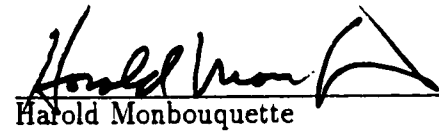

Harold Monbouquette

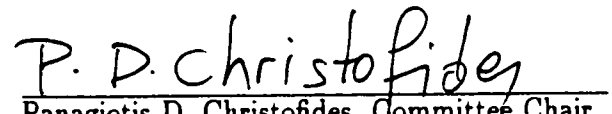

Panagiotis D. Christofides, Committee Chair

University of California, Los Angeles

2001

Contents

List of Figures

List of Tables

ACKNOWLEDGMENTS

I am grateful to my advisor, Professor Panagiotis Christofides, for his guidance and support in the course of this project.

I would like to thank Professor Vasilios I. Manousiouthakis, Professor Harold Monbouquete and Professor Jason L. Speyer for agreeing to participate in my examination committee.

Special acknowledgments to my family and Sandrine Fabien, for their constant support, encouragement, and dedication.

VITA

October 11, 1972	Born, Athens, Greece
1991-1996	Chemical Engineering Undergraduate program, National Technical University Athens, Greece
1995-1996	Research Assistant Microelectronics Division, National Centre of Scientific Research "Demokritos" Athens, Greece
1996	Diploma, Chemical Engineering National Technical University Athens, Greece
1996	"Apostolos Tiftilis" Institution Award
1996	"Thomaides" Institution Award
1996	Second best graduating chemical engineer award, National Technical University
1996	Chemical Engineering Graduate program University of California Los Angeles, California
1997	Research scholarship, Center for Environmental Risk Reduction
1997-2001	Research Assistant Department of Chemical Engineering University of California Los Angeles, California
1997-2000	Teaching Assistant Department of Chemical Engineering University of California Los Angeles, California
2000	O. Hugo Schuck Best Paper Award, American Automatic Control Council
2000-2001	Doctoral Dissertation Fellowship, University of California, Los Angeles
2001	Outstanding Ph.D. Student Award, Department of Chemical Engineering, University of California, Los Angeles

PUBLICATIONS AND PRESENTATIONS

Armaou, A. and P. D. Christofides, "Bounded Output Feedback Control of the Kuramoto-Sivashinsky Equation with Input Constraints," *Proceedings of American Control Conference*, accepted, Arlington, Virginia, 2001.

Armaou, A. and P. D. Christofides, "Computation of Empirical Eigenfunctions and Order Reduction of Nonlinear Parabolic PDEs with Time-Dependent Spatial Domains," *Nonlinear Analysis: Theory, Methods & Applications*, **47**, 2869-2874, 2001.

Armaou, A. and P. D. Christofides, "Finite-Dimensional Control of Nonlinear Parabolic PDEs with Time-Dependent Spatial Domains Using Empirical Eigenfunctions," *Int. J. Appl. Math. & Comp. Sci.*, **11**, 101-131, 2001.

Armaou, A., J. Baker and P. D. Christofides, "Feedback Control of Plasma Etching Reactors for Improved Etching Uniformity," *Chem. Eng. Sci.*, **56**, 257-265, 2001.

Armaou, A. and P. D. Christofides, "Robust Control of Parabolic PDE Systems with Time-Dependent Spatial Domains," *Automatica*, **37**, 61-69, 2001.

Armaou, A. and P. D. Christofides, "Crystal Temperature Control in the Czochralski Crystal Growth Process," *AIChE Journal*, **47**, 79-106, 2001.

Armaou, A. and P. D. Christofides, "Wave Suppression by Nonlinear Finite Dimensional Control," *Chem. Eng. Sci.*, **55**, 2627-2640, 2000.

Armaou, A. and P. D. Christofides, "Real-Time Control of a PECVD Reactor," AIChE Annual Meeting, paper 260i, Los Angeles, California, 2000.

Armaou, A., N. El-Farra and P. D. Christofides, "Wave Suppression by Nonlinear Control: Input Constraint Handling and Uncertainty Attenuation," AIChE Annual

Meeting, paper 273f, Los Angeles, California, 2000.

Armaou, A. and P. D. Christofides, "Optimization of Dynamic Transport-Reaction Systems Using Nonlinear Model Reduction," AIChE Annual Meeting, paper 259c, Los Angeles, California, 2000.

Armaou, A. and P. D. Christofides, "Feedback Control of the Kuramoto Sivashinsky Equation," *Physica D*, **137**, 49-61, 2000.

Armaou, A. and P. D. Christofides, "Wave Suppression by Nonlinear Finite Dimensional Control," *Proceedings of American Control Conference*, 1091-1095, San Diego, California, 1999 (**2000 O. Hugo Schuck Best Paper Award**).

Armaou, A. and P. D. Christofides, "Nonlinear Feedback Control of Parabolic PDE Systems with Time-Dependent Spatial Domains," *J. Math. Anal. Appl.*, **239**, 124-157, 1999.

Armaou, A. and P. D. Christofides, "Plasma-Enhanced Chemical Vapor Deposition: Modeling and Control," *Chem. Eng. Sci.*, **54**, 3305-3314, 1999.

Armaou, A. and P. D. Christofides, "Nonlinear Model Reduction of Processes with Moving Domains: Computation of Empirical Eigenfunctions," AIChE Annual Meeting, paper 235c, Dallas, Texas, 1999.

Armaou, A. and P. D. Christofides, "Integrated Nonlinear Control of Crystal Radius and Thermal Strain in the Czochralski Crystal Growth," AIChE Annual Meeting, paper 193d, Dallas, Texas, 1999.

Armaou A., J. Baker and P. D. Christofides, "Feedback Control of Plasma Etching," AIChE Annual Meeting, paper 169w, Dallas, Texas, 1999.

Armaou, A. and P. D. Christofides, "Nonlinear Control of Incompressible Fluid Flows Based on Navier-Stokes Equations," AIChE Annual Meeting, paper 247d, Miami Beach, Florida, 1998.

Armaou, A. and P. D. Christofides, "Modeling and Control of Plasma Enhanced Chemical Vapor Deposition," AIChE Annual Meeting, paper 197s, Miami Beach, Florida, 1998 **(Finalist Best Student Paper Award, Materials Division Poster Session)**.

Armaou, A. and P. D. Christofides, "Model Reduction and Control of Nonlinear Parabolic PDEs with Free Boundaries: Application to Crystal Growth," AIChE Annual Meeting, paper 248c, Miami Beach, Florida, 1998.

Armaou, A. and P. D. Christofides, "Nonlinear Feedback Control of Parabolic PDE Systems with Time-Dependent Spatial Domains," *Proceedings of American Control Conference*, 2539-2543, Philadelphia, Pennsylvania, 1998.

Baker, J., A. Armaou and P. D. Christofides, "Nonlinear Control of Incompressible Fluid Flows: Application to Burgers' Equation and 2D Channel Flow," *J. Math. Anal. Appl.*, **252**, 230-255, 2000.

Baker, J., A. Armaou and P. D. Christofides, "Drag Reduction in Incompressible Channel Flow Using Electromagnetic Forcing," *Proceedings of American Control Conference*, 4269-4273, Chicago, Illinois, 2000.

Baker, J., A. Armaou and P. D. Christofides, "Nonlinear Feedback Control of Chemical Vapor Deposition Processes," AIChE Annual Meeting, paper 169e, Los Angeles, California, 1997.

Christofides, P. D. and A. Armaou , "Nonlinear Model Reduction and Control of

Transport-Reaction Processes: Recent Developments and Future Challenges," AIChE Annual Meeting, paper 348e, Los Angeles, California, 2000.

Christofides, P. D. and A. Armaou, "Global Stabilization of the Kuramoto-Sivashinsky Equation via Distributed Output Feedback Control," *Syst. & Contr. Lett.*, **39**, 283-294, 2000.

Christofides, P. D. and A. Armaou, "Nonlinear Control of Incompressible Fluid Flows," *Proceedings of Mathematical Theory of Networks and Systems-98 Conference*, 455-458, Padova, Italy, 1998.

Christofides, P. D. and A. Armaou, "Nonlinear Control of Navier-Stokes Equations," *Proceedings of American Control Conference*, 1355-1359, Philadelphia, Pennsylvania, 1998.

El-Farra, N., A. Armaou and P. D. Christofides, "Constrained Nonlinear Control of Nonlinear Parabolic PDE Systems," *Proceedings of American Control Conference*, 2275-2279, Chicago, Illinois, 2000.

El-Farra, N., A. Armaou and P. D. Christofides, "Analysis and Control of Parabolic PDEs with Constraints," AIChE Annual Meeting, paper 208ag, Dallas, Texas, 1999.

Gogolides, E., E. Tegou, A. Armaou, P. Argitis, A. Boudouvis and M. Hatzakis, "Surface silylation and oxygen plasma etching of epoxidised novolac photoresists for microlithographic applications," *Proceedings of 6th European Polymer Federation Symposium on Polymeric Materials*, Crete, Greece, 1996.

ABSTRACT OF THE THESIS

Nonlinear Order Reduction and Control of
Dissipative Partial Differential Equation Systems:
Methods and Applications to
Transport-Reaction Processes and Fluid Flows

by

Antonios Armaou
Doctor of Philosophy in Chemical Engineering
University of California, Los Angeles, 2001

Professor Panagiotis D. Christofides, Chair

The development of general and practical control algorithms for dissipative nonlinear partial differential equation (PDE) systems that mathematically describe fluid flow and

transport-reaction processes is a fundamental problem with a variety of industrially important applications. Examples range from the feedback control of turbulence for drag reduction, to suppression of fluid mechanical instabilities in coating processes and suppression of waves exhibited by falling liquid films, and from the suppression of thermal dislocations in high-purity crystals during the Czochralski crystallization to the feedback control of chemical vapor deposition and etching of thin films for microelectronics manufacturing to achieve spatially uniform thickness.

Traditional approaches for controlling chemical distributed processes are based

on the simplifying assumption that the control variables are spatially uniform; yet, many industrial control problems involve regulation of variables which are distributed in space and cannot be effectively solved with these approaches. These limitations together with the recent advances in the development of fundamental mathematical models that accurately predict the behavior of transport-reaction and fluid flow processes, provide a strong motivation for developing a general framework for nonlinear controller design based on detailed models, thus exploiting the ability of a model to predict the behavior of a process and the fundamental knowledge of the underlying physico-chemical phenomena that the model contains. The key difficulty in developing model-based control methods for transport-reaction and fluid flow processes lies in the "infinite-dimensional" nature of the distributed process models, which prohibits their direct use for control system design.

Motivated by the above, this doctoral thesis presents a general and practical methodology for the nonlinear order reduction and control of a general class of process models, described by dissipative partial differential equation systems, which arise in the modeling of diffusion-convection-reaction processes with fixed and time-varying spatial domains and fluid dynamic systems. The methodology proposes a combination of Galerkin's method with approximate inertial manifolds to derive low-dimensional approximations of the distributed process model, which are employed for the selection of the control configuration and the synthesis of high-performance nonlinear feedback controllers using geometric control methods and Lyapunov techniques. A rigorous analysis of the closed-loop system (distributed process model and controller) is performed to derive precise conditions which guarantee that the desired stability and performance properties are achieved in the presence of uncertainty in the values of the parameters of the process model.

The developed methodology is applied, via computer simulations, to industrially important transport-reaction processes such as the Czochralski crystal growth, plasma-enhanced chemical vapor deposition and plasma etching and towards the suppression of instabilities exhibited by falling and shallow liquid films, described by the Kuramoto-Sivashinsky and Korteweg-de-Vries Burgers equations respectively.

Chapter 1

Introduction

The conventional approach for the control of partial differential equation (PDE) systems is based on the spatial discretization (typically with finite-difference or finite-element methods) of the PDE system followed by the controller design on the basis of the resulting ordinary differential equation (ODE) system. However, there are certain well-known disadvantages associated with this approach. For example, fundamental control-theoretic properties, like controllability and observability, which should depend only on the location of sensors and actuators, may also depend on the discretization method and the number and location of discretization points. Moreover, neglecting the infinite dimensional nature of the original system may lead to erroneous conclusions concerning the stability properties of the open-loop and/or the closed-loop system. Furthermore, in processes where the spatially distributed nature is very strong, due to the underlying convection and diffusion phenomena, such an approach limits the controller performance, and may lead to unacceptable control quality.

Motivated by the above considerations, significant research efforts have focused on the development of control methods for PDE systems that directly account for their

spatially distributed nature. In this direction, the well-known classification of PDE systems to hyperbolic and parabolic [165], according to the properties of the spatial differential operator, essentially determines the approach followed for the solution of the control problem.

In this thesis we focus on dissipative nonlinear PDE systems which arise naturally in the modeling of a wide variety of industrially important processes, such as transport-reaction and fluid flow systems. Let us first proceed with a description of the main challenges for the control problem and recent research results for transport-reaction processes, followed by an analysis of the control problem for fluid dynamic systems and towards the end of the chapter, we will present an overview of the objectives and the structure of the present work.

There is a large number of industrial control problems which involve highly nonlinear transport-reaction processes with moving boundaries such as, crystal growth, metal casting, gas-solid reaction systems and coatings. In these processes, nonlinear behavior typically arises from complex reaction mechanisms and their Arrhenius dependence on temperature, while motion of boundaries is usually a result of phase change, such as chemical reaction, mass and heat transfer, and melting or solidification. The mathematical models of transport-reaction processes with moving boundaries are usually obtained from the dynamic conservation equations and consist of nonlinear parabolic partial differential equations (PDEs) with time-dependent spatial domains.

Research on control of linear/quasi-linear parabolic PDEs has been extensive in the past and has mainly focused on systems with fixed spatial domains (see, for example, the review papers [12, 117, 44] and the references therein). The main feature of parabolic PDE systems is that the eigenspectrum of the spatial differential operator

can be partitioned into a finite-dimensional slow one and an infinite-dimensional stable fast complement [73]. This implies that the dominant dynamic behavior of such systems can be approximately described by finite-dimensional systems. Therefore, the standard approach to the control of linear/quasi-linear parabolic PDE systems (e.g. [11, 34]) involves the application of standard Galerkin's method to the parabolic PDE system to derive ODE systems that accurately describe the dominant dynamics of the PDE system, which are subsequently used as the basis for controller synthesis. The main disadvantage of this approach is that the number of modes that should be retained to derive an ODE system which yields the desired degree of approximation, may be very large (e.g. [14, 1]), thereby leading to complex controller synthesis and high dimensionality of the resulting controllers.

These controller synthesis and implementation problems, together with the need to develop computationally efficient numerical solution algorithms for nonlinear parabolic PDEs, have motivated extensive research efforts on the problem of deriving low-order ODE systems that accurately reproduce the dynamics and solutions of nonlinear parabolic PDEs. The concept of inertial manifold (IM) has provided a natural framework for addressing this problem [168]. If it exists, an IM is a positively invariant, exponentially attracting, finite-dimensional Lipschitz manifold. The IM is an appropriate tool for model reduction because if the trajectories of the PDE system are on the IM, then this system is exactly described by a low-order ODE system (called inertial form). Unfortunately, even for PDE systems for which an IM is known to exist, the computation of the closed-form expression of the IM (and therefore the derivation of the corresponding inertial form) is a formidable task. Motivated by this, various approaches have been proposed in the literature for the construction of approximations of the inertial manifold [71, 70, 45] (called approximate inertial

manifolds (AIMs)). The AIMs are subsequently used for the derivation of approximations of the inertial form that accurately reproduce the solutions and dynamics of the parabolic PDE system.

In the context of control of parabolic PDE systems with fixed spatial domains, the concept of inertial manifold has been used: a) in [26, 25], to determine the extent to which linear boundary proportional control influences the dynamic and steady-state closed-loop response of a nonlinear parabolic PDE system, and b) in [155, 113, 154], to address the problem of stabilization of a parabolic PDE with boundary low-order linear output feedback control; while the concept of approximate inertial manifold has been used in [45], to synthesize nonlinear low-order output feedback controllers that enforce closed-loop stability and output tracking in quasi-linear parabolic PDE systems with distributed control action.

Despite the recent progress on nonlinear control of parabolic PDE systems with fixed spatial domains, few results are available on control and estimation of parabolic PDE systems with time-dependent spatial domains. In this area, important contributions include Wang's work on the synthesis of linear optimal controllers (e.g. [176, 177]) and their application to temperature and thermal gradient regulation in crystal growth processes [178], as well as the synthesis of nonlinear distributed state estimators using stochastic methods in [147].

In addition to being nonlinear and time-varying, such systems are usually characterized by the presence of uncertain variables owing to unknown or partially known process parameters and disturbances. Uncertain variables, if they are not appropriately accounted for in the controller design, can significantly deteriorate the nominal closed-loop performance, and even lead to closed-loop instability. In the past, most of the research on control of linear/quasi-linear parabolic PDEs with uncer-

tainty has focused on systems with fixed spatial domains. Initially, H^∞ control algorithms were developed for linear parabolic PDE systems in the frequency domain (e.g., [135, 51, 77]). The development of concrete relations between frequency-domain and state-space control theoretic concepts (e.g., controllability and observability) in [101] allowed the derivation of the state-space counterparts of the frequency domain H^∞ results (see, for example, the book [174]). More recently, Lyapunov-based robust controller design methods were proposed [180, 39, 42] for quasi-linear parabolic PDEs with uncertainty. Other results on control of PDE systems with uncertainty include disturbance decoupling for linear parabolic PDEs [50], Lyapunov-based [46] and sliding-mode control [86] of hyperbolic PDE systems, Lyapunov-based [104] and H^∞ (e.g., [23, 108]) control of Navier-Stokes equations, as well as adaptive control (e.g., [27, 179, 55]).

Another issue in the control of transport-reaction processes with moving boundaries is the fact that in many cases the spatial operator is highly nonlinear. In these processes, the nonlinear behavior typically arises from the complex transport mechanisms or dependence of the process parameters on the temperature and concentration (e.g., conduction and diffusion coefficients), while motion of boundaries is usually a result of phase change, such as chemical reaction, mass and heat transfer, and melting or solidification. The mathematical models of transport-reaction processes with moving boundaries are usually obtained from the dynamic conservation equations and consist of nonlinear parabolic partial differential equations (PDEs) with time-dependent spatial domains.

Unfortunately, the developed control methods for quasi-linear parabolic PDE systems cannot be directly employed for the design of low-dimensional controllers for systems that include nonlinear spatial differential operators. The reason is that, in

general, the eigenvalue problem of nonlinear spatial differential operators cannot be solved analytically and thus, it is difficult to a priori choose an optimal (in the sense that it will lead to a low-dimensional ODE system) basis to expand the solution of the PDE system. An approximate way to address this problem [146] is to linearize the nonlinear spatial differential operator around a steady state and address the controller design problem on the basis of the resulting quasi-linear system. However, this approach is only valid in a small neighborhood of the steady state where the linearization takes place. An alternative approach which is not based on linearization is to utilize detailed finite difference/element simulations of the PDE system to compute a set of empirical eigenfunctions (dominant spatial patterns) of the system through Karhunen-Loève expansion (also known as proper orthogonal decomposition and principal component analysis), using the method of snapshots [158]. The use of empirical eigenfunctions as basis functions in Galerkin's method has been shown to lead to the derivation of accurate nonlinear low-dimensional approximations of several dissipative PDE systems arising in the modeling of diffusion-reaction processes and fluid flows [136, 14]. Recently, empirical eigenfunctions were computed using K-L expansion for PDE systems whose solutions contain traveling structures by exploiting symmetry [150]. In the area of control, linear feedback controllers were synthesized in [156, 169] for specific diffusion-reaction systems on the basis of low-dimensional models obtained using empirical eigenfunctions as basis functions in Galerkin's method, and a method for the design of nonlinear output feedback controllers for nonlinear parabolic PDE systems was developed in [9] by combining Galerkin's method with empirical eigenfunctions. However, research on nonlinear PDE systems has only focused on transport reaction processes with fixed spatial domains and no results in this direction exist for nonlinear systems with moving boundaries.

Another important problem is the development of general and practical control algorithms for the nonlinear dissipative PDEs that describe fluid flow processes (e.g., Navier-Stokes equations, KdVB, KS) whose practical significance ranges from feedback control of turbulence for drag reduction, to suppression of fluid mechanical instabilities in coating processes and suppression of waves exhibited by falling liquid films. For example, drag reduction through active feedback control may have a very significant impact on the design and operation of underwater vehicles, airplanes and automobiles, since according to some estimates keeping the flow over the surface of a vehicle laminar could yield up to 30% reduction in fuel consumption. Active control of fluid flow can be achieved by injection of polymers [126], mass transport through porous walls (e.g., blowing/suction) [30, 53] and application of electro-magnetic forcing [164].

The development of an efficient control system for a fluid flow should be based on the underlying PDE model that describes the flow in order to exploit its ability to accurately predict the spatiotemporal behavior of the flow field. The main obstacle for the synthesis of practically implementable output feedback controllers for fluid flow processes is the infinite-dimensional nature of the underlying PDE models, which does not allow their direct use for the design of low-order (and therefore, easy-to-implement) controllers. This fact, together with the need to develop efficient numerical methods for nonlinear PDEs, has motivated significant research on the understanding of the dynamic behavior of various fluid flows. This research has led to the discovery that turbulent flows involve coherent structures (e.g., [10, 127, 28, 159]) which implies that the dominant dynamic behavior of such flows can in principle be approximated by low-dimensional systems. These results have motivated the development of model reduction methods for the derivation of low-dimensional systems

that accurately describe the dominant dynamics of PDEs which model fluid flows including nonlinear Galerkin's method (e.g., [170, 54, 14]) and reduced basis methods (e.g., [99]).

In the area of control of fluid flow processes, previous research has mainly focused on: a) control of Navier-Stokes equations via proportional-integral [18, 37], linear optimal [61, 103, 92], H_∞ optimal [23, 22, 108], Lyapunov-based [104] and nonlinear [41] control, b) linear distributed [152] and point [151] control of the Korteweg-de Vries equation and nonlinear boundary control of the KdVB equation [123], and nonlinear boundary control [124] of the KS equation that enhances the rate of convergence to the spatially uniform steady-state when this steady-state is naturally stable. At this stage, not much work has been done on the utilization of the aforementioned nonlinear model reduction techniques for the design of nonlinear low-order feedback controllers for PDEs that describe fluid flows.

Another problem in the control of fluid flows is the the problem of constraints in the capacity of the control actuators commonly used. Input constraints may restrict our ability to freely modify the dynamic behavior of a dynamical system and may lead to sluggishness of response, oscillations, and loss of stability if they are not accounted for in the controller design. Results on control of systems with input constraints include controller design and stability analysis within the model predictive control framework (e.g., [145]), constrained nonlinear optimal control (e.g., [67]), and the design of "anti-windup" schemes (e.g., [110, 105]).

Motivated by the lack of a general methodology for the synthesis of model-based controllers for industrially important processes that are described by nonlinear dissipative PDE systems the objectives of the present doctoral thesis are:

- to develop a general and practical methodology for the nonlinear model reduction

and control of a general class of processes that are mathematically described by nonlinear dissipative partial differential equation systems.

- to present the application of the proposed methods to industrially important transport-reaction processes such as the Czochralski crystal growth, plasma-enhanced chemical vapor deposition and plasma etching.
- to develop methods for order reduction and active feedback control for the suppression of instabilities exhibited by falling and shallow liquid films (mathematically described by the Kuramoto-Sivashinsky and Korteweg-de-Vries Burgers equations respectively).

Throughout the thesis, we will assume that all the PDE systems under consideration (with and without feedback control) possess a unique solution which is also sufficiently smooth (i.e., all the spatial and time derivatives in the PDE systems are smooth functions of space and time); the reader may refer to the books [139, 16, 17, 52, 181] for techniques and results for studying the mathematically delicate questions of existence, uniqueness and regularity of solutions for various classes of PDE systems. In addition, we focus our attention on quasi-linear hyperbolic and parabolic PDE systems for which the manipulated inputs, measured and controlled outputs are bounded. From a practical point of view, this means that we do not deal with control problems that involve boundary actuation, measurements and control objectives, even though several problems of this kind can be addressed by the proposed methods. Linear infinite dimensional systems with unbounded manipulated inputs, measurements and control objectives have been studied extensively (see, for example, [48, 143, 118, 174, 16, 17]).

The rest of the thesis is structured as follows.

Chapter 2 presents a methodology for the synthesis of nonlinear finite-dimensional

time-varying output feedback controllers for systems of quasi-linear parabolic partial differential equations (PDEs) with time-dependent spatial domains, whose dynamics can be partitioned into slow and fast ones. A nonlinear model reduction scheme based on combination of Galerkin's method with the concept of approximate inertial manifold is employed for the derivation of low-order ordinary differential equation (ODE) approximations of the PDE which are subsequently used as the basis for the explicit construction of nonlinear time-varying output feedback controllers via geometric control methods. The proposed control method is used to stabilize an unstable steady-state of a diffusion-reaction process whose spatial domain changes with time.

In Chapter 3 robust nonlinear static output feedback controllers for the systems of the type studied in Chapter 2 that also include uncertain variables are synthesized. Specifically, utilizing nonlinear order-reduction methods and a combination of geometric control concepts with Lyapunov's direct method, robust nonlinear static output feedback controllers are synthesized that guarantee boundedness of the state and achieve asymptotic output tracking with arbitrary degree of asymptotic attenuation of the effect of the uncertain variables on the output of the closed-loop system. The controllers are successfully applied to a typical diffusion-reaction process with moving boundary and uncertainty.

Chapter 4 focuses on the challenging problem of synthesis of finite-dimensional nonlinear output feedback controllers for nonlinear parabolic PDE systems with time-dependent spatial domains. Initially, the nonlinear parabolic PDE system is expressed with respect to an appropriate time-invariant spatial coordinate and a representative (with respect to different initial conditions and input perturbations) ensemble of solutions of the resulting time-varying PDE system is constructed. Karhunen-Loève

expansion is applied to the ensemble of solutions to derive a small set of empirical eigenfunctions that capture the dominant spatial patterns of the ensemble. The empirical eigenfunctions are subsequently used as basis functions within a Galerkin's model reduction framework to derive low-order ODE systems that accurately describe the dominant dynamics of the PDE system. The ODE systems are subsequently used for the synthesis of nonlinear output feedback controllers using geometric control methods. The proposed control method is used to stabilize an unstable steady-state of a diffusion-reaction process with nonlinearities, spatially-varying coefficients and time-dependent spatial domain.

In Chapter 5 we propose a novel control configuration and a nonlinear multivariable model-based controller for the reduction of thermal gradients inside the crystal in the Czochralski crystal growth process after the crystal radius has reached its final value. The proposed in Chapter 2 method is used to construct a fourth-order model that describes the dominant thermal dynamics of the Czochralski process and synthesize a fourth-order nonlinear multivariable controller that can be readily implemented in practice. The proposed control scheme is successfully implemented on a Czochralski process used to produce a 0.7 m long silicon crystal with a radius of 0.05 m and is shown to significantly reduce the axial and radial thermal gradients inside the crystal.

In Chapter 6 we turn our attention to the Korteweg-de Vries-Burgers (KdVB) and Kuramoto-Sivashinsky (KS) equations which are two nonlinear partial differential equations (PDEs) that adequately describe motion of waves in a variety of fluid flow processes. We synthesize nonlinear low-dimensional output feedback controllers for the KdVB and KS equations with periodic boundary conditions that enhance convergence rate and achieve stabilization to spatially uniform steady-states, respectively. The approach used for controller synthesis is similar to the one developed in Chapter

2 and employs nonlinear Galerkin's method to derive low-dimensional approximations of the PDEs, which are subsequently used for controller synthesis via geometric control methods. The controllers use measurements obtained by point sensors and are implemented through point control actuators. The performance of these nonlinear controllers controllers is successfully tested through simulations.

Chapter 7 addresses the problem of global exponential stabilization of the KS equation (presented in Chapter 6) via distributed static output feedback control. Under the assumption that the number of measurements is equal to the total number of unstable and critically stable eigenvalues of the KS and a necessary and sufficient stability condition is satisfied, linear static output feedback controllers are designed that globally exponentially stabilize the zero solution of the KS for any given value of the instability parameter. These linear controllers are designed on the basis of finite-dimensional approximations of the KS, obtained through Galerkin's method, and the stability of the closed loop system (distributed process model and controller) is analyzed within a singular perturbation framework. The theoretical results are confirmed through computer simulations of the closed-loop system.

In Chapter 8 we focus on the stabilization of the KS equation with periodic boundary conditions at the zero solution in the presence of input constraints. Bounded nonlinear stabilizing controllers are synthesized on the basis of low-order approximations of the KS, derived using Galerkin's method. The controller design accounts explicitly for the presence of input constraints while an explicit characterization of the limitations imposed by the input constraints on the allowable control actuator locations is provided. The theoretical results are illustrated through computer simulations of the closed-loop system using a high-order discretization of the KSE.

The last two chapters of the thesis present applications of the developed control

methodologies towards the design of novel control configurations for two important microelectronics manufacturing processes. Chapter 9 focuses on modeling and control of a single-wafer parallel electrode plasma-enhanced chemical vapor deposition (PECVD) process with showerhead arrangement used to deposit a 500 A amorphous silicon thin film on a 8 cm wafer. A feedback control system is designed and implemented on the process to reduce the film thickness nonuniformity. The control system consists of three spatially-distributed proportional integral controllers that use measurements of the deposition rate at three locations across the wafer, to manipulate the inlet concentration of silane in the showerhead and achieve a uniform deposition rate across the wafer. The implementation of the proposed control system is shown to reduce the film thickness radial nonuniformity to 3.8%.

Similarly, Chapter 10 focuses on the design and implementation of a feedback control system on another process used for microelectronics manufacturing, the parallel electrode Plasma Etching (PE) process with showerhead arrangement used to etch a 500 A amorphous silicon thin film on a 4 in wafer. The feedback control system consists of three spatially-distributed proportional integral controllers that use measurements of the etching rate at three locations across the wafer to manipulate the inlet concentration of carbon tetrafluoride in the showerhead. The controller is implemented on a detailed fundamental model of the process, which accounts for diffusive and convective mass transfer, bulk and surface reactions, and nonuniform fluid flow and plasma electron density profiles, and is shown to reduce the etching rate nonuniformity from 30.2% to 3.8%.

Finally, Chapter 11 presents the main conclusions of this thesis work.

Chapter 2

Nonlinear Feedback Control of Parabolic PDE Systems With Time-dependent Spatial Domains

2.1 Introduction

This chapter focuses on a broad class of quasi-linear parabolic PDE systems with time-dependent spatial domains whose dynamics can be partitioned into slow and fast ones. Such systems arise naturally in the modeling of diffusion-reaction processes with moving boundaries. The objective is to develop a general method for the synthesis of low-order (and therefore, practically-implementable) nonlinear time-varying output feedback controllers that enforce stability and output tracking in the closed-loop system.

The chapter is structured as follows: Initially, the class of parabolic PDE systems considered in the manuscript is given and is formulated as an evolution equation in an appropriate Hilbert space. Then, a nonlinear model reduction scheme, similar to the one introduced in [45], which is based on combination of Galerkin's method with

the concept of approximate inertial manifold is employed for the derivation of ODE systems that yield solutions which are close, up to a desired accuracy, to the ones of the PDE system, for almost all times. Then, these ODE systems are used as the basis for the explicit construction of nonlinear time-varying output feedback controllers via geometric control methods. The controllers guarantee stability and enforce the output of the closed-loop parabolic PDE system to follow, up to a desired accuracy, a prespecified response for almost all times, provided that the separation of the slow and fast dynamics is sufficiently large. Differences in the nature of the model reduction and control problems between parabolic PDE systems with fixed and moving spatial domains are identified and discussed. Finally, the proposed control method is applied to a typical diffusion-reaction process whose spatial domain changes with time, and is shown to lead to a significant reduction on the order of the stabilizing controller, as well as to outperform a nonlinear controller synthesis method which does not account for the variation of the spatial domain.

2.2 Preliminaries

2.2.1 Parabolic PDE systems with time-dependent spatial domains

We consider quasi-linear parabolic PDE systems with time-dependent spatial domains with the following state-space description:

$$\begin{aligned} \frac{\partial \bar{x}}{\partial t} &= A\frac{\partial \bar{x}}{\partial z} + B\frac{\partial^2 \bar{x}}{\partial z^2} + wb(z,t)u + f(t,\bar{x}) \\ y_{c_i} &= \int_0^{l(t)} c_i(z,t)k\bar{x}dz, \quad i = 1,\ldots,l \\ y_{m_\kappa} &= \int_0^{l(t)} s_\kappa(z,t)\omega\bar{x}dz, \quad \kappa = 1,\ldots,q \end{aligned} \tag{2.1}$$

subject to the boundary conditions:

$$\begin{aligned} C_1\bar{x}(0,t) + D_1\frac{\partial \bar{x}}{\partial z}(0,t) &= R_1 \\ C_2\bar{x}(l(t),t) + D_2\frac{\partial \bar{x}}{\partial z}(l(t),t) &= R_2 \end{aligned} \tag{2.2}$$

and the initial condition:

$$\bar{x}(z,0) = \bar{x}_0(z) \tag{2.3}$$

where the rate of change of the length of the domain, $l(t)$, is governed by the following ordinary differential equation:

$$\frac{dl}{dt} = \mathcal{G}(t,l,\int_0^{l(t)} \bar{a}(z,t,l,\bar{x},\frac{\partial \bar{x}}{\partial z})dz) \tag{2.4}$$

where $\bar{x}(z,t) = [\bar{x}_1(z,t) \cdots \bar{x}_n(z,t)]^T$ denotes the vector of state variables, $[0,l(t)] \subset \mathbb{R}$ is the domain of definition of the process, $z \in [0,l(t)]$ is the spatial coordinate, $t \in [0,\infty)$ is the time, $u = [u_1\ u_2 \cdots u_l]^T \in \mathbb{R}^l$ denotes the vector of manipulated inputs, $y_{c_i} \in \mathbb{R}$ denotes the i-th controlled output and $y_{m_\kappa} \in \mathbb{R}$ denotes the κ-th measured output. $\frac{\partial \bar{x}}{\partial z}$, $\frac{\partial^2 \bar{x}}{\partial z^2}$ denote the first- and second-order spatial derivatives of $\bar{x}$, $f(t,\bar{x})$, $\mathcal{G}(t,l,\int_0^{l(t)} \bar{a}(z,t,l,\bar{x},\frac{\partial \bar{x}}{\partial z})dz)$ are nonlinear vector functions, $\bar{a}(z,t,l,\bar{x},\frac{\partial \bar{x}}{\partial z})$ is a nonlinear scalar function, k, w, ω are constant vectors, A, B, C_1, D_1, C_2, D_2 are constant matrices, R_1, R_2 are column vectors, and $\bar{x}_0(z)$ is the initial condition.

$b(z,t)$ is a known smooth vector function of (z,t) of the general form $b(z,t) = [b_1(z,t)\ b_2(z,t) \cdots b_l(z,t)]$, where $b_i(z,t)$ describes how the control action $u_i(t)$ is distributed in the interval $[0,l(t)]$ (e.g. point/distributed actuation), $c_i(z,t)$ is a known smooth function of (z,t) which is determined by the desired performance specifications in the interval $[0,l(t)]$ (e.g. regulation of the entire temperature profile of a crystal or regulation of the temperature at a specific point), and $s_\kappa(z,t)$ is a known smooth function of (z,t) which is determined by the location and type of the κ-th measurement sensor (e.g. point/distributed sensing). In the case of point actuation

(i.e. the control action enters the system at a single point z_0, with $z_0 \in [0, l(t)]$), the function $b_i(z,t)$ is taken to be nonzero in a finite spatial interval of the form $[z_0-\epsilon, z_0+\epsilon]$, where ϵ is a small positive real number, and zero elsewhere in $[0, l(t)]$. We note that in contrast to the case of parabolic PDE systems defined on a fixed spatial domain [45], we allow the actuator, performance specification and measurement sensor functions to depend explicitly on time (i.e. moving control actuators and objectives, and measurement sensors). The value of using moving control actuators and sensors in certain applications will be illustrated in the example of section 2.5. Throughout the thesis, we will use the order of magnitude notation $O(\epsilon)$ (i.e. $\delta(\epsilon) = O(\epsilon)$ if there exist positive real numbers k_1 and k_2 such that $|\delta(\epsilon)| \leq k_1|\epsilon|$, $\forall\ |\epsilon| < k_2$).

In order to simplify the notation of this manuscript, we assume that $l(t)$ is a known and smooth function of time and develop the proposed nonlinear control method on the basis of the following parabolic PDE system with time-dependent spatial domain (the development of the results for systems of the form of Eqs.2.2-2.4 is conceptually similar):

$$\begin{aligned} \frac{\partial \bar{x}}{\partial t} &= A\frac{\partial \bar{x}}{\partial z} + B\frac{\partial^2 \bar{x}}{\partial z^2} + wb(z,t)u + f(t,\bar{x}) \\ y_{c_i} &= \int_0^{l(t)} c_i(z,t)k\bar{x}dz, \quad i = 1,\ldots,l \\ y_{m_\kappa} &= \int_0^{l(t)} s_\kappa(z,t)\omega\bar{x}dz, \quad \kappa = 1,\ldots,q \end{aligned} \tag{2.5}$$

subject to the boundary conditions:

$$\begin{aligned} C_1\bar{x}(0,t) + D_1\frac{\partial \bar{x}}{\partial z}(0,t) &= R_1 \\ C_2\bar{x}(l(t),t) + D_2\frac{\partial \bar{x}}{\partial z}(l(t),t) &= R_2 \end{aligned} \tag{2.6}$$

and the initial condition:

$$\bar{x}(z,0) = \bar{x}_0(z) \tag{2.7}$$

Our assumptions on the properties of $l(t)$ are precisely stated below:

Assumption 2.1: *$l(t)$ is a known smooth (i.e. $\dot{l}$ exists and is bounded, $\forall\ t \in [0,\infty)$)*

function of time which satisfies $l(t) \in (0, l_{max}]$, $\forall\, t \in [0, \infty)$, *where* l_{max} *denotes the maximum length of the spatial domain.*

2.2.2 Formulation of the parabolic PDE system in Hilbert space

We formulate the system of Eqs.2.5-2.7 in a Hilbert space $\mathcal{H}(t)$ consisting of n-dimensional vector functions defined on $[0, l(t)]$ that satisfy the boundary conditions of Eq.2.6, with inner product and norm:

$$\begin{aligned} (\omega_1, \omega_2) &= \int_0^{l(t)} (\omega_1(z), \omega_2(z))_{\mathbb{R}^n} dz \\ \|\omega_1\|_2 &= (\omega_1, \omega_1)^{\frac{1}{2}} \end{aligned} \tag{2.8}$$

where ω_1, ω_2 are two elements of $\mathcal{H}(t)$ and the notation $(\cdot, \cdot)_{\mathbb{R}^n}$ denotes the standard inner product in $\mathbb{R}^n$. To this end, we define the state function x on $\mathcal{H}(t)$ as

$$x(t) = \bar{x}(z, t), \quad t > 0, \quad z \in [0, l(t)], \tag{2.9}$$

the time-varying operator:

$$\begin{aligned} &\mathcal{A}(t)x = A\frac{\partial \bar{x}}{\partial z} + B\frac{\partial^2 \bar{x}}{\partial z^2} + \frac{\dot{l}(t)}{l(t)} z \frac{\partial \bar{x}}{\partial z}, \\ &x \in D(\mathcal{A}) = \Big\{ x \in \mathcal{H}(t) : \; C_1 \bar{x}(0,t) + D_1 \frac{\partial \bar{x}}{\partial z}(0,t) = R_1, \\ &\qquad\qquad C_2 \bar{x}(l(t),t) + D_2 \frac{\partial \bar{x}}{\partial z}(l(t),t) = R_2 \Big\} \end{aligned} \tag{2.10}$$

and the input, controlled output and measurement operators as:

$$\mathcal{B}(t)u = wb(t)u, \quad \mathcal{C}(t)x = (c(t), kx), \quad \mathcal{S}(t)x = (s(t), \omega x) \tag{2.11}$$

where $c(t) = [c_1(t)\; c_2(t)\; \cdots c_l(t)]^T$ and $s(t) = [s_1(t)\; s_2(t)\; \cdots s_q(t)]^T$, and $c_i(t) \in \mathcal{H}(t)$, $s_\kappa(t) \in \mathcal{H}(t)$. The system of Eqs.2.5-2.7 can then be written as:

$$\begin{aligned} \dot{x} &= \mathcal{A}(t)x + \mathcal{B}(t)u + f(t, x), \quad x(0) = x_0 \\ y_c &= \mathcal{C}(t)x, \quad y_m = \mathcal{S}(t)x \end{aligned} \tag{2.12}$$

where $f(t, x(t)) = f(t, \bar{x}(z, t))$ and $x_0 = \bar{x}_0(z)$. We assume that the nonlinear term $f(t, x)$ satisfies $f(t, 0) = 0$ and is also locally Lipschitz continuous uniformly in t, i.e.

there exist positive real numbers a_0, K_0 such that for any $x_1, x_2 \in \mathcal{H}(t)$ that satisfy $\max\{\|x_1\|_2, \|x_2\|_2\} \leq a_0$, we have that:

$$\|f(t, x_1) - f(t, x_2)\|_2 \leq K_0 \|x_1 - x_2\|_2, \quad \forall\, t \in [0, \infty) \tag{2.13}$$

Remark 2.1: In the formulation of the PDE system of Eqs.2.5-2.7 in $\mathcal{H}(t)$, the time-varying term $-\dot{l}(t)\dfrac{\partial \bar{x}}{\partial z}$ in the expression of $\mathcal{A}(t)$ (Eq.2.10) accounts for convective transport owing to the motion of the domain. This term was not present in the expression of the differential operator in the case of parabolic PDE systems with fixed spatial domains (where $\dot{l}(t) \equiv 0$), and makes $\mathcal{A}(t)$ an explicit function of time.

2.2.3 Singular perturbation formulation

In this subsection, we precisely state our assumption that the dynamics of the infinite-dimensional system of Eq.2.12 can be partitioned into slow (finite-dimensional) and fast (infinite-dimensional) ones. We note that this assumption is usually satisfied by most diffusion-reaction processes (see, for example, [34, 43] and the application of section 2.5). Assumption 2.2 that follows states our requirement.

Assumption 2.2: *Let* $\{\phi_j(t)\}$, $j = 1, \ldots, \infty$, *be an orthogonal and countable,* $\forall\, t \in [0, \infty)$, *basis of* $\mathcal{H}(t)$. *Let also* $\mathcal{H}_s(t) = span\{\phi_1(t), \phi_2(t), \ldots, \phi_m(t)\}$ *and* $\mathcal{H}_f(t) = span\{\phi_{m+1}(t), \phi_{m+2}(t), \ldots, \}$ *be two modal subspaces of* $\mathcal{H}(t)$ *such that* $\mathcal{H}_s(t) \oplus \mathcal{H}_f(t) = \mathcal{H}(t)$, *and define the orthogonal (pointwise in time) projection operators* $P_s : \mathcal{H}(t) \rightarrow \mathcal{H}_s(t)$ *and* $P_f : \mathcal{H}(t) \rightarrow \mathcal{H}_f(t)$ *so that the state* x *of the system of Eq.2.12 can be written as* $x = x_s + x_f = P_s x + P_f x$. *Using this decomposition for* x, *we assume that*

the system of Eq.2.12 can be written in the following singularly perturbed form:

$$\begin{aligned} \frac{dx_s}{dt} &= \mathcal{A}_s(t)x_s + \mathcal{B}_s(t)u + f_s(t, x_s, x_f), \;\; x_s(0) = P_s x_0 \\ \epsilon\frac{\partial x_f}{\partial t} &= \mathcal{A}_{f\epsilon}(t)x_f + \epsilon\mathcal{B}_f(t)u + \epsilon f_f(t, x_s, x_f), \;\; x_f(0) = P_f x_0 \\ y_c &= \mathcal{C}(t)(x_s + x_f), \;\; y_m = \mathcal{S}(t)(x_s + x_f) \end{aligned} \tag{2.14}$$

where $\mathcal{A}_s(t) = P_s\mathcal{A}(t)$, $\mathcal{B}_s(t) = P_s\mathcal{B}(t)$, $f_s(t, x_s, x_f) = P_s f(t, x) + P_s\mathcal{A}(t)x_f$, $\mathcal{A}_{f\epsilon}(t) = \epsilon P_f\mathcal{A}(t)$ *is an unbounded differential operator,* $\mathcal{B}_f(t) = P_f\mathcal{B}(t)$ *and* $f_f(t, x_s, x_f) = P_f f(t, x) + P_f\mathcal{A}(t)x_s$, $\epsilon \ll 1$ *and the operators* $\mathcal{A}_s(t)$, $\mathcal{A}_{f\epsilon}(t)$ *generate semigroups with growth rates which are of the same order of magnitude.*

The notation $\frac{\partial x_f}{\partial t}$ is used to denote that the state x_f belongs in an infinite-dimensional space.

Remark 2.2: The statement "the operators $\mathcal{A}_s(t)$, $\mathcal{A}_{f\epsilon}(t)$ generate semigroups with growth rates which are of the same order of magnitude" in assumption 2.2 means that the solutions x_s and x_f of the systems $\dot{x}_s = \mathcal{A}_s(t)x_s$ and $\dot{x}_f = \mathcal{A}_{f\epsilon}(t)x_f$, respectively, satisfy: $|x_s(t)| \leq K|x_s(0)|e^{k_1 t}$, $\|x_f(t)\|_2 \leq K\|x_f(0)\|_2 e^{k_2 t}$, where K, k_1, k_2 are real numbers, and $O(k_1) = O(k_2)$. The norm notation $|x_s|$ denotes that x_s belongs in a finite-dimensional Hilbert space. This assumption ensures that the system of Eq.2.14 is in the standard singularly perturbed form (the reader may refer to the classic book [109] for results on singular perturbations).

Remark 2.3: In assumption 2.2, the basis, $\{\phi_j(t)\}$, $j = 1, \ldots, \infty$, of $\mathcal{H}(t)$ can be chosen from standard basis functions sets, or it can be computed by solving an eigenvalue problem of the form $\mathcal{A}(t)\phi_j(t) = \lambda_j(t)\phi_j(t)$ or by applying Karhunen-Loève expansion on an appropriately chosen ensemble of solutions of the system of Eq.2.12 (see [14, 34] for details on Karhunen-Loève expansion). The terms $P_s\mathcal{A}(t)x_f$ in $f_s(t, x_s, x_f)$ and $P_f\mathcal{A}(t)x_s$ in $f_f(t, x_s, x_f)$ account for the use of, possibly arbitrary,

basis function sets.

Remark 2.4: Assumption 2.2 can be thought of as a natural generalization of the following one (which was introduced in [45] for parabolic PDE systems with fixed spatial domains): "*the eigenspectrum of the spatial differential operator, $\mathcal{A}$ (i.e. $\mathcal{A}(t)$ with $\dot{l} \equiv 0$), can be partitioned into a finite set of eigenvalues which are close to the imaginary axis, and an infinite set of eigenvalues which are far in the left half-plane*", to parabolic PDE systems with time-dependent spatial domains. Furthermore, for parabolic PDE systems with fixed spatial domains, ϵ was defined as $\epsilon = \frac{|Re\ \lambda_1|}{|Re\ \lambda_{m+1}|}$, where λ_1, λ_{m+1} are the eigenvalues of the operator $\mathcal{A}$, which are obtained by solving the eigenvalue problem $\mathcal{A}\phi_j = \lambda_j \phi_j$, where ϕ_j is an eigenfunction. Generalizing this definition to systems with time-dependent spatial domains, one can define $\epsilon = \sup_{t\in[0,\infty)} \frac{|Re\ \lambda_1(t)|}{|Re\ \lambda_{m+1}(t)|}$, where $\lambda_1(t)$ is the largest eigenvalue of the matrix $\mathcal{A}_s(t)$ and $\lambda_{m+1}(t)$ is the largest eigenvalue of the operator (infinite range matrix) $P_f\mathcal{A}(t)$. Moreover, the presence of ϵ in the right-hand-side of the x_f-subsystem in Eq.2.14 is consistent with the development in the case of parabolic PDE systems with fixed spatial domains [45], where a structurally similar system to the one of Eq.2.14 was derived by using $\epsilon = \frac{|Re\ \lambda_1|}{|Re\ \lambda_{m+1}|}$.

2.3 Nonlinear model reduction

In this section, we construct nonlinear low-dimensional ODE systems that accurately reproduce the dynamics and solutions of the infinite dimensional system of Eq.2.14. The construction of the ODE systems is achieved by generalizing a nonlinear model reduction procedure introduced in [45] for systems with fixed spatial domains, to the class of systems of Eq.2.14. The nonlinear model reduction procedure is based on a combination of standard Galerkin's method with the concept of approximate inertial

manifold and provides a characterization of the accuracy of the ODE systems in terms of ϵ.

We begin with the introduction of the concepts of inertial manifold and approximate inertial manifold. Our definition of the concept of inertial manifold is a direct generalization of the one used in [45] (see also [168]) for systems with time-invariant differential operators, to systems with time-varying operators (the reader may also refer to [102, 163] for concepts of IMs for infinite-dimensional systems with time-varying forcing inputs). An inertial manifold $\mathcal{M}(t)$ for the system of Eq.2.14 is a subset of $\mathcal{H}(t)$, which satisfies the following properties:

i) $\mathcal{M}(t)$ is a finite-dimensional Lipschitz manifold,

ii) $\mathcal{M}(t)$ is a graph of a Lipschitz function $\Sigma(t, x_s, u, \epsilon)$ mapping $[0, \infty) \times \mathcal{H}_s(t) \times \mathbb{R}^l \times (0, \epsilon^*]$ into $\mathcal{H}_f(t)$ and for every solution $x_s(t), x_f(t)$ of Eq.2.14 with $x_f(0) = \Sigma(0, x_s(0), u, \epsilon)$, then

$$x_f(t) = \Sigma(t, x_s(t), u, \epsilon), \quad \forall\, t \geq 0 \tag{2.15}$$

iii) $\mathcal{M}(t)$ attracts every trajectory exponentially.

The evolution of the state x_f on $\mathcal{M}(t)$ is given by Eq.2.15, while the evolution of the state x_s is governed by the following finite-dimensional system (called inertial form):

$$\begin{aligned} \frac{dx_s}{dt} &= \mathcal{A}_s(t)x_s + \mathcal{B}_s(t)u + f_s(t, x_s, \Sigma(t, x_s, u, \epsilon)) \\ y_c &= \mathcal{C}(t)(x_s + \Sigma(t, x_s, u, \epsilon)), \quad y_m = \mathcal{S}(t)(x_s + \Sigma(t, x_s, u, \epsilon)) \end{aligned} \tag{2.16}$$

Assuming that $u(t)$ is smooth, by differentiating Eq.2.15 and utilizing Eq.2.14, we can compute $\Sigma(t, x_s, u, \epsilon)$ as the solution of the following partial differential equation:

$$\begin{aligned} \epsilon\frac{\partial \Sigma}{\partial t} &= -\epsilon\frac{\partial \Sigma}{\partial x_s}[\mathcal{A}_s(t)x_s + \mathcal{B}_s(t)u + f_s(t, x_s, \Sigma)] - \epsilon\frac{\partial \Sigma}{\partial u}\dot{u} \\ &\quad + \mathcal{A}_{fs}(t)\Sigma + \epsilon\mathcal{B}_f(t)u + \epsilon f_f(t, x_s, \Sigma) \end{aligned} \tag{2.17}$$

which $\Sigma(t, x_s, u, \epsilon)$ has to satisfy for all $t \in [0, \infty)$, $x_s \in \mathcal{H}_s(t)$, $u \in \mathbb{R}^l$, $\epsilon \in (0, \epsilon^*]$.

From the complex structure of Eq.2.17, it is obvious that the computation of the explicit form of $\Sigma(t, x_s, u, \epsilon)$ is impossible in most practical applications. To circumvent this problem, a procedure based on singular perturbations (introduced in [45]) is used to compute approximations of $\Sigma(t, x_s, u, \epsilon)$ (approximate inertial manifolds) and approximations of the inertial form, of desired accuracy. More specifically, the vectors $\Sigma(t, x_s, u, \epsilon)$ and u are expanded in a power series in ϵ:

$$\begin{aligned} u &= \bar{u}_0 + \epsilon\bar{u}_1 + \epsilon^2\bar{u}_2 + \cdots + \epsilon^k\bar{u}_k + O(\epsilon^{k+1}) \\ \Sigma(t, x_s, u, \epsilon) &= \Sigma_0(t, x_s, u) + \epsilon\Sigma_1(t, x_s, u) \\ &\quad + \epsilon^2\Sigma_2(t, x_s, u) + \cdots + \epsilon^k\Sigma_k(t, x_s, u) + O(\epsilon^{k+1}) \end{aligned} \tag{2.18}$$

where $\bar{u}_k$, Σ_k are smooth vector functions. Substituting the expressions of Eq.2.18 into Eq.2.17, and equating terms of the same power in ϵ, one can obtain approximations of $\Sigma(t, x_s, u, \epsilon)$ up to a desired order. Substituting the $O(\epsilon^{k+1})$ approximation of $\Sigma(t, x_s, u, \epsilon)$ and u into Eq.2.16, the following approximation of the inertial form is obtained:

$$\begin{aligned} \frac{dx_s}{dt} &= \mathcal{A}_s(t)x_s + \mathcal{B}_s(t)\left(\bar{u}_0 + \epsilon\bar{u}_1 + \cdots + \epsilon^k\bar{u}_k\right) \\ &\quad + f_s(t, x_s, \Sigma_0(t, x_s, u) + \epsilon\Sigma_1(t, x_s, u) + \cdots + \epsilon^k\Sigma_k(t, x_s, u)) \\ y_c &= \mathcal{C}(t)(x_s + \Sigma_0(t, x_s, u) + \epsilon\Sigma_1(t, x_s, u) + \cdots + \epsilon^k\Sigma_k(t, x_s, u)) \\ y_m &= \mathcal{S}(t)(x_s + \Sigma_0(t, x_s, u) + \epsilon\Sigma_1(t, x_s, u) + \cdots + \epsilon^k\Sigma_k(t, x_s, u)) \end{aligned} \tag{2.19}$$

In order to characterize the discrepancy between the solution of the open-loop finite-dimensional system of Eq.2.19 and the solution of the x_s-subsystem of the open-loop infinite-dimensional system of Eq.2.14, we need to impose the following stability requirements on the slow and fast dynamics of the system of Eq.2.14.

Assumption 2.3 states that the system of Eq.2.19 with $u(t) \equiv 0$ and $\epsilon = 0$ is exponentially stable.

Assumption 2.3: *The finite-dimensional system of Eq.2.19 with* $u(t) \equiv 0$ *and* $\epsilon = 0$

is exponentially stable, in the sense that there exists a smooth Lyapunov function $V : \mathcal{H}_s(t) \rightarrow \mathbb{R}_{\geq 0}$ *and a set of positive real numbers* $(a_1, a_2, a_3, a_4, a_5)$*, such that for all* $x_s \in \mathcal{H}_s(t)$ *that satisfy* $|x_s| \leq a_5$*, the following conditions hold:*

$$\begin{aligned} a_1|x_s|^2 &\leq V(t, x_s) \leq a_2|x_s|^2 \\ \dot{V}(t, x_s) &= \frac{\partial V}{\partial t} + \frac{\partial V}{\partial x_s}[\mathcal{A}_s(t)x_s + f_s(t, x_s, 0)] \leq -a_3|x_s|^2 \\ |\frac{\partial V}{\partial x_s}| &\leq a_4|x_s| \end{aligned} \tag{2.20}$$

To state our stability requirements on the fast dynamics of Eq.2.14, we write the system of Eq.2.14 in the fast time-scale $\tau = \frac{t}{\epsilon}$ and set $\epsilon = 0$, to derive the following infinite-dimensional fast subsystem:

$$\frac{\partial x_f}{\partial \tau} = \mathcal{A}_{f\epsilon}(t)x_f \tag{2.21}$$

Assumption 2.4 that follows states that the above system is exponentially stable, uniformly in $t \in [0, \infty)$.

Assumption 2.4: *The fast subsystem of Eq.2.21 is exponentially stable, uniformly in* $t \in [0, \infty)$*, in the sense that there exists a Lyapunov functional* $W : \mathcal{H}_f(t) \rightarrow \mathbb{R}_{\geq 0}$ *and a set of positive real numbers* $(b_1, b_2, b_3, b_4, b_5, b_6)$*, such that for all* $x_f \in \mathcal{H}_f(t)$ *that satisfy* $\|x_f\|_2 \leq b_6$*, the following conditions hold:*

$$\begin{aligned} b_1\|x_f\|_2^2 &\leq W(t, x_f) \leq b_2\|x_f\|_2^2 \\ \frac{\partial W}{\partial x_f}\mathcal{A}_{f\epsilon}(t)x_f &\leq -b_3\|x_f\|_2^2 \\ \|\frac{\partial W}{\partial x_f}\|_2 &\leq b_4\|x_f\|_2 \\ \|\frac{\partial W}{\partial t}\|_2 &\leq b_5\|x_f\|_2^2 \end{aligned} \tag{2.22}$$

We are now in a position to state the main result of this section, which characterizes the discrepancy between the solution obtained from the open-loop system of

Eq.2.19 and the expansion for $\Sigma(t, x_s, u, \epsilon)$ of Eq.2.18 and the solution of the infinite-dimensional open-loop system of Eq.2.14, in terms of ϵ. The proof is given in Appendix B.

Proposition 2.1: *Consider the system of Eq.2.12 with* $u(t) \equiv 0$ *and suppose that assumptions 2.1, 2.2, 2.3 and 2.4 hold. Then, there exist positive real numbers* μ_1, μ_2, ϵ^* *such that if* $|x_s(0)| \leq \mu_1$, $\|x_f(0)\|_2 \leq \mu_2$ *and* $\epsilon \in (0, \epsilon^*]$, *then the solutions* $x_s(t), x_f(t)$ *of the system of Eq.2.14 satisfy* $\forall\, t \in [t_b, \infty)$*:*

$$\begin{aligned} x_s(t) &= \tilde{x}_s(t) + O(\epsilon^{k+1}) \\ x_f(t) &= \tilde{x}_f(t) + O(\epsilon^{k+1}) \end{aligned} \tag{2.23}$$

where t_b *is the time required for* $x_f(t)$ *to approach* $\tilde{x}_f(t)$, $\tilde{x}_s(t)$ *is the solution of Eq.2.19 with* $u(t) \equiv 0$, *and* $\tilde{x}_f(t) = \Sigma_0(t, \tilde{x}_s, 0) + \epsilon\Sigma_1(t, \tilde{x}_s, 0) + \epsilon^2\Sigma_2(t, \tilde{x}_s, 0) + \cdots + \epsilon^k\Sigma_k(t, \tilde{x}_s, 0)$.

Remark 2.5: An estimate of ϵ^* can be obtained, in principle, from the proof of the theorem. However, such an estimate is typically conservative, and thus, it is useful to check its appropriateness through computer simulations.

Remark 2.6: Utilizing the result of proposition 2.1, one can show that $x(t) = \tilde{x}(t) + O(\epsilon^{k+1})$, $\forall\, t \geq t_b$, where $x(t)$ is the solution of the open-loop infinite-dimensional system of Eq.2.12 and $\tilde{x}(t) = \tilde{x}_s(t) + \tilde{x}_f(t)$ is the solution obtained from the $O(\epsilon^{k+1})$ approximation of the open-loop inertial form (Eq.2.19) and the inertial manifold (Eq.2.18).

Remark 2.7: For $k = 0$, the expansion of Eq.2.18 yields $\Sigma(t, x_s, u, \epsilon) = \Sigma_0(t, x_s, u) = 0$, and the corresponding approximate inertial form is:

$$\begin{aligned} \frac{dx_s}{dt} &= \mathcal{A}_s(t)x_s + \mathcal{B}_s(t)\bar{u}_0 + f_s(t, x_s, 0) \\ y_c &= \mathcal{C}(t)x_s, \;\; y_m = \mathcal{S}(t)x_s \end{aligned} \tag{2.24}$$

The above system is identical to the one obtained by directly applying Galerkin's method to the system of Eq.2.14 and does not utilize any information about the

structure of the fast subsystem, thus yielding solutions which are only $O(\epsilon)$ close to the solutions of the open-loop system of Eq.2.12 (result of proposition 2.1 with $k = 0$). On the other hand, for $k = 1$, the expansion of Eq.2.18 yields $\Sigma(t, x_s, u, \epsilon) = \epsilon\Sigma_1(t, x_s, \bar{u}_0) = -\epsilon(\mathcal{A}_{f\epsilon})^{-1}(t)[\mathcal{B}_f(t)\bar{u}_0 + f_f(t, x_s, 0)]$ (note that from assumption 2.4 we have that $(\mathcal{A}_{f\epsilon})^{-1}(t)$ exists and is bounded, $\forall\ t \geq 0$), and the corresponding approximate inertial form is:

$$\begin{aligned} \frac{dx_s}{dt} &= \mathcal{A}_s(t)x_s + \mathcal{B}_s(t)(\bar{u}_0 + \epsilon\bar{u}_1) + f_s(t, x_s, \epsilon\Sigma_1(t, x_s, \bar{u}_0)) \\ y_c &= C(t)(x_s + \epsilon\Sigma_1(t, x_s, \bar{u}_0)) \\ y_m &= S(t)(x_s + \epsilon\Sigma_1(t, x_s, \bar{u}_0)) \end{aligned} \tag{2.25}$$

The above system does utilize information about the structure of the fast subsystem, thereby yielding solutions which are $O(\epsilon^2)$ close to the solutions of the open-loop system of Eq.2.12.

Remark 2.8: The expansion of $\Sigma(t, x_s, u, \epsilon)$ in a power series in ϵ (Eq.2.18) is motivated and validated from the fact that as $\epsilon \to 0$ the inertial form of Eq.2.19 reduces to the system of Eq.2.24 obtained from the standard Galerkin's method, which ensures that the inertial form is well-posed with respect to ϵ. The expansion of u in a power series in ϵ in Eq.2.18 is motivated by our intention to appropriately modify the synthesis of the controller such that the outputs of the $O(\epsilon^{k+1})$ approximation of the closed-loop inertial form, y_{cs_i}, $i = 1, \ldots, l$, satisfy $\lim_{t\to\infty} |y_{cs_i} - v_i| = 0$, where v_i is the reference input.

2.4 Nonlinear output feedback control

In this section, we synthesize nonlinear finite-dimensional output feedback controllers that guarantee local exponential stability and force the controlled output of the closed-loop PDE system to follow, up to a desired accuracy, a prespecified response, provided

that ϵ is sufficiently small. The output feedback controllers are constructed through combination of state feedback controllers with state observers.

More specifically, we use the system of Eq.2.19 to synthesize nonlinear state feedback controllers of the following general form:

$$\begin{aligned} u &= \bar{u}_0 + \epsilon\bar{u}_1 + \epsilon^2\bar{u}_2 + \cdots + \epsilon^k\bar{u}_k \\ &= p_0(t, x_s) + Q_0(t, x_s)v \\ &\quad +\epsilon[p_1(t, x_s) + Q_1(t, x_s)v] + \cdots + \epsilon^k[p_k(t, x_s) + Q_k(t, x_s)v] \end{aligned} \tag{2.26}$$

where $p_0(t, x_s), \ldots, p_k(t, x_s)$ are smooth vector functions, $Q_0(t, x_s), \ldots, Q_k(t, x_s)$ are smooth matrices, and $v \in \mathbb{R}^l$ is the constant reference input vector. The nonlinear controllers are constructed by following a sequential procedure. Specifically, the component $\bar{u}_0 = p_0(t, x_s) + Q_0(t, x_s)v$ is initially synthesized on the basis of the $O(\epsilon)$ approximation of the inertial form; then the component $\bar{u}_1 = p_1(t, x_s) + Q_1(t, x_s)v$ is synthesized on the basis of the $O(\epsilon^2)$ approximation of the inertial form. In general, at the k-th step, the component $\bar{u}_k = p_k(t, x_s) + Q_k(t, x_s)v$ is synthesized on the basis of the $O(\epsilon^{k+1})$ approximation of the inertial form (Eq.2.19). The synthesis of $[p_\nu(t, x_s), Q_\nu(t, x_s)]$, $\nu = 0, \ldots, k$, so that a nonlinear controller of the form of Eq.2.26 guarantees local exponential stability and forces the output of the system of Eq.2.19 to follow a desired linear response, is performed by utilizing geometric control methods for nonlinear ODEs (the details of the controller synthesis can be found in [98, 134], and are omitted for brevity).

Since measurements of $\bar{x}(z, t)$ (and thus, $x_s(t)$) are usually not available in practice, we assume that there exists an L so that the nonlinear dynamical system:

$$\begin{aligned} \frac{d\eta}{dt} &= \mathcal{A}_s(t)\eta + \mathcal{B}_s(t)\left[\bar{u}_0 + \epsilon\bar{u}_1 + \epsilon^2\bar{u}_2 + \cdots + \epsilon^k\bar{u}_k\right] \\ &\quad +f_s(t, \eta, \epsilon\Sigma_1(t, \eta, u) + \epsilon^2\Sigma_2(t, \eta, u) + \cdots + \epsilon^k\Sigma_k(t, \eta, u)) \\ &\quad +L[y_m - \mathcal{S}(t)(\eta + \epsilon\Sigma_1(t, \eta, u) + \epsilon^2\Sigma_2(t, \eta, u) + \cdots + \epsilon^k\Sigma_k(t, \eta, u))] \end{aligned} \tag{2.27}$$

where η denotes an m-dimensional state vector, is a local exponential observer for the system of Eq.2.19 (i.e. the discrepancy $|\eta(t) - x_s(t)|$ tends exponentially to zero).

Theorem 2.1 that follows provides the synthesis formula of the output feedback controller and conditions that guarantee closed-loop stability in the case of considering an $O(\epsilon^2)$ approximation of the exact slow system for the synthesis of the controller. The derivation of synthesis formulas for higher-order approximations of the output feedback controller is notationally complicated, although conceptually straightforward, and thus, they are omitted for reasons of brevity. To state our result, we need to use the Lie derivative notation and the concepts of relative order and characteristic matrix (which are defined in appendix B), for the system of Eq.2.25. The proof of the theorem is given in appendix B.

Theorem 2.1: *Consider the parabolic PDE system of Eq.2.12, for which assumptions 2.1, 2.2 and 2.4 hold. Consider also the $O(\epsilon^2)$ approximation of the inertial form and assume that its characteristic matrix $C_1(t, x_s, \epsilon)$ is invertible $\forall\ t \in [0, \infty)$, $\forall\ x_s \in \mathcal{H}_s(t)$, $\forall\ \epsilon \in (0, \epsilon^*]$. Suppose also that the following conditions hold:*

1. *The roots of the equation:*

$$det(B(s)) = 0 \tag{2.28}$$

   where $B(s)$ is an $l \times l$ matrix whose (i,j)-th element is of the form $\sum_{k=0}^{r_i} \beta_{jk}^i s^k$, lie in the open left-half of the complex plane, where β_{jk}^i are adjustable controller parameters.

2. *The zero dynamics of the $O(\epsilon^2)$ approximation of the inertial form are locally exponentially stable.*

Then, there exist positive real numbers $\tilde{\mu}_1, \tilde{\mu}_2, \tilde{\epsilon}^*$ such that if $|x_s(0)| \leq \tilde{\mu}_1$, $\|x_f(0)\|_2 \leq$

$\tilde{\mu}_2$ and $\epsilon \in (0, \bar{\epsilon}^*]$, and $\eta(0) = x_s(0)$, the dynamic output feedback controller:

$$\begin{aligned}
\frac{d\eta}{dt} &= \mathcal{A}_s(t)\eta + \mathcal{B}_s(t)[\bar{u}_0(t,\eta) + \epsilon\bar{u}_1(t,\eta)] \\
&\quad + f_s(t,\eta,\epsilon(\mathcal{A}_{f\epsilon})^{-1}(t)[-\mathcal{B}_f(t)\bar{u}_0(t,\eta) - f_f(t,\eta,0)]) \\
&\quad + L\left(y - (\mathcal{S}(t)\eta + \mathcal{S}(t)\epsilon(\mathcal{A}_{f\epsilon})^{-1}(t)[-\mathcal{B}_f(t)\bar{u}_0(t,\eta) - f_f(t,\eta,0)])\right) \\
u &= \bar{u}_0(t,\eta) + \epsilon\bar{u}_1(t,\eta) := \{[\beta_{1r_1}\cdots\beta_{lr_l}]C_0(t,\eta)\}^{-1}\left\{v - \sum_{i=1}^{l}\sum_{k=0}^{r_i}\beta_{ik}L_{f_0}^k h_{0i}(t,\eta)\right\} \\
&\quad + \epsilon\{[\beta_{1r_1}\cdots\beta_{lr_l}]C_1(t,\eta,\epsilon)\}^{-1}\left\{v - \sum_{i=1}^{l}\sum_{k=0}^{r_i}\beta_{ik}L_{f_1}^k h_{1i}(t,\eta,\epsilon)\right\}
\end{aligned} \tag{2.29}$$

a) guarantees local exponential stability of the closed-loop system, and

b) ensures that the outputs of the closed-loop system satisfy for all $t \in [t_b, \infty)$:

$$y_{ci}(t) = y_{csi}(t) + O(\epsilon^2)\ ,\ i = 1,\ldots,l \tag{2.30}$$

where t_b is the time required for the off-manifold fast transients to decay to zero exponentially, and $y_{csi}(t)$ is the solution of:

$$\sum_{i=1}^{l}\sum_{k=0}^{r_i}\beta_{ik}\frac{d^k y_{csi}}{dt^k} = v \tag{2.31}$$

Remark 2.9: The implementation of the controller of Eq.2.29 requires to explicitly compute the vector function $\Sigma_1(t,\eta,\bar{u}_0)$. However, $\Sigma_1(t,\eta,\bar{u}_0)$ has an infinite-dimensional range and therefore cannot be implemented in practice. Instead a finite-dimensional approximation of $\Sigma_1(t,\eta,\bar{u}_0)$, say $\Sigma_{1\ell}(t,\eta,\bar{u}_0)$, can be derived by keeping the first $\tilde{m}$ elements of $\Sigma_1(t,\eta,\bar{u}_0)$ and neglecting the remaining infinite ones. Clearly, as $\tilde{m} \to \infty$, $\Sigma_{1\ell}(t,\eta,\bar{u}_0)$ approaches $\Sigma_1(t,\eta,\bar{u}_0)$. This implies that by picking $\tilde{m}$ to be sufficiently large, the controller of Eq.2.29 with $\Sigma_{1\ell}(t,\eta,\bar{u}_0)$ instead of $\Sigma_1(t,\eta,\bar{u}_0)$ guarantees stability and enforces the requirement of Eq.2.31 in the closed-loop infinite-dimensional system.

Remark 2.10: Note that in the presence of small initialization errors of the observer states (i.e. $\eta(0) \neq x_s(0)$), uncertainty in the model parameters and external disturbances, although a slight deterioration of the performance may occur, (i.e. the requirement of Eq.2.30 will not be exactly imposed in the closed-loop system), the output feedback controller of theorem 2.1 will continue to enforce exponential stability and asymptotic output tracking in the closed-loop system. Furthermore, the assumption that the characteristic matrix $C_1(t, x_s, \epsilon)$ is invertible $\forall\, t \in [0, \infty)$, $\forall\, x_s \in \mathcal{H}_s(t)$, $\forall\, \epsilon \in (0, \epsilon^*]$ is made in order to simplify the development and can be relaxed by using dynamic state feedback instead of static state feedback (see [98] for details).

Remark 2.11: The exponential stability of the closed-loop system guarantees that in the presence of small errors in process parameters, the states of the closed-loop system will be bounded. Furthermore, since the input/output spaces of the closed-loop system are finite-dimensional, and the controller of Eq.2.29 enforces an approximately linear input/output response between y_{c_i} and v_i, it is possible to implement a linear error feedback controller around the $(y_{c_i} - v_i)$ loop to ensure asymptotic offsetless output tracking in the closed-loop system, in the presence of constant unknown process parameters and unmeasured disturbance inputs. (the reader may refer to [180, 39] for recent results on control of quasi-linear parabolic PDE systems with uncertainty).

Remark 2.12: The nonlinear controller of Eq.2.29 possesses a robustness property with respect to fast and asymptotically stable unmodeled dynamics (i.e. the controller enforces exponential stability and output tracking in the closed-loop system, despite the presence of additional dynamics in the process model, as long as they are stable and sufficiently fast). This property of the controller can be rigorously established by analyzing the closed-loop system with the unmodeled dynamics using singular perturbations, and is of particular importance for many practical applica-

tions where unmodeled dynamics often occur due to actuator and sensor dynamics, fast process dynamics, etc. A comprehensive numerical study of the robustness of the nonlinear controller of Eq.2.29 in the presence of various sources of uncertainty for the Czochralski crystal growth process is presented in section 5.4.2.

Remark 2.13: We also note that the validity of the approach which we followed here to synthesize the nonlinear controller of Eq.2.29 relies on the large separation (expressed in terms of ϵ) of the slow and fast dynamics of the parabolic PDE system of Eq.2.5. This approach is not directly applicable to hyperbolic PDE systems where the eigenmodes cluster along vertical or nearly vertical asymptotes in the complex plane, and thus, the controller has to be modified to compensate for the destabilizing effect of the residual modes (see [13] for details).

Remark 2.14: Finally, we note that the nonlinear model reduction and control methods of subsections 4.2. and 4.3. can be readily generalized to parabolic PDE systems in which the manipulated inputs enter in a nonlinear fashion and can be represented by the following infinite-dimensional form:

$$\begin{aligned} \dot{x} &= \mathcal{A}(t)x + \mathcal{B}(t)g(u) + f(t,x), \;\; x(0) = x_0 \\ y_c &= \mathcal{C}(t)x, \;\; y_m = \mathcal{S}(t)x \end{aligned} \tag{2.32}$$

where $g(\cdot)$ is a nonlinear smooth function. This can be done by using $g(u)$ as a "virtual manipulated input", computing a virtual control action, u_v, for $g(u)$, and then solving through Newton's method the nonlinear equation $g_u = u_v$ at each time instant to compute the value of u (the reader may refer to chapter 5 for an application of this approach to the Czochralski crystal growth process where the manipulated input T_κ (κ-th heater temperature) enters the PDE in the form T_i^4 due to the nonlinear dependence of the radiation mechanism on temperature).

2.5 Application to a diffusion-reaction process with moving boundary

We consider a diffusion-reaction process with moving boundary which is described by the following parabolic PDE:

$$\frac{\partial \bar{x}}{\partial t} = \frac{\partial^2 \bar{x}}{\partial z^2} + \beta_T e^{-\frac{\gamma}{1+\bar{x}}} - \beta_T e^{-\gamma} + \beta_u (b(z,t)u(t) - \bar{x}) \tag{2.33}$$

subject to the Dirichlet boundary conditions:

$$\bar{x}(0,t) = 0, \quad \bar{x}(l(t),t) = 0 \tag{2.34}$$

and the initial condition:

$$\bar{x}(z,0) = \bar{x}_0(z) \tag{2.35}$$

where $\bar{x}$ is the state, $u = [u_1\ u_2]^T$ is the manipulated input vector, β_T, γ, β_u are dimensionless process parameters and $b(z,t) = [b_1(z,t)\ b_2(z,t)]$ are the actuator distribution functions. The spatial domain is assumed to change according to the relation:

$$l(t) = \pi(1.4 - 0.4e^{(-0.02t^{2.7})}) \tag{2.36}$$

(it can be easily seen that the above function satisfies the requirements of assumption 2.1) and the following typical values were given to the process parameters:

$$\beta_T = 85.0, \ \ \beta_U = 2.0, \ \ \gamma = 4.0 \tag{2.37}$$

For the system of Eq.2.33, the differential operator is of the form:

$$\begin{aligned} &\mathcal{A}(t)x = \frac{\partial^2 \bar{x}}{\partial z^2} + \frac{\dot{l}}{l} z \frac{\partial \bar{x}}{\partial z}, \\ &x \in D(\mathcal{A}) = \{x \in \mathcal{H}([0,l(t)]; \mathbb{R}); \quad x(0) = 0; \quad x(l(t)) = 0\} \end{aligned} \tag{2.38}$$

and a countable, $\forall\, t \in [0,\infty)$, orthogonal basis of $\mathcal{H}(t)$ is:

$$\phi_j(t,z) = \sqrt{\frac{2}{l(t)}} sin(j\ \frac{\pi}{l(t)}\ z), \quad j = 1,\ldots,\infty \tag{2.39}$$

Note that the above set of basis functions satisfies the conditions of assumption 2.2.

A 20-th order Galerkin truncation of the system of Eq.2.33 was used in our simulations (it was verified that further increase of the order of the Galerkin model provided no substantial improvement on the accuracy of the simulation results). It was found

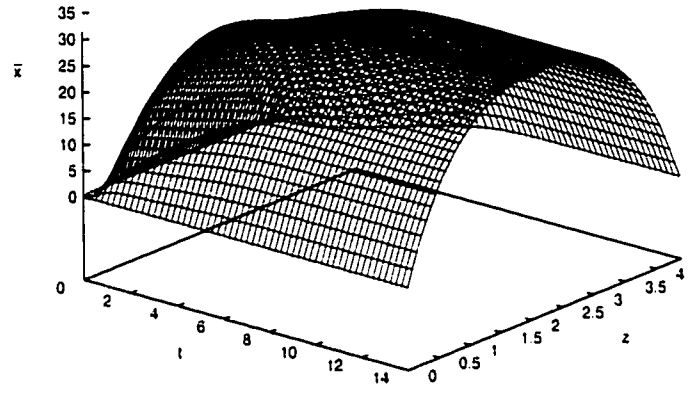

Figure 2.1: Evolution of state of open-loop system.

that the operating steady state $\bar{x}(z,t) = 0$ is an unstable one (Figure 2.1 shows the evolution of the open-loop state starting from initial conditions close to the steady state $\bar{x}(z,t) = 0$; the system moves to another stable steady state characterized by a maximum at $z = \frac{l(t)}{2}$). Moreover, the linearization of the system of Eq.2.33 around the steady-state $\bar{x}(z,t) = 0$ possesses *two* positive eigenvalues $\forall\, l(t) \in [\pi, 1.4\pi]$.

The control objective is to stabilize the system at the unstable spatially uniform steady state $\bar{x}(z,t) = 0$ by employing a nonlinear output feedback controller which uses a point measurement of the state at $z = 0.7l(t)$ (i.e. moving sensor with $s(z,t) = \delta(z - 0.7l(t))$, where $\delta(\cdot)$ is the standard Dirac function). Since the maximum open-loop value of $\bar{x}(z,t)$ occurs for $z = \frac{l(t)}{2}$ and the first two modes of the process are

unstable $\forall\, l(t) \in [\pi, 1.4\pi]$, the controlled outputs were defined as:

$$\begin{aligned} y_{c_1}(t) &= \int_0^{l(t)} \sqrt{\frac{2}{l(t)}} sin(\frac{\pi}{l(t)} z) \bar{x}(z,t) dz \\ y_{c_2}(t) &= \int_0^{l(t)} \sqrt{\frac{2}{l(t)}} sin(2\frac{\pi}{l(t)} z) \bar{x}(z,t) dz \end{aligned} \tag{2.40}$$

The actuator distribution functions were taken to be $b_1(z,t) = 1$ (uniform in space, distributed control action) and $b_2(z,t) = \delta(z - \frac{2}{3} l(t))$ (moving point control actuation).

Several simulations runs were performed to evaluate: a) the reduction on the order of the controller achieved when the controller is synthesized on the basis of ODE models derived from combination of Galerkin's method with approximate inertial manifolds, and b) the choice of using moving control actuators and measurement sensors. In all the simulation runs, the process was assumed to be at a nonzero initial condition.

We initially employed the standard Galerkin's method to derive an approximate ODE system that was used for the synthesis of a nonlinear output feedback controller. It was found that the *lowest-order* model obtained from standard Galerkin's method which leads to the synthesis of a controller that stabilizes the open-loop system at $\bar{x}(z,t) = 0$ is 8 (i.e. $m = 8$, $\tilde{m} = 0$). Figures 2.2 and 2.3 show the evolution of the state of the closed-loop system and the profile of the manipulated input under an 8-th order nonlinear output feedback controller of the form of Eq.2.29 (the controller parameters are $\epsilon = 0$, $\beta_{10} = [1.00\ 0.00]^T$, $\beta_{11} = [0.25\ 0.00]^T$, $\beta_{20} = [0.00\ 1.00]^T$, $\beta_{21} = [0.00\ 0.25]^T$ and $L = [0.7\ -25.0\ -9.6\ 0.0\ \cdots\ 0.0]^T$). It is clear that this controller stabilizes the state of the system at $\bar{x}(z,t) = 0$.

We subsequently used the proposed combination of Galerkin's method with approximate inertial manifolds to derive an ODE system which was used for the synthesis of a nonlinear output feedback controller. For the case of using an $O(\epsilon^2)$ ap-

proximation of the AIM, it was found that the *lowest-order* ODE model, which leads to the synthesis of a controller that stabilizes the open-loop system at $\bar{x}(z,t) = 0$, is

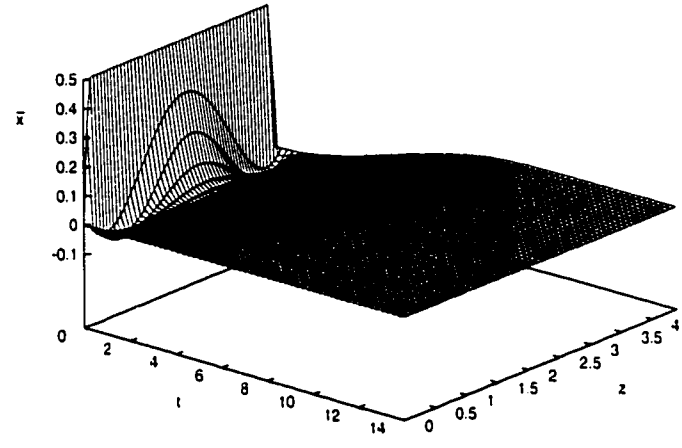

Figure 2.2: Evolution of state of closed-loop system under an 8-th order nonlinear time-varying output feedback controller synthesized on the basis of an ODE system obtained from standard Galerkin's method.

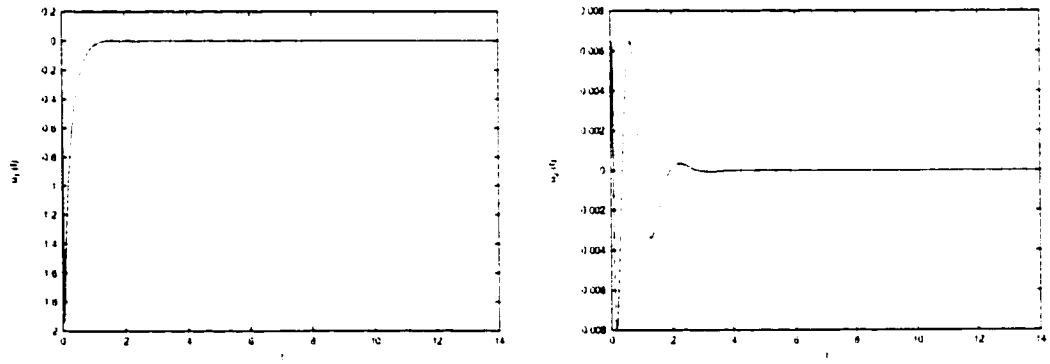

Figure 2.3: Manipulated input profiles of 8-th order nonlinear time-varying output feedback controller.

one of order 5 which uses a 6-th order approximation for x_f (i.e. $m = 5$ and $\tilde{m} = 6$). Figures 2.4 and 2.5 show the evolution of the state of the closed-loop system and the profile of the manipulated input under a 5-th order controller of the form of Eq.2.29 (the controller parameters are $\epsilon = 0.0278$, $\beta_{10} = [1.00\ 0.00]^T$, $\beta_{11} = [0.25\ 0.00]^T$,

$\beta_{20} = [0.00\ 1.00]^T$, $\beta_{21} = [0.00\ 0.25]^T$ and $L = [0.7\ -25.0\ -9.6\ 0.0\ \cdots\ 0.0]^T$). The controller clearly regulates the system at $\bar{x}(z,t) = 0$.

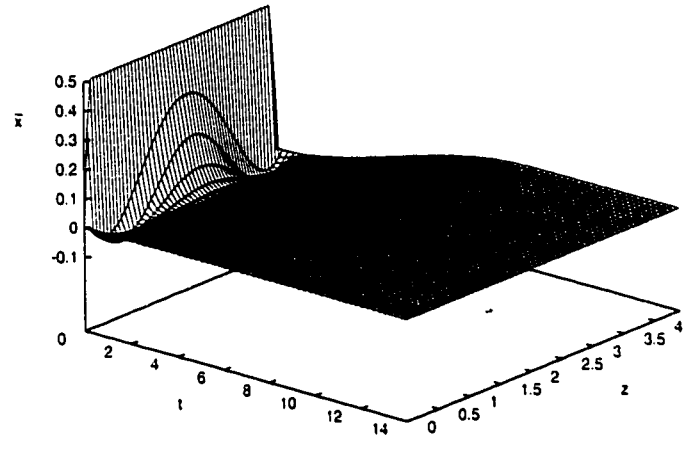

Figure 2.4: Evolution of state of closed-loop system under a 5-th order nonlinear time-varying output feedback controller synthesized on the basis of an ODE system obtained from combination of Galerkin's method with approximate inertial manifolds.

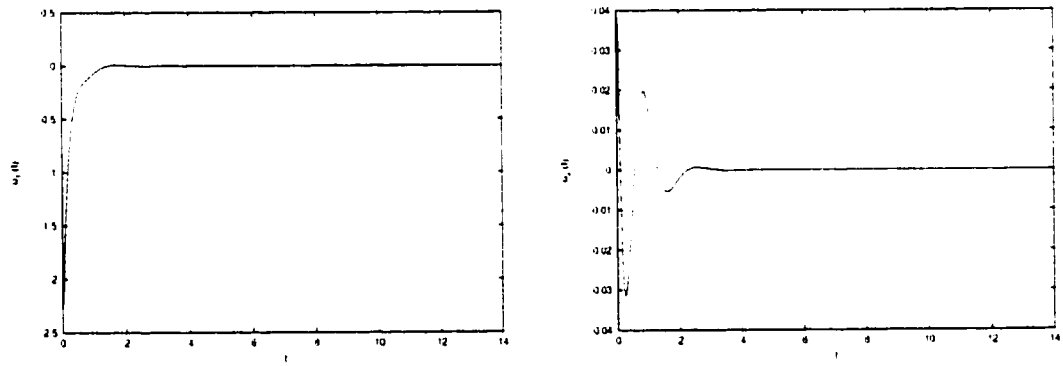

Figure 2.5: Manipulated input profiles of 5-th order nonlinear time-varying output feedback controller.

We also implemented on the process a nonlinear output feedback controller which was synthesized on the basis of an 8-th order Galerkin truncation of the system of Eq.2.33 with $l(t) = \pi$ (i.e. the domain is assumed to be fixed in the design of the controller). Figure 2.6 shows the evolution of the state of the closed-loop system and

Figure 2.7 shows the corresponding manipulated input profiles. Clearly, this controller leads to closed-loop instability because the PDE system becomes "uncontrollable" (i.e. the position of the point control actuator approaches the location of the zero of the second eigenfunction at $z = 0.5l(5.29)$ which makes the stabilization of the second unstable mode impossible, thereby leading to closed-loop instability). We finally note that similar closed-loop instabilities were observed when: a) the nonlinear output feedback controller was synthesized on the basis of an 8-th order Galerkin truncation of the system of Eq.2.33 with $l(t)$ equal to 1.2π and 1.4π, and b) the nonlinear output feedback controller was synthesized on the basis of a 5-th order model obtained from combination of Galerkin's method with AIMs ($m = 5$, $\tilde{m} = 6$), for $l(t) = \pi,\ 1.2\pi,\ 1.4\pi$.

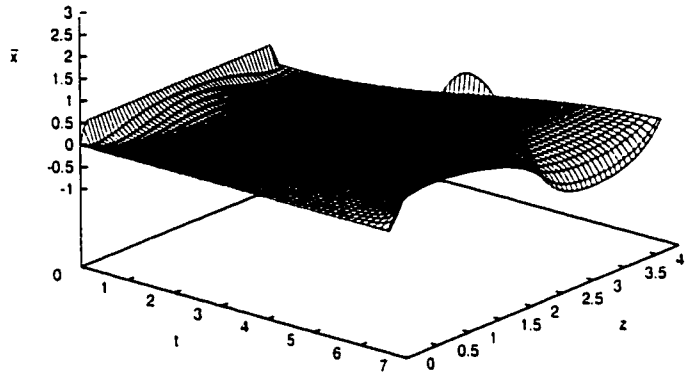

Figure 2.6: Evolution of state of closed-loop system under an 8-th order nonlinear output feedback controller, synthesized under the assumption of fixed spatial domain (i.e. $l(t) = \pi,\ \forall\ t \geq 0$).

From the results of the simulation study, it is evident that the combination of Galerkin's method and approximate inertial manifolds to derive ODE models used for controller synthesis, leads to a significant reduction on the order of the stabilizing controller, while the use of moving control actuators and sensors allows controlling

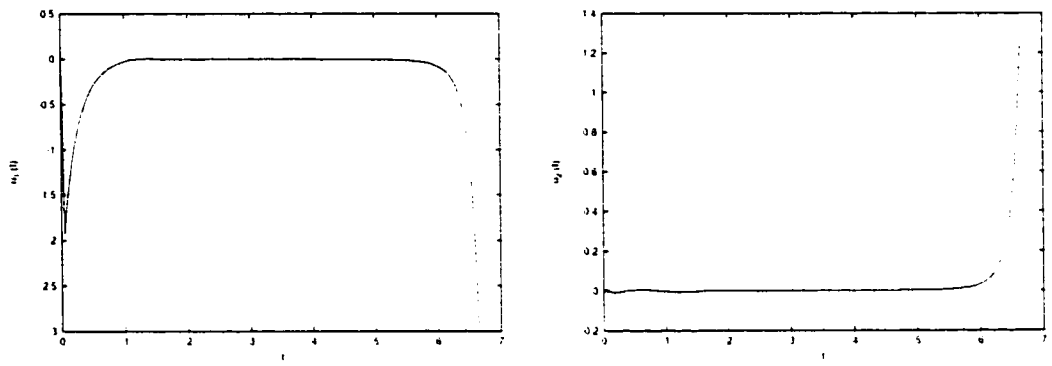

Figure 2.7: Manipulated input profiles of 8-th order nonlinear output feedback controller synthesized under the assumption of fixed spatial domain (i.e. $l(t) = \pi$, $\forall\, t \geq 0$).

processes with moving boundaries, which are difficult to control with actuators and sensors placed at fixed locations.

2.6 Conclusions

In this chapter, a methodology was developed for the synthesis of nonlinear finite-dimensional time-varying output feedback controllers for systems consisting of quasi-linear parabolic partial differential equations (PDEs) with time-dependent spatial domains, whose dynamics can be separated into slow and fast ones. Initially, a nonlinear model reduction procedure, based on combination of Galerkin's method with the concept of approximate inertial manifold, was employed for the derivation of ODE systems that yield solutions which are close, up to a desired accuracy, to the ones of the PDE system, for almost all times. Then, these ODE systems were used as the basis for the explicit construction of nonlinear time-varying output feedback controllers via geometric control methods. The controllers guaranteed stability and enforced the output of the closed-loop parabolic PDE system to follow, up to a desired accuracy, a prespecified response for almost all times, provided that the separation

of the slow and fast dynamics was sufficiently large. Differences in the nature of the model reduction and control problems between parabolic PDE systems with fixed and moving spatial domains were identified and discussed. The proposed control method was used to stabilize an unstable steady-state of a diffusion-reaction process with time-dependent spatial domain, and was shown to lead to a significant reduction on the order of the stabilizing controller, as well as to outperform a controller synthesis method which does not account for the variation of the spatial domain.

Chapter 3

Robust Control of Parabolic PDE Systems with Time-Dependent Spatial Domains

3.1 Introduction

This chapter focuses on a broad class of uncertain quasi-linear parabolic PDE systems with time-dependent spatial domains whose dynamics can be partitioned into slow and fast ones. Such systems arise naturally in the modeling of diffusion-reaction processes with moving boundaries. The objective is to develop a general method for the synthesis of robust time-varying static output feedback controllers. Initially, Galerkin's method is used to derive an approximate ODE model that describes the slow dynamics of the parabolic PDE for all times. Then, under the assumption that the number of available measurements is equal to the number of slow modes for all times, the approximate ODE model is used to synthesize robust static output feedback controllers through combination of geometric techniques and Lyapunov's direct method. We show that the proposed controllers guarantee boundedness of the state

and output tracking with arbitrary degree of asymptotic attenuation of the effect of the uncertain variables on the controlled output of the closed-loop system, provided that the separation between the slow and fast dynamical phenomena is sufficiently large. The proposed controllers are successfully applied to a typical diffusion-reaction process with moving boundary and uncertainty, and are shown to outperform controllers that do not account for the presence of uncertainty and the variation of the spatial domain with time.

3.2 Preliminaries

We consider quasi-linear uncertain parabolic PDE systems with uncertain variables of the form:

$$\begin{aligned} \frac{\partial \bar{x}}{\partial t} &= A\frac{\partial \bar{x}}{\partial z} + B\frac{\partial^2 \bar{x}}{\partial z^2} + wb(z,t)u + f(t,\bar{x}) + W(t,\bar{x},r(z)\theta(t)) \\ y_{c_i} &= \int_0^{l(t)} c_i(z,t)k\bar{x}dz, \quad i = 1,\ldots,l \\ y_{m_\kappa} &= \int_0^{l(t)} s_\kappa(z,t)\omega\bar{x}dz, \quad \kappa = 1,\ldots,q \end{aligned} \tag{3.1}$$

subject to the boundary conditions:

$$\begin{aligned} C_1\bar{x}(0,t) + D_1\frac{\partial \bar{x}}{\partial z}(0,t) &= R_1 \\ C_2\bar{x}(l(t),t) + D_2\frac{\partial \bar{x}}{\partial z}(l(t),t) &= R_2 \end{aligned} \tag{3.2}$$

and the initial condition:

$$\bar{x}(z,0) = \bar{x}_0(z) \tag{3.3}$$

where $\bar{x}(z,t) = [\bar{x}_1(z,t) \cdots \bar{x}_n(z,t)]^T$ denotes the vector of state variables, $[0,l(t)] \subset \mathbb{R}$ is the domain of definition of the process, $z \in [0,l(t)]$ is the spatial coordinate, $t \in [0,\infty)$ is the time, $u = [u_1\ u_2 \cdots u_l]^T \in \mathbb{R}^l$ denotes the vector of manipulated inputs, $y_{c_i} \in \mathbb{R}$ denotes the i-th controlled output, $\theta(t) = [\theta_1(t) \cdots \theta_q(t)] \in \mathbb{R}^q$ denotes the vector of uncertain variables, which may include unknown/partially known process

model parameters or exogenous disturbances, and $y_{m_\kappa} \in \mathbb{R}$ denotes the κ-th measured output. $\frac{\partial \bar{x}}{\partial z}$, $\frac{\partial^2 \bar{x}}{\partial z^2}$ denote the first- and second-order spatial derivatives of $\bar{x}$, $f(t, \bar{x})$, $W(t, \bar{x}, r(z)\theta(t))$ are nonlinear vector functions, $l(t)$ is a known and smooth function of time which describes the change of the domain size, k, w, ω are constant vectors, A, B, C_1, D_1, C_2, D_2 are constant matrices, R_1, R_2 are column vectors, and $\bar{x}_0(z)$ is the initial condition.

$b(z,t)$ is a smooth vector function of the form $b(z,t) = [b_1(z,t)\ b_2(z,t)\ \dots\ b_l(z,t)]$, where $b_i(z,t)$ describes how the control action $u_i(t)$ is distributed in the interval $[0, l(t)]$ (e.g., point/distributed actuation), $r(z) = [r_1(z)\ \cdots\ r_q(z)]$, where $r_k(z)$ is a known smooth function of z which specifies the position of action of the uncertain variable $\theta_k(t)$ on $[\alpha, \beta]$, $c_i(z,t)$ is a known smooth function of (z,t) which is determined by the desired performance specifications in the interval $[0, l(t)]$ (e.g., regulation of the entire temperature profile of a crystal or regulation of the temperature at a specific point), and $s_\kappa(z,t)$ is a known smooth function of (z,t) which is determined by the location and type of the κ-th measurement sensor (e.g., point/distributed sensing). In the case of point actuation (i.e., the control action enters the system at a single point z_0, with $z_0 \in [0, l(t)]$), the function $b_i(z,t)$ is taken to be nonzero in a finite spatial interval of the form $[z_0 - \epsilon, z_0 + \epsilon]$, where ϵ is a small positive real number, and zero elsewhere in $[0, l(t)]$. A schematic of a typical process with moving boundaries is shown in Figure 3.1, in the case of point control actuators and sensors. Note that as the length of the process changes with time, the position of the control actuators and sensors may change with time which can be described mathematically with the time dependency of the controllers and sensors "shape" functions $b(z,t)$ and $s_\kappa(z,t)$.

Throughout the chapter, we will use the order of magnitude notation $O(\epsilon)$ (i.e., $\delta(\epsilon) = O(\epsilon)$ if there exist positive real numbers k_1 and k_2 such that the following hold

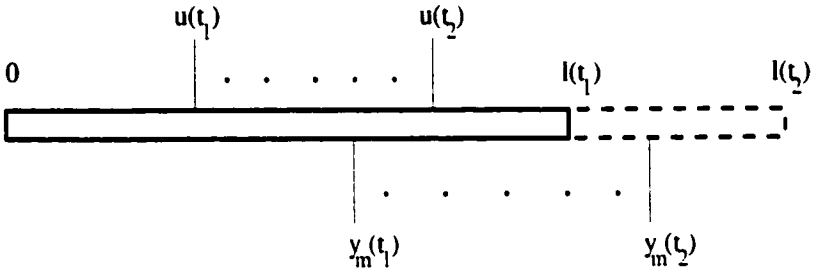

Figure 3.1: Schematic of a prototype system with time-dependent spatial domain, moving control actuators and moving measurement sensors.

$|\delta(\epsilon)| \leq k_1|\epsilon|$, $\forall\ |\epsilon| < k_2$) and $\|\theta\|$ denotes the $ess.sup.|\theta|$, $t \geq 0$ for any measurable function $\theta : \mathbb{R}_{\geq 0} \rightarrow \mathbb{R}^q$.

Our assumptions on the properties of $l(t)$ are precisely stated below:

Assumption 3.1: *$l(t)$ is a known smooth (i.e., $\dot{l}$ exists and is bounded, $\forall\ t \in [0, \infty)$) function of time which satisfies $l(t) \in (0, l_{max}]$, $\forall\ t\ \in [0, \infty)$, where l_{max} denotes the maximum length of the spatial domain.*

We consider the Hilbert space $\mathcal{H}(t)$ of n-dimensional vector functions defined on $[0, l(t)]$ that satisfy the boundary conditions of Eq.3.2, with inner product and norm:

$$\begin{aligned} (\omega_1, \omega_2) &= \int_0^{l(t)} (\omega_1(z), \omega_2(z))_{\mathbb{R}^n} dz \\ \|\omega_1\|_2 &= (\omega_1, \omega_1)^{\frac{1}{2}} \end{aligned} \tag{3.4}$$

where ω_1, ω_2 are two elements of $\mathcal{H}(t)$ and the notation $(\cdot, \cdot)_{\mathbb{R}^n}$ denotes the standard inner product in $\mathbb{R}^n$. In $\mathcal{H}(t)$, we define the state x as:

$$x(t) = \tilde{x}(z, t), \quad t > 0, \quad z \in [0, l(t)], \tag{3.5}$$

the time-varying operator:

$$\mathcal{A}(t)x = A\frac{\partial \bar{x}}{\partial z} + B\frac{\partial^2 \bar{x}}{\partial z^2} + \dot{l}(t)\frac{z}{l(t)}\frac{\partial \bar{x}}{\partial z},$$

$$x \in D(\mathcal{A}(t)) = \Big\{ x \in \mathcal{H}(t) : \; C_1\bar{x}(0,t) + D_1\frac{\partial \bar{x}}{\partial z}(0,t) = R_1, \qquad C_2\bar{x}(l(t),t) + D_2\frac{\partial \bar{x}}{\partial z}(l(t),t) = R_2 \Big\} \tag{3.6}$$

and the input, controlled output and measurement operators as:

$$\mathcal{B}(t)u = wb(t)u, \;\; \mathcal{C}(t)x = (c(t), kx), \;\; \mathcal{S}(t)x = (s(t), \omega x) \tag{3.7}$$

where $c(t) = [c_1(t)\; c_2(t)\; \cdots c_l(t)]^T$ and $s(t) = [s_1(t)\; s_2(t)\; \cdots s_q(t)]^T$, and $c_i(t) \in \mathcal{H}(t)$, $s_\kappa(t) \in \mathcal{H}(t)$. Then, in $\mathcal{H}(t)$, the system of Eqs.3.1-3.2-3.3 takes the form:

$$\begin{aligned} \dot{x} &= \mathcal{A}(t)x + \mathcal{B}(t)u + f(t,x) + \mathcal{W}(t,x,\theta), \;\; x(0) = x_0 \\ y_c &= \mathcal{C}(t)x, \;\; y_m = \mathcal{S}(t)x \end{aligned} \tag{3.8}$$

where $f(t,x(t)) = f(t,\bar{x}(z,t))$, $\mathcal{W}(t,x(t),\theta(t)) = W(t,\bar{x}(z,t),r(z)\theta(t))$ and $x_0 = \bar{x}_0(z)$.

Finally, we state our assumption that the dynamics of the infinite-dimensional system of Eq.3.8 can be partitioned into slow (which are finite-dimensional) and fast (which are infinite-dimensional) ones. We note that this assumption is usually satisfied by most diffusion-reaction processes with moving boundary (e.g., [2]).

Assumption 3.2: *Let* $\{\phi_j(t)\}$, $j = 1, \ldots, \infty$, *be an orthogonal and countable,* $\forall\, t \in [0,\infty)$, *basis of* $\mathcal{H}(t)$. *Let also* $\mathcal{H}_s(t) = span\{\phi_1(t), \phi_2(t), \ldots, \phi_m(t)\}$ *and* $\mathcal{H}_f(t) = span\{\phi_{m+1}(t), \phi_{m+2}(t), \ldots\}$ *be two subspaces of* $\mathcal{H}(t)$ *such that* $\mathcal{H}_s(t) \oplus \mathcal{H}_f(t) = \mathcal{H}(t)$, *and define the orthogonal (pointwise in time) projection operators* $P_s : \mathcal{H}(t) \to \mathcal{H}_s(t)$ *and* $P_f : \mathcal{H}(t) \to \mathcal{H}_f(t)$ *so that the state* x *of the system of Eq.3.8 can be written as* $x = x_s + x_f = P_s x + P_f x$. *Using this decomposition for* x, *we assume that the system*

of Eq.3.8 can be written in the following singularly perturbed form:

$$\begin{aligned}
\frac{dx_s}{dt} &= \mathcal{A}_s(t)x_s + \mathcal{B}_s(t)u + f_s(t,x_s,x_f) + \mathcal{W}_s(t,x_s,x_f,\theta), \;\; x_s(0) = P_s x_0 \\
\epsilon\frac{dx_f}{dt} &= \mathcal{A}_{fe}(t)x_f + \epsilon\mathcal{B}_f(t)u + \epsilon f_f(t,x_s,x_f) + \mathcal{W}_f(t,x_s,x_f,\theta), \;\; x_f(0) = P_f x_0 \\
y_c &= \mathcal{C}(t)(x_s + x_f), \;\; y_m = \mathcal{S}(t)(x_s + x_f)
\end{aligned} \tag{3.9}$$

where $\mathcal{A}_s(t) = P_s\mathcal{A}(t)$, $\mathcal{B}_s(t) = P_s\mathcal{B}(t)$, $f_s(t,x_s,x_f) = P_s f(t,x) + P_s\mathcal{A}(t)x_f$ *and* $\mathcal{W}_s(t,x_s,x_f,\theta) = P_s\mathcal{W}(t,x,\theta)$, $\mathcal{A}_{fe}(t) = \epsilon P_f\mathcal{A}(t)$ *is an unbounded differential operator,* $\mathcal{B}_f(t) = P_f\mathcal{B}(t)$, $f_f(t,x_s,x_f) = P_f f(t,x) + P_f\mathcal{A}(t)x_s$ *and* $\mathcal{W}_f(t,x_s,x_f,\theta) = P_f\mathcal{W}(t,x,\theta)$, $\epsilon \ll 1$ *and the operators* $\mathcal{A}_s(t)$, $\mathcal{A}_{fe}(t)$ *generate semigroups with growth rates which are of the same order of magnitude.*

Remark 3.1: Referring to assumption 3.1, we note that the requirement that the length of the domain is a smooth function of time is needed for the system of Eq.3.8 to be well posed in $\mathcal{H}(t)$, while the requirement that the length of the domain is always finite is necessary for the dominant dynamics of the parabolic PDE system to be described by a finite number of degrees of freedom (assumption 3.2). We note that both requirements are usually satisfied in practice: a typical example is the Czochralski crystal growth process where a seed crystal is pulled smoothly from the melt within a well-regulated thermal environment with the final crystal size being finite.

Remark 3.2: In the formulation of the PDE system of Eqs.3.1-3.3 in $\mathcal{H}(t)$, the time-varying term $\dot{l}(t)\frac{z}{l(t)}\frac{\partial\bar{x}}{\partial z}$ in the expression of $\mathcal{A}(t)$ (Eq.3.6) accounts for convective transport owing to the motion of the domain. This term makes $\mathcal{A}(t)$ an explicit function of time. We also note that in contrast to the case of parabolic PDE systems defined on a fixed spatial domain [39], we allow the actuator, performance specification and measurement sensor functions to depend explicitly on time (i.e., moving control

actuators and objectives, and measurement sensors).

Remark 3.3: We note that the representation of Eq.3.9 can be obtained by using basis functions, $\{\phi_j(t)\}$, $j = 1, \ldots, \infty$, of $\mathcal{H}(t)$ taken from standard basis functions sets, or computed by solving an eigenvalue problem of the form $\mathcal{A}(t)\phi_j(t) = \lambda_j(t)\phi_j(t)$, or computed by applying Karhunen-Loève expansion on an appropriately chosen ensemble of solutions of the system of Eq.3.8 (see [90, 3] for details on Karhunen-Loève expansion). The terms $P_s\mathcal{A}(t)x_f$ in $f_s(t, x_s, x_f)$ and $P_f\mathcal{A}(t)x_s$ in $f_f(t, x_s, x_f)$ account for the use of basis function sets which are not solutions of the problem $\mathcal{A}(t)\phi_j(t) = \lambda_j(t)\phi_j(t)$. We finally note that when $\phi_j(t)$ solve $\mathcal{A}(t)\phi_j(t) = \lambda_j(t)\phi_j(t)$, $\epsilon = \sup_{t\in[0,\infty)} \frac{|Re\ \lambda_1(t)|}{|Re\ \lambda_{m+1}(t)|}$, where $\lambda_1(t)$ is the largest eigenvalue of the matrix $\mathcal{A}_s(t)$ and $\lambda_{m+1}(t)$ is the largest eigenvalue of the operator (infinite range matrix) $P_f\mathcal{A}(t)$ (see example in section 4).

3.3 Robust nonlinear output feedback control

We consider the synthesis of robust time-varying output feedback control laws of the form:

$$u_0 = p_0(t, y_m) + Q_0(t, y_m)\bar{v} + r_0(t, y_m) \tag{3.10}$$

where $p_0(t, y_m)$, $r_0(t, y_m)$ are vector functions, $Q_0(t, y_m)$ is a matrix, and $\bar{v}$ is a vector of the form $\bar{v} = \mathcal{V}(v_i, v_i^{(1)}, \ldots, v_i^{(r_i)})$ where $\mathcal{V}(v_i, v_i^{(1)}, \ldots, v_i^{(r_i)})$ is a smooth vector function, $v_i^{(k)}$ is the $k-th$ time derivative of the external reference input v_i (which is assumed to be a smooth function of time) and r_i is a positive integer.

We initially state our stability requirements on the fast dynamics of Eq.3.9. To this end, we write the system of Eq.3.9 in the fast time-scale $\tau = \frac{t}{\epsilon}$ and set $\epsilon = 0$, to

derive the following infinite-dimensional fast subsystem:

$$\frac{\partial x_f}{\partial \tau} = \mathcal{A}_{f\epsilon}(t)x_f \tag{3.11}$$

Assumption 3.3: *The fast subsystem of Eq.3.11 is exponentially stable, uniformly in* $t \in [0, \infty)$.

Setting $\epsilon = 0$ in the system of Eq.3.9, we end up with the following m-dimensional slow system:

$$\begin{aligned} \frac{dx_s}{dt} &= \mathcal{A}_s(t)x_s + f_s(t, x_s, 0) + \mathcal{B}_s(t)u + \mathcal{W}_s(t, x_s, 0, \theta) \\ &=: F_0(t, x_s) + \sum_{i=1}^{l} \mathcal{B}_0^i(t)u_0^i + \mathcal{W}_0(t, x_s, 0, \theta) \\ y_{ci} &= C_i(t)x_s =: h_{i0}(t, x_s), \quad y_m = \mathcal{S}(t)x_s \end{aligned} \tag{3.12}$$

where the subscript 0 in $(F_0, \mathcal{B}_0^i, u_0^i, \mathcal{W}_0, h_{i0})$ denotes that they are elements of the $O(\epsilon)$ approximation of the x_s-subsystem of Eq.3.9 (see Theorem 3.1 below for a precise characterization of the accuracy of the system of Eq.3.12).

We now state three assumptions on the system of Eq.3.12 which are needed to synthesize a robust state feedback controller of the form of Eq.3.10. To simplify the statement of these assumptions, we use the Lie derivative of the scalar function $h_{i0}(t, x_s)$ with respect to the vector function $f_0(t, x_s)$, defined as $L_{f_0}h_{i0}(t, x_s) = \frac{\partial h_{i0}}{\partial x_s} f_0(t, x_s) + \frac{\partial h_{i0}}{\partial t}$ (this definition of Lie derivative was introduced in [134] and is different than the standard one used in [98] for the case of time-invariant h_{i0}, f_0). Furthermore, $L_{f_0}^k h_{i0}(t, x_s)$ denotes the k-th order Lie derivative and $L_{g_{0_i}} L_{f_0}^k h_{i0}(t, x_s)$ denotes the mixed Lie derivative, where $g_{0_i}(t, x_s)$ is a vector function.

Assumption 3.4: *Referring to the system of Eq.3.12, there exist a set of integers* $(r_1, r_2, \ldots, r_l)$ *and a coordinate transformation* $(\zeta, \eta) = T(x_s, \theta)$ *such that the repre-*

sentation of the system, in the coordinates (ζ, η)*, takes the form:*

$$
\begin{aligned}
\dot{\zeta}_1^{(1)} &= \zeta_2^{(1)} \\
&\vdots \\
\dot{\zeta}_{r_1-1}^{(1)} &= \zeta_{r_1}^{(1)} \\
\dot{\zeta}_{r_1}^{(1)} &= L_{F_0}^{r_1} h_{10}(t, x_s) + \sum_{i=1}^{l} L_{B_0^i} L_{F_0}^{r_1-1} h_{10}(t, x_s) u_0^i + L_{W_0} L_{F_0}^{r_1-1} h_{10}(t, x_s) \\
&\vdots \\
\dot{\zeta}_1^{(l)} &= \zeta_2^{(l)} \\
&\vdots \\
\dot{\zeta}_{r_l-1}^{(l)} &= \zeta_{r_l}^{(l)} \\
\dot{\zeta}_{r_l}^{(l)} &= L_{F_0}^{r_l} h_{l0}(t, x_s) + \sum_{i=1}^{l} L_{B_0^i} L_{F_0}^{r_l-1} h_{l0}(t, x_s) u_0^i + L_{W_0} L_{F_0}^{r_l-1} h_{l0}(t, x_s) \\
\dot{\eta}_1 &= \Psi_1(t, \zeta, \eta, \theta, \dot{\theta}) \\
&\vdots \\
\dot{\eta}_{m-\sum_i r_i} &= \Psi_{m-\sum_i r_i}(t, \zeta, \eta, \theta, \dot{\theta}) \\
y_{c_i} &= \zeta_1^{(i)}, \quad i = 1, \ldots, l
\end{aligned}
\tag{3.13}
$$

where $x_s = T^{-1}(\zeta, \eta, \theta)$, $\zeta = [\zeta^{(1)} \ \cdots \ \zeta^{(l)}]^T \in \mathbb{R}^{r_1+r_2\cdots+r_l}$, $\eta = [\eta_1 \ \cdots \ \eta_{m-\sum_i r_i}]^T \in \mathbb{R}^{m-(r_1+r_2\cdots+r_l)}$.

The above assumption is always satisfied for systems for which $r_i = 1$, for all $i = 1, \ldots, l$; this requirement can be easily achieved by selecting $b_i(z,t) \neq \phi_j(z,t)$, for $i = 1, \ldots, l$, $j = 2, \ldots, \infty$.

Referring to the system of Eq.3.13, we assume that the matrix:

$$
C_0(t, x_s) = \begin{bmatrix}
L_{B_0^1} L_{f_0}^{r_1-1} h_{10}(t, x_s) & \cdots & L_{B_0^l} L_{f_0}^{r_1-1} h_{10}(t, x_s) \\
L_{B_0^1} L_{f_0}^{r_2-1} h_{20}(t, x_s) & \cdots & L_{B_0^l} L_{f_0}^{r_2-1} h_{20}(t, x_s) \\
\vdots & \cdots & \vdots \\
L_{B_0^1} L_{f_0}^{r_l-1} h_{l0}(t, x_s) & \cdots & L_{B_0^l} L_{f_0}^{r_l-1} h_{l0}(t, x_s)
\end{bmatrix}
\tag{3.14}
$$

is nonsingular $\forall\ t \in [0, \infty)$, $\forall\ x_s \in \mathcal{H}_s(t)$. This assumption is made to simplify the presentation of the controller synthesis results and can be relaxed (see [98] for details). The following assumption is a standard one in geometric nonlinear con-

trol and states that the zero dynamics of the finite-dimensional slow subsystem is exponentially stable.

Assumption 3.5: *The dynamical system:*

$$\begin{aligned} \dot{\eta}_1 &= \Psi_1(t,\zeta,0,0,0) \\ &\vdots \\ \dot{\eta}_{m-\sum_i r_i} &= \Psi_{m-\sum_i r_i}(t,\zeta,0,0,0) \end{aligned} \tag{3.15}$$

is locally exponentially stable.

To design a nonlinear controller that explicitly compensates for the effect of uncertain variables, we need to assume the existence of a nonlinear time-varying bounding function which captures the size of the uncertain terms in the $\zeta-$subsystem of Eq.3.13. Such a bounding function may be computed from physical considerations, preliminary simulations and experimental data.

Assumption 3.6: *There exists a known function $c_0(t,x_s)$ such that the following condition holds:*

$$|[L_{W_0}L_{F_0}^{r_1-1}h_{10}(t,x_s)\ \cdots\ L_{W_0}L_{F_0}^{r_l-1}h_{l0}(t,x_s)]^T| \leq c_0(t,x_s) \tag{3.16}$$

for all $t \in [0,\infty)$, $x_s \in \mathcal{H}_s(t)$, $\theta \in \mathbb{R}^q$, $t \geq 0$.

The following assumption is needed in order to obtain estimates of the states x_s of the system of Eq.3.12 from the measurements y_{m_κ}, $\kappa = 1,\ldots,p$.

Assumption 3.7: *$p=m$ (i.e., the number of measurements is equal to the number of slow modes), and the inverse of the operator $S(t)$ for all $t \in [0,\infty)$ exists so that $\hat{x}_s = S^{-1}(t)y_m$, where $\hat{x}_s$ is an estimate of x_s.*

Theorem 3.1 that follows provides an explicit formula for the robust controller, conditions that ensure boundedness of the state, and a precise characterization of the ultimate uncertainty attenuation level. To simplify the statement of the theorem, we

set $\bar{v}_i = [v_i \; v_i^{(1)} \; \cdots \; v_i^{(r_i)}]^T$ and $\tilde{v} = [\bar{v}_1^T \; \bar{v}_2^T \; \cdots \; \bar{v}_m^T]^T$ The proof of Theorem 3.1 is presented in Appendix C.

Theorem 3.1: *Consider the parabolic PDE system of Eq.3.8 for which assumptions 3.1, 3.2 and 3.3 hold, and the finite-dimensional system of Eq.3.12, for which assumptions 3.4, 3.5, 3.6 and 3.7 hold, under the robust output feedback controller:*

$$\begin{aligned} u_0 \;=\; a_0(x_s, x_f, \bar{v}, t) := [C_0(t, \hat{x}_s)]^{-1} \Bigg\{ & \sum_{i=1}^{l} \sum_{k=1}^{r_i} \frac{\beta_{ik}}{\beta_{ir_i}} (v_i^{(k)} - L_{F_0}^k h_{i0}(t, \hat{x}_s)) \\ & + \sum_{i=1}^{l} \sum_{k=1}^{r_i} \frac{\beta_{ik}}{\beta_{ir_i}} (v_i^{(k-1)} - L_{F_0}^{k-1} h_{i0}(t, \hat{x}_s)) \\ & - \chi[c_0(t, \hat{x}_s)] \frac{\sum_{i=1}^{l} \sum_{k=1}^{r_i} \frac{\beta_{ik}}{\beta_{ir_i}} (L_{F_0}^{k-1} h_{i0}(t, \hat{x}_s) - v_i^{(k-1)})}{|\sum_{i=1}^{l} \sum_{k=1}^{r_i} \frac{\beta_{ik}}{\beta_{ir_i}} (L_{F_0}^{k-1} h_{i0}(t, \hat{x}_s) - v_i^{(k-1)})| + \phi} \Bigg\} \end{aligned} \tag{3.17}$$

where $\hat{x}_s = S^{-1} y_m$, $\frac{\beta_{ik}}{\beta_{ir_i}} = [\frac{\beta_{ik}^1}{\beta_{ir_i}^1} \; \cdots \; \frac{\beta_{ik}^l}{\beta_{ir_i}^l}]^T$ *are column vectors of parameters chosen so that the roots of the equation* $det(B(s)) = 0$, *where* $B(s)$ *is an* $l \times l$ *matrix, whose* (i,j)*-th element is of the form* $\sum_{k=1}^{r_i} \frac{\beta_{jk}^i}{\beta_{jr_i}^i} s^{k-1}$, *lie in the open left-half of the complex plane, and* χ, ϕ *are adjustable parameters with* $\chi > 1$ *and* $\phi > 0$. *Then, there exist positive real numbers* (δ, ϕ^*) *such that for each* $\phi \leq \phi^*$, *there exists* $\epsilon^*(\phi)$, *such that if* $\phi \leq \phi^*$, $\epsilon \leq \epsilon^*(\phi)$ *and* $\max\{|x_s(0)|, \|x_f(0)\|_2, \|\theta\|, \|\dot{\theta}\|, \|\tilde{v}\|\} \leq \delta$,

a) the state of the infinite-dimensional closed-loop system is bounded, and

b) the outputs of the infinite-dimensional closed-loop system satisfy:

$$\limsup_{t \to \infty} |y_{ci} - v_i| \leq d_0, \;\; i = 1, \ldots, l \tag{3.18}$$

where $d_0 = O(\phi + \epsilon)$ *is a positive real number.*

Note that we use the notation $|x_s|$ to denote the norm of x_s in the finite-dimensional Hilbert space $\mathcal{H}_s(t)$.

Remark 3.4: The nonlinear controller of Eq.3.17 was derived through combination

of geometric and Lyapunov techniques (the details of the derivation of this controller are omitted for brevity and the reader may refer to [39] for details on the synthesis of a similar controller for parabolic PDE systems with fixed spatial domains). The controller tuning parameters include β^i_{jk}, which can be chosen to influence the speed of the output response, and ϕ, χ which can be chosen to achieve the desired degree of attenuation (d_0) of the effect of the uncertain variables (unknown/partially known process model parameters or exogenous disturbances), $\theta_k(t)$, on the controlled output.

Remark 3.5: Regarding the practical implementation of the result of Theorem 3.1, one has to initially construct an approximate finite-dimensional system which captures the dominant dynamics of the PDE system (making certain that assumption 3.3 is satisfied), then verify that such a system satisfies assumptions 3.4, 3.5 and 3.6, and the number and location of the measurement sensors satisfies assumption 3.7, and finally, use the formula of Eq.3.17 to synthesize the controller on the basis of the finite-dimensional system and tune the controller (i.e., pick the values for the parameters β^i_{jk}, ϕ, χ) so that the desired degree of uncertainty attenuation is achieved in the closed-loop system.

Remark 3.6: We note that even though the controller of Eq.3.17 uses static feedback of the measured outputs y_{m_κ}, $\kappa = 1, \ldots, p$, and thus, it feeds back both x_s and x_f, the use of x_f feedback cannot lead to destabilization of the stable fast subsystem. This is due to the large separation of the slow and fast modes of the spatial differential operator (i.e., assumption that ϵ is sufficiently small) and the fact that the controller does not include terms of the form $O(\frac{1}{\epsilon})$.

3.4 Application to a diffusion-reaction process with moving boundary and uncertainty

We consider the diffusion-reaction process with moving boundary presented in Chapter 2 with uncertain parameters, which is described by the following parabolic PDE:

$$\frac{\partial \bar{x}}{\partial t} = \frac{\partial^2 \bar{x}}{\partial z^2} + \beta_T e^{-\frac{\gamma}{1+\bar{x}}} + \beta_U (b(z,t)u(t) - \bar{x}) - \beta_{T,n} e^{-\gamma} \tag{3.19}$$

subject to the Dirichlet boundary conditions:

$$\bar{x}(0,t) = 0, \quad \bar{x}(l(t),t) = 0 \tag{3.20}$$

and the initial condition:

$$\bar{x}(z,0) = 0.5 \tag{3.21}$$

where $\bar{x}$ is the state, γ, β_u are dimensionless process parameters, β_T denotes a dimensionless heat of reaction (which is assumed to be unknown and time-varying; uncertain variable), $\beta_{T,n}$ denotes a *nominal* dimensionless heat of reaction, $b(z,t) = [b_1(z,t)\ b_2(z,t)]$ are the actuator distribution functions and $u = [u_1\ u_2]^T$ is the manipulated input vector. The spatial domain is assumed to change according to the relation:

$$l(t) = \pi(1.4 - 0.4e^{(-0.02t^{2.7})}) \tag{3.22}$$

(it can be easily seen that the above function satisfies the requirements of assumption 3.1) and the following typical values were given to the process parameters:

$$\beta_{T,n} = 60.0, \ \beta_U = 2.0, \ \gamma = 4.0 \tag{3.23}$$

The following countable, $\forall\ t \in [0,\infty)$, orthogonal basis of $\mathcal{H}(t)$ was used in our calculations:

$$\phi_j(z,t) = \sqrt{\frac{2}{l(t)}} sin(j\ \pi\ \frac{z}{l(t)}), \quad j = 1,\ldots,\infty \tag{3.24}$$

Note that the above set of basis functions satisfies the conditions of assumption 3.2.

A 20-th order Galerkin truncation of the system of Eq.3.19, with $\phi_j(z,t)$ of Eq.3.24 as the basis functions, was used in our simulations (it was verified that further increase of the order of the Galerkin model provided no substantial improvement on the accuracy of the simulation results). It was found that the operating steady state $\bar{x}(z,t) = 0$ is an unstable one (the open-loop state starting from initial conditions close to the steady state $\bar{x}(z,t) = 0$ moves to another stable steady state characterized by a maximum at $z = \frac{l(t)}{2}$). Moreover, the linearization of the system of Eq.3.19

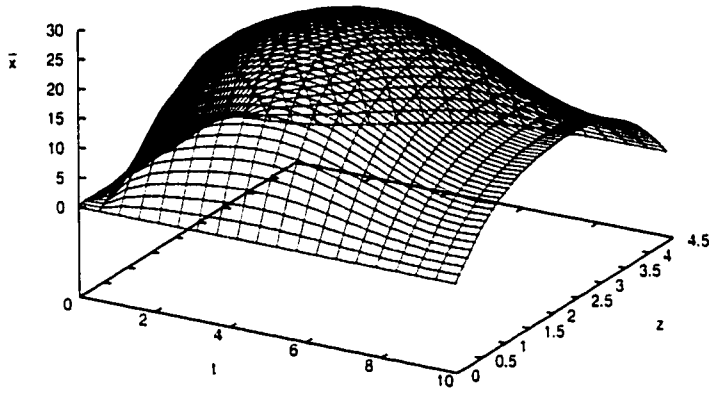

Figure 3.2: Open-loop profile of $\bar{x}$ in the presence of uncertainty.

around the steady-state $\bar{x}(z,t) = 0$ possesses one positive eigenvalue $\forall\ l(t) \in [\pi, 1.4\pi]$ and a second eigenvalue which becomes periodically positive as the domain size $l(t)$ and the value of β_T change.

The control objective is to stabilize the system at the unstable spatially-uniform steady state $\bar{x}(z,t) = 0$ in the presence of time-varying uncertainty in the dimensionless heat of the reaction β_T, (i.e., $\beta_T = \beta_{T,n} + \theta(t)$ where $\theta(t) = 0.35\ \beta_{T,n}\ sin(0.524\ t)$) by employing a nonlinear output feedback controller which uses two point measurements of the state at $z = 0.25l(t)$ and $z = 0.625l(t)$ (i.e., moving sensors with

$s(z,t) = \delta(z - 0.25l(t))$ and $s(z,t) = \delta(z - 0.625l(t))$, respectively, where $\delta(\cdot)$ is the standard Dirac function). We note that this selection for $\theta(t)$ satisfies the requirements of Theorem 3.1 that $\theta(t)$, $\dot{\theta}(t)$ should be sufficiently small (see closed-loop simulations below), while it leads to a very poor open-loop behavior for $\bar{x}(z,t)$ (see Figure 3.2). Since the maximum open-loop value of $\bar{x}(z,t)$ occurs for $z = \dfrac{l(t)}{2}$ and the first two modes of the process become unstable for some $l(t) \in [\pi, 1.4\pi]$, the controlled outputs were defined as:

$$\begin{aligned} y_{c1}(t) &= \int_0^{l(t)} \phi_1(z,t)\bar{x}(z,t)dz, \\ y_{c2}(t) &= \int_0^{l(t)} \phi_2(z,t)\bar{x}(z,t)dz \end{aligned} \tag{3.25}$$

The actuator distribution functions were taken to be $b_1(z,t) = 1$ (uniform in space, distributed control action) and $b_2(z,t) = \delta(z - \frac{2}{3}l(t))$ (moving point control actuation).

For the system of Eq.3.19, we considered the first two eigenvalues as the dominant ones ($\epsilon = 0.11$) and used Galerkin's method to derive a two dimensional ODE that was used for the synthesis of a nonlinear robust output feedback controller through an application of Eq.3.17. The resulting controller formula is:

$$\begin{aligned} u_1 = & \frac{1}{\sqrt{2\,l(t)\frac{2\beta_u}{\pi}}} \left[(\beta_u - \left(\frac{\pi}{l(t)}\right)^2 - 1)(\phi_1, \hat{x}_s) - (\phi_1, e^{-\frac{\gamma}{1+\hat{x}_s}} - e^{-\gamma}) \right. \\ & \left. -\beta_u \phi_1(\frac{2}{3}\pi, t)u_2(t) - \chi\theta_{max}|(\phi_1, e^{-\frac{\gamma}{1+\hat{x}_s}})|\frac{(\phi_1, \hat{x}_s)}{(\phi_1, \hat{x}_s) + \phi}\right] \\ u_2 = & \frac{1}{\beta_u \phi_2(\frac{2}{3}\pi, t)} \left[(\beta_u - \left(\frac{2\pi}{l(t)}\right)^2 - 1)(\phi_2, \hat{x}_s) - (\phi_2, e^{-\frac{\gamma}{1+\hat{x}_s}} - e^{-\gamma}) \right. \\ & \left. -\chi\theta_{max}|(\phi_2, e^{-\frac{\gamma}{1+\hat{x}_s}})|\frac{(\phi_2, \hat{x}_s)}{(\phi_2, \hat{x}_s) + \phi}\right] \end{aligned} \tag{3.26}$$

The controller was implemented with the following values of the parameters $\theta_{max} = 21$ (where θ_{max} is an upper bound of the disturbance $\theta_{max} \geq \sup_{t\in[0,\infty)} \{|\theta(t)|\}$), $\chi = 1.2$,

$\phi = 0.005$, and achieved an uncertainty attenuation level $d = 0.05$ (note that $0.05 = O(\epsilon + \phi) = O(0.11 + 0.005)$).

Figure 3.3 shows the evolution of the closed-loop rod temperature profile under the nonlinear robust output feedback controller, while Figure 3.4 shows the corresponding manipulated input profile. Clearly, the proposed controller regulates the temperature

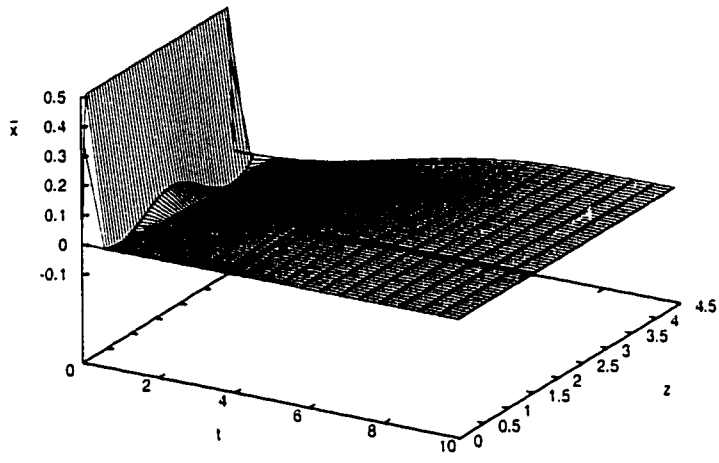

Figure 3.3: Closed-loop profile of $\tilde{x}$ under nonlinear robust output feedback control.

profile at $\tilde{x}(z,t) = 0$, attenuating the effect of the uncertain variable (note that the requirement $\limsup_{t\to\infty} |y_c| \leq 0.05$ is enforced in the closed-loop system; Figure 3.5). For the sake of comparison, we also implemented on the process the same controller as before without the term which compensates for the effect of the uncertainty (i.e., $\chi = 0$). Figure 3.6 shows the evolution of the closed-loop rod temperature profile. It is clear that this controller cannot regulate the temperature profile at the desired steady state, leading to close-loop instability.

We finally note that we also tested through simulations nonlinear robust static output feedback controllers which were synthesized under the assumption of fixed spatial domain (i.e., $l(t) = \pi$ and $l(t) = 1.4\pi$, for all times) which led to an unstable closed-loop system; the detail simulations are omitted for brevity.

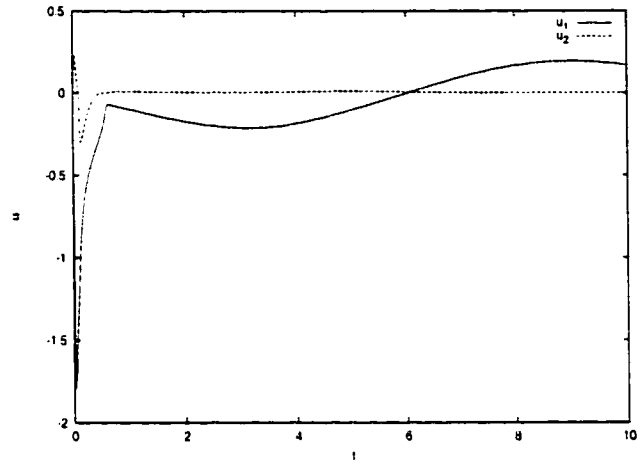

Figure 3.4: Manipulated input profiles for nonlinear robust output feedback controller.

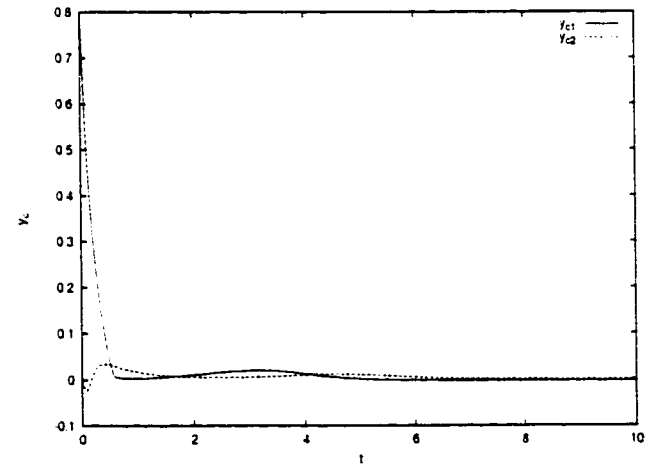

Figure 3.5: Closed-loop output profile under nonlinear robust output feedback control.

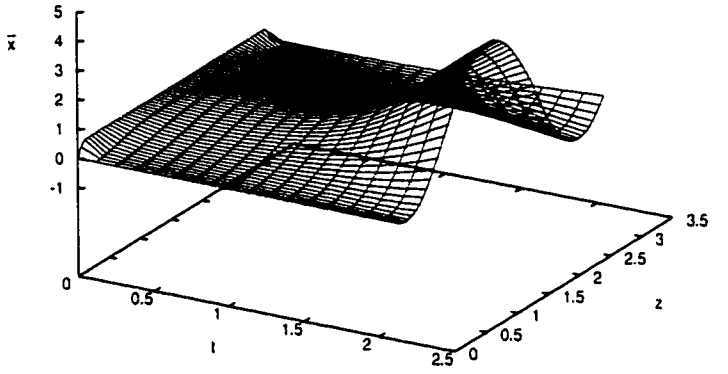

Figure 3.6: Closed-loop profile of $\bar{x}$ under nonlinear output feedback control (no uncertainty compensation).

3.5 Conclusions

In this chapter, we considered a broad class of quasi-linear parabolic PDE systems with time-dependent spatial domains and time-varying uncertain variables whose dynamics can be partitioned into slow and fast ones. For these systems, under the assumption that the number of available measurements is equal to the number of slow modes for all times, we synthesized robust static output feedback controllers through combination of geometric techniques and Lyapunov's direct method. The developed controllers guarantee boundedness of the state and output tracking with arbitrary degree of asymptotic attenuation of the effect of the uncertain parameters on the controlled output of the closed-loop system, provided that the separation between the slow and fast dynamical phenomena is sufficiently large. The controllers were successfully applied to a typical diffusion-reaction process with moving boundary and time-varying uncertainty and were shown to outperform controllers that do not account for the presence of the uncertainty.

Chapter 4

Finite-Dimensional Control of Nonlinear Parabolic PDE Systems with Time-Dependent Spatial Domains Using Empirical Eigenfunctions

4.1 Introduction

The objective of this chapter is to present a methodology for the synthesis of finite-dimensional nonlinear output feedback controllers for nonlinear parabolic PDE systems with time-dependent spatial domains. Initially, the nonlinear parabolic PDE system is expressed with respect to an appropriate time-invariant spatial coordinate and a representative (with respect to different initial conditions and input perturbations) ensemble of solutions of the resulting time-varying PDE system is constructed by computing and solving a high-order discretization of the PDE. Then, Karhunen-

Loève expansion is directly applied to the ensemble of solutions to derive a small set of empirical eigenfunctions (dominant spatial patterns) that capture almost all the energy of the ensemble of solutions. The empirical eigenfunctions are subsequently used as basis functions within a Galerkin's model reduction framework to derive low-order ODE systems that accurately describe the dominant dynamics of the PDE system. The ODE systems are subsequently used for the synthesis of nonlinear output feedback controllers using geometric control methods. The proposed control method is used to stabilize an unstable steady-state of a diffusion-reaction process with nonlinearities, spatially-varying coefficients and time-dependent spatial domain, and is shown to lead to the construction of accurate low-order models and the synthesis of low-order controllers. The performance of the low-order models and controllers is successfully tested through computer simulations.

4.2 Nonlinear parabolic PDE systems with moving domains

4.2.1 Description of PDE systems

We consider nonlinear parabolic PDE systems in one spatial dimension with the following state space description:

$$\begin{aligned} \frac{\partial \bar{x}}{\partial t} &= L(\bar{x}) + wb(z,t)u + f(t,\bar{x}) \\ y_{c_i} &= \int_0^{l(t)} c_i(z,t)k\bar{x}dz, \quad i = 1,\ldots,l \\ y_{m_\kappa} &= \int_0^{l(t)} s_\kappa(z,t)\omega\bar{x}dz, \quad \kappa = 1,\ldots,q \end{aligned} \tag{4.1}$$

subject to the boundary conditions:

$$\begin{aligned} C_1\bar{x}(0,t) + D_1\frac{\partial \bar{x}}{\partial z}(0,t) &= R_1 \\ C_2\bar{x}(l(t),t) + D_2\frac{\partial \bar{x}}{\partial z}(l(t),t) &= R_2 \end{aligned} \tag{4.2}$$

and the initial condition:

$$\bar{x}(z,0) \;=\; \bar{x}_0(z) \tag{4.3}$$

where the rate of change of the length of the domain, $l(t)$, is governed by the following ordinary differential equation:

$$\frac{dl}{dt} \;=\; \mathcal{G}(t,l,\int_0^{l(t)} \bar{a}(z,t,l,\bar{x},\frac{\partial \bar{x}}{\partial z})dz) \tag{4.4}$$

where $\bar{x}(z,t) = [\bar{x}_1(z,t) \;\cdots\; \bar{x}_n(z,t)]^T$ denotes the vector of state variables, $[0,l(t)] \subset \mathbb{R}$ is the domain of definition of the process, $z \in [0,l(t)]$ is the spatial coordinate, $t \in [0,\infty)$ is the time, $u = [u_1\; u_2 \;\cdots\; u_l]^T \in \mathbb{R}^l$ denotes the vector of manipulated inputs, $y_{c_i} \in \mathbb{R}$ denotes the i-th controlled output and $y_{m_\kappa} \in \mathbb{R}$ denotes the κ-th measured output. $L(\bar{x})$ is a nonlinear differential operator which involves first- and second-order spatial derivatives, $f(t,\bar{x})$, $\mathcal{G}(t,l,\int_0^{l(t)} \bar{a}(z,t,l,\bar{x},\frac{\partial \bar{x}}{\partial z})dz)$ are nonlinear vector functions, $\bar{a}(z,t,l,\bar{x},\frac{\partial \bar{x}}{\partial z})$ is a nonlinear scalar function, k,w,ω are constant vectors, A,B,C_1,D_1,C_2,D_2 are constant matrices, R_1,R_2 are column vectors, and $\bar{x}_0(z)$ is the initial condition.

$b(z,t)$ is a known smooth vector function of (z,t) of the following form $b(z,t) = [b_1(z,t)\; b_2(z,t) \;\cdots\; b_l(z,t)]$, where $b_i(z,t)$ describes how the control action $u_i(t)$ is distributed in the interval $[0,l(t)]$ (e.g. point/distributed actuation), $c_i(z,t)$ is a known smooth function of (z,t) which is determined by the desired performance specifications in the interval $[0,l(t)]$ (e.g. regulation of the entire temperature profile of a crystal or regulation of the temperature at a specific point), and $s_\kappa(z,t)$ is a known smooth function of (z,t) which is determined by the location and type of the κ-th measurement sensor (e.g. point/distributed sensing). In the case of point actuation (i.e. the control action enters the system at a single point z_0, with $z_0 \in [0,l(t)]$), the function $b_i(z,t)$ is taken to be nonzero in a finite spatial interval of the form $[z_0-\epsilon, z_0+\epsilon]$, where ϵ is a small positive real number, and zero elsewhere in $[0,l(t)]$.

We note that in contrast to the case of parabolic PDE systems defined on a fixed spatial domain, we allow the actuator, performance specification and measurement sensor functions to depend explicitly on time (i.e. moving control actuators and objectives, and measurement sensors). The value of using moving control actuators

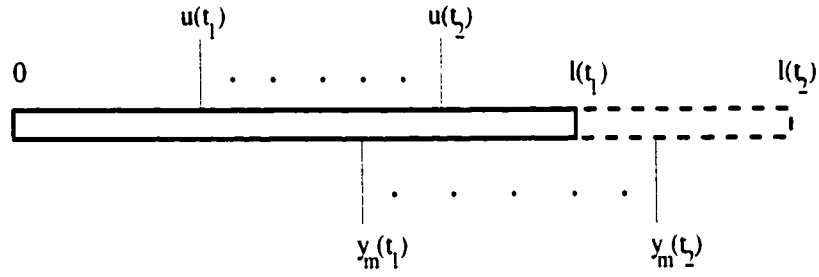

Figure 4.1: Schematic of a process with moving boundaries.

and sensors in applications with time-dependent domains has been illustrated in [5]. In order to simplify the notation of this manuscript, we assume that $l(t)$ is a known and smooth function of time. Specifically, our assumptions on the properties of $l(t)$ are precisely stated below:

Assumption 4.1: *$l(t)$ is a known smooth (i.e. $\dot{l}$ exists and is bounded, $\forall\, t \in [0, \infty)$) function of time which satisfies $l(t) \in (0, l_{max}]$, $\forall\, t \in [0, \infty)$, where l_{max} denotes the maximum length of the spatial domain.*

Finally, throughout the chapter, we assume that the nonlinear parabolic PDE systems under consideration, with and without feedback control, possess a unique solution which is also sufficiently smooth (i.e., all the spatial and temporal derivatives in the PDEs are smooth functions of space and time); the reader may refer to the books [139, 52] for techniques and results for studying the mathematically delicate questions of existence, uniqueness and regularity of solutions for various classes of PDE systems. In addition, we focus our attention on nonlinear parabolic PDE systems for which the manipulated inputs, measured and controlled outputs are bounded.

From a practical point of view, this means that we do not deal with control problems that involve boundary actuation, measurements and control objectives, even though several problems of this kind can be addressed by the proposed method. Linear infinite dimensional systems with unbounded manipulated inputs, measurements and control objectives have been studied extensively (see, for example, [48, 174]).

4.2.2 Formulation of the parabolic PDE system in Hilbert space

We formulate the system of Eqs.4.1-4.3 in a Hilbert space $\mathcal{H}(t)$ consisting of n-dimensional vector functions defined on $[0, l(t)]$ that satisfy the boundary conditions of Eq.4.2, with inner product and norm:

$$\begin{aligned} (\omega_1, \omega_2) &= \int_0^{l(t)} (\omega_1(z), \omega_2(z))_{\mathbb{R}^n} dz \\ \|\omega_1\|_2 &= (\omega_1, \omega_1)^{\frac{1}{2}} \end{aligned} \tag{4.5}$$

where ω_1, ω_2 are two elements of $\mathcal{H}(t)$ and the notation $(\cdot,\cdot)_{\mathbb{R}^n}$ denotes the standard inner product in $\mathbb{R}^n$. To this end, we define the state function x on $\mathcal{H}(t)$ as

$$x(t) = \bar{x}(z,t), \quad t > 0, \quad z \in [0, l(t)], \tag{4.6}$$

the time-varying operator:

$$\begin{aligned} \mathcal{L}(t,x) &= L(\bar{x}) + \frac{\dot{l}}{l(t)} z \frac{\partial \bar{x}}{\partial z}, \\ x \in D(\mathcal{L}) &= \left\{ x \in \mathcal{H}(t) : \; C_1 \bar{x}(0,t) + D_1 \frac{\partial \bar{x}}{\partial z}(0,t) = R_1, \right. \\ &\qquad \left. C_2 \bar{x}(l(t),t) + D_2 \frac{\partial \bar{x}}{\partial z}(l(t),t) = R_2 \right\} \end{aligned} \tag{4.7}$$

and the input, controlled output and measurement operators as:

$$\mathcal{B}(t)u = wb(t)u, \quad \mathcal{C}(t)x = (c(t), kx), \quad \mathcal{S}(t)x = (s(t), \omega x) \tag{4.8}$$

where $c(t) = [c_1(t)\ c_2(t)\ \cdots c_l(t)]^T$ and $s(t) = [s_1(t)\ s_2(t)\ \cdots s_q(t)]^T$, and $c_i(t) \in \mathcal{H}(t)$, $s_\kappa(t) \in \mathcal{H}(t)$. The system of Eqs.4.1-4.3 can then be written as:

$$\begin{aligned} \dot{x} &= \mathcal{L}(t,x) + \mathcal{B}(t)u + f(t,x), \quad x(0) = x_0 \\ y_c &= C(t)x, \quad y_m = S(t)x \end{aligned} \tag{4.9}$$

where $f(t,x(t)) = f(t,\bar{x}(z,t))$ and $x_0 = \bar{x}_0(z)$. We assume that the nonlinear term $f(t,x)$ satisfies $f(t,0) = 0$ and is also locally Lipschitz continuous uniformly in t, i.e. there exist positive real numbers a_0, K_0 such that for any $x_1, x_2 \in \mathcal{H}(t)$ that satisfy $\max\{\|x_1\|_2, \|x_2\|_2\} \leq a_0$, we have that:

$$\|f(t,x_1) - f(t,x_2)\|_2 \leq K_0\|x_1 - x_2\|_2, \quad \forall\, t \in [0,\infty) \tag{4.10}$$

Remark 4.1: In the formulation of the PDE system of Eqs.4.1-4.3 in $\mathcal{H}(t)$, the time-varying term $\dfrac{\dot{l}(t)}{l(t)} z \dfrac{\partial \bar{x}}{\partial z}$ in the expression of $\mathcal{L}(t,x)$ (Eq.4.7) accounts for convective transport owing to the motion of the domain. This term was not present in the expression of the differential operator in the case of parabolic PDE systems with fixed spatial domains (where $\dot{l}(t) \equiv 0$), and makes $\mathcal{L}(t,x)$ an explicit function of time.

4.2.3 Methodology for model reduction and control

The main obstacles in developing a general model reduction method for systems of the form of Eq.4.1 are: a) the spatial differential operator is nonlinear, and b) the domain of definition of the process is generally time-varying. These issues do not allow the computation of analytic expressions for the eigenvalues and eigenfunctions of the spatial differential operator of the system, and thus, they prohibit the direct use of Galerkin's methods or orthogonal collocation methods with the eigenfunctions as basis functions, to derive finite dimensional approximations of the PDE system.

To overcome the above problems, we employ the following methodology for the derivation of finite-dimensional approximations and the synthesis of low-dimensional

nonlinear output feedback controllers for systems of the form of Eq.4.1.

1. Initially, the nonlinear parabolic PDE system is expressed with respect to an appropriate time-invariant spatial coordinate and a representative (with respect to different initial conditions and input perturbations) ensemble of solutions of the resulting time-varying PDE system is constructed either by computing and solving a high-order discretization of the PDE, or alternatively, using available process data (see Remark 4.5).

2. Then, Karhunen-Loève expansion (and in particular the method of snapshots [158]) is directly applied to the ensemble of solutions to derive a small set of empirical eigenfunctions (dominant spatial patterns) that capture almost all the energy of the ensemble of solutions.

3. The empirical eigenfunctions are subsequently used as basis functions within a Galerkin's model reduction framework to derive low-order ODE systems that accurately describe the dominant dynamics of the PDE system.

4. These ODE systems are used as a basis for the synthesis of low dimensional nonlinear controllers, which use on-line measurements of process outputs to stabilize the closed-loop infinite-dimensional system and force its outputs to follow their respective set-points.

4.3 Order reduction

4.3.1 Computation of empirical eigenfunctions

In this section, we present a review of the K-L expansion in the context of nonlinear one-dimensional parabolic PDE systems of the form of Eq.4.1 with $n = 1$ (see [74, 90]

for a general presentation and analysis of the K-L expansion). Introducing the time-invariant spatial coordinate $\zeta = \frac{z}{l(t)}$, the system of Eqs.4.1-4.3 can be written in the following form:

$$\begin{aligned} \frac{\partial \bar{x}}{\partial t} &= L(\bar{x}) + \frac{\dot{l}}{l(t)}\zeta\frac{\partial \bar{x}}{\partial \zeta} + wb(\zeta,t)u + f(t,\bar{x}) \\ y_{c_i} &= l(t)\int_0^1 c_i(\zeta,t)k\bar{x}d\zeta, \quad i = 1,\ldots,l \\ y_{m_\kappa} &= l(t)\int_0^1 s_\kappa(\zeta,t)\omega\bar{x}d\zeta, \quad \kappa = 1,\ldots,q \end{aligned} \tag{4.11}$$

with boundary conditions:

$$\begin{aligned} C_1\bar{x}(0,t) + \frac{D_1}{l(t)}\frac{\partial \bar{x}}{\partial \zeta}(0,t) &= R_1 \\ C_2\bar{x}(1,t) + \frac{D_2}{l(t)}\frac{\partial \bar{x}}{\partial \zeta}(1,t) &= R_2 \end{aligned} \tag{4.12}$$

and the initial condition:

$$\bar{x}(\zeta,0) = \bar{x}_0(\zeta l(t)) \tag{4.13}$$

We assume that the solution of the system of Eq.4.11 is known and consider a sufficiently large set (called ensemble), $\{\bar{x}_\kappa\}$, consisting of N sampled states, $\bar{x}_\kappa(\zeta)$ (typically called "snapshots") of the solution of Eq.4.1. To simplify our presentation, we assume uniform in time sampling of $\bar{x}_\kappa(\zeta)$, (i.e. the time interval between any two successive sampled states is the same), while we define the ensemble average of snapshots as $< \bar{x}_\kappa >:= \frac{1}{N}\sum_{\kappa=1}^{N}\bar{x}_\kappa(\zeta)$ (we note that non-uniform sampling of the snapshots and weighted ensemble average can be also considered; see, for example, [83]). Furthermore, the ensemble average of snapshots $< \bar{x}_\kappa >$ is subtracted out from the snapshots i.e.,:

$$x_\kappa = \bar{x}_\kappa - < \bar{x}_\kappa > \tag{4.14}$$

so that only fluctuations are analyzed. The issue is how to obtain the most typical or characteristic structure $\phi(\zeta)$ among these snapshots $\{x_\kappa\}$. Mathematically, this

problem can be posed as the one of obtaining a function $\phi(\zeta)$ that maximizes the following objective function:

$$\begin{aligned} &\text{Maximize } \frac{<(\phi, x_\kappa)^2>}{(\phi,\phi)} \\ &s.t.\ (\phi,\phi) = 1,\ \ \phi \in L^2([0,1]) \end{aligned} \tag{4.15}$$

The constraint $(\phi,\phi) = 1$ is imposed to ensure that the function, $\phi(\zeta)$, computed as a solution of the above maximization problem, is unique. The Lagrangian functional corresponding to this constrained optimization problem is:

$$\bar{L} =< (\phi, x_\kappa)^2 > -\lambda((\phi,\phi) - 1) \tag{4.16}$$

and necessary conditions for extrema is that the functional derivative vanishes for all variations $\phi + \delta\psi \in L^2[0,1]$, where δ is a real number:

$$\left.\frac{d\bar{L}(\phi + \delta\psi)}{d\delta}\right|_{\delta=0} = 0,\ (\phi,\phi) = 1 \tag{4.17}$$

Using the definitions of inner product and ensemble average, $\left.\frac{d\bar{L}(\phi + \delta\psi)}{d\delta}\right|_{\delta=0}$ can be computed as follows:

$$\begin{aligned} \left.\frac{d\bar{L}(\phi + \delta\psi)}{d\delta}\right|_{\delta=0} &= \frac{d}{d\delta}[< (x_\kappa, \phi + \delta\psi)(\phi + \delta\psi, x_\kappa) > -\lambda(\phi + \delta\psi, \phi + \delta\psi)]_{\delta=0} \\ &= 2Re[< (x_\kappa, \psi)(\phi, x_\kappa) > -\lambda(\phi,\psi)] \\ &= \left\langle \int_0^1 \psi(\zeta) x_\kappa(\zeta) d\zeta \int_0^1 \phi(\xi) x_\kappa(\xi) d\xi \right\rangle - \lambda \int_0^1 \phi(\xi)\psi(\xi) d\xi \\ &= \int_0^1 \int_0^1 < x_\kappa(\zeta) x_\kappa(\xi) > \phi(\zeta) d\zeta \psi(\xi) d\xi - \int_0^1 \lambda\phi(\xi)\psi(\xi) d\xi \end{aligned} \tag{4.18}$$

Since $\psi(\xi)$ is an arbitrary function, the necessary conditions for optimality take the form:

$$\int_0^1 < x_\kappa(\zeta) x_\kappa(\xi) > \phi(\zeta) d\zeta = \lambda\phi(\xi),\ \ (\phi,\phi) = 1 \tag{4.19}$$

Introducing the two-point correlation function:

$$K(\zeta,\xi) =< x_\kappa(\zeta) x_\kappa(\xi) >= \frac{1}{N}\sum_{\kappa=1}^{N} x_\kappa(\zeta) x_\kappa(\xi) \tag{4.20}$$

and the linear operator:

$$R := \int_0^1 K(\zeta, \xi) d\xi \tag{4.21}$$

the optimality condition of Eq.4.19 reduces to the following eigenvalue problem of the integral equation:

$$R\phi = \lambda\phi \Longrightarrow \int_0^1 K(\zeta, \xi)\phi(\xi) d\xi = \lambda\phi(\zeta) \tag{4.22}$$

The computation of the solution of the above integral eigenvalue problem is, in general, a very expensive computational task. To circumvent this problem, Sirovich introduced in 1987 [158] the method of snapshots. The central idea of this technique is to assume that the requisite eigenfunction, $\phi(\zeta)$, can be expressed as a linear combination of the snapshots i.e.,:

$$\phi(\zeta) = \sum_k c_k x_k(\zeta) \tag{4.23}$$

Substituting the above expression for $\phi(\zeta)$ on Eq.4.22, we obtain the following eigenvalue problem:

$$\int_0^1 \frac{1}{N} \sum_{\kappa=1}^{N} x_\kappa(\zeta) x_\kappa(\xi) \sum_{k=1}^{N} c_k x_k(\xi) d\xi = \lambda \sum_{k=1}^{N} c_k x_k(\zeta) \tag{4.24}$$

Defining:

$$B^{\kappa k} := \frac{1}{N} \int_0^1 x_\kappa(\xi) x_k(\xi) d\xi \tag{4.25}$$

the eigenvalue problem of Eq.4.24 can be equivalently written as:

$$Bc = \lambda c \tag{4.26}$$

The solution of the above eigenvalue problem (which can be obtained by utilizing standard methods from matrix theory) yields the eigenvectors $c = [c_1 \cdots c_N]$ which can be used in Eq.4.23 to construct the eigenfunction $\phi(\zeta)$. Due to it's structure, it follows that the matrix B is symmetric and positive semi-definite, and thus, its

eigenvalues, λ_κ, $\kappa = 1, \ldots, N$, are real and non-negative. Furthermore,

$$\int_0^1 \phi_\kappa(\zeta)\phi_k(\zeta)d\zeta = 0, \quad \kappa \neq k \tag{4.27}$$

Remark 4.2: The calculated eigenvalues, once normalized, represent the percent of energy or equivalently time that the solution of the PDE system spends along the spatial structure of the empirical eigenfunction.

Remark 4.3: Note that the empirical eigenfunctions that were derived using the above methodology can be used directly as basis functions of the Hilbert space defined in subsection 4.2.2 since the two spaces are completely analogous, and the basis functions can be interchanged through the coordinate transformation $z = \zeta\ l(t)$ (note that in order for the basis functions to be orthonormal instead of just orthogonal to each other, the multiplication $\phi_j(z) = \sqrt{l(t)}\ \phi_j(\zeta)$ must also take place).

Remark 4.4: The K-L expansion can also be used to compute a set of empirical eigenfunctions when the optimization objective of Eq.4.15 is modified to $< (\dot{\phi}, \dot{x}_\kappa)^2 >$ under the same constraints. The modified objective focuses on the acceleration energy of the fluctuations towards the average value, rather than the energy of the fluctuations which is used in our development. It has been shown that the empirical eigenfunctions that are generated using the modified objective function also form a set of orthonormal basis functions (the reader may refer to [160] for a detailed discussion on this issue). A variety of optimization objectives have been formulated in the literature to address the specific characteristics of processes, such as periodic phenomena, etc.

Remark 4.5: The ensemble of solutions may be derived from process data as well as through the solution of a high-order discretization of the PDE system of Eq.4.11. Process data-based construction may be more suitable in controller design problems

for which there is an abundance of measured data and the model of the process is too complex to be solved in a time-effective manner with reasonable computing power (note that numerous model solutions are needed to obtain a representative ensemble).

4.3.2 Galerkin's method

In this section, we use Galerkin's method to derive low-dimensional dynamical systems of nonlinear ordinary differential equations that accurately reproduce the dynamics and solutions of the nonlinear parabolic PDE system of Eq.4.1. To this end, we assume that we have available an orthogonal and complete set of global (in the sense that they span the entire spatial domain of definition of the process) basis functions, $\phi_i(\zeta)$, that satisfy the boundary conditions of Eq.4.2. In practice, $\phi_i(\zeta)$ may be the set of empirical eigenfunctions obtained through K-L expansion.

Let $\mathcal{H}_s$, $\mathcal{H}_f$ be two subspaces of $\mathcal{H}$, defined as $\mathcal{H}_s = span\{\phi_1, \phi_2, \ldots, \phi_m\}$ and $\mathcal{H}_f = span\{\phi_{m+1}, \phi_{m+2}, \ldots, \}$. The basis functions ϕ_j may be obtained through K-L expansion. Defining the orthogonal projection operators P_s and P_f such that $x_s = P_s x$, $x_f = P_f x$, the state x of the system of Eq.4.9 can be decomposed as:

$$x = x_s + x_f = P_s x + P_f x \tag{4.28}$$

Applying P_s and P_f to the system of Eq.4.9 and using the above decomposition for x, the system of Eq.4.9 can be equivalently written in the following form:

$$\begin{aligned} \frac{dx_s}{dt} &= \mathcal{L}_s(t, x_s, x_f) + \mathcal{B}_s(t)u + f_s(t, x_s, x_f) \\ \frac{\partial x_f}{\partial t} &= \mathcal{L}_f(t, x_s, x_f) + \mathcal{B}_f(t)u + f_f(t, x_s, x_f) \\ y_c &= \mathcal{C}(t)x_s + \mathcal{C}(t)x_f, \quad y_m = \mathcal{S}(t)x_s + \mathcal{S}(t)x_f \\ x_s(0) &= P_s x(0) = P_s x_0, \quad x_f(0) = P_f x(0) = P_f x_0 \end{aligned} \tag{4.29}$$

where $\mathcal{L}_s(t, x_s, x_f) = P_s\mathcal{L}(t, x_s + x_f)$, $\mathcal{B}_s(t) = P_s\mathcal{B}(t)$, $f_s(t, x_s, x_f) = P_s f(t, x_s + x_f)$, $\mathcal{L}_f(t, x_s, x_f) = P_f\mathcal{L}(t, x_s + x_f)$, $\mathcal{B}_f(t) = P_f\mathcal{B}(t)$, and $f_f(t, x_s, x_f) = P_f f(t, x_s + x_f)$.

Owing to the parabolic nature of the spatial differential operator, the nonlinear vector $\mathcal{L}_f(t, x_s, x_f)$ satisfies $\mathcal{L}_f(t, x_s, x_f) = L_{fs}(t)x_s + \frac{1}{\epsilon}L_f(t)x_f + \tilde{f}_f(t, x_s, x_f)$ where ϵ is a small positive parameter quantifying the separation between the slow (dominant) and fast (negligible) eigenmodes of the spatial operator, and $L_{fs}(t)$, $L_f(t)$ are matrices with $L_f(t)$ being stable (in the sense that the state of the system $\frac{\partial x_f}{\partial t} = L_f(t)x_f$ tends exponentially to zero), and $\tilde{f}_f(t, x_s, x_f)$ is a nonlinear vector function which does not include linear terms. Note that the partial derivative in the term $\partial x_f/\partial t$ is used to denote that x_f belongs to an infinite dimensional Hilbert space. Neglecting the infinite dimensional x_f-subsystem in the system of Eq.4.29 (this is equivalent to assuming that $\epsilon = 0$ when the system of Eq.4.29 is formulated within a singular perturbations framework), the following m-dimensional slow system is obtained:

$$\begin{aligned} \frac{dx_s}{dt} &= \mathcal{L}_s(t, x_s) + \mathcal{B}_s(t)u + f_s(t, x_s) \\ y_c &= C(t)x_s, \quad y_m = S(t)x_s \\ x_s(0) &= P_s x(0) = P_s x_0 \end{aligned} \tag{4.30}$$

where $\mathcal{L}_s(t, x_s) = P_s\mathcal{L}(t, x_s)$, $f_s(t, x_s) = P_s f(t, x_s)$ are Lipschitz vector functions, and $\mathcal{B}_s(t) = P_s\mathcal{B}(t)$.

Remark 4.6: We note that when the approximate ODE model of Eq.4.30 is obtained through Galerkin's method with empirical eigenfunctions, it provides a valid approximation of the parabolic PDE model in a broad region of the state space and not only in the region that was used for the computation of the snapshots, provided that the ensemble of snapshots is sufficiently large and contains sufficient information of the global dynamics of the PDE system. This property is a consequence of the fact that the empirical eigenfunctions form an orthogonal set of functions whose dimension is equal to the number of snapshots, and thus, it can be made arbitrarily large (even though completeness of this set cannot be guaranteed). Therefore, the use of empirical eigenfunctions for discretization of the PDE system is not fundamentally

different from the use of other standard basis functions sets (sine and cosine functions, Legendre polynomials, etc.) for discretization with Galerkin's method, and thus, the finite-dimensional approximation obtained through Galerkin's method with empirical eigenfunctions is valid in a broad region of the state space, as long as the dimension of the ensemble is sufficiently large.

4.4 Nonlinear output feedback control

In this section, we synthesize nonlinear finite-dimensional output feedback controllers that guarantee local exponential stability and force the controlled output of the closed-loop PDE system to follow the reference input, provided that ϵ is sufficiently small. The output feedback controllers are constructed through combination of state feedback controllers with state observers.

More specifically, we use the system of Eq.4.30 to synthesize nonlinear state feedback controllers of the following general form:

$$u = p(t, x_s) + Q(t, x_s)v \tag{4.31}$$

where $p(t, x_s)$ is a smooth vector function, $Q(t, x_s)$ is a smooth matrix, and $v \in \mathbb{R}^l$ is the constant reference input vector. The synthesis of $[p(t, x_s), Q(t, x_s)]$ so that a nonlinear controller of the form of Eq.4.31 guarantees local exponential stability and forces the output of the system of Eq.4.30 to follow a desired linear response, is performed by utilizing geometric control methods for nonlinear ODEs (the details of the controller synthesis can be found in [134], and are omitted for brevity).

Since measurements of $\bar{x}(z, t)$ (and thus, $x_s(t)$) are usually not available in practice, we assume that there exists a matrix L so that the nonlinear dynamical system:

$$\frac{d\eta}{dt} = \mathcal{L}_s(t, \eta) + \mathcal{B}_s(t)u + f_s(t, \eta) + L[y_m - \mathcal{S}(t)\eta] \tag{4.32}$$

where η denotes an m-dimensional state vector, is a local exponential observer for the system of Eq.4.30 (i.e. the discrepancy $|\eta(t) - x_s(t)|$ tends exponentially to zero).

Theorem 4.1 that follows provides the synthesis formula of the output feedback controller and conditions that guarantee closed-loop stability and output tracking. To state our result, we need to use the Lie derivative notation and the concepts of relative order and characteristic matrix (which are defined in the appendix), for the system of Eq.4.30. First, the Lie derivative of the scalar function $h_i(t, x_s)$ with respect to the vector function $f(t, x_s)$ is defined as $L_f h_i(t, x_s) = \frac{\partial h_i}{\partial x_s} f(t, x_s) + \frac{\partial h_i}{\partial t}$ (this definition of Lie derivative was introduced in [134] and is different than the standard one used in [98] for the case of time-invariant h_i, f_0), $L_f^k h_i(t, x_s)$ denotes the k-th order Lie derivative and $L_{g_l} L_f^k h_l(t, x_s)$ denotes the mixed Lie derivative. Now, referring to the system of Eq.4.30, we set $\mathcal{L}_s(t, x_s) + f_s(t, x_s) = f(t, x_s)$, $\mathcal{B}_s(t) = g(t, x_s)$, $C_i(t) x_s = h_i(t, x_s)$ to obtain:

$$\begin{aligned} \frac{dx_s}{dt} &= f(t, x_s) + g(t, x_s) u \\ y_{cs_i} &= h_i(t, x_s) \end{aligned} \tag{4.33}$$

For the above system, the relative order of the output y_{cs_i} with respect to the vector of manipulated inputs u is defined as the smallest integer r_i for which:

$$\left[L_{g_1} L_f^{r_i - 1} h_i(t, x_s) \; \cdots \; L_{g_l} L_f^{r_i - 1} h_i(t, x_s) \right] \not\equiv [0 \; \cdots \; 0] \tag{4.34}$$

or $r_i = \infty$ if such an integer does not exist. Furthermore, the matrix:

$$C(t, x_s) = \begin{bmatrix} L_{g_1} L_f^{r_1 - 1} h_1(t, x_s) & \cdots & L_{g_l} L_f^{r_1 - 1} h_1(t, x_s) \\ L_{g_1} L_f^{r_2 - 1} h_2(t, x_s) & \cdots & L_{g_l} L_f^{r_2 - 1} h_2(t, x_s) \\ \vdots & & \\ L_{g_1} L_f^{r_l - 1} h_l(t, x_s) & \cdots & L_{g_l} L_f^{r_l - 1} h_l(t, x_s) \end{bmatrix} \tag{4.35}$$

is the characteristic matrix of the system of Eq.4.33. The proof of Theorem 4.1 is presented in Appendix D.

Theorem 4.1: *Suppose that the following conditions hold:*

1. *The roots of the equation:*

$$det(B(s)) = 0 \tag{4.36}$$

where $B(s)$ is an $l \times l$ matrix whose (i,j)-th element is of the form $\sum_{k=0}^{r_i} \beta_{jk}^i s^k$, lie in the open left-half of the complex plane, where β_{jk}^i are adjustable controller parameters.

2. *The zero dynamics of the system of Eq.4.33 are locally exponentially stable.*

Then, there exist positive real numbers $\tilde{\mu}_1, \tilde{\mu}_2, \tilde{\epsilon}^*$ such that if $|x_s(0)| \leq \tilde{\mu}_1$, $\|x_f(0)\|_2 \leq \tilde{\mu}_2$ and $\epsilon \in (0, \tilde{\epsilon}^*]$, and $\eta(0) = x_s(0)$, the dynamic output feedback controller:

$$\begin{aligned} \frac{d\eta}{dt} &= \mathcal{L}_s(t,\eta) + \mathcal{B}_s(t)\left\{[\beta_{1r_1}\cdots\beta_{lr_l}]C(t,\eta)\right\}^{-1}\left\{v - \sum_{i=1}^{l}\sum_{k=0}^{r_i}\beta_{ik}L_f^k h_i(t,\eta)\right\} \\ &\quad + f_s(t,\eta) + L\left(y_m - \mathcal{S}(t)\eta\right) \\ u &= \left\{[\beta_{1r_1}\cdots\beta_{lr_l}]C(t,\eta)\right\}^{-1}\left\{v - \sum_{i=1}^{l}\sum_{k=0}^{r_i}\beta_{ik}L_f^k h_i(t,\eta)\right\} \end{aligned} \tag{4.37}$$

a) guarantees local exponential stability of the closed-loop system, and

b) ensures that the outputs of the closed-loop system satisfy :

$$lim_{t\to\infty}|y_{ci}(t) - v_i| = O(\epsilon)\ ,\ i = 1,\ldots,l \tag{4.38}$$

where v_i is the set-point for the i-th controlled output

Remark 4.7: We note that the approach followed here for the synthesis of output feedback controllers is not applicable to hyperbolic PDE systems (i.e., convection-reaction processes) where the eigenvalues cluster along vertical or nearly vertical asymptotes in the complex plane and thus, the controller synthesis problem has to be addressed directly on the basis of the hyperbolic PDE system (see, for example, [111, 112] for results on optimal control and [40] for results on geometric and Lyapunov-based control).

Remark 4.8: It is important to point out that the result of Theorem 4.1 can be generalized to the case where the ODE systems used for controller design are obtained from combination of Galerkin's method with approximate inertial manifolds (see [40, 2] for details on the design of output feedback controllers on the basis of such ODE systems and [26, 25, 155] for other applications of inertial manifold theory to control of nonlinear parabolic PDEs).

4.5 Application to a diffusion-reaction process

In this section, the proposed method is applied to a diffusion-reaction process with nonlinear terms, spatially-varying coefficients and a time-dependent spatial domain. Specifically, we consider a diffusion-reaction process which is described by the following parabolic PDE in dimensionless form:

$$\frac{\partial \bar{x}}{\partial t} = \frac{\partial}{\partial z}(k(z)\frac{\partial \bar{x}}{\partial z}) + \beta_T(z)(e^{-\frac{\gamma}{1+\bar{x}}} - e^{-\gamma}) + \beta_U(b(z,t)u(t) - \bar{x}) \tag{4.39}$$

subject to the Dirichlet boundary conditions:

$$\bar{x}(0,t) = 0, \quad \bar{x}(l(t),t) = 0 \tag{4.40}$$

and the initial condition:

$$\bar{x}(z,0) = 0.5 \tag{4.41}$$

where $\bar{x} \in \mathbb{R}$ is the state of the system, γ, β_u are constant dimensionless process parameters, $\beta_T(z), k(z)$ are dimensionless process parameters that are explicit functions of the spatial coordinate z, $u(t) = [u_1(t)\ u_2(t)]^T$ is the vector of the inputs (which will be used in the construction of the ensemble of solutions), and $b(z,t) = [b_1(z,t)\ b_2(z,t)]$ is a vector function which determines how the inputs $u_1(t), u_2(t)$ are distributed in space. The values and expressions of the process parameters that were used in our calculations are: $\beta_U = 2.0$, $\gamma = 4.0$, $\beta_T(z) = 45(1.5 - e^{-0.5\,z})$, $k(z) = e^{-0.5\,z}$ and

$l(t) = \pi[1.4 - 0.4exp(-0.02t^{2.7})]$. Note that $l(t)$ is a smooth function of time (i.e., $\frac{dl}{dt}$ exists and is continuous) as requested per assumption 4.1.

An accurate high-order discretization of the PDE of Eq.4.39 was constructed using Galerkin's method with the following set of basis functions (which is the set of eigenfunctions resulting form the solution of the eigenvalue problem of the spatial operator for the constant value of $k = 1$):

$$\phi_j(z,t) = \sqrt{\frac{2}{l(t)}} sin(j\,\pi\,\frac{z}{l(t)}), \quad j = 1, \ldots, \infty \tag{4.42}$$

It was found that a 30-th order Galerkin truncation of the system of Eq.4.39 using the above basis functions leads to an accurate solution of the PDE (it was verified that further increase in the order of the Galerkin model as well as reduction in the temporal discretization step provide no substantial improvement on the accuracy of the simulation results). Figure 4.2 shows the evolution of the state of the PDE for $u(t) = 0$ starting from initial conditions which are very close to the steady-state $\bar{x}(z,t) = 0$. We observe that the system moves to another steady-state which is

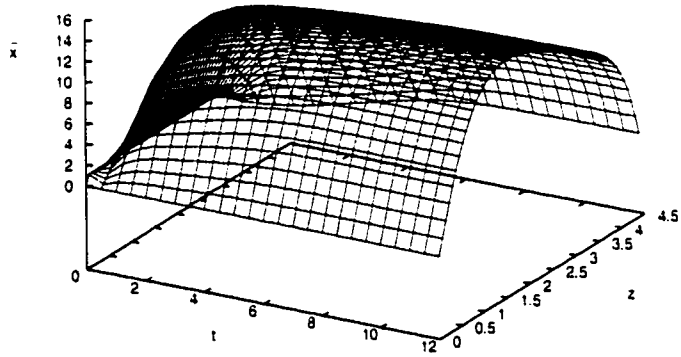

Figure 4.2: Profile of $\bar{x}$ for spatially varying β_T, k; $u(t) = 0$.

characterized by a maximum at $z = 0.375\ l(t)$. This implies that the steady state $\bar{x}(z,t) = 0$ is an unstable one, and thus, the system moves to a stable spatially non-uniform steady state.

We now continue with the computation of the set of empirical eigenfunctions. We initially constructed an ensemble of solutions. This was accomplished by solving the high order discretization of the Eq.4.39 for four different initial conditions (including the initial condition in the examined problem and the unstable steady-state as an initial condition) and for five different time-profiles of the manipulated variables. This led to a total of 20 spatiotemporal solution profiles. Subsequently, 51 "snapshots" of the profile of the state of Eq.4.39 as a function of the spatial coordinate, z, for 51 fixed time instants (during the process time and domain size) were taken from each solution data set and were combined, to generate an ensemble of 1020 solutions. To successfully apply Karhunen-Loève expansion we first expressed the developed ensemble of solutions into an appropriate spatial coordinate $\zeta = \frac{z}{l(t)}$ whose domain of definition is time-invariant. The Karhunen-Loève expansion was then applied to

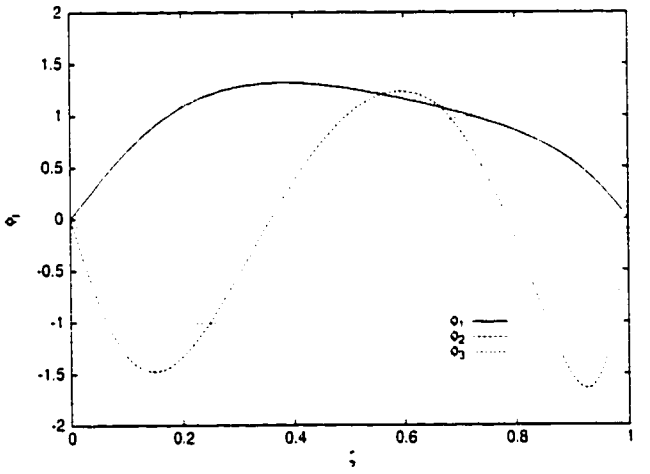

Figure 4.3: First three empirical eigenfunctions.

the developed ensemble of solutions to compute seven empirical eigenfunctions that describe the dominant spatial solution patterns embedded in the ensemble (they account for more than 99.9% of the energy included in the entire ensemble). The first three of these empirical eigenfunctions are presented in Figure 4.3. Note that they

are not symmetric with respect to the center of the system, $\zeta = 0.5$, owing to the spatial nonuniformity of $\beta_T = 45(1.5 - e^{-0.5\,z})$ and $k = e^{-0.5\,z}$.

We now proceed with the use of the computed empirical eigenfunctions as basis functions in Galerkin's method to construct accurate low-dimensional ODE approximations of the PDE. To accomplish this, the parabolic PDE system of Eq.4.39-4.40 is equivalently expressed in terms of $\zeta = \frac{z}{l(t)}$ as follows:

$$\frac{\partial \bar{x}}{\partial t} = \frac{1}{l(t)^2}\frac{\partial}{\partial \zeta}(k(\zeta)\frac{\partial \bar{x}}{\partial \zeta}) + \frac{\dot{l}}{l(t)}\zeta\frac{\partial \bar{x}}{\partial \zeta} + \beta_T(\zeta)(e^{-\frac{\gamma}{1+\bar{x}}} - e^{-\gamma}) + \beta_U(b(\zeta,t)u(t) - \bar{x}) \tag{4.43}$$

subject to the boundary and initial conditions:

$$\bar{x}(0,t) = 0, \quad \bar{x}(1,t) = 0, \quad \bar{x}(\zeta,0) = 0.5 \tag{4.44}$$

We initially applied Galerkin's method with the first two of the seven empirical eigenfunctions as basis functions to the PDE of Eq.4.43 to construct a second-order model. Figure 4.4 shows the deviation between the spatiotemporal profiles of the state of the

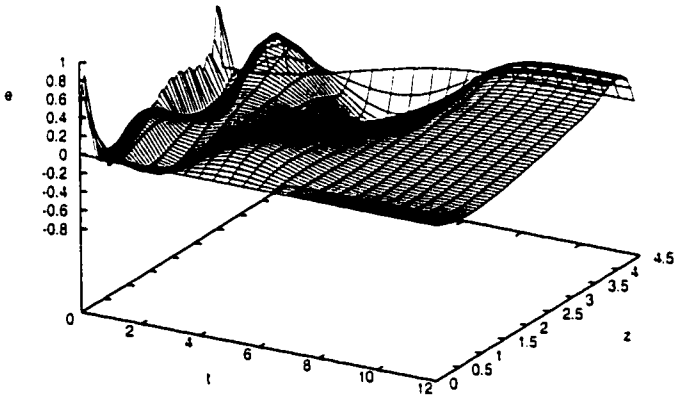

Figure 4.4: Deviation between the second-order model and the high-order discretization of the PDE (nominal case).

system computed by the second-order ODE model and the high-order discretization of the PDE; we observe a very good agreement between the two models for all times,

with the maximum deviation being lower than 3.4% (the deviation is computed to be the maximum error in the solution profile divided by the value of the state at that point; for accuracy results in the sense of L_2 norms the reader may refer to table 4.1).

To further improve the accuracy of the second-order ODE model, we noted that the spatial pattern of the error in Figure 4.4 resembles the shape of the third empirical eigenfunction (see Figure 4.3), and thus, we applied Galerkin's method with the first three empirical eigenfunctions as basis functions to the PDE of Eq.4.43 to construct a third-order model. Figure 4.5 shows the discrepancy between the third-order model

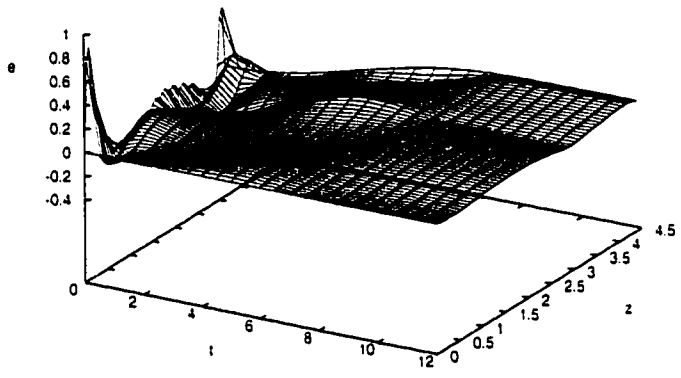

Figure 4.5: Deviation between the third-order model and the high-order discretization of the PDE (nominal case).

and the high-order discretization of the PDE; it is clear that the addition of the third eigenfunction has greatly improved the accuracy of the low-order approximation (the maximum deviation in this case is less than 0.5%).

For the sake of comparison, we also constructed a third-order approximation of the PDE of Eq.4.39 using Galerkin's method with the first three eigenfunctions of Eq.4.42 as basis functions. We observe that the error (Figure 4.6) between this third-order model and the high-order discretization of the PDE is significant (about 11%), which is mainly a result of the fact that this approach does not account for the spatial dis-

tribution of the diffusion coefficient $k(z)$. We note that higher-order approximations

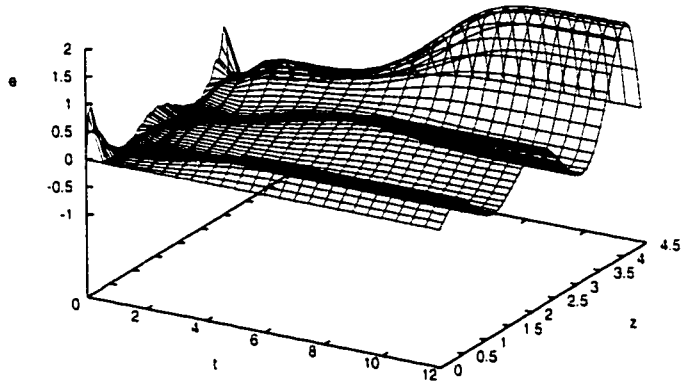

Figure 4.6: Deviation between the third-order model and the high-order discretization of the PDE (sinusoidal functions used as basis functions).

computed using this approach result in more accurate models; specifically, we found that a 7th order model was needed in order to produce the same error of 3.4% as the second order model based on empirical eigenfunctions, and a 10th order model was needed to have the same error of 0.5% as the third order model based on empirical eigenfunctions. This comparison is also presented in Figure 4.7, where the relative error between the norm of the reduced-order model, and the norm of the high-order discretization of the PDE, $\left|\frac{\|\bar{x}_{low}\|_2 - \|\bar{x}_{high}\|_2}{\|\bar{x}_{high}\|_2}\right|$, is shown as a function of time, for the cases of a third-order model derived using empirical eigenfunctions, a third-order model derived using sinusoids and an eighth-order model based on sinusoids. We observe that initially the model based on empirical eigenfunctions gives the highest error, but as time progresses the error becomes insignificant. This is due to the fact that the empirical eigenfunctions capture the dominant spatial structures of the PDE and as a result the third-order model follows the process dynamics closely after the fast dynamics of the PDE system die out.

Having numerically established the ability of the computed reduced-order models to describe the PDE, we then tested the ability of the third-order model to give

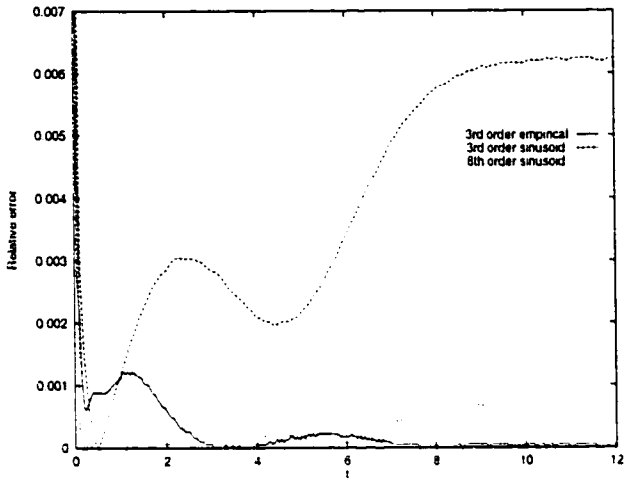

Figure 4.7: Relative error profiles (defined as $abs[||\bar{x}_{low}||_2 - ||\bar{x}_{high}||_2]/||\bar{x}_{high}||_2$) between the reduced-order models, based on empirical or analytical basis functions, and the high-order discretization of the PDE (nominal case).

accurate predictions when the process parameters have values which are different from the ones used in the construction of the ensemble of solutions for the computation of the empirical eigenfunctions. Specifically, for $\beta_T = 55(1.5 - e^{-0.5\,z})$ (which corresponds to an about +20% variation with respect to the nominal value of β_T), the maximum error between the third-order model and the high-order discretization of the PDE is less than 0.5% for all times as can be seen in Figure 4.8. On the other hand, for $\beta_T = 45(1.5 - e^{-0.4\,z})$ (which corresponds to an about −20% variation with respect to the nominal value of β_T), the error between the two models remains under 0.7% for all times as can be seen in Figure 4.9. We also tested the robustness of the third-order model for a +20% ($k = e^{-0.4\,z}$) and −20% ($k = e^{-0.6\,z}$) variation in the spatial dependence of k. The corresponding errors between the third-order model and the high-order discretization of the PDE are shown in Figures 4.10 and 4.11 respectively; they remain small for all times under 0.6% in the first and 1.6% in the second case.

We also tested the robustness of the third-order model for two initial conditions

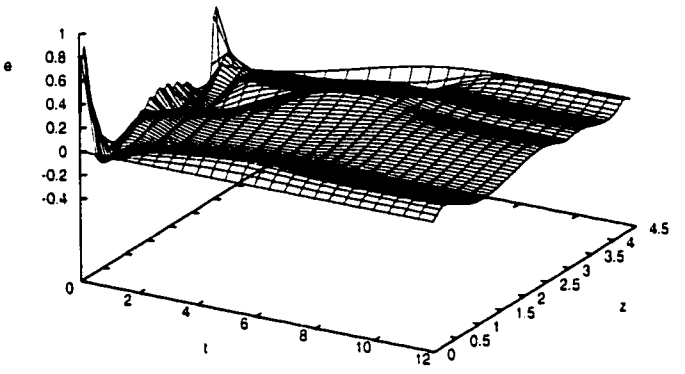

Figure 4.8: Deviation between the third-order model and the high-order discretization of the PDE ($\beta_T(z) = 55(1.5 - e^{-0.5\,z})$).

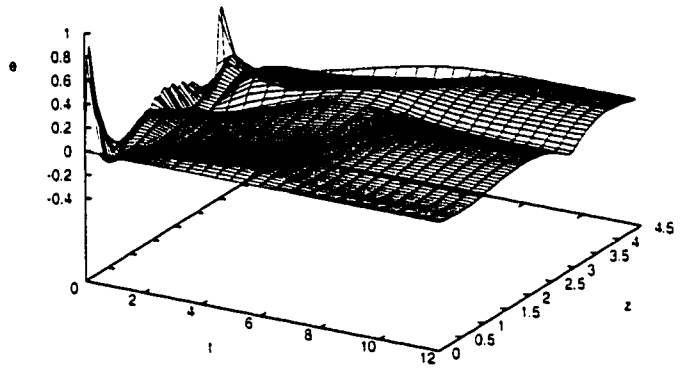

Figure 4.9: Deviation between the third-order model and the high-order discretization of the PDE ($\beta_T(z) = 45(1.5 - e^{-0.4\,z})$).

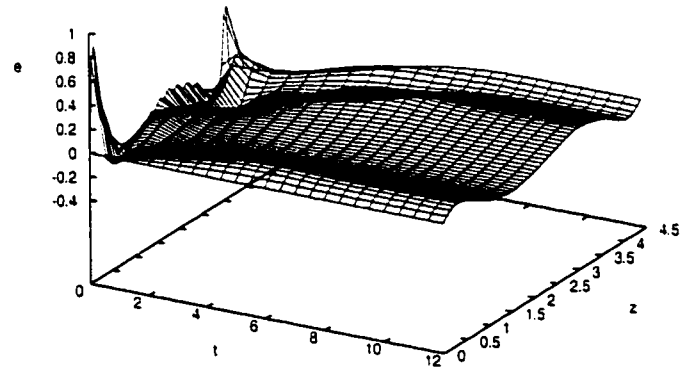

Figure 4.10: Deviation between the third-order model and the high-order discretization of the PDE ($k(z) = e^{-0.4\,z}$).

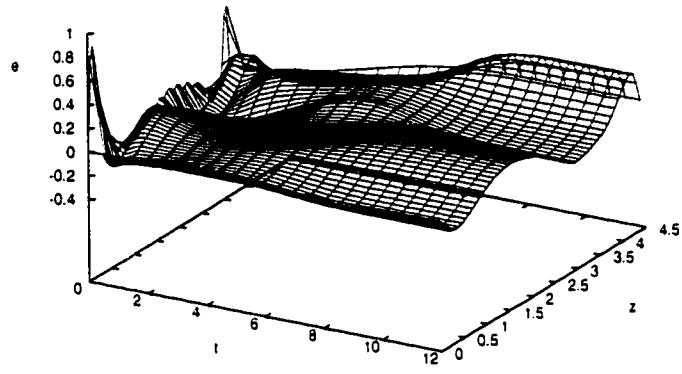

Figure 4.11: Deviation between the third-order model and the high-order discretization of the PDE ($k(z) = e^{-0.6\,z}$).

which are different from the ones used for the construction of the empirical eigenfunctions. Specifically, for the initial condition $\bar{x}_0(z) = 0.5 + 0.5sin(z)$, the deviation between the third-order model and the high-order discretization of the PDE is presented in Figure 4.12, while for $\bar{x}_0(z) = 0.4 + 0.6sin(3\ z)$, the same deviation is shown in Figure 4.13. In both cases, the maximum error between the two models is less

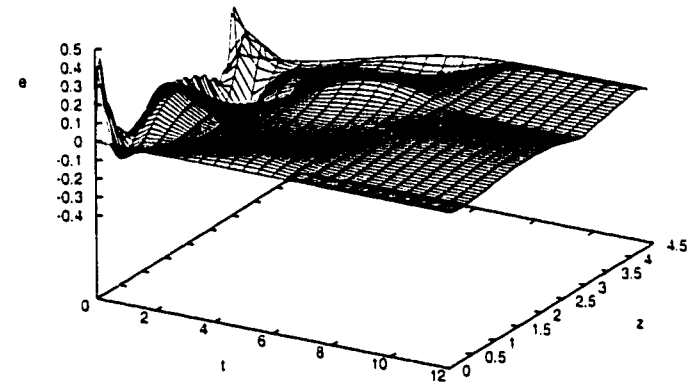

Figure 4.12: Deviation between the third-order model and the high-order discretization of the PDE ($\bar{x}_0(z) = 0.5 + 0.5sin(z)$).

than 1.6%, implying the robustness of the proposed model reduction procedure with respect to significant variations in the initial conditions. The aforementioned results are summarized in the following table 4.1 which presents the integral error between

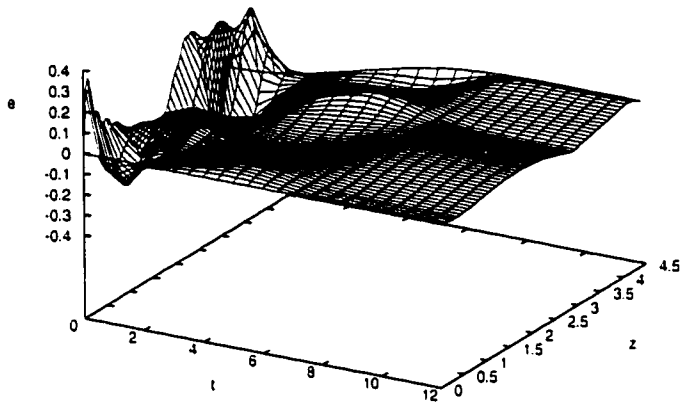

Figure 4.13: Deviation between the third-order model and the high-order discretization of the PDE ($\bar{x}_0(z) = 0.4 + 0.6sin(3\ z)$).

the reduced- and high-order models during the process cycle, for the different process conditions that we presented in this section. Specifically the error was calculated using the following formula:

$$\int_0^{t_f} \left| \frac{\|\bar{x}_{low}\|_2 - \|\bar{x}_{high}\|_2}{\|\bar{x}_{high}\|_2} \right| dt \tag{4.45}$$

where $t_f = 12$ is the final time of the process simulation run. We note that, even though the third-order model closely tracks the solution of the high-discretization for almost all times, in the case of $\bar{x}_0(z) = 0.4 + 0.6sin(3\ z)$, the integral error is computed to be large compared to the rest of the simulation runs. This is due to the large initial error between the two models as can be seen in Figure 4.13, caused by the excitation of the stable and fast-dissipating higher modes that the reduced-order model does not capture. In comparison, the models that were derived based on the eigenfunctions of Eq.4.42 exhibit a larger error in the spatial profile of the solution for all times, as can be seen in Figure 4.6.

Finally, we used the proposed method to control the process. Specifically, the controller synthesis formula of Theorem 4.1 was used to synthesize a second-order controller on the basis of a second-order model obtained using Galerkin's method

Table 4.1: Model error for different process conditions

Basis functions	Model order	Process conditions	Error [%] ⋆	Figure
Empirical	2	nominal	3.300	4.4
Empirical	3	nominal	0.352	4.5
Sinusoids	3	nominal	4.939	4.6
Sinusoids	8	nominal	0.483	
Empirical	3	+20% change in β_T	0.358	4.8
Empirical	3	-20% change in β_T	0.353	4.9
Empirical	3	+20% change in k	0.588	4.10
Empirical	3	-20% change in k	0.459	4.11
Empirical	3	arbitrary initial condition	0.515	4.12
Empirical	3	arbitrary initial condition	2.905	4.13
Empirical	5	constant process parameters	0.037	4.16
Analytical	5	constant process parameters	0.710	

⋆ The error is calculated using Eq.4.45

with the first two empirical eigenfunctions as basis functions. The control objective is to stabilize the system at the unstable steady state $\bar{x}(z,t) = 0$, using one point measurement of the state at $z = \frac{l(t)}{3}$ (i.e., moving sensor with $s(z,t) = \delta(z - \frac{1}{3}l(t))$, where $\delta(\cdot)$ is the Dirac function). Performing a linearization of the PDE system around the spatially uniform steady-state, we found that the first two modes are unstable. Therefore, the controlled outputs were defined as:

$$\begin{aligned} y_{c1}(t) &= \int_0^{l(t)} \phi_1(z,t)\bar{x}(z,t)dz, \\ y_{c2}(t) &= \int_0^{l(t)} \phi_2(z,t)\bar{x}(z,t)dz \end{aligned} \tag{4.46}$$

where ϕ_i denotes the i-th empirical eigenfunction. The actuator distribution functions were taken to be $b_1(z,t) = 1$ (uniform in space, distributed control action) and $b_2(z,t) = \delta(z - \frac{2}{3}l(t))$ (moving point control actuation).

Figure 4.14 shows the evolution of the closed-loop rod temperature profile under the nonlinear output feedback controller, while Figure 4.15 shows the corresponding manipulated input profiles. Clearly, the proposed controller achieves regulating

the temperature profile at the spatially uniform steady state $\bar{x}(z,t) = 0$. For the sake of comparison, we also constructed finite-dimensional models using Galerkin's method with the analytical eigenfunctions of Eq.4.42 as basis functions, and we used the resulting models for the synthesis of nonlinear output feedback controller utilizing the result of Theorem 4.1. We found that the lowest-order controller that

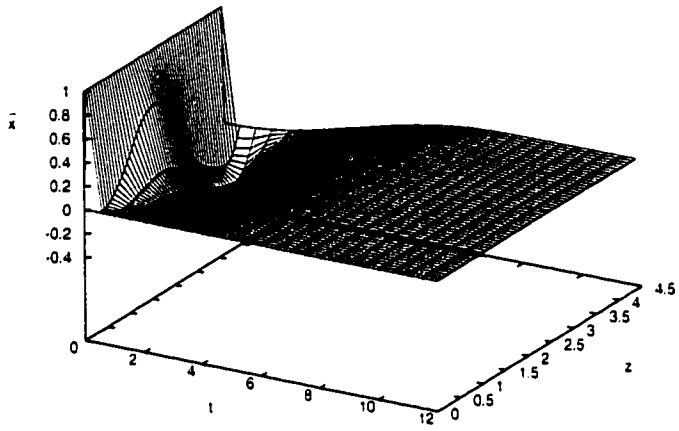

Figure 4.14: Closed-loop profile of $\bar{x}$ under nonlinear output feedback control using empirical eigenfunctions ($m = 2$).

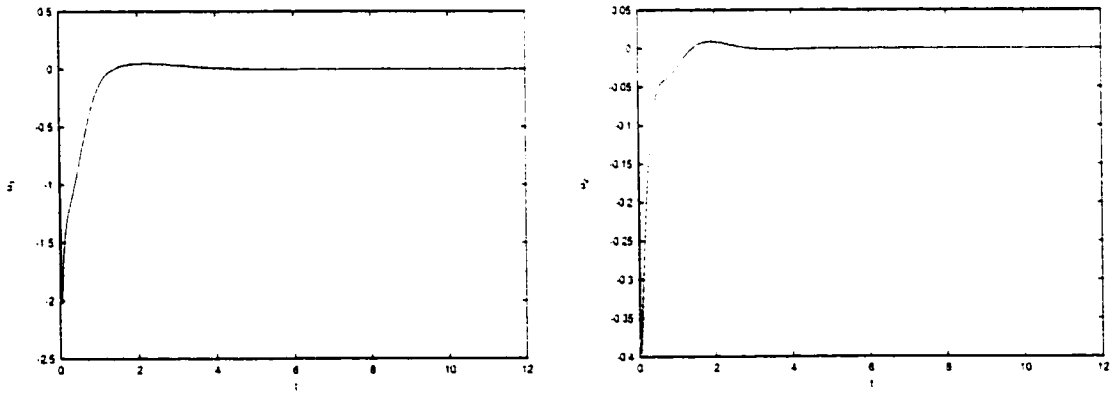

Figure 4.15: Manipulated input profiles for output feedback controller.

achieves stabilization of the PDE system at $\bar{x}(z,t) = 0$ is of order 4. Therefore, we observe a significant reduction on the order of the controller that stabilizes the system at the spatially uniform steady state when we use empirical eigenfunctions as

basis functions. This again happens because the empirical eigenfunctions take into consideration the spatial variation of the coefficients of the process model, while the analytical eigenfunctions were derived on the basis of the spatial operator with spatially uniform coefficients, and thus, they do not capture the spatially varying features of the process.

Remark 4.9: To illustrate the applicability of the proposed approach to parabolic PDE systems with spatially-uniform coefficients we considered the PDE system of Eq.4.39 with:

$$\beta_T = 75.0, \quad k = 1.0 \tag{4.47}$$

For this system, the steady-state $\tilde{x}(z,t) = 0$ is also unstable and the eigenfunctions of the spatial operator can be computed analytically and are given in Eq.4.42. Furthermore, for this system, we constructed a representative ensemble of solutions by varying the initial conditions and the inputs and used it to construct a set of seven empirical eigenfunctions. Then, we employed Galerkin's method to construct two fifth-order models corresponding to the two different sets of basis functions (analytical and empirical). Figure 4.16 shows the discrepancy between the fifth-order model based on empirical eigenfunctions and a high-order discretization of the PDE. We can see that this discrepancy remains small for all times, thereby implying that the use of empirical eigenfunctions leads to accurate low-order models for parabolic PDE systems with spatially-uniform coefficients as well. For comparison purposes, we also present in Table 4.1 the integral error of Eq.4.45 for both the fifth-order models that we derived. We can see that the integral error of the model derived using the proposed methodology is 20 times smaller than the error of the model based on analytical eigenfunctions of the spatial operator. The reason for this difference is that the empirical eigenfunctions take into consideration all the characteristics of the process including

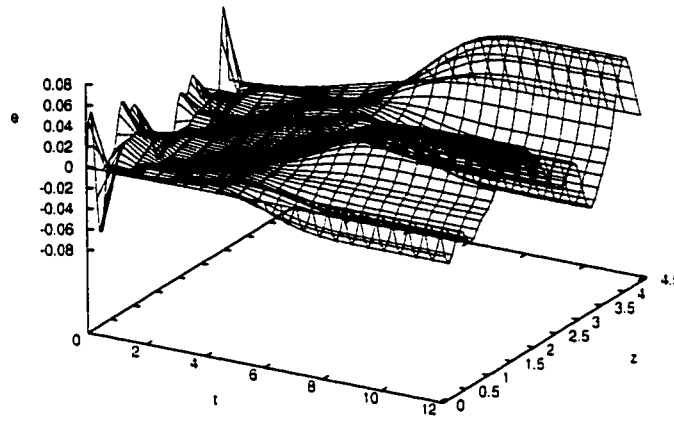

Figure 4.16: Deviation between reduced and full-order models for spatially uniform process parameters β_T and k.

the effect of nonlinearities, while the analytical eigenfunctions account only for the structure of the linear spatial differential operator and of the boundary conditions.

4.6 Conclusions

In this chapter, we presented a methodology for the synthesis of finite-dimensional nonlinear output feedback controllers for nonlinear parabolic PDE systems with time-dependent spatial domains. Initially, the nonlinear parabolic PDE system was expressed with respect to an appropriate time-invariant spatial coordinate and a representative (with respect to different initial conditions and input perturbations) ensemble of solutions of the resulting time-varying PDE system was constructed by computing and solving a high-order discretization of the PDE. Then, the Karhunen-Loève expansion was directly applied to the ensemble of solutions to derive a small set of empirical eigenfunctions (dominant spatial patterns) that capture almost all the energy of the ensemble of solutions. The empirical eigenfunctions were subsequently used as basis functions within a Galerkin's model reduction framework to derive low-order ODE systems that accurately describe the dominant dynamics of the PDE

system. The ODE systems were used for the synthesis of nonlinear output feedback controllers using geometric control methods. The proposed control method was successfully used to stabilize an unstable steady-state of a diffusion-reaction process with nonlinearities, spatially-varying coefficients and time-dependent spatial domain, and was shown to lead to the construction of accurate low-order models and the synthesis of low-order controllers.

Chapter 5

Crystal Temperature Control in the Czochralski Crystal Growth Process

5.1 Introduction

This chapter proposes a control configuration and a nonlinear multivariable model-based feedback controller for the reduction of thermal gradients inside the crystal in the Czochralski crystal growth process after the crystal radius has reached its final value. Even though the process model is a distributed system, the proposed controller is of low-order, and therefore, it can be readily implemented in real-time.

Czochralski crystal growth (CZ) is a well-established industrial process used for the production of single crystals like silicon (Si) and gallium arsenide (GaAs). Such crystals are widely used for the construction of wafers employed in the production of microelectronic chips. The central idea of the CZ process is to grow a crystal from a melt by pulling a seed crystal very slowly within a well-regulated thermal environment in a furnace. For the subsequent processing steps, it is important to

form a cylindrical crystal with desired radius and length dimensions which includes very low concentrations of impurities and dislocations, as well as a uniform dopant distribution.

The current practice in achieving a constant crystal radius is to use a proportional-integral-derivative (PID) controller that manipulates the pulling rate of the crystal from the melt to adjust the crystal radius, while the regulation of the crystal temperature is addressed by adjusting the heat transfered to the melt and crystal by manipulation (typically via PID) of the heater power. The tuning of such PID controllers based on fundamental lumped parameter models that describe the dominant dynamic characteristics of the CZ process has been addressed in a series of papers published by Gevelber and Stephanopoulos [82, 80, 81, 78, 79]. Even though these works provide valuable insights for the nature of the crystal radius and thermal dynamics, identify natural control objectives and variables, as well as structural limitations on the best achievable closed-loop performance, they do not account for the presence of spatial variations of the temperature inside the crystal which constitute the main cause for dislocations and defects [167, 78]. Furthermore, PID controllers do not account for the fact that CZ processes exhibit nonlinear and time-varying behavior and involve coupling of variables evolving in widely different time-scales. In an effort to overcome the limitations of conventional controllers, the problems of controlling the radius of the crystal and reducing the thermal strain in the interface between crystal and melt were recently addressed within a model predictive control framework [96, 97]. However, in these papers, the key practical issue of deriving accurate low-order approximations of the distributed process model that can be used in real-time control implementation was not addressed.

The main challenge in the design of model-based feedback controllers for CZ pro-

cesses is the fact that the dynamic models of such processes are typically in the form of nonlinear parabolic partial differential equations (PDE) with time-dependent spatial domains. These are distributed parameter (infinite-dimensional) systems, and therefore, they cannot be directly used for the design of practically implementable (low-dimensional) controllers.

The chapter is structured as follows. A fundamental mathematical model which describes the evolution of the temperature inside the crystal in the radial and axial directions and accounts for radiative heat exchange between the crystal and its surroundings and motion of the crystal boundary is initially presented. This model is numerically solved by using Galerkin's method and the behavior of the crystal temperature is studied to obtain valuable insights which lead to the precise formulation of the control problem and the derivation of a simplified one-dimensional in space PDE model with moving domain which is used for controller synthesis. Then, a general nonlinear model reduction and control method for PDE systems with moving domains developed in [2] is briefly presented. This method is used to construct a fourth-order model that describes the dominant thermal dynamics of the Czochralski process and synthesize a fourth-order nonlinear controller that can be readily implemented in practice. The proposed control scheme is successfully implemented on a Czochralski process used to produce a 0.7 m long silicon crystal with a radius of 0.05 m and is shown to significantly reduce the axial and radial thermal gradients inside the crystal compared to the open-loop operation and to the case of using a single control actuator. The robustness of the proposed controller with respect to parametric model uncertainty, melt and chamber temperature disturbances and unmodeled actuator and sensor dynamics is demonstrated through simulations.

5.2 Czochralski crystal growth: Description and modeling of crystal thermal behavior

We focus on a Czochralski crystal growth process shown in Figure 5.1 used to produce a 0.7 m long silicon crystal with a radius of 0.05 m. The process comprises of a cylindrical chamber which includes a rotating pedestal that can move in the axial direction. A crucible containing silicon (Si) crystals is placed on the pedestal and heaters (placed on the sides of the chamber and under the pedestal) are used to increase the temperature of the Si crystals inside the crucible (through radiation) above the melting point of Si. A Si seed crystal comes in contact with the melt and the temperature of the melt is adjusted until the meniscus is supported by the end of the seed. Once the meniscus has been stabilized, the seed crystal is pulled away from the melt and new crystal is formed [100]. The interface between the crystal and

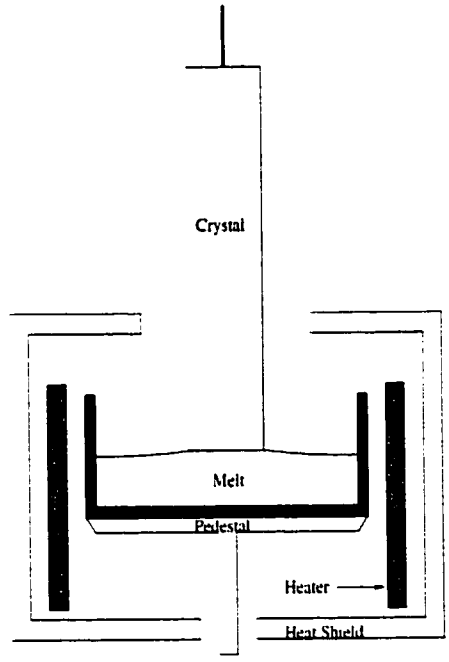

Figure 5.1: Schematic of the Czochralski crystal growth.

the melt is maintained at a constant position during the operation of the process by

moving the position of the pedestal higher with time. As the length of the crystal becomes larger, part of it leaves the chamber and starts cooling, at which point the thermal gradients inside the crystal become large and may cause thermal strain inside the crystal [167]. If the cooling conditions are not properly regulated, large thermal strain may cause microdefects (e.g., dislocations) inside the crystal [78], and may even lead to fracture. As a result, the cooling process should be carefully regulated. Finally, the process is terminated when the crystal-melt interface reaches the crucible bottom.

The development of detailed mathematical models for the Czochralski crystal growth process is an area that has received significant attention (see, for example, the book [94]), and at this point, comprehensive models are available [57, 58, 59, 7, 60, 56, 182, 172, 173]. Since the objective of this chapter is to develop a control configuration and a model-based feedback controller which will smoothly regulate the cooling process of the crystal as it leaves the chamber, our modeling effort focuses on the development of a mathematical model that describes the spatiotemporal evolution of the crystal temperature, after the crystal radius has obtained its final value, and accounts for radiative heat exchange between the crystal, heater shield, crucible, melt surface and the environment. Moreover, our control objective allows making the following simplifying assumptions in the model development: a) the crystal radius and the meniscus height are assumed to be constant; this is typically achieved by using a controller that manipulates the pulling rate and the chamber temperature to maintain these variables constant and allows neglecting the detailed dynamics of the crystal/melt interface in our analysis (see also remark 5.9 and discussion in Appendix E), b) the temperature distribution inside the crystal is assumed to be axisymmetric owing to the constant rotation of the crucible, c) radiation is assumed to be the

dominant heat transfer mechanism; this assumption is justified from the fact that the temperatures of the chamber, melt and crystal surfaces are very high ($1000-1700\ K$), d) secondary radiation is not taken into account since it has a smaller effect on the crystal temperature profile compared to the primary radiation and the temperatures of the surrounding surfaces are kept constant at the desired set-points using control, e) the melt and chamber temperature and the pulling rate are assumed to be constant and the melt/crystal interface is assumed to be flat; this allows us to neglect the melt dynamics, f) the solidification front remains in a specified region of the heater as the melt level drops; this is achieved in practice by raising the crucible through movement of the pedestal [57], g) the concentration of dopant, oxygen and carbon are not explicitly included in the model; this is done to simplify the controller synthesis task and special consideration is taken in the tuning of the controller (see subsection 5.2 below) to ensure that large and abrupt heater temperature (manipulated input) changes, which could cause large variations in the concentration fields, do not occur.

Under these assumptions, an application of an energy balance to a differential element of the crystal yields the following two-dimensional parabolic PDE:

$$\frac{\partial T_c}{\partial t} + v_p \frac{\partial T_c}{\partial z} = \frac{k}{\rho c_p}\left[\frac{1}{r}\frac{\partial}{\partial r}\left(r\frac{\partial T_c}{\partial r}\right) + \frac{\partial^2 T_c}{\partial z^2}\right] \tag{5.1}$$

subject to the following boundary conditions:

$$T_c(r,0,t) = T_{mp}, \quad 0 \le r \le R \tag{5.2}$$

$$\left.\frac{\partial T_c}{\partial r}\right|_0 = 0, \quad 0 \le z \le l(t) \tag{5.3}$$

$$\begin{aligned}\left.\frac{k}{\sigma}\frac{\partial T_c}{\partial r}\right|_R =& \epsilon_{w_{cr}}\epsilon_{w_m}F_{cr\to m}(R,z)[T_m^4 - T_c^4(R,z,t)] \\ &+\epsilon_{w_{cr}}\epsilon_{w_{ch}}F_{cr\to ch}(R,z)[T_{ch}^4 - T_c^4(R,z,t)] \\ &+\epsilon_{w_{cr}}\epsilon_{w_{amb}}F_{cr\to amb}(R,z)[T_{amb}^4 - T_c^4(R,z,t)], \quad 0 \le z \le l(t)\end{aligned} \tag{5.4}$$

$$\left.\frac{k}{\sigma}\frac{\partial T_c}{\partial z}\right|_{l(t)} = \epsilon_{w_{cr}}\epsilon_{w_m}F_{cr\to m}(r,l(t))[T_m^4 - T_c^4(r,l(t),t)]$$
$$+\epsilon_{w_{cr}}\epsilon_{w_{ch}}F_{cr\to ch}(r,l(t))[T_{ch}^4 - T_c^4(r,l(t),t)] \quad (5.5)$$
$$+\epsilon_{w_{cr}}\epsilon_{w_{amb}}F_{cr\to amb}(r,l(t))[T_{amb}^4 - T_c^4(r,l(t),t)], \quad 0 \le r \le R$$

In the above equations, T_c is the temperature of the crystal, t is the time, r is the radial direction, z is the axial direction, v_p is the pulling speed, T_{ch} is the chamber temperature, T_{amb} is the ambient temperature, T_{mp} is the melting point temperature of silicon, T_m is the temperature of the melt, σ is the Stefan-Boltzmann constant, $\epsilon_{w_{cr}}$, ϵ_{w_m}, $\epsilon_{w_{ch}}$, $\epsilon_{w_{amb}}$ denote the emissivities of the crystal, melt, chamber and ambient respectively, $F_{cr\to j}$ is the view factor from the surface of a differential element of the crystal at $r = R$, cr, to surface j, and $l(t)$ is the total height of the crystal at time t. The model of Eqs.5.1-5.5 constitutes a parabolic PDE system with moving boundary owing to the variation of the length, $l(t)$, of the crystal in the axial direction ($l(t) = \int_0^t v_p(s)ds$, where $v_p(t)$ is the pulling rate).

Table 5.1: Physical properties of Si

Melting point	T_{mp}	1683	K
Crystal specific heat	c_p	1000	$J\ kg^{-1}\ K^{-1}$
Crystal density	ρ	2420	$kg\ m^{-3}$
Crystal thermal conductivity	k	22	$J\ (s\ m\ K)^{-1}$
Crystal emissivity	$\epsilon_{w_{cr}}$	0.7	
Melt emissivity	ϵ_{w_m}	0.7	

In Eq.5.1, the terms $\frac{\partial T_c}{\partial t}$ and $v_p\frac{\partial T_c}{\partial z}$ describe the rate of change of crystal temperature and the convection effect due to the motion of the crystal , respectively, while the terms $\frac{k}{\rho c_p}\left[\frac{1}{r}\frac{\partial}{\partial r}\left(r\frac{\partial T_c}{\partial r}\right) + \frac{\partial^2 T_c}{\partial z^2}\right]$ account for heat conduction inside the crystal. On the other hand, the boundary condition of Eq.5.2 states that the crystal temperature in the crystal/melt interface is equal to the Si melting point temperature and the boundary condition of Eq.5.3 is based on the assumption of axisymmet-

ric crystal. Furthermore, the boundary condition of Eq.5.4 accounts for radiative heat exchange between the *differential surface at the side of the crystal* and melt (term $\epsilon_{w_{cr}}\epsilon_{w_m}F_{cr\to m}(R,z)[T_m^4-T_c^4(R,z,t)]$), chamber (term $\epsilon_{w_{cr}}\epsilon_{w_{ch}}F_{cr\to ch}(R,z)[T_{ch}^4-T_c^4(R,z,t)]$) and ambient (term $\epsilon_{w_{cr}}\epsilon_{w_{amb}}F_{cr\to amb}(R,z)[T_{amb}^4-T_c^4(R,z,t)]$), and the boundary condition of Eq.5.5 accounts for radiative heat exchange between the *differential surface at the top of the crystal* and melt (term $\epsilon_{w_{cr}}\epsilon_{w_m}F_{cr\to m}(r,l(t))[T_m^4-T_c^4(r,l(t),t)]$), chamber (term $\epsilon_{w_{cr}}\epsilon_{w_{ch}}F_{cr\to ch}(r,l(t))[T_{ch}^4-T_c^4(r,l(t),t)]$) and ambient (term $\epsilon_{w_{cr}}\epsilon_{w_{amb}}F_{cr\to amb}(r,l(t))[T_{amb}^4-T_c^4(r,l(t),t)]$). The computation of the various view factors through decomposition of the corresponding complex geometries into simple geometries for which view factors can be computed analytically is discussed in Appendix E.

Finally, the values of the physical properties of Si are given in Table 5.1, and the values of the parameters of the process are given in Table 5.2. We note that: a) the Si crystal properties are assumed to be independent of the temperature and concentrations of dopant, carbon and oxygen, and b) even though our study does not focus on a specific experimental or industrial Czochralski crystallizer, the values of the process parameters in Table 5.2 are within the range of values normally employed in industrial crystallizers (compare with the values given in [59]).

Remark 5.1: Regarding the development of the above model, we must note that the focus of our control effort is on the reduction of the magnitude of the thermal gradients inside the body of the crystal and thus we focus on the development of a model that describes the spatiotemporal evolution of the crystal temperature, once the crystal radius has obtained its final value, and accounts for the interactions (radiative heat transfer) between the crystal and its surroundings. There is an extensive literature on the development of integrated (global) models for the Czochralski process that include

Table 5.2: Process parameters

Chamber height	h_{ch}	0.18	m
Chamber radius	R_{ch}	0.15	m
Chamber emissivity	$\epsilon_{w_{ch}}$	0.3	
Chamber wall temperature	T_{ch}	1500	K
Pulling velocity	v_p	$1.66\ 10^{-5}$	$m\ sec^{-1}$
Melt temperature	T_m	1705	K
Initial length of crystal	l_0	0.05	m
Final length of crystal	l_f	0.70	m
Radius of crystal	R	0.05	m
Ambient emissivity	$\epsilon_{w_{ch}}$	0.3	
Ambient temperature	T_{amb}	600	K
Reference temperature for i-th heater	T_{sp_i}	1000	K

the crystal-melt interface shape and melt temperature dynamics (see, for example, [57, 58, 59, 182] for details). We finally note that the technique for order reduction and controller design that is presented in the next section can also be applied to these integrated crystal growth models to design controllers for crystal temperature regulation, but such an application is outside the scope of this chapter.

5.3 Control-relevant analysis of the Czochralski process

The objective of this section is to study the thermal gradients inside the crystal in the Czochralski crystal growth process to obtain insights which will be used to formulate a meaningful control problem and derive an appropriate model for controller synthesis. The mathematical model of the Czochralski crystal growth process of Figure 5.1 consisting of the two-dimensional parabolic PDE of Eq.5.1 and the boundary conditions of Eqs.5.2-5.5 was solved using Galerkin's method. Specifically, 30 global eigenfunctions (i.e., trigonometric functions that cover the entire domain) in the axial direction and 30 global (Bessel) eigenfunctions in the radial direction were used as basis functions in Galerkin's method to discretize the process model in space and re-

duce it into a large set (900 equations) of ODEs. The time-integration of the large set

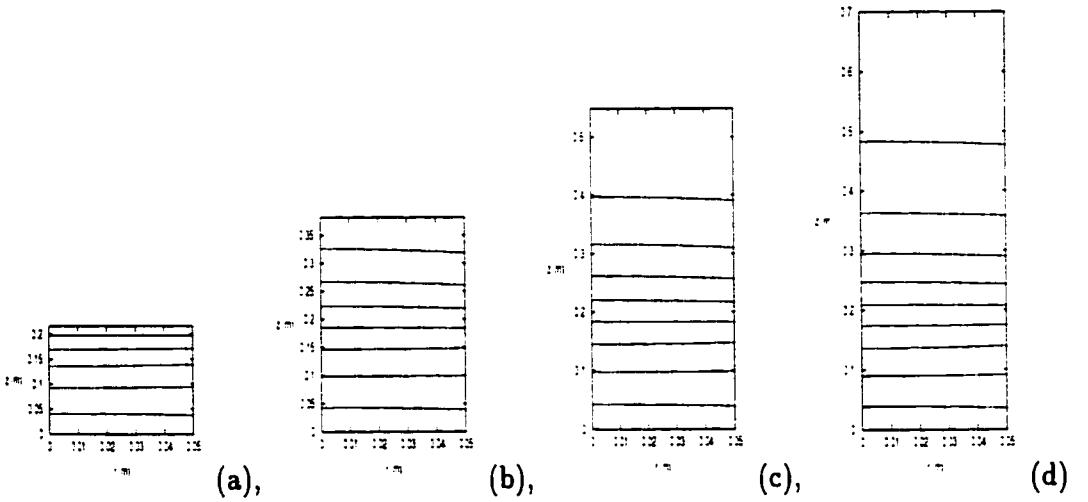

Figure 5.2: Temperature of crystal as a function of radial and axial coordinates for $T_{amb} = 600\ K$. (a) $t = 1 \times 10^4\ s$, (b) $t = 2 \times 10^4\ s$, (c) $t = 3 \times 10^4\ s$ and (d) $t = 4 \times 10^4\ s$. Each contour represents a 100 K temperature difference.

of ODEs was performed utilizing explicit Euler. It was verified that further increase in the number of eigenfunctions in both r and z directions as well as reduction in the step of time-integration results in negligible change in the accuracy of the computed solution. In all the simulation runs, the crystal is initially assumed to be at $l(0) = 0.05\ m$ and $T_c(r, z, 0) = 1670\ K$.

Figures 5.2 and 5.3a show the contour plots of the crystal temperature as a function of the axial and radial directions at four different time instants during the operation of the process and the temporal evolution of the crystal temperature in the axial direction at the center of the crystal respectively, when the temperature of the ambient (void space in the furnace surrounding the crystal) is set at $T_{amb} = 600\ K$. We observe that the temperature drop inside the crystal in the axial direction is much larger (almost 700 K) than the temperature drop inside the crystal in the radial direction (less than 20 K; see also Figure 5.3b). This can also be seen in Figures 5.3c

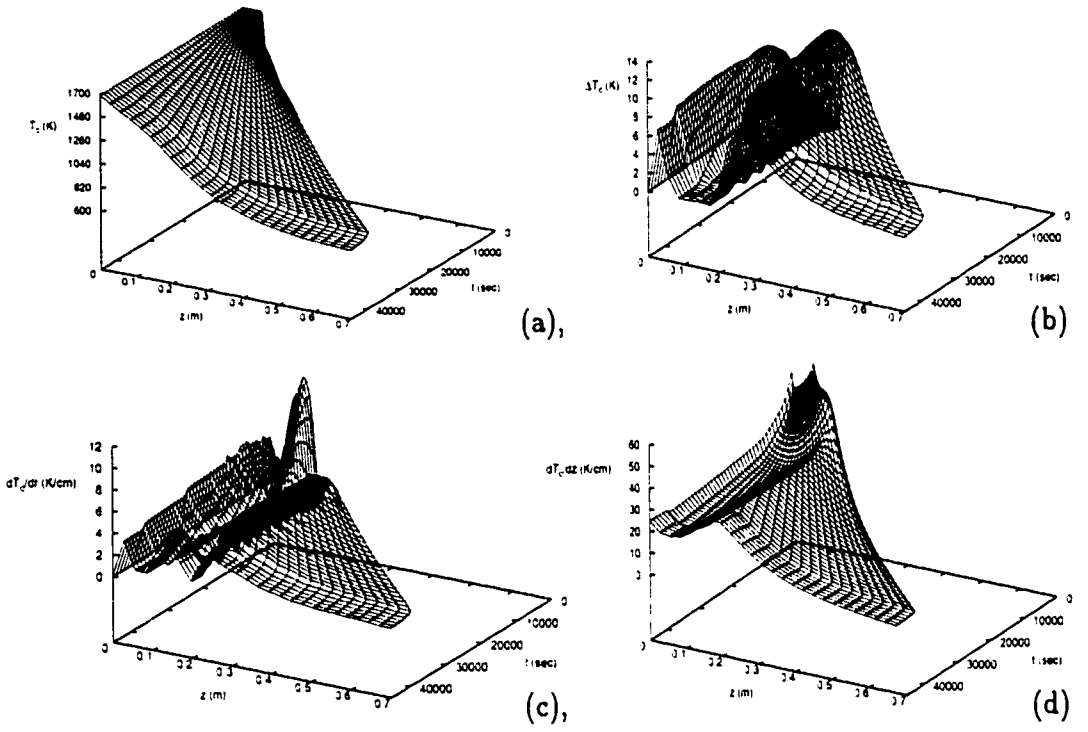

Figure 5.3: (a) Temperature of crystal at $r = 0.0\ m$, (b) Maximum temperature difference inside the crystal in the radial direction, (c) Maximum thermal gradient inside the crystal in the radial direction, (d) Maximum thermal gradient inside the crystal in the axial direction, as a function of time and axial coordinate for $T_{amb} = 600\ K$.

and 5.3d that show the maximum thermal gradient in the radial and axial direction respectively, as a function of the axial parameter and time. We observe that the maximum thermal gradient in the axial direction is 5 times larger than the maximum thermal gradient in the radial direction, for all times.

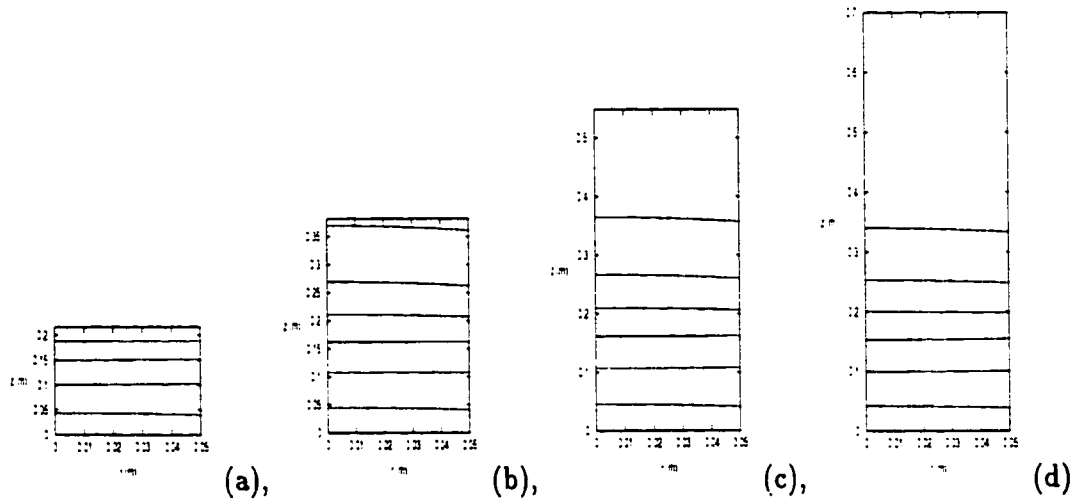

Figure 5.4: Temperature of crystal as a function of radial and axial coordinates for $T_{amb} = 1000\ K$. (a) $t = 1 \times 10^4\ s$, (b) $t = 2 \times 10^4\ s$, (c) $t = 3 \times 10^4\ s$ and (d) $t = 4 \times 10^4\ s$. Each contour represents a 100 K temperature difference.

To further investigate this observation, we show in Figures 5.5 and 5.7 the temporal evolution of the crystal temperature when the temperature of the ambient is set at $T_{amb} = 1000\ K$ and $T_{amb} = 1400\ K$, respectively. Again, it is clear that the variation of the crystal temperature in the radial direction is negligible compare to the variation in the axial one. This can also be seen in Figures 5.4 and 5.6 presenting contour plots of the crystal temperature, when the ambient temperature is $T_{amb} = 1000\ K$ and $T_{amb} = 1400\ K$, respectively. This conclusion is very important because it allows neglecting the radial dependence of the crystal temperature in the process model which will be used as the basis for the synthesis of a nonlinear feedback controller,

thereby yielding the following one-dimensional parabolic PDE with moving boundary:

$$\frac{\partial T_c}{\partial t} + v_p \frac{\partial T_c}{\partial z} = \frac{k}{\rho c_p} \frac{\partial^2 T_c}{\partial z^2} + \frac{2\sigma \epsilon_{w_{cr}} \epsilon_{w_m}}{\rho c_p R} F_{cr \to m}(R, z)[T_m^4 - T_c^4(z,t)]$$
$$+ \frac{2\sigma \epsilon_{w_{cr}} \epsilon_{w_{ch}}}{\rho c_p R} F_{cr \to ch}(R, z)[T_{ch}^4 - T_c^4(z,t)] \tag{5.6}$$
$$+ \frac{2\sigma \epsilon_{w_{cr}} \epsilon_{w_{amb}}}{\rho c_p R} F_{cr \to amb}(R, z)[T_{amb}^4 - T_c^4(z,t)]$$

subject to the boundary conditions:

$$T_c(0,t) = T_{mp} \tag{5.7}$$

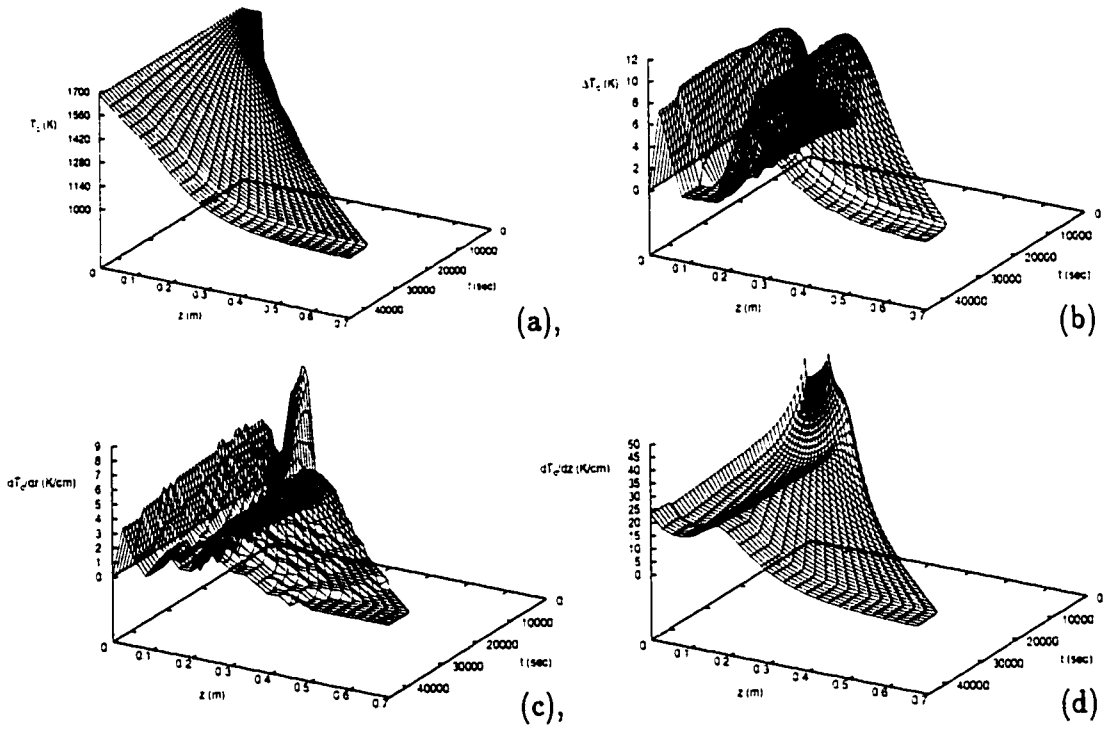

Figure 5.5: (a) Temperature of crystal at $r = 0.0\ m$, (b) Maximum temperature difference inside the crystal in the radial direction, (c) Maximum thermal gradient inside the crystal in the radial direction, (d) Maximum thermal gradient inside the crystal in the axial direction, as a function of time and axial coordinate for $T_{amb} = 1000\ K$.

$$\left.\frac{k}{\sigma}\frac{\partial T_c}{\partial z}\right|_{l(t)} = \epsilon_{w_{cr}}\epsilon_{w_m}F_{cr\to m}(l(t))[T_m^4 - T_c^4(l(t),t)] + \epsilon_{w_{cr}}\epsilon_{w_{ch}}F_{cr\to ch}(l(t))[T_{ch}^4 - T_c^4(l(t),t)] + \epsilon_{w_{cr}}\epsilon_{w_{amb}}F_{cr\to amb}(l(t))[T_{amb}^4 - T_c^4(l(t),t)] \tag{5.8}$$

An additional conclusion which follows from the study of Figures 5.3, 5.5 and 5.7 is that the ambient temperature T_{amb} has a very significant effect on the axial profile of the crystal temperature. This suggests that T_{amb} is a meaningful choice for ma-

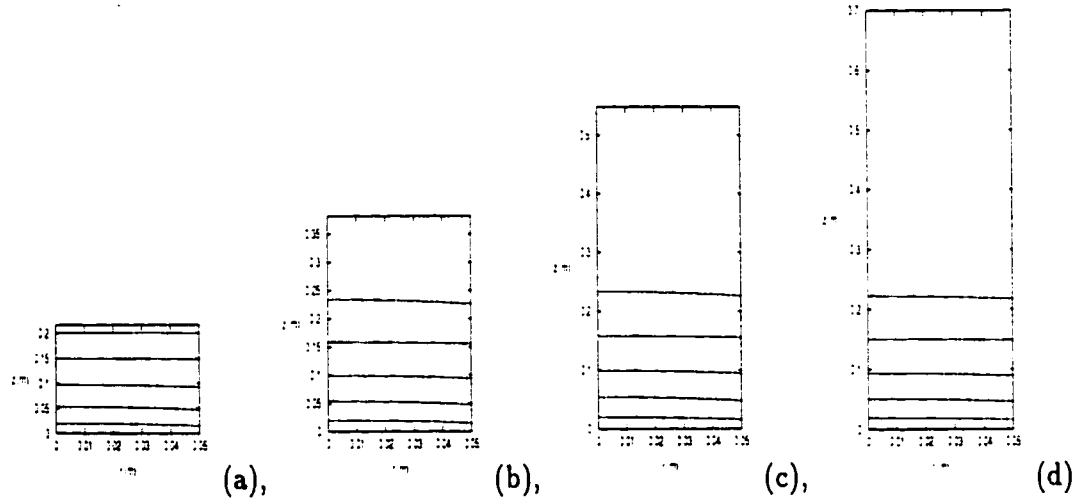

Figure 5.6: Temperature of crystal as a function of radial and axial coordinates for $T_{amb} = 1400\ K$. (a) $t = 1 \times 10^4\ s$, (b) $t = 2 \times 10^4\ s$, (c) $t = 3 \times 10^4\ s$ and (d) $t = 4 \times 10^4\ s$. Each contour represents a 50 K temperature difference.

nipulated variable in order to enforce a desired temperature drop inside the crystal. Therefore, we formulate the control problem as the one of controlling the temperature gradient of the crystal in the axial direction by manipulating the temperature of extra heaters placed above the chamber at equispaced intervals. The use of extra heaters to control the crystal temperature is also motivated by the realization that the regulation of thermal gradients in the axial direction requires the use of a manipulated variable which is distributed along the length of the crystal. We will show later on that the use of extra heaters to control axial thermal gradients will also lead to

significant reduction of the radial thermal gradients inside the crystal (which cannot be directly controlled) owing to the well-regulated thermal environment in which the crystal grows in such a case.

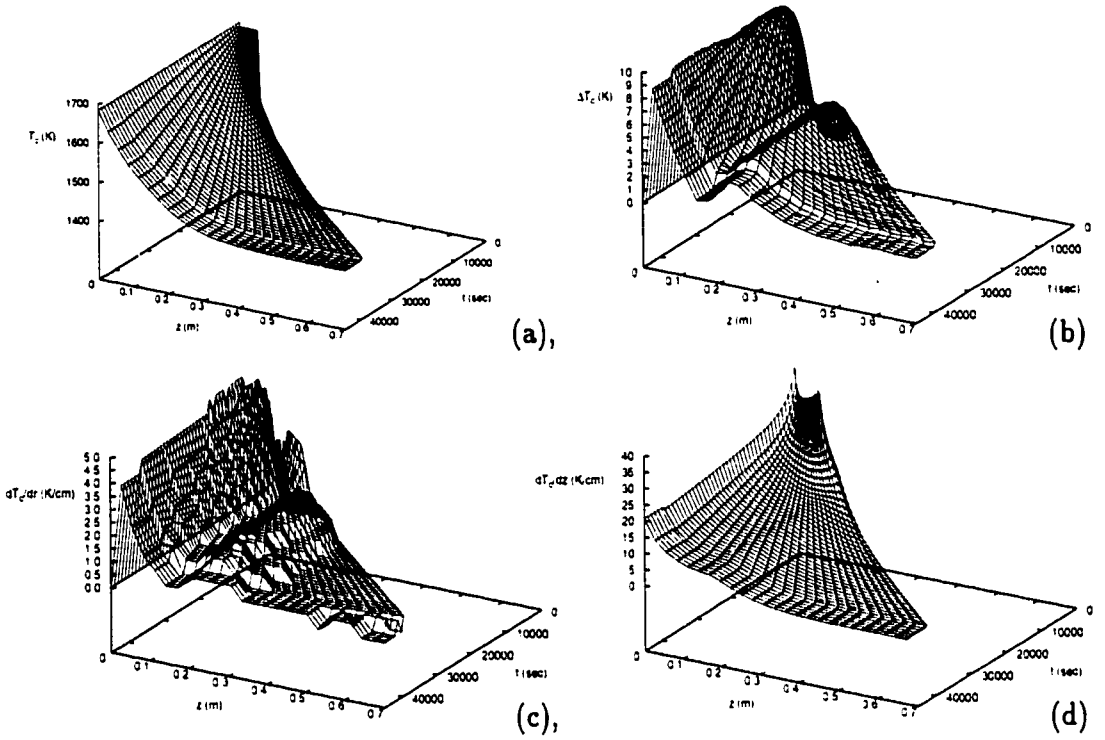

Figure 5.7: (a) Temperature of crystal at $r = 0.0\ m$, (b) Maximum temperature difference inside the crystal in the radial direction, (c) Maximum thermal gradient inside the crystal in the radial direction, (d) Maximum thermal gradient inside the crystal in the axial direction, as a function of time and axial coordinate for $T_{amb} = 1400\ K$.

Our attention now turns to the development of the control configuration that will be used to regulate the thermal gradients inside the crystal; this entails the computation of the number of separate components of the heaters needed to achieve the desired regulation of the thermal gradients. To this end, we initially assumed that the temperature of the heaters is spatially uniform and used a single proportional

integral controller to manipulate this temperature of the form:

$$\begin{aligned} \dot{\xi} &= y_{sp} - y,\ \xi(0) = 0 \\ u &= K(y_{sp} - y) + \frac{1}{\tau}\xi \end{aligned} \tag{5.9}$$

The objective of the controller was to keep the surface temperature of the crystal at position $z = 0.48\ m$ at a constant value of 1250 K, and enforce a smooth temperature inside the crystal, below the critical value of 20 K/cm [78]. The parameters of the controller are given in Table 5.3.

Table 5.3: PI Control parameters

$z_s\ [m]$	$z_f\ [m]$	$z_m\ [m]$	K	τ	$T_s\ [K]$
0.18	0.71	0.48	3	1.0	1250

Figure 5.9a shows the temporal evolution of the temperature at the center of the crystal in the axial direction in the closed-loop system. Clearly, the controller drives the temperature of the crystal to its new set-point, and the temperature gradients in

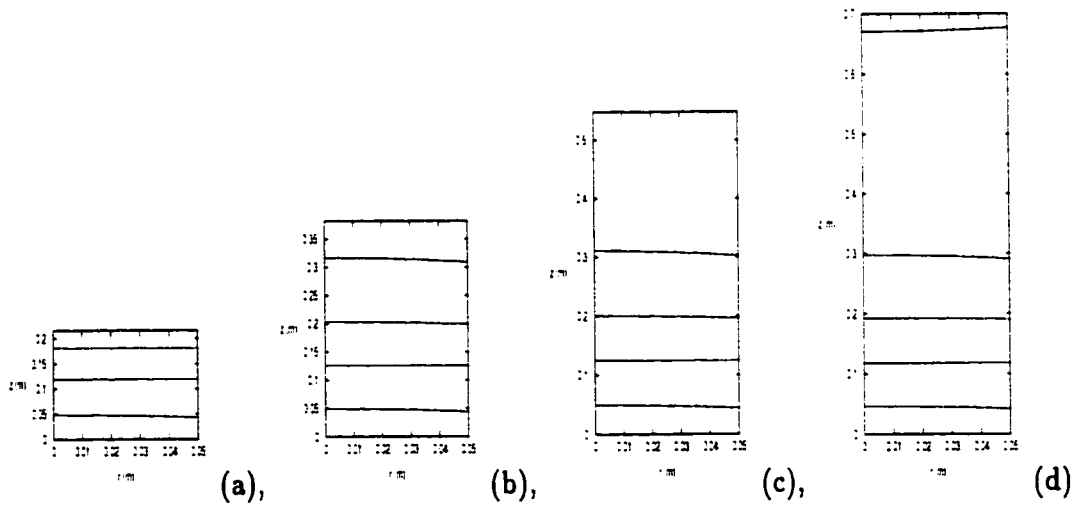

Figure 5.8: Temperature of crystal as a function of radial and axial coordinates - one PI controller. (a) $t = 1 \times 10^4\ s$, (b) $t = 2 \times 10^4\ s$, (c) $t = 3 \times 10^4\ s$ and (d) $t = 4 \times 10^4\ s$. Each contour represents a 100 K temperature difference.

the radial direction remain small for almost all times (see Figure 5.9c and compare with 5.3c). However, the controller fails to establish a smooth temperature drop

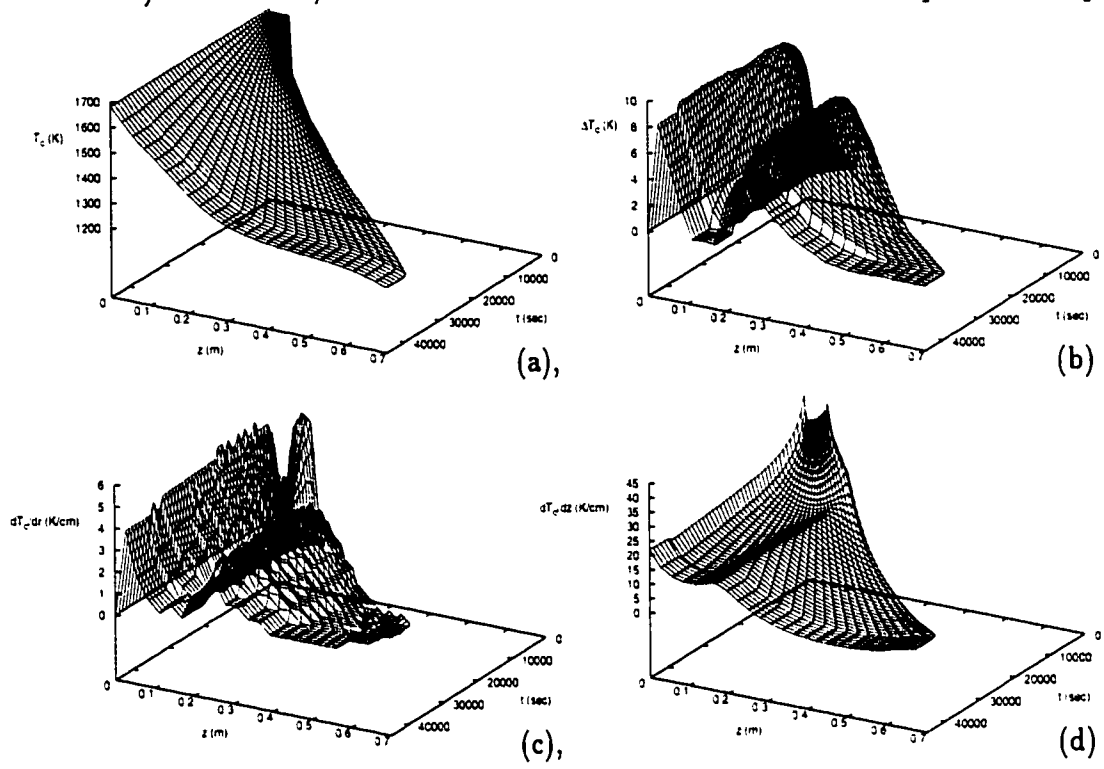

Figure 5.9: (a) Temperature of crystal at $r = 0.0\ m$, (b) Maximum temperature difference inside the crystal in the radial direction, (c) Maximum thermal gradient inside the crystal in the radial direction, (d) Maximum thermal gradient inside the crystal in the axial direction, as a function of time and axial coordinate - one PI controller.

inside the crystal in the axial direction, enforcing a large temperature drop close to the crystal-melt interface and achieving an almost uniform crystal temperature far away from the interface; this can be seen in Figure 5.8 which shows the contour plots of the crystal temperature as a function of the axial and radial directions at four different time instants during the operation of the process. Figure 5.10 shows the corresponding profile for the manipulated input, which changes smoothly with time to achieve the control objective (the initial sharp change of the manipulated input is actually a smooth change which occurs over a time period of 250 s and is

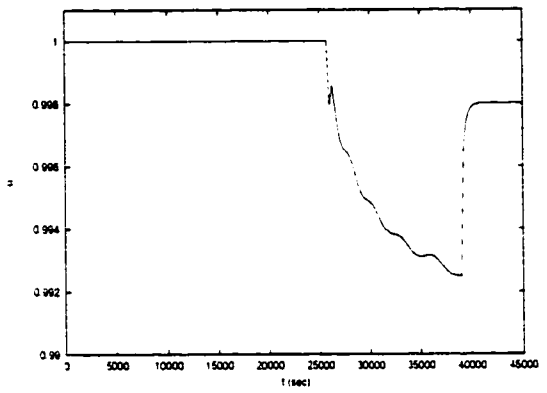

Figure 5.10: Manipulated input profile - PI controller.

due to the fact that the time axis covers the entire process cycle). Note that the controller is activated (i.e., $u(t) \neq 1$) when the crystal enters in the zone in which the control actuator operates. Regarding Figure 5.9, it is worth noting that the radial temperature non-uniformity remains small (less than 10 K) for the whole process time, which further validates the conclusion that we drawn on the basis of the open-loop behavior that radial thermal gradients are much smaller than axial thermal gradients (see also last paragraph in subsection 5.2 for more discussion on this issue).

Based on the simulation results for the case of using a single control actuator and driven by our desire to achieve a smooth temperature drop inside the crystal, we formulate the control problem as the one of controlling the temperature gradient of the crystal in the axial direction by manipulating the temperature of three extra heaters placed at three equispaced intervals as shown in Figure 5.11. To account for the heaters used for crystal temperature control in the two-dimensional process model, we substitute the boundary conditions of Eqs.5.4 and 5.5 with the following

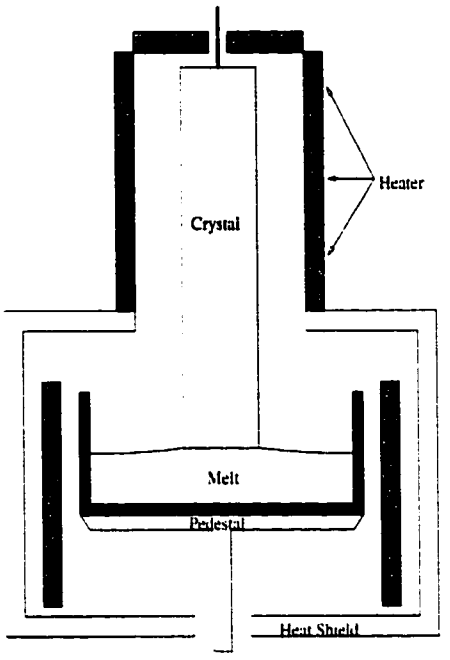

Figure 5.11: Control configuration for crystal temperature control in the Czochralski crystal growth.

boundary conditions:

$$\begin{aligned}\left.\frac{k}{\sigma}\frac{\partial T_c}{\partial r}\right|_R =& \epsilon_{w_{cr}}\epsilon_{w_m}F_{cr\to m}(R,z)[T_m^4 - T_c^4(R,z,t)] \\ &+\epsilon_{w_{cr}}\epsilon_{w_{ch}}F_{cr\to ch}(R,z)[T_{ch}^4 - T_c^4(R,z,t)] \\ &+\epsilon_{w_{cr}}\sum_{i=1}^{n}\epsilon_{w_i}F_{cr\to i}(R,z)[T_i^4(t) - T_c^4(R,z,t)], \quad 0 \le z \le l(t)\end{aligned} \tag{5.10}$$

$$\begin{aligned}\left.\frac{k}{\sigma}\frac{\partial T_c}{\partial z}\right|_{l(t)} =& \epsilon_{w_{cr}}\epsilon_{w_m}F_{cr\to m}(r,l(t))[T_m^4 - T_c^4(r,l(t),t)] \\ &+\epsilon_{w_{cr}}\epsilon_{w_{ch}}F_{cr\to ch}(r,l(t))[T_{ch}^4 - T_c^4(r,l(t),t)] \\ &+\epsilon_{w_{cr}}\sum_{i=1}^{n}\epsilon_{w_i}F_{cr\to i}(r,l(t))[T_i^4(t) - T_c^4(r,l(t),t)], \quad 0 \le r \le R\end{aligned} \tag{5.11}$$

where n is the number of heaters used for control, $T_i(t)$ is the temperature of the i-th heater, $F_{cr\to i}$ is the view factor of a differential crystal surface element to the heater surface.

Moreover, with the addition of the heaters, the one-dimensional model which will

be used for controller design takes the form:

$$\begin{aligned}\frac{\partial T_c}{\partial t}+v_p\frac{\partial T_c}{\partial z} =&\frac{k}{\rho c_p}\frac{\partial^2 T_c}{\partial z^2}+\frac{2\sigma\epsilon_{w_{cr}}\epsilon_{w_m}}{\rho c_p R}F_{cr\to m}(R,z)[T_m^4-T_c^4(z,t)]\\ &+\frac{2\sigma\epsilon_{w_{cr}}\epsilon_{w_{ch}}}{\rho c_p R}F_{cr\to ch}(R,z)[T_{ch}^4-T_c^4(z,t)]\\ &+\frac{2\sigma\epsilon_{w_{cr}}}{\rho c_p R}\sum_{i=1}^{n}\epsilon_{w_i}F_{cr\to i}(R,z)[T_i^4(t)-T_c^4(z,t)]\end{aligned} \tag{5.12}$$

subject to the following boundary conditions,

$$\begin{aligned}T_c(0,t) =&T_{mp}\\ \frac{k}{\sigma}\frac{\partial T_c}{\partial z}\Big|_{l(t)} =&\epsilon_{w_{cr}}\epsilon_{w_m}F_{cr\to m}(l(t))[T_m^4-T_c^4(l(t),t)]\\ &+\epsilon_{w_{cr}}\epsilon_{w_{ch}}F_{cr\to ch}(l(t))[T_{ch}^4-T_c^4(l(t),t)]\\ &+\epsilon_{w_{cr}}\sum_{i=1}^{n}\epsilon_{w_i}F_{cr\to i}(l(t))[T_i^4(t)-T_c^4(l(t),t)]\end{aligned} \tag{5.13}$$

Referring to Eqs.5.12-5.13, note the lack of the terms corresponding to heat transfer between the crystal and the ambient (compare with Eqs.5.6-5.8); these terms have been substituted by the terms that account for heat transfer between the crystal and the extra heaters that are used as control actuators.

The performance of the proposed control configuration that employs three heaters to regulate the thermal gradients inside the crystal compared to the open-loop system and the closed-loop system in the case of using one heater will be evaluated in section 5.2.

Remark 5.2: We note that another approach for the simulation of the crystal temperature concerns the elimination of the thermal dynamics of the process on the basis that they are slower than the dynamics of the crystal radius, and solves for the temperature profile inside the growing crystal as a series of solutions of a steady state thermal model for different lengths (see, for example, [59, 60]). However, in the present study, we have decided to include the thermal dynamics in the model of the process which is used for the implementation of the controller, because the use

of feedback control or the presence of disturbances (for example, variations in the pulling rate, melt temperature) may significantly modify the dynamic behavior of the process compared to the open-loop behavior.

5.4 Crystal temperature regulation during the Czochralski crystal growth

5.4.1 Nonlinear model reduction

In this section, our objective is to synthesize and implement a low-order nonlinear output feedback controller on the crystal growth process that enforces a desired smooth temperature profile in the axial direction inside the crystal. We begin with the re-

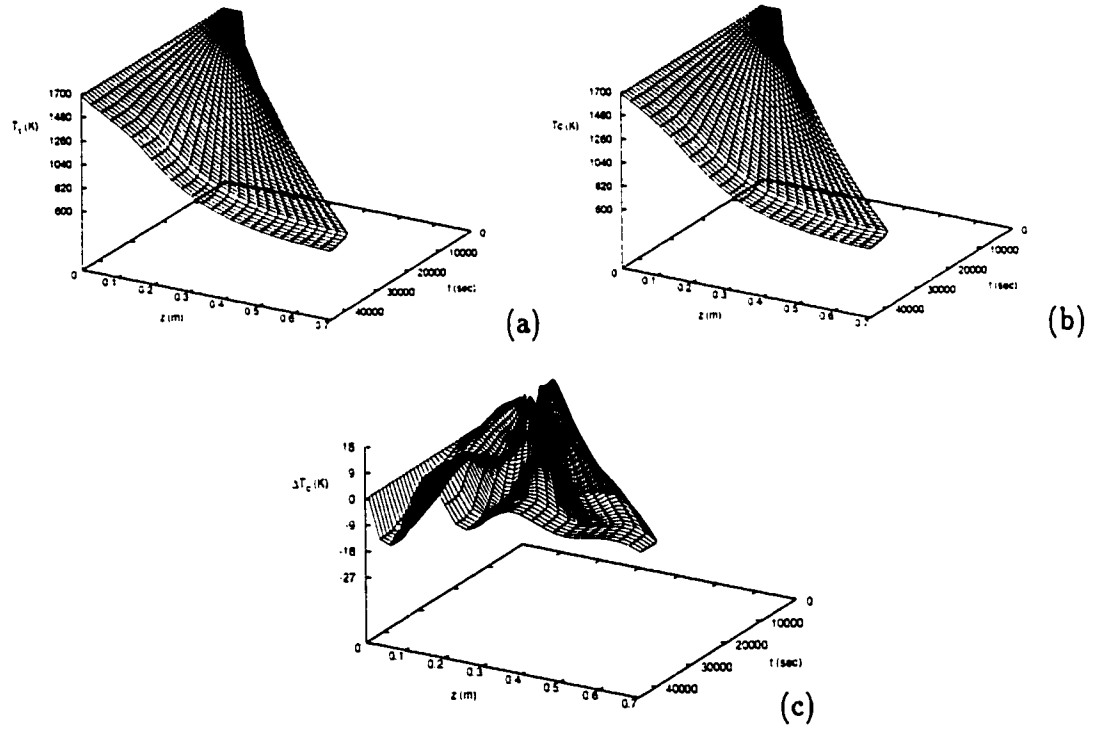

Figure 5.12: Comparison of temperature profiles of open loop system at $T_{amb} = 600\ K$. (a) Two-dimensional model at $r = 0.034\ m$, (b) reduced-order model and (c) temperature difference between the two-dimensional model at $r = 0.034\ m$ and the reduced-order model.

duction of the one-dimensional parabolic PDE model of Eq.5.12-5.13 into a small set of nonlinear ODEs utilizing the model reduction algorithm of section 2.3. This set of ODEs will be subsequently used for controller design.

The one-dimensional model of Eq.5.12-5.13 can be formulated in the general form of Eq.2.1-2.2-2.3 with:

$$
\begin{aligned}
& A = 0.0, \quad B = \frac{k}{\rho c_p}, \quad w = \frac{\sigma \epsilon_{w_{cr}}}{\rho c_p}, \\
& b(z,t) = \begin{bmatrix} \epsilon_{w_1}\left(\frac{2}{R}F_{cr\to 1}(R,z) + \frac{\delta(z-l(t))}{kl(t)}F_{cr\to 1}(z)\right)T^4_{1_{set}} \\ \vdots \\ \epsilon_{w_m}\left(\frac{2}{R}F_{cr\to m}(R,z) + \frac{\delta(z-l(t))}{kl(t)}F_{cr\to m}(z)\right)T^4_{m_{set}} \end{bmatrix}^T, \\
& f(z,t,T_c) = -v_p\frac{\partial T_c}{\partial z} + \frac{2\sigma\epsilon_{w_{cr}}}{\rho c_p R}\left(\epsilon_{w_m}F_{cr\to m}(R,z)[T^4_m - T^4_c]\right. \\
& \qquad \left. + \epsilon_{w_{ch}}F_{cr\to ch}(R,z)[T^4_{ch} - T^4_c] - \sum_{i=1}^{n}\epsilon_{w_i}F_{cr\to i}(R,z)T^4_c\right) \\
& \qquad + \delta(z-l(t))\frac{\sigma\epsilon_{w_{cr}}}{k\rho c_p l(t)}\left(\epsilon_{w_m}F_{cr\to m}(z)[T^4_m - T^4_c]\right. \\
& \qquad \left. + \epsilon_{w_{ch}}F_{cr\to ch}(z)[T^4_{ch} - T^4_c] - \sum_{i=1}^{n}\epsilon_{w_i}F_{cr\to i}(z)T^4_c\right)
\end{aligned}
\tag{5.14}
$$

where $\delta(\cdot)$ is the standard Dirac function. Defining the new variable $x = \frac{T_c - T_{mp}}{T_{mp}}$ and nondimensionalizing the temperature for this parabolic PDE system, the spatial differential operator $\mathcal{A}$ can be defined as:

$$
\begin{aligned}
& \mathcal{A}(t)x = \frac{k}{\rho c_p}\frac{\partial^2 \bar{x}}{\partial z^2}, \\
& x \in D(\mathcal{A}(t)) = \left\{x \in \mathcal{H}([0,l(t)];\mathbb{R}); \quad \bar{x}(0,t) = 0; \quad \frac{\partial \bar{x}}{\partial z}(l(t),t) = 0\right\}
\end{aligned}
\tag{5.15}
$$

Note that $\mathcal{A}(t)$ includes the higher-order spatial derivative (conduction term) included in the PDE of Eq.5.12, while owing to the time dependent nature of the pulling rate v_p (in general) it does not include the first-order spatial derivative (convective term).

The eigenvalue problem of $\mathcal{A}$ can be solved analytically and yields:

$$\lambda_j(t) = -\frac{k}{\rho c_p}\left[\frac{\pi(2j+1)}{2l(t)}\right]^2, \quad \phi_j(t,z) = \sqrt{\frac{2}{l(t)}} sin\left(\frac{\pi(2j+1)}{2l(t)}\, z\right), \quad j = 0,\ldots,\infty \tag{5.16}$$

where the eigenfunctions $\phi_j(t,z)$ form a countable, $\forall\, t \in [0,\infty)$, and orthogonal basis of $\mathcal{H}(t)$.

We used the nonlinear model reduction method discussed in section 2.3 i.e., combination of Galerkin's method with approximate inertial manifolds, to derive a fourth-order ODE model which uses a 4-th order $O(\epsilon^2)$ approximation for x_f (i.e., $m = 4$ and $\tilde{m} = 4$). The eigenfunctions $\phi_j(t,z)$ were used as basis functions in Galerkin's method. Figure 5.12 shows the temporal evolution of the crystal temperature in the axial direction at $r = 0.034$ computed by the two-dimensional model (Figure 5.12a), the temporal evolution of the crystal temperature in the axial direction computed by the fourth-order model (Figure 5.12b), and the difference between the crystal temperatures predicted by the two-dimensional model (r=0.034) and the fourth-order model (Figure 5.12c), for $T_{amp} = 600$. It is clear that the predictive capabilities of the reduced-order model are very good for a wide range of operating conditions, and thus, it makes sense to use this fourth-order model as a basis for the synthesis of a nonlinear output feedback controller.

5.4.2 Nonlinear controller synthesis - Closed-loop simulations

The control objective is to enforce an almost linear axial temperature profile in the crystal by manipulating the temperature of the heaters and using point measurements of the surface temperature of the crystal. Specifically, we consider the control configuration shown in Figure 5.11. The heater was assumed to be divided into three equispaced regions and the temperature in each one of these regions is adjusted by

the controller. The region where the $i-$th controller operates is determined by the variables z_{s_i}, z_{f_i}, which represent the minimum and maximum distances of the controller region from the melt-crystal interface, respectively, (note that the distribution function of the i-th control actuator is $b_i(z) = H(z - z_{s_i}) - H(z - z_{f_i})$ where $H(\cdot)$ is the standard Heavyside function). The controlled and measured outputs were taken to be identical and defined as:

$$\begin{aligned} y_{c_1}(t) = y_{m_1}(t) &= \int_0^{l(t)} \delta(z - z_{m_1}) T_c(R, z, t) dz \\ y_{c_2}(t) = y_{m_2}(t) &= \int_0^{l(t)} \delta(z - z_{m_2}) T_c(R, z, t) dz \\ y_{c_3}(t) = y_{m_3}(t) &= \int_0^{l(t)} \delta(z - z_{m_3}) T_c(R, z, t) dz \end{aligned} \tag{5.17}$$

where $T_c(R, z, t)$ is the surface temperature of the crystal. The point measurements of the temperature on the surface of the crystal can be readily obtained in practice with optical pyrometers. Finally, the fourth-order model obtained through Galerkin's method with approximate inertial manifolds with the specifications for manipulated inputs, controlled and measured outputs was used for the synthesis of a nonlinear output feedback controller by utilizing the formula of theorem 2.1. In order to incorporate integral action in this controller, the term $v_i - h_{0_i}(\eta)$ was substituted by the term $v_i - y_{c_i}$. All the parameters used in the control problem are given in Table 5.4.

Table 5.4: Control parameters

Controller κ	z_{s_κ} $[m]$	z_{f_κ} $[m]$	z_{m_κ} $[m]$	β_κ	T_s $[K]$
1	0.18	0.38	0.28	1.0	1400
2	0.38	0.58	0.48	1.0	1250
3	0.58	0.71	0.68	1.0	1100

Several simulations runs were performed to evaluate: a) the ability of the nonlinear controller to enforce a linear temperature profile in the axial direction inside the crystal, b) the robustness properties of the nonlinear controller with respect to

parametric model uncertainty, disturbances and unmodeled actuator and sensor dynamics. In all the simulation runs, the crystal was initially ($t = 0\ sec$) assumed to be at $T_c(z, r, 0) = 1670\ K$ and have a length of $l(0) = 0.05\ m$. The initial conditions of the fourth-order observer included in the nonlinear output controller were computed by using the initial condition assumed for the crystal. Moreover, in all the simulation runs, the objective of the controller is to regulate the three controlled outputs at $y_{c1} = 1400\ K$, $y_{c2} = 1250\ K$, $y_{c3} = 1100\ K$; this motivated by our objective to enforce a linear temperature drop inside the crystal of 8 K/cm. As we will see in our results below, these set-points allow enforcing a smooth linear temperature drop inside the crystal at all times during the growth. Furthermore, we note that in order to avoid disturbing the concentration profiles of the dopant and oxygen through unnecessarily large variations of the manipulated inputs, a lower bound (constraint) is implemented on the control action which does not allow $u_i(t)$ to become smaller than 0.82 (note that $u_i(t) = \dfrac{T_i}{T_{sp_i}}$ where $T_{sp_i} = 1000\ K$ for all $i = 1, 2, 3$ is a reference temperature for

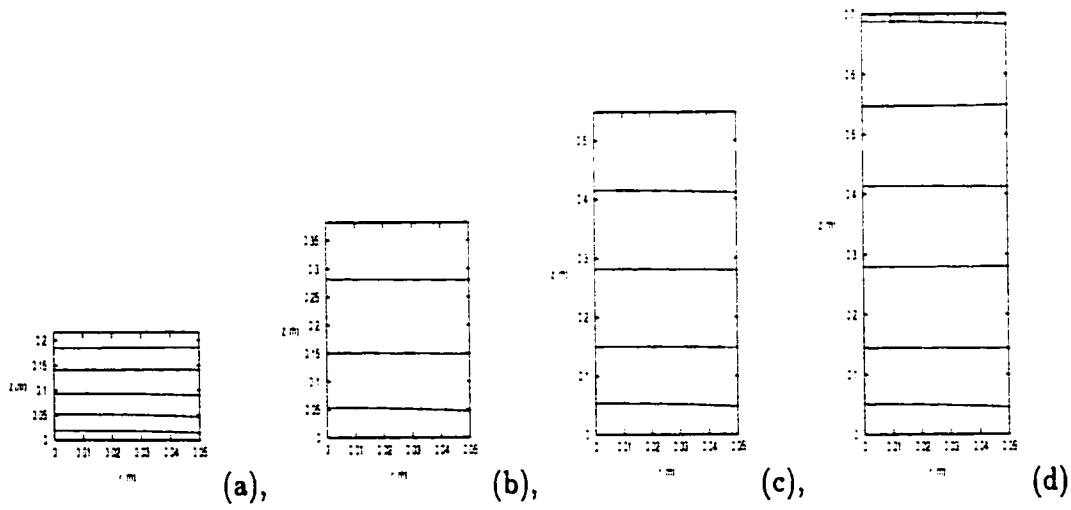

Figure 5.13: Temperature of crystal as a function of radial and axial coordinates under nonlinear control - nominal case. (a) $t = 1 \times 10^4\ s$, (b) $t = 2 \times 10^4\ s$, (c) $t = 3 \times 10^4\ s$ and (d) $t = 4 \times 10^4\ s$. Each contour represents a 100 K temperature difference.

the i-th heater). Finally, the tuning parameters of the nonlinear controller are chosen so that the computed variations in the control action with respect to time are small.

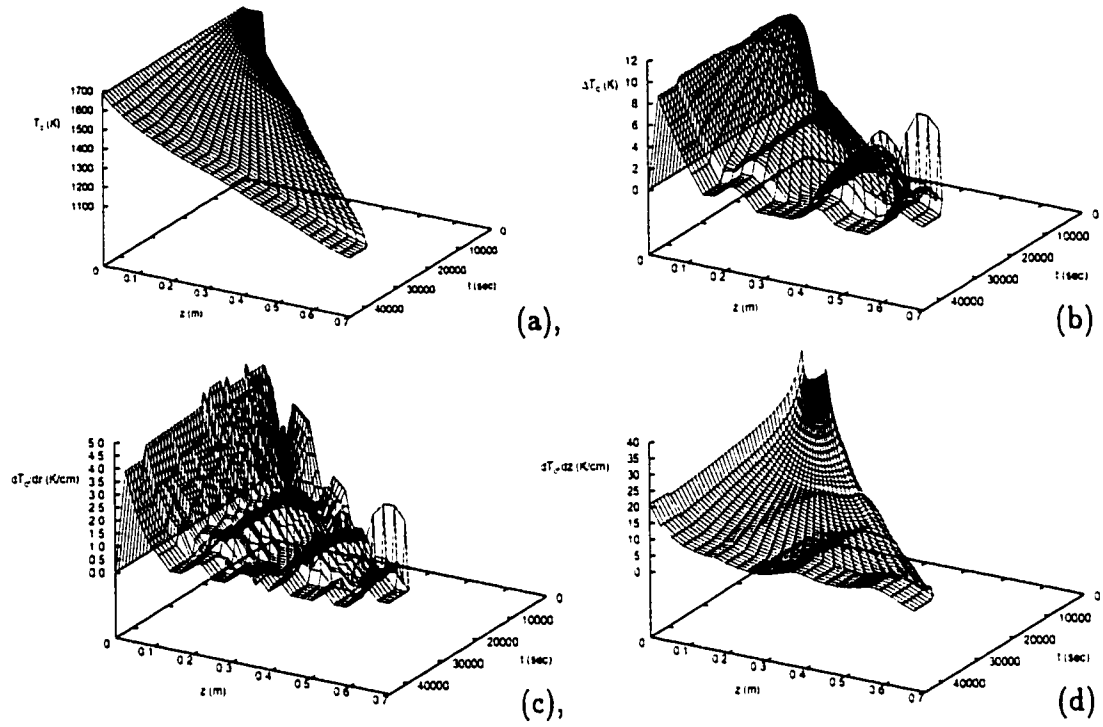

Figure 5.14: (a) Temperature of crystal at $r = 0.0\ m$, (b) Maximum temperature difference inside the crystal in the radial direction, (c) Maximum thermal gradient inside the crystal in the radial direction, (d) Maximum thermal gradient inside the crystal in the axial direction, as a function of time and axial coordinate under nonlinear control - nominal case.

Initially, the set-point tracking capability of the nonlinear controller was evaluated under nominal conditions. Figures 5.13 and 5.14a show the contour plots of the crystal temperature as a function of the axial and radial directions at four different time instants during the operation of the process and the temporal evolution of the crystal temperature in the axial direction at the center of the crystal, respectively, in the closed-loop system. Clearly, the nonlinear controller drives the controlled outputs to their new set-points, while enforcing the desired temperature drop inside the crystal at all radial positions (note that the radial temperature non-uniformity is

less than 20 K which is clearly smaller to the one computed for the open-loop system; compare Figure 5.14b and Figure 5.3b), without creating large radial temperature gradients at any time (the radial temperature gradients remain small for all times; see Figure 5.14c and compare with 5.3c). As can be seen from Figure 5.14d, the

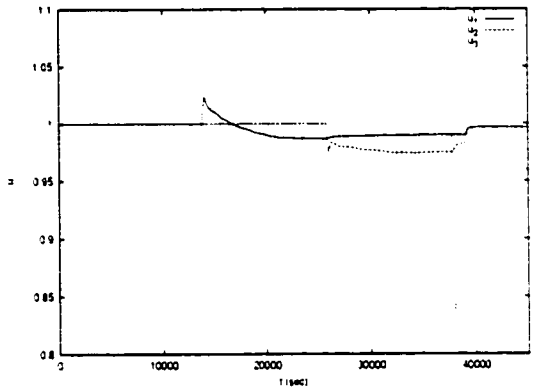

Figure 5.15: Manipulated input profiles - nominal case.

temperature gradient in the axial direction remains bounded throughout the length of the crystal, and is much smaller than in the open loop case (Figure 5.3d). Figure 5.15 shows the corresponding profiles for the three manipulated inputs, which change smoothly with time to achieve the control objective Note also that each one of the three controllers is activated (i.e., $u_i(t) \neq 1$) when the crystal enters in the zone in

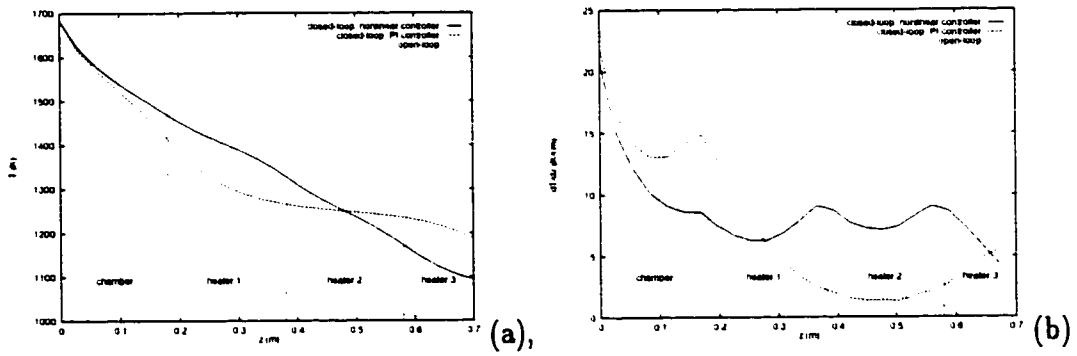

Figure 5.16: (a) Temperature of crystal at $r = 0.05\ m$, (b) Maximum thermal gradient inside the crystal in the axial direction, at the end of the process - nominal case.

which the corresponding control actuator operates and the initial sharp profiles are actually the slow activation of the controllers over a period of 250 s. Figure 5.16a shows the crystal temperature at $r = 0.005\ m$, and Figure 5.16b shows the maximum thermal gradient inside the crystal in the axial direction, at the end of the process cycle under the proposed nonlinear control system, the PI controller, and the case of constant ambient temperature; it is clear that the proposed control scheme reduces the thermal gradients in the axial direction compared to the other approaches.

Next, the robustness properties of the nonlinear controller in the presence of parametric uncertainties, disturbances and unmodeled actuator and sensor dynamics were investigated. Figures 5.17 and 5.18a show the crystal temperature contours as a func-

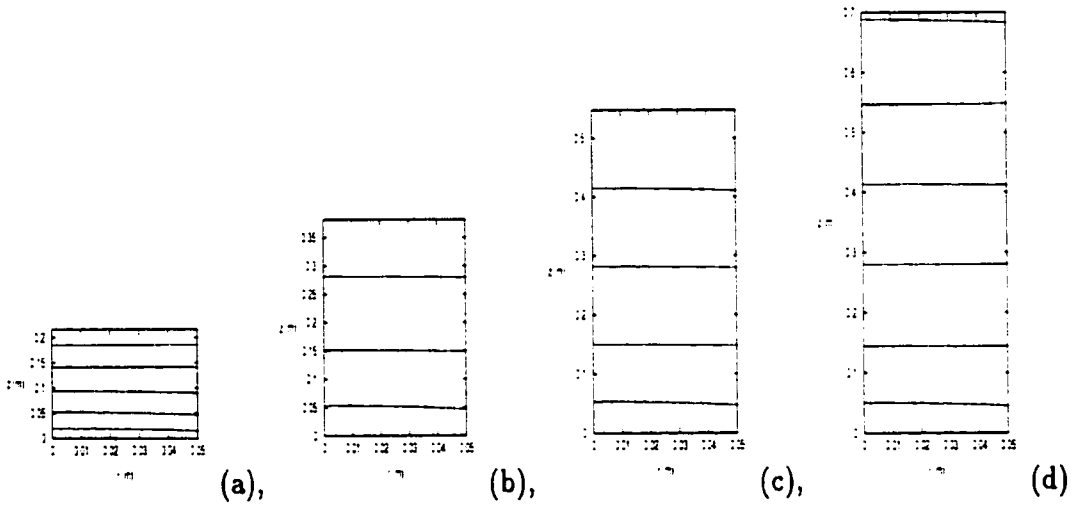

Figure 5.17: Temperature of crystal as a function of radial and axial coordinates under nonlinear control - parametric uncertainty. (a) $t = 1 \times 10^4\ s$, (b) $t = 2 \times 10^4\ s$, (c) $t = 3 \times 10^4\ s$ and (d) $t = 4 \times 10^4\ s$. Each contour represents a 100 K temperature difference.

tion of the axial and radial directions at four different time instants during the operation of the process and the temporal evolution of the closed-loop crystal temperature in the axial direction at the center of the crystal, respectively, in the presence of 10% error in the emissivity of the crystal $e_{w_{cr}}$. The nonlinear controller exhibits very good

robustness properties, driving the output to its set-point with small temperature

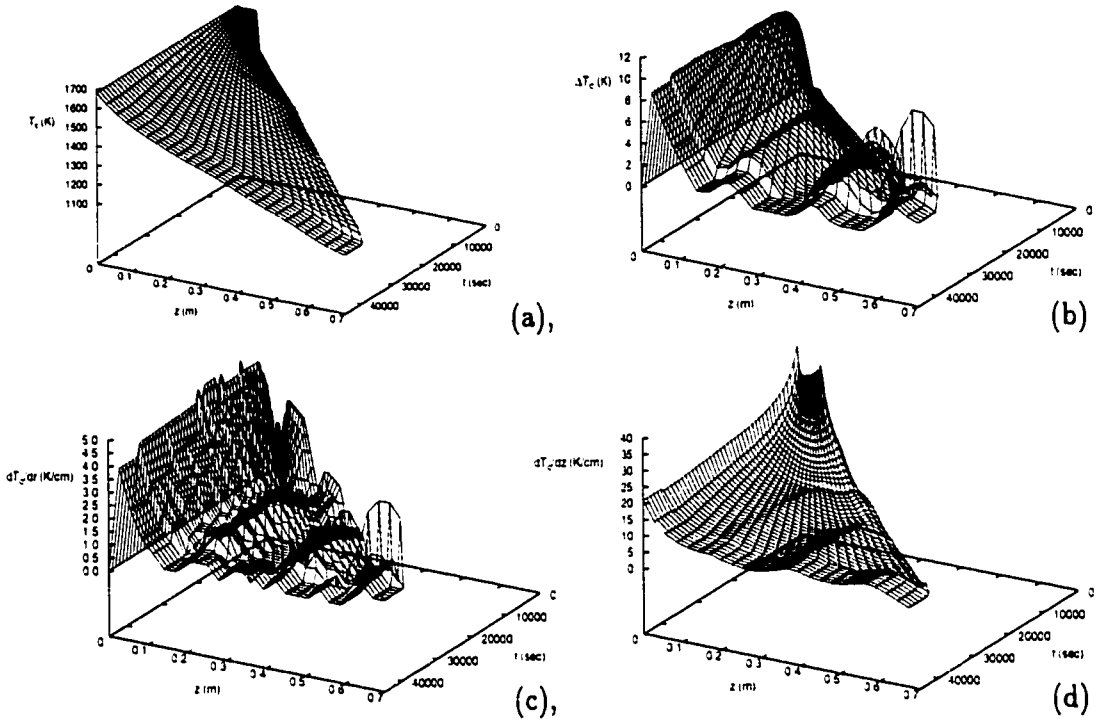

Figure 5.18: (a) Temperature of crystal at $r = 0.0\ m$, (b) Maximum temperature difference inside the crystal in the radial direction, (c) Maximum thermal gradient inside the crystal in the radial direction, (d) Maximum thermal gradient inside the crystal in the axial direction, as a function of time and axial coordinate under nonlinear control - parametric uncertainty.

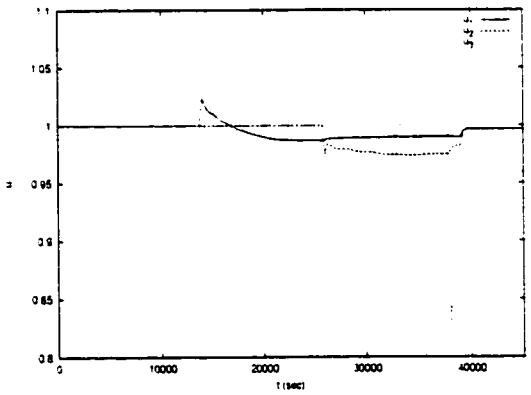

Figure 5.19: Manipulated input profiles - parametric uncertainty.

gradients in the radial (Figure 5.18c) and axial (Figure 5.18d) directions (compare

with the open-loop temperature gradient profiles Figures 5.18c, 5.18d) while requesting smooth control actions (Figure 5.19). Figure 5.17 shows the crystal temperature contours at four different time instants and Figure 5.23a shows the closed-loop crystal temperature in the axial direction at the center of the crystal in the presence of a 10% disturbance in the melt temperature and 20% disturbance in the temperature of the chamber, while Figure 5.24 shows the manipulated input profiles. Again, the

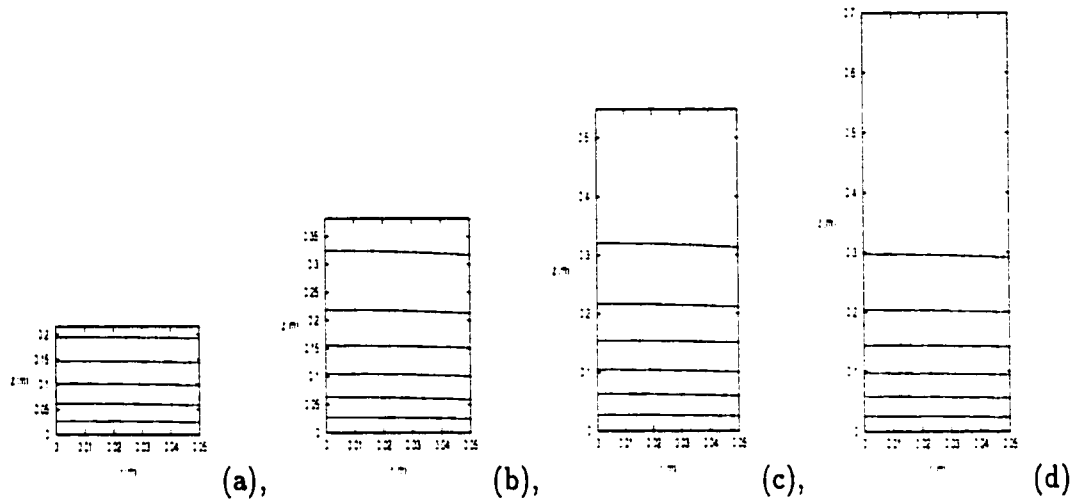

Figure 5.20: Temperature of crystal as a function of radial and axial coordinates for $T_{amb} = 1000\ K$ - exogenous disturbances. (a) $t = 1 \times 10^4\ s$, (b) $t = 2 \times 10^4\ s$, (c) $t = 3 \times 10^4\ s$ and (d) $t = 4 \times 10^4\ s$. Each contour represents a 100 K temperature difference.

nonlinear controller enforces the desired linear drop in the crystal temperature in the axial direction, attenuating the effect of the disturbances (compare the closed-loop temperature profiles of Figures 5.22 and 5.23 with the open-loop temperature profiles of Figure 5.21 ($T_{amb} = 1000\ K$), under the same disturbances), while keeping the temperature gradients in the radial (Figure 5.18c) and axial (Figure 5.18d) directions small.

Figures 5.25 and 5.26a show the closed-loop crystal temperature as a function of the axial and radial directions at four different time instants during the operation of

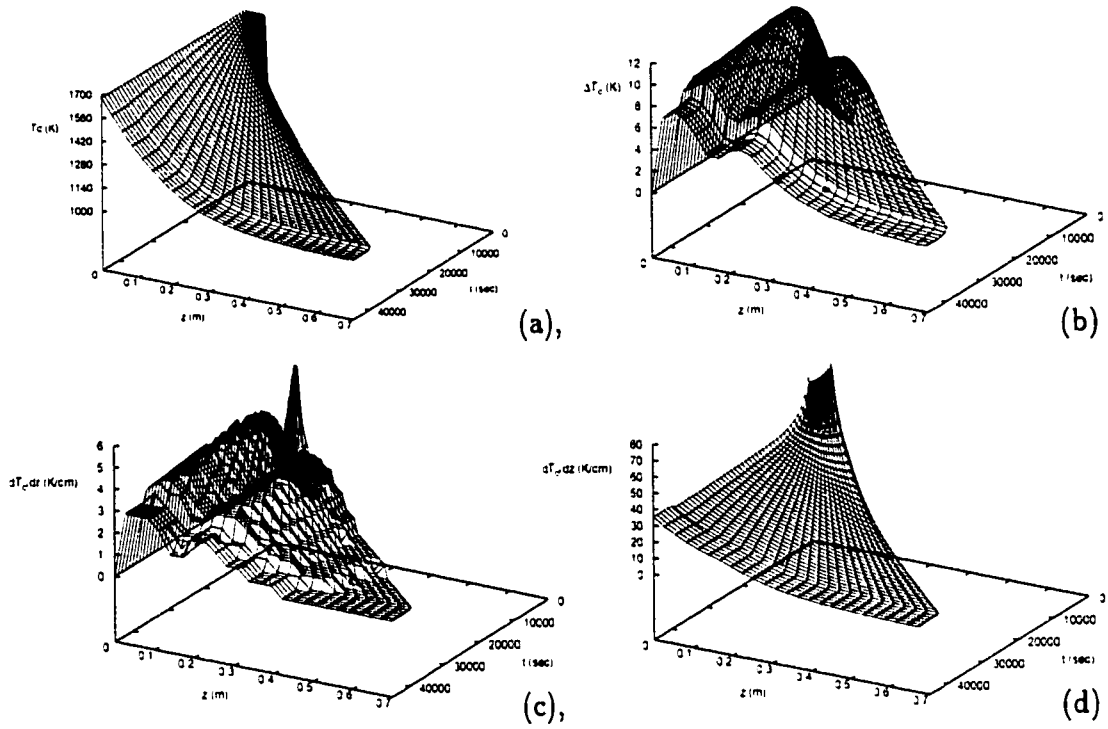

Figure 5.21: (a) Temperature of crystal at $r = 0.0\ m$, (b) Maximum temperature difference inside the crystal in the radial direction, (c) Maximum thermal gradient inside the crystal in the radial direction, (d) Maximum thermal gradient inside the crystal in the axial direction as a function of time and axial coordinate for $T_{amb} = 1000\ K$ - exogenous disturbances.

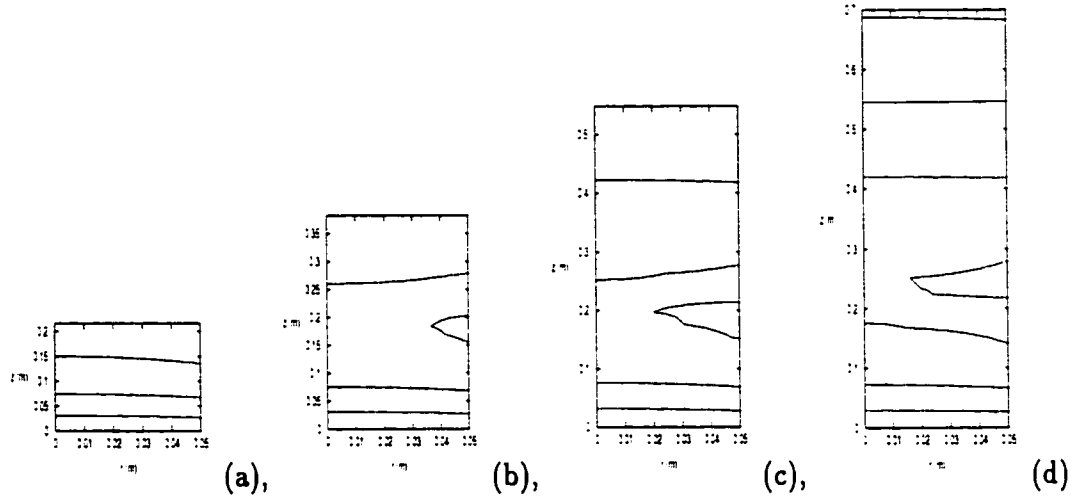

Figure 5.22: Temperature of crystal as a function of radial and axial coordinates under nonlinear control - exogenous disturbances. (a) $t = 1 \times 10^4$ s, (b) $t = 2 \times 10^4$ s, (c) $t = 3 \times 10^4$ s and (d) $t = 4 \times 10^4$ s. Each contour represents a 100 K temperature difference.

the process and the temporal evolution of the closed-loop crystal temperature in the axial direction at the center of the crystal, respectively, in the presence of unmodeled actuator and sensor dynamics, and Figure 5.27 shows the manipulated input profiles. To account for the actuator dynamics, the process model of Eq.5.1 was augmented with the dynamical system $\epsilon_c \dot{z}_{1i} = -z_{1i} + z_{2i}$, $\epsilon_c \dot{z}_{2i} = -z_{2i} + u_i$, $i = 1, 2, 3$, where $z_{1i}, z_{2i} \in \mathbb{R}$ are the actuator states, z_{1i} is the actuator output and ϵ_c is a small parameter characterizing how fast are the actuator dynamics. To account for the sensor dynamics, the process model of Eq.5.1 was augmented with the dynamical system $\epsilon_m \dot{z}_{3i} = -z_{3i} + z_{4i}$, $\epsilon_m \dot{z}_{4i} = -z_{4i} + y_{mi}$, $i = 1, 2, 3$, where $z_{3i}, z_{4i} \in \mathbb{R}$ are the sensor states, z_{3i} is the sensor output and ϵ_m is a small parameter characterizing how fast are the sensor dynamics. We found that the maximum values of ϵ_c and ϵ_m for which the stability of the closed-loop system is guaranteed are $\epsilon_c = 0.02$ and $\epsilon_m = 0.02$, thereby implying that the nonlinear controller is robust with respect to stable and sufficiently fast unmodeled sensor and actuators dynamics. From the

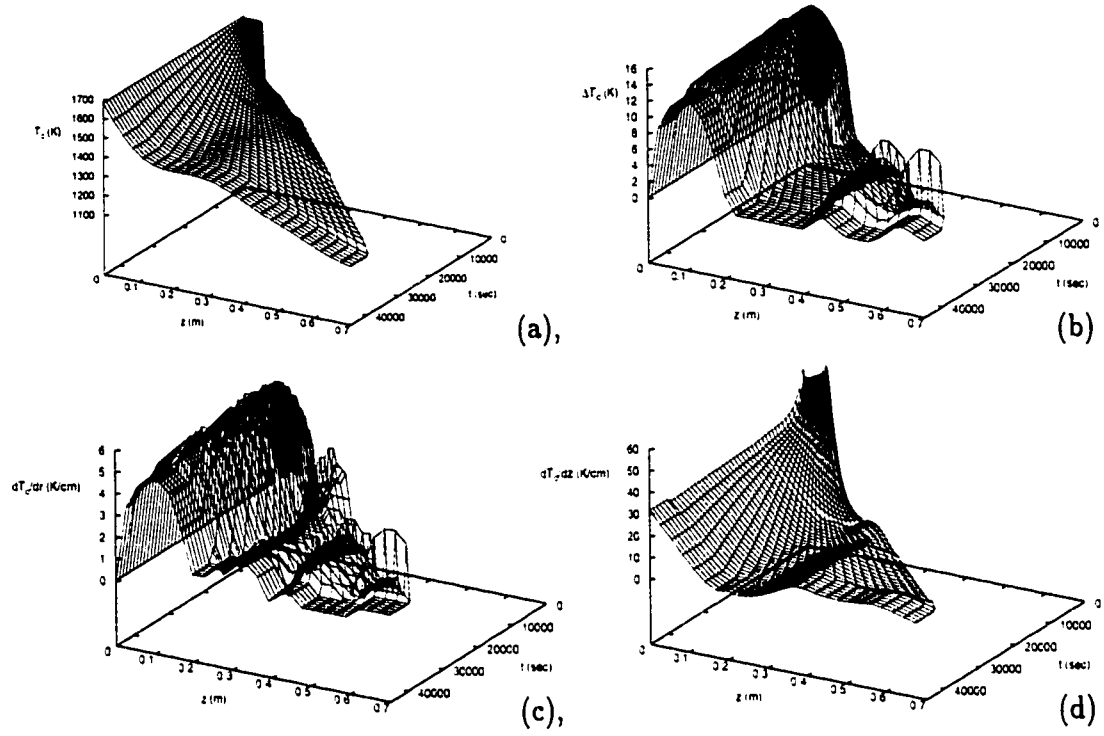

Figure 5.23: (a) Temperature of crystal at $r = 0.0\ m$, (b) Maximum temperature difference inside the crystal in the radial direction, (c) Maximum thermal gradient inside the crystal in the radial direction, (d) Maximum thermal gradient inside the crystal in the axial direction, as a function of time and axial coordinate under nonlinear control - exogenous disturbances.

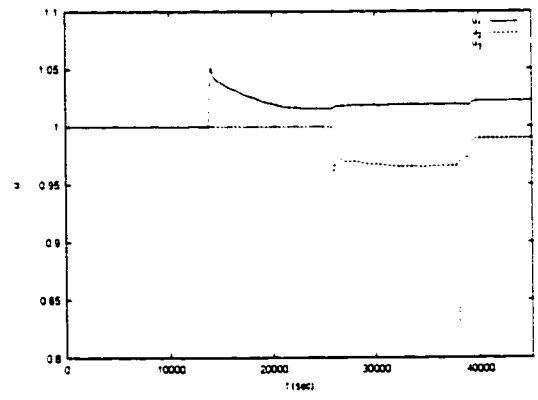

Figure 5.24: Manipulated input profiles - exogenous disturbances.

results of the simulation study, it is evident that the nonlinear controller which was synthesized on the basis of a fourth-order model constructed through combination of Galerkin's method and approximate inertial manifolds, possesses excellent closed-loop performance and robustness properties.

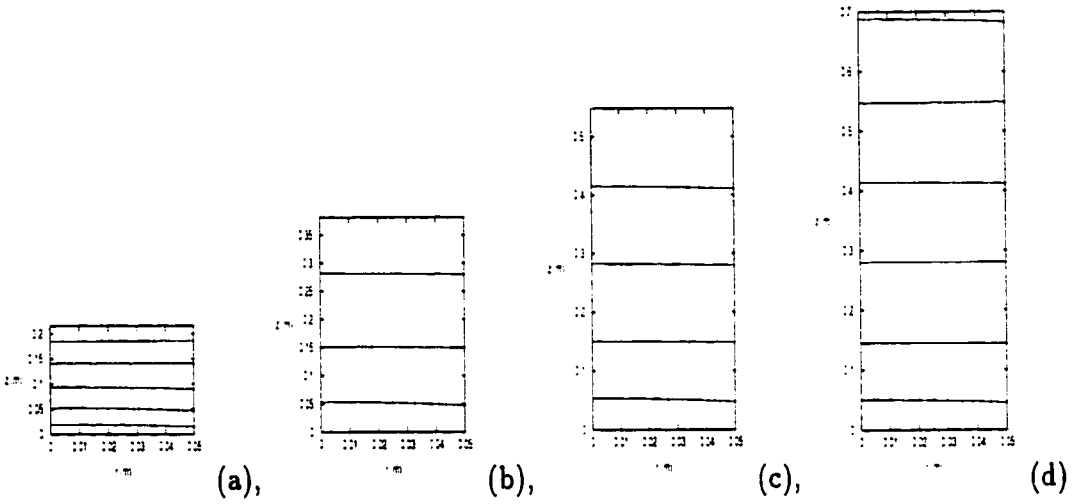

Figure 5.25: Temperature of crystal as a function of radial and axial coordinates under nonlinear control - unmodeled actuator and sensor dynamics. (a) $t = 1 \times 10^4$ s, (b) $t = 2 \times 10^4$ s, (c) $t = 3 \times 10^4$ s and (d) $t = 4 \times 10^4$ s. Each contour represents a 100 K temperature difference.

Finally, it is important to point out another advantage of the proposed control configuration. Even though there is no explicit way to reduce the thermal gradients in the radial direction inside the crystal through direct feedback control, reduction of such gradients is accomplished indirectly during the regulation of the thermal gradients in the axial direction, due to the well regulated environment in which the crystal grows in such a case. This point is made clear by comparing Figures 5.3c, 5.5c, 5.7c, 5.21c with Figures 5.14c, 5.18c, 5.23c, 5.26c that present the evolution of the radial thermal gradients inside the crystal in the open- and closed-loop systems respectively, and show that a significant reduction of the thermal gradients in the radial direction is achieved in the case of using the proposed control scheme compared

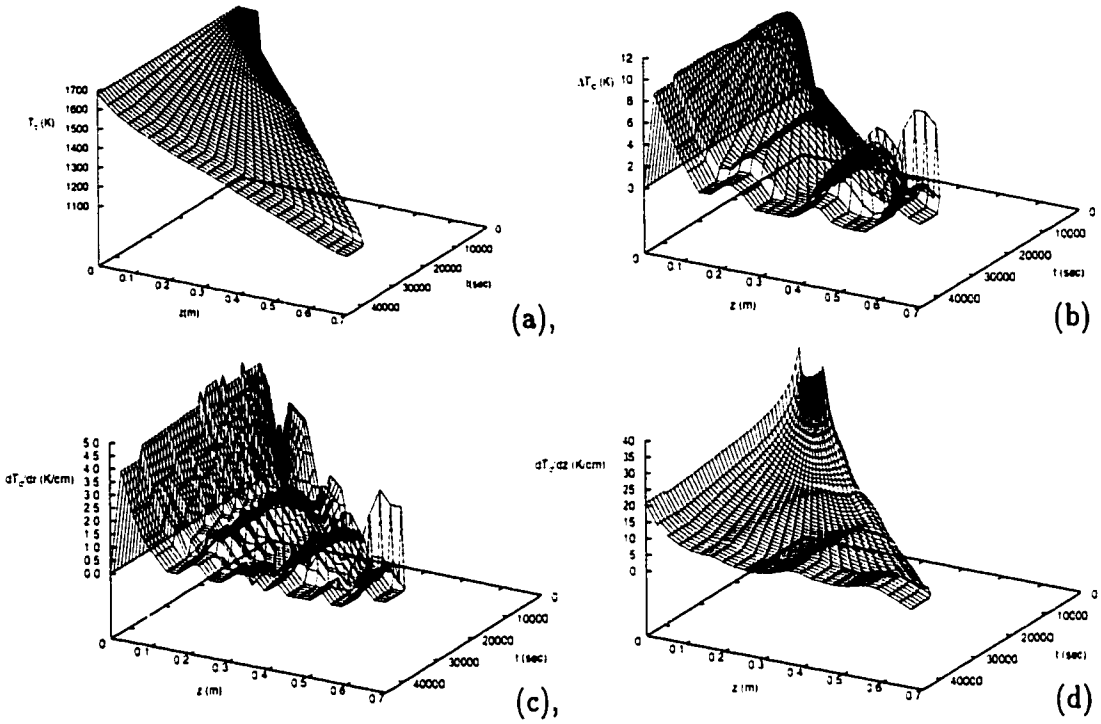

Figure 5.26: (a) Temperature of crystal at $r = 0.0\ m$, (b) Maximum temperature difference inside the crystal in the radial direction, (c) Maximum thermal gradient inside the crystal in the radial direction, (d) Maximum thermal gradient inside the crystal in the axial direction, as a function of time and axial coordinate under nonlinear control - unmodeled actuator and sensor dynamics.

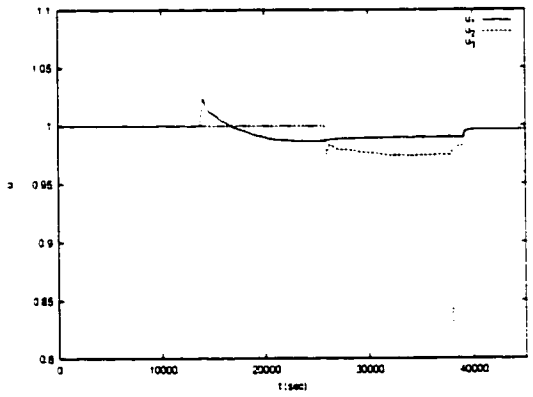

Figure 5.27: Manipulated input profiles - unmodeled actuator and sensor dynamics.

to the open-loop system.

Remark 5.3: The decision to pick the three set-point values so that an almost linear axial temperature drop is enforced inside the crystal was motivated by our objective to reduce the axial thermal gradient $\frac{\partial T_c}{\partial z}$ for all $z \in [0, l(t)]$ and all $t \in [0, \infty)$, thereby reducing the possibilities for crystal dislocation and defects due to temperature nonuniformity (the reader may refer to [78, 167] for more information). We note that the nonlinear controller can be used to enforce any other desired smooth temperature drop inside the crystal by appropriate choice of the values of the three set-points.

Remark 5.4: It is important to point out that even though the fourth-order model obtained through Galerkin's method and approximate inertial manifolds was used to synthesize a nonlinear geometric controller which can be readily implemented in practice, this fourth-order model can be also used for the design of optimization-based controllers including model predictive controllers because it is of very low-order, and therefore, it leads to optimization programs which can be rapidly solved on-line.

Remark 5.5: The variation of the crystal size with respect to time is a moving boundary characteristic that should be included in the context of controlling the thermal gradients. Of course, there are other moving boundary issues in the Czochralski process which should be included in the development of an integrated simulation of the process, however, these are not important in the context of controlling thermal gradients inside the crystal, when the crystal radius has reached a constant value.

Remark 5.6: We note that even though our study on control of the Czochralski process focused on the regulation of the temperature profile in the axial direction inside the crystal under the assumption that the crystal radius is constant, the proposed

nonlinear controller can be *directly* coupled with another nonlinear controller which manipulates the pulling velocity and chamber temperature to regulate the crystal radius. This is possible because the time-scale of operation of the pulling velocity-crystal radius control loop is much faster than the time-scale of operation of the heater temperature-crystal temperature control loop, while the manipulation of the chamber temperature, T_{ch}, keeps the pulling velocity within specified limits, which allows decoupling the synthesis of the two controllers (see also [96] for similar conclusions). The synthesis of a nonlinear controller on the basis of an ODE model that describes the rate of change of the crystal radius as a function of the pulling velocity is presented in Appendix E.

5.5 Conclusions

In this chapter, we presented a control configuration and a nonlinear multivariable model-based controller for the reduction of thermal gradients inside the crystal in the Czochralski crystal growth process after the crystal radius has reached its final value. Initially, a detailed mathematical model which describes the evolution of the temperature inside the crystal in the radial and axial directions and accounts for radiative heat exchange between the crystal and its surroundings and motion of the crystal boundary was presented. This model was used to study the behavior of the crystal temperature, formulate the control problem, design a new control configuration for the reduction of thermal gradients inside the crystal, and derive a one-dimensional in space PDE model with moving domain which was used for controller synthesis. The controller was synthesized by following a control method proposed in [2] for the synthesis of low-order (easy-to-implement) controllers for parabolic PDEs with time-dependent spatial domains. The proposed control scheme was successfully im-

plemented on a Czochralski process used to produce a 0.7 m long silicon crystal with a radius of 0.05 m and was shown to significantly reduce the axial and radial thermal gradients inside the crystal compared to the open-loop operation and to the case of using a single control actuator. The robustness of the proposed controller with respect to parametric model uncertainty, melt and chamber temperature disturbances and unmodeled actuator and sensor dynamics was demonstrated through simulations.

Chapter 6

Wave Suppression by Nonlinear Finite-Dimensional Control

6.1 Introduction

In this chapter, we focus on nonlinear finite-dimensional control of the KdVB and KS equations which can adequately describe motion of waves in a variety of fluid flow processes (see, for example, [152, 31] for appropriate discussions). We initially propose a nonlinear controller design method for quasi-linear evolutionary PDEs. The method employs nonlinear Galerkin's method to derive low-dimensional ODE models, which are subsequently used for the synthesis of low-order nonlinear output feedback controllers that enforce local exponential stability in the closed-loop system. We then use this method to synthesize nonlinear low-order controllers for the KdVB and KS equations that enhance convergence rate and achieve stabilization to spatially uniform steady-states, respectively. The controllers use measurements obtained by point sensors and are implemented via point control actuators. The performance of the proposed controllers is successfully tested through simulations.

The development of general and practical control algorithms for nonlinear PDEs

that describe fluid flow processes (e.g., Navier-Stokes equations, KdVB, KS) is a fundamental problem whose practical significance ranges from feedback control of turbulence for drag reduction, to suppression of fluid mechanical instabilities in coating processes and suppression of waves exhibited by falling liquid films. For example, drag reduction through active feedback control may have a very significant impact on the design and operation of underwater vehicles, airplanes and automobiles, since according to some estimates keeping the flow over the surface of a vehicle laminar could yield up to 30% reduction in fuel consumption. Active control of fluid flow can be achieved by injection of polymers [126], mass transport through porous walls (e.g., blowing/suction) [30, 53] and application of electro-magnetic forcing [164].

The development of an efficient control system for a fluid flow should be based on the underlying PDE model that describes the flow in order to exploit its ability to accurately predict the spatiotemporal behavior of the flow field. The main obstacle for the synthesis of practically implementable output feedback controllers for fluid flow processes is the infinite-dimensional nature of the underlying PDE models, which does not allow their direct use for the design of low-order (and therefore, easy-to-implement) controllers. This fact, together with the need to develop efficient numerical methods for nonlinear PDEs, has motivated significant research on the understanding of the dynamic behavior of various fluid flows. This research has led to the discovery that turbulent flows involve coherent structures (e.g., [10, 127, 28, 159]) which implies that the dominant dynamic behavior of such flows can in principle be approximated by low-dimensional systems. These results have motivated the development of model reduction methods for the derivation of low-dimensional systems that accurately describe the dominant dynamics of PDEs which model fluid flows including nonlinear Galerkin's method (e.g., [170, 54, 14]) and reduced basis methods

(e.g., [99]).

In the area of control of fluid flow processes, previous research has mainly focused on: a) control of Navier-Stokes equations via proportional-integral [18, 37], linear optimal [61, 103, 92], H_∞ optimal [23, 22, 108], Lyapunov-based [104] and nonlinear [41] control, b) linear distributed [152] and point [151] control of the Korteweg-de Vries equation and nonlinear boundary control of the KdVB equation [123], and nonlinear boundary control [124] of the KS equation that enhances the rate of convergence to the spatially uniform steady-state when this steady-state is naturally stable. At this stage, not much work has been done on the utilization of the aforementioned nonlinear model reduction techniques for the design of nonlinear low-order feedback controllers for PDEs that describe fluid flows.

6.2 Nonlinear controller design

6.2.1 Preliminaries

We consider quasi-linear infinite dimensional systems with the following state-space description:

$$\begin{aligned} \dot{x} &= \mathcal{A}x + \mathcal{B}u + \mathcal{R}(x), \;\; x(0) = x_0 \\ y_m &= \mathcal{S}x, \;\; y_c = \mathcal{C}x \end{aligned} \tag{6.1}$$

where $x \in \mathcal{H}$ is the state of the system ($\mathcal{H}$ is an appropriate Hilbert space), $u \in \mathbb{R}^l$ is the vector of manipulated inputs, $y_m \in \mathbb{R}^q$ is the vector of measured outputs, $y_c \in \mathbb{R}^l$ is the vector of controlled outputs and $x_0 \in \mathcal{H}$ is the initial condition. $\mathcal{A} : D(\mathcal{A}) \subset \mathcal{H} \to \mathcal{H}$ is a densely defined unbounded operator with compact inverse, $\mathcal{R} : D(\mathcal{R}) \subset \mathcal{H} \to \mathcal{H}$ is a nonlinear map which satisfies $\mathcal{R}(0) = 0$, and $\mathcal{B} : \mathbb{R}^l \to \mathcal{H}$, $\mathcal{S} : \mathcal{H} \to \mathbb{R}^q$, $\mathcal{C} : \mathcal{H} \to \mathbb{R}^l$ are operators describing the spatial distribution of the manipulated inputs, measured outputs and controlled outputs, respectively.

The eigenvalue problem for $\mathcal{A}$ is defined as:

$$\mathcal{A}\phi_j = \lambda_j \phi_j, \;\; j = 1, \ldots, \infty \tag{6.2}$$

where λ_j and ϕ_j denote the j-th eigenvalue and eigenfunction, respectively. The eigenvalues of $\mathcal{A}$ satisfy $\Re(\lambda_1) \geq \Re(\lambda_2) \geq, \ldots$ (where $\Re(\cdot)$ denotes the real part of a complex number), while the eigenfunctions $\{\phi_1, \phi_2, \ldots\}$ form a complete orthonormal set in $\mathcal{H}$.

The inner product and norm in the Hilbert space $\mathcal{H}$ are defined as:

$$(\omega_1, \omega_2) = \int_\Omega (\omega_1(z), \omega_2(z))_{\mathbb{R}^n} dz, \;\; ||\omega_1||_2 = (\omega_1, \omega_1)^{\frac{1}{2}} \tag{6.3}$$

where ω_1, ω_2 are two elements of $\mathcal{H}$, Ω is the domain of definition of the process, and the notation $(\cdot, \cdot)_{\mathbb{R}^n}$ denotes the standard inner product in $\mathbb{R}^n$.

Finally, we recall the Lie derivative notation which will be used in our development: $L_f h$ denotes the Lie derivative of a scalar field h with respect to the vector field f, $L_f^k h$ denotes the k-th order Lie derivative and $L_g L_f^{k-1} h$ denotes the mixed Lie derivative.

6.2.2 Nonlinear model reduction

We apply nonlinear Galerkin's method [170, 54, 14] to the system of Eq.6.1 to derive an approximate finite-dimensional system. Let $\mathcal{H}_s$, $\mathcal{H}_f$ be modal subspaces, defined as $\mathcal{H}_s = span\{\phi_1, \phi_2, \ldots, \phi_m\}$ and $\mathcal{H}_f = span\{\phi_{m+1}, \phi_{m+2}, \ldots\}$ where ϕ_j, $j = 1, \ldots, \infty$ are eigenfunctions of $\mathcal{A}$. Clearly, $\mathcal{H}_s \ominus \mathcal{H}_f = \mathcal{H}$. Defining the orthogonal projection operators $P_s : \mathcal{H} \to \mathcal{H}_s$ and $P_f : \mathcal{H} \to \mathcal{H}_f$ such that $x_s = P_s x$, $x_f = P_f x$, the state x of the system of Eq.6.1 can be decomposed to:

$$x \;\; = \;\; x_s + x_f = P_s x + P_f x \tag{6.4}$$

Applying P_s and P_f to the system of Eq.6.1 and using the above decomposition for x, the system of Eq.6.1 can be written in the following form:

$$\begin{aligned} \frac{dx_s}{dt} &= \mathcal{A}_s x_s + \mathcal{B}_s u + \mathcal{R}_s(x_s, x_f), \quad x_s \in \mathcal{H}_s \\ \frac{\partial x_f}{\partial t} &= \mathcal{A}_f x_f + \mathcal{B}_f u + \mathcal{R}_f(x_s, x_f), \quad x_f \in \mathcal{H}_f \\ y_m &= \mathcal{S} x_s + \mathcal{S} x_f, \quad y_c = \mathcal{C} x_s + \mathcal{C} x_f \\ x_s(0) &= P_s x(0) = P_s x_0, \quad x_f(0) = P_f x(0) = P_f x_0 \end{aligned} \tag{6.5}$$

where $\mathcal{A}_s = P_s\mathcal{A}$, $\mathcal{B}_s = P_s\mathcal{B}$, $\mathcal{R}_s = P_s\mathcal{R}$, $\mathcal{A}_f = P_f\mathcal{A}$, $\mathcal{B}_f = P_f\mathcal{B}$ and $\mathcal{R}_f = P_f\mathcal{R}$ and the notation $\frac{\partial x_f}{\partial t}$ is used to denote that the state x_f belongs in an infinite-dimensional space. In the above system, $\mathcal{A}_s$ is a diagonal matrix of dimension $m \times m$ of the form $\mathcal{A}_s = diag\{\lambda_j\}$, $\mathcal{R}_s(x_s, x_f)$ and $\mathcal{R}_f(x_s, x_f)$ are Lipschitz vector functions, and $\mathcal{A}_f$ is a stable unbounded differential operator. The standard Galerkin's method is to approximate the solution $x(t)$ of the system of Eq.6.1 by $\bar{x}_s \in \mathcal{H}_s$ which is given by the following m-dimensional system:

$$\begin{aligned} \frac{d\bar{x}_s}{dt} &= \mathcal{A}_s \bar{x}_s + \mathcal{B}_s u + \mathcal{R}_s(\bar{x}_s, 0) \\ y_m &= \mathcal{S}\bar{x}_s, \quad y_c = \mathcal{C}\bar{x}_s \end{aligned} \tag{6.6}$$

A finite-dimensional system of order m which yield solutions which are closer to the one of the system of Eq.6.1 than the ones obtained by the system of Eq.6.6 can be obtained by using the concept of inertial manifold (IM). If exists, an inertial manifold $\mathcal{M}$ for the system of Eq.6.1 is a subset of $\mathcal{H}$, which satisfies the following properties [168]: *i*) $\mathcal{M}$ is a finite-dimensional Lipschitz manifold, *ii*) $\mathcal{M}$ is a graph of a Lipschitz function $\Sigma(x_s, u)$ mapping $\mathcal{H}_s \times \mathbb{R}^l$ into $\mathcal{H}_f$ and for every solution $x_s(t), x_f(t)$ of Eq.6.5 with $x_f(0) = \Sigma(x_s(0), u)$, then

$$x_f(t) = \Sigma(x_s(t), u), \quad \forall\, t \geq 0 \tag{6.7}$$

and *iii*) $\mathcal{M}$ attracts every trajectory exponentially. The evolution of the state x_f on $\mathcal{M}$ is given by Eq.6.7, while the evolution of the state x_s is governed by the following

finite-dimensional inertial form:

$$\begin{aligned} \frac{d\tilde{x}_s}{dt} &= \mathcal{A}_s\tilde{x}_s + \mathcal{B}_s u + \mathcal{R}_s(\tilde{x}_s, \Sigma(\tilde{x}_s, u)) \\ y_m &= \mathcal{S}x_s + \mathcal{S}\Sigma(\tilde{x}_s, u) \\ y_c &= \mathcal{C}x_s + \mathcal{C}\Sigma(\tilde{x}_s, u) \end{aligned} \tag{6.8}$$

Assuming that $u(t)$ is smooth, differentiating Eq.6.7 and utilizing Eq.6.5, $\Sigma(x_s, u)$ can be computed as the solution of the following partial differential equation:

$$\frac{\partial\Sigma}{\partial x_s}[\mathcal{A}_s x_s + \mathcal{B}_s u + \mathcal{R}_s(x_s, \Sigma(x_s, u))] + \frac{\partial\Sigma}{\partial u}\dot{u} = \mathcal{A}_f\Sigma(x_s, u) + \mathcal{B}_f u + \mathcal{R}_f(x_s, \Sigma(x_s, u)) \tag{6.9}$$

which $\Sigma(x_s, u)$ has to satisfy for all $x_s \in \mathcal{H}_s$, $u \in \mathbb{R}^l$. Unfortunately, even for PDEs for which an IM is known to exist, the derivation of an explicit analytic form of $\Sigma(x_s, u)$ is an almost impossible task. The nonlinear Galerkin method attempts to overcome the problems associated with the construction of inertial manifolds by replacing $\Sigma(\tilde{x}_s, u)$ with an approximate relation $\Sigma_{app}(\tilde{x}_s, u)$ (called approximate inertial manifold (AIM)). In this case, the solution x of the system of Eq.6.1 is approximated by $\tilde{x}_s + \Sigma_{app}(\tilde{x}_s, u)$ which is given by the following m-dimensional system:

$$\begin{aligned} \frac{d\tilde{x}_s}{dt} &= \mathcal{A}_s\tilde{x}_s + \mathcal{B}_s u + \mathcal{R}_s(\tilde{x}_s, \Sigma_{app}(\tilde{x}_s, u)) \\ y_m &= \mathcal{S}\tilde{x}_s + \mathcal{S}\Sigma_{app}(\tilde{x}_s, u) \\ y_c &= \mathcal{C}\tilde{x}_s + \mathcal{C}\Sigma_{app}(\tilde{x}_s, u) \end{aligned} \tag{6.10}$$

A function $\Sigma_{app}(\tilde{x}_s, u)$ which is frequently used in the literature (see, for example, [102]) is:

$$\Sigma_{app}(\tilde{x}_s, u) = (\mathcal{A}_f)^{-1}[-\mathcal{B}_f u - \mathcal{R}_f(\tilde{x}_s, 0)] \tag{6.11}$$

The reader may also refer to [45, 72, 156] for alternative approaches for the construction of AIMs. The AIM of Eq.6.11 leads to the following m-dimensional system:

$$\begin{aligned} \frac{d\tilde{x}_s}{dt} &= \mathcal{A}_s\tilde{x}_s + \mathcal{B}_s u + \mathcal{R}_s(\tilde{x}_s, (\mathcal{A}_f)^{-1}[-\mathcal{B}_f u - \mathcal{R}_f(\tilde{x}_s, 0)]) \\ y_m &= \mathcal{S}\tilde{x}_s + \mathcal{S}(\mathcal{A}_f)^{-1}[-\mathcal{B}_f u - \mathcal{R}_f(\tilde{x}_s, 0)] \\ y_c &= \mathcal{C}\tilde{x}_s + \mathcal{C}(\mathcal{A}_f)^{-1}[-\mathcal{B}_f u - \mathcal{R}_f(\tilde{x}_s, 0)] \end{aligned} \tag{6.12}$$

Remark 6.1: We note that the above model reduction procedure which led to the approximate ODE system of Eq.6.12 can be also used, when empirical eigenfunctions of the system of Eq.6.1 computed through Karhunen-Loève expansion (known also as proper orthogonal decomposition) are used as basis functions in $\mathcal{H}_s$ and $\mathcal{H}_f$, instead of the eigenfunctions of $\mathcal{A}$.

6.2.3 Nonlinear control

In this section, the finite-dimensional system of Eq.6.12 is used to synthesize a nonlinear finite-dimensional output feedback controller that guarantees stability and enforces output tracking in the closed-loop ODE system, and establish that the same controller exponentially stabilizes the closed-loop infinite-dimensional system. The finite-dimensional output feedback controller which achieves the desired objectives for the system of Eq.6.12 is constructed through a standard combination of a state feedback controller with a state observer.

Since the manipulated input in the system of Eq.6.12 appears in a nonlinear fashion, we initially apply the following preliminary dynamic feedback law:

$$\begin{aligned} \frac{d\xi}{dt} &= \bar{u} \\ u &= \xi \end{aligned} \tag{6.13}$$

where $\bar{u}$ is an auxiliary input, to the system of Eq.6.12 to obtain:

$$\begin{aligned} \frac{d\xi}{dt} &= \bar{u} \\ \frac{d\tilde{x}_s}{dt} &= \mathcal{A}_s\tilde{x}_s + \mathcal{B}_s\xi + \mathcal{R}_s(\tilde{x}_s, (\mathcal{A}_f)^{-1}[-\mathcal{B}_f\xi - \mathcal{R}_f(\tilde{x}_s, 0)]) \\ y_m &= S\tilde{x}_s + S(\mathcal{A}_f)^{-1}[-\mathcal{B}_f\xi - \mathcal{R}_f(\tilde{x}_s, 0)] \\ y_c &= C\tilde{x}_s + C(\mathcal{A}_f)^{-1}[-\mathcal{B}_f\xi - \mathcal{R}_f(\tilde{x}_s, 0)] \end{aligned} \tag{6.14}$$

which can be written in the following compact form:

$$\begin{aligned} \frac{d\hat{x}_s}{dt} &= f(\hat{x}_s) + g(\hat{x}_s)\bar{u} \\ y_m &= h_m(\hat{x}_s), \;\; y_c = h_c(\hat{x}_s) \end{aligned} \tag{6.15}$$

where $\hat{x}_s = [\xi^T \ \tilde{x}_s^T]$ and the specific form of f, g, h_m, h_c can be readily obtained by comparing Eq.6.14 and Eq.6.15. On the basis of the system of Eq.6.15, one can utilize geometric control methods [98] to synthesize a nonlinear state feedback control law of the general form:

$$\bar{u} = p(\hat{x}_s) + Q(\hat{x}_s)v \tag{6.16}$$

where $p(\hat{x}_s)$ is a smooth vector function, $Q(\hat{x}_s)$ is a smooth matrix, and $v \in \mathbb{R}^l$ is the constant reference input vector. Under the hypothesis that the system of Eq.6.15 is locally observable (i.e., its linearization around the zero solution is observable), the practical implementation of the state feedback law of Eq.6.16 will be achieved by employing the following nonlinear state observer:

$$\frac{d\eta}{dt} = f(\eta) + g(\eta)\bar{u} + L(y_m - h_m(\eta)) \tag{6.17}$$

where η denotes the observer state vector (the dimension of the vector η is equal to the dimension of $\hat{x}_s$ in the system of Eq.6.15), and L is a matrix chosen so that the eigenvalues of the matrix $C_L = \left.\frac{\partial f}{\partial \eta}\right|_{(\eta=0)} - L \left.\frac{\partial h_m}{\partial \eta}\right|_{(\eta=0)}$ lie in the open left-half of the complex plane.

The dynamic control law of Eq.6.13, the state feedback law of Eq.6.16 and the state observer of Eq.6.17 can be combined to yield the following nonlinear output feedback controller:

$$\begin{aligned} \frac{d\eta}{dt} &= f(\eta) + g(\eta)(p(\eta) + Q(\eta)v) + L(y_m - h_m(\eta)) \\ \frac{d\xi}{dt} &= p(\eta) + Q(\eta)v \\ u &= \xi \end{aligned} \tag{6.18}$$

Theorem 6.1 below provides an explicit synthesis formula of the output feedback controller and conditions that guarantee closed-loop stability. In order to state the result of the theorem, referring to the system of Eq.6.15, we define the relative order of the output y_{c_i} with respect to the vector of manipulated inputs $\bar{u}$ as the smallest

integer r_i for which

$$\left[L_{g_1}L_f^{r_i-1}h_{ci}(\hat{x}_s)\ \cdots\ L_{g_l}L_f^{r_i-1}h_{ci}(\hat{x}_s)\right] \not\equiv [0\ \cdots\ 0] \tag{6.19}$$

or $r_i = \infty$ if such an integer does not exist, and the characteristic matrix

$$C(\hat{x}_s) = \begin{bmatrix} L_{g_1}L_f^{r_1-1}h_{c1}(\hat{x}_s) & \cdots & L_{g_l}L_f^{r_1-1}h_{c1}(\hat{x}_s) \\ L_{g_1}L_f^{r_2-1}h_{c2}(\hat{x}_s) & \cdots & L_{g_l}L_f^{r_2-1}h_{c2}(\hat{x}_s) \\ \vdots & \cdots & \vdots \\ L_{g_1}L_f^{r_l-1}h_{cl}(\hat{x}_s) & \cdots & L_{g_l}L_f^{r_l-1}h_{cl}(\hat{x}_s) \end{bmatrix} \tag{6.20}$$

where h_{ci} is the i-th element of the vector h_c and g_i is the i-th vector of the matrix g. The proof of Theorem 6.1 is presented in Appendix F.

Theorem 6.1: *Consider the system of Eq.6.15 and assume that:* 1) *it is locally observable and* $C_L = \frac{1}{\epsilon}A$ *where* ϵ *is a small positive parameter and* A *is a Hurwitz matrix,* 2) *its characteristic matrix is nonsingular* $\forall\ \hat{x}_s \in D \subset \mathbb{R}^{m+l}$, *and* 3) *its unforced* ($v \equiv 0$) *zero dynamics are locally exponentially stable. Consider also the system of Eq.6.1 under the nonlinear output feedback controller:*

$$\begin{aligned} \frac{d\eta}{dt} &= f(\eta) + L(y_m - h_m(\eta)) + g(\eta)\left\{[\beta_{1r_1}\cdots\beta_{lr_l}]C(\eta)\right\}^{-1}\left\{v - \sum_{i=1}^{l}\sum_{k=0}^{r_i}\beta_{ik}L_f^k h_{ci}(\eta)\right\} \\ \frac{d\xi}{dt} &= \left\{[\beta_{1r_1}\cdots\beta_{lr_l}]C(\eta)\right\}^{-1}\left\{v - \sum_{i=1}^{l}\sum_{k=0}^{r_i}\beta_{ik}L_f^k h_{ci}(\eta)\right\} \\ u &= \xi \end{aligned} \tag{6.21}$$

where the l*-dimensional vectors of the parameters* β_{ik} *are chosen so that the roots of the equation* $det(B(s)) = 0$ *are in the open left-half of the complex plane* ($B(s)$ *is a* $l \times l$ *matrix, whose* (i,j)*-th element is of the form* $\sum_{k=0}^{r_i}\beta_{jk}^i s^k$). *Then, there exist positive real numbers* μ, ϵ^* *such that if* $||x_0||_2 \leq \mu$ *and* $\epsilon \in (0, \epsilon^*]$, *the zero solution of the closed-loop system (Eq.6.1 and 6.21) is exponentially stable.*

Remark 6.2: The assumption that the zero dynamics of the system of Eq.6.15 are locally exponentially stable is standard in geometric control (see [98] for details), while

the assumption $C_L = \frac{1}{\epsilon}A$, where ϵ is a small positive parameter and A is a Hurwitz matrix, is needed to ensure that the presence of closed-loop system states, which are not included in the model used for controller synthesis, in the state observer does not lead to closed-loop instability. Finally, the assumption that the characteristic matrix $C(\hat{x}_s)$ is nonsingular is made to simplify the presentation of the controller synthesis results and can be relaxed (see [98]).

Remark 6.3: The exponential stability property of the closed-loop system guarantees a degree of robustness with respect to sufficiently small disturbances and uncertainty in the process parameters. The design of robust controllers is beyond the scope of this chapter.

Remark 6.4: It is important to note that even though the presence of feedback control in the system of Eq.6.1 makes very difficult (if not impossible) to answer the mathematical question of existence of an inertial manifold (i.e., exact solution of Eq.6.9), the use of the proposed method for synthesizing nonlinear controllers with guaranteed closed-loop stability for dissipative PDEs is based on the concept of approximate inertial manifold and does not require knowledge of the existence of an inertial manifold for the PDE. Moreover, referring to the expression for the approximate inertial manifold of Eq.6.11, we note that it constitutes a direct generalization to the one presented in [71, 70] for dissipative PDEs without time-varying inputs, to systems with time-varying inputs. This approximation for Σ is clearly not unique; the reader may also refer to [102, 156] for other approximations of Σ for systems with time-varying inputs.

Remark 6.5: The implementation of the controller of Eq.6.21 requires to explicitly compute the vector function $\Sigma_{app}(\eta, u)$. However, $\Sigma_{app}(\eta, u)$ has an infinite-

dimensional range and therefore cannot be implemented in practice. Instead a finite-dimensional approximation of $\Sigma_{app}(\eta, u)$, say $\Sigma_{app_t}(\eta, u)$, can be derived by keeping the first $\bar{m}$ elements of $\Sigma_{app}(\eta, u)$ and neglecting the remaining infinite ones. Clearly, as $\bar{m} \to \infty$, $\Sigma_{app_t}(\eta, u)$ approaches $\Sigma_{app}(\eta, u)$. This implies that by picking $\bar{m}$ to be sufficiently large, the controller of Eq.6.21 with $\Sigma_{app_t}(\eta, u)$ instead of $\Sigma_{app}(\eta, u)$ enforces local exponential stability in the closed-loop infinite-dimensional system.

Remark 6.6: It is instructive to compare the approach proposed in this work for finite-dimensional nonlinear controller design for dissipative infinite-dimensional systems with the method developed in [34, 35, 144] for the design of nonlinear controllers for diffusion-reaction processes with unknown dynamics using Karhunen-Loève-based Galerkin's method and center manifold theory. The central difference is that the proposed approach can be applied to all dissipative PDEs (including hyperbolic-type PDEs like Korteweg-de Vries-Burgers equation and parabolic-type PDEs like Kuramoto-Sivashinsky equation), while the method in [34, 35, 144] is mainly suitable for dissipative PDEs that include spatial differential operators whose eigenspectrum can be partitioned into a finite-dimensional set of eigenvalues which are close to the imaginary axis and an infinite-dimensional stable complement of eigenvalues which are far in the left-half of the complex plane (a typical feature of parabolic PDEs modeling diffusion-reaction processes). We have been able to relax this restriction by imposing additional requirements on the observability and the design of the gain of the state observer used to provide estimates of the states of the finite-dimensional model used for controller design. In contrast, the approach in [34, 35, 144], motivated by the objective to control diffusion-reaction processes with unknown dynamics, employs a sufficiently large number of measurements to reconstruct the eigenmodes/eigenfunctions corresponding to the slow dynamics of the closed-loop system using Karhunen-Loève

expansion.

6.3 Korteweg-de Vries-Burgers equation

We consider the one-dimensional Korteweg-de Vries-Burgers equation with distributed control:

$$\frac{\partial U}{\partial t} = -\frac{\partial^3 U}{\partial z^3} + a_1 \frac{\partial^2 U}{\partial z^2} - U\frac{\partial U}{\partial z} + b(z)u(t) \tag{6.22}$$

subject to the periodic boundary conditions:

$$\frac{\partial^j U}{\partial z^j}(0,t) = \frac{\partial^j U}{\partial z^j}(\pi,t), \quad j = 0,\ldots,2 \tag{6.23}$$

and the initial condition:

$$U(z,0) = U_0(z) \tag{6.24}$$

where $U(z,t)$ is the state, $z \in [0,\pi]$ is the spatial coordinate, a_1 is a positive real number and $b(z)$ is the vector of the actuator distribution functions.

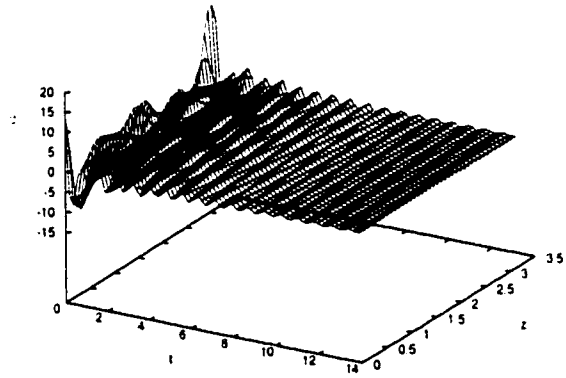

Figure 6.1: Open-loop spatiotemporal profile of $U(z,t)$ (KdVB).

Introducing the Hilbert space $\mathcal{H}$ of functions defined on $[0,\pi]$ that satisfy the boundary conditions of Eq.6.23 and defining the state function x on $\mathcal{H}$ as:

$$x(t) = U(z,t), \quad z \in [0,\pi] \tag{6.25}$$

the system of Eqs.6.22-6.24 can be written in the form of Eq.6.1, where the spatial differential operator takes the form:

$$\begin{aligned} \mathcal{A}x =& -\frac{\partial^3 x}{\partial z^3} + a_1 \frac{\partial^2 x}{\partial z^2}, \\ & x \in D(\mathcal{A}) = \left\{ x \in \mathcal{H}([0,\pi];\mathbb{R});\ \frac{\partial^j x}{\partial z^j}(0) = \frac{\partial^j x}{\partial z^j}(\pi),\quad j = 0,\ldots,2 \right\} \end{aligned} \tag{6.26}$$

The eigenvalue problem for $\mathcal{A}$ can be solved analytically and its solution is of the form:

$$\lambda_j = -4a_1 j^2 + I8j^3,\quad \phi_j(z) = \sqrt{\frac{1}{\pi}} e^{(I\,2j\,z)},\quad j = 0, \pm 1, \ldots, \pm\infty \tag{6.27}$$

where λ_j denotes the j-th eigenvalue, $\phi_j(z)$ denotes the j-th eigenfunction and $I = \sqrt{-1}$.

For the system of Eq.6.22, the spatiotemporal evolution of the open-loop $U(z,t)$ is shown in Figure 6.1. For all the simulations presented in this section, we use $a_1 = 0.05$ and $U_0(z) = 2.5 \sum_{j=-5}^{5} [cos(2j\ z) - sin(2j\ z)] - 2.5$, while a 21-st order nonlinear ODE system obtained by applying Galerkin's method to the system of Eqs.6.22-6.24 is used in the simulation (use of higher order approximations led to identical numerical results). Clearly, the time required for the $U(z,t)$ to approach the stable zero solution is significant (i.e., more than 12 time units). To enhance the convergence rate to the steady-state, we use three control actuators and the methodology of section 2 to design a nonlinear multivariable finite-dimensional output feedback controller. We assume that a single measurement of $U(z,t)$ at $z = \frac{\pi}{2}$ (i.e., $y_m = \int_0^\pi \delta(z - \frac{\pi}{2}) U(z,t) dz$; see also remark 6.5) is available. The three controlled outputs are defined as:

$$\begin{aligned} y_{c_1}(t) &= \int_0^\pi 2\sqrt{\frac{1}{\pi}} cos(2z) U(z,t) dz \\ y_{c_2}(t) &= \int_0^\pi 2\sqrt{\frac{1}{\pi}} sin(2z) U(z,t) dz \\ y_{c_3}(t) &= \int_0^\pi \sqrt{\frac{1}{\pi}} U(z,t) dz \end{aligned} \tag{6.28}$$

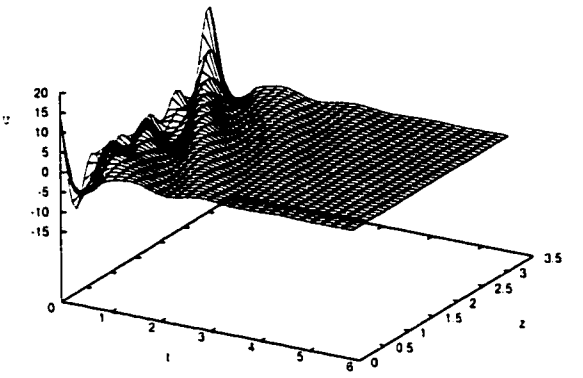

Figure 6.2: Closed-loop spatiotemporal profile of $U(z,t)$ (KdVB).

and the actuator distribution functions are taken to be:

$$\begin{aligned} b_1(z) &= \delta(z - \frac{\pi}{2}) \\ b_2(z) &= \delta(z - \frac{\pi}{4}) \\ b_3(z) &= \sqrt{\frac{1}{\pi}} \end{aligned} \tag{6.29}$$

The use of two point actuators and one distributed actuator ensures that the condition $\int_0^\pi U(z,t)dz = 0$ holds for all times (e.g., mass conservation, see also [152]). For the system of Eq.6.22, Galerkin's method was used to derive an approximate three-dimensional ODE model which was employed for controller design. Improvement of the accuracy of the three-dimensional model through approximate inertial manifolds was found to be insignificant. The ODE model was used for the synthesis of a nonlinear controller of the form of Eq.6.21 which was implemented with $\beta_{10} = \begin{bmatrix} 1.00 \\ 0.00 \\ 0.00 \end{bmatrix}$, $\beta_{20} = \begin{bmatrix} 0.00 \\ 1.00 \\ 0.00 \end{bmatrix}$, $\beta_{30} = \begin{bmatrix} 0.00 \\ 0.00 \\ 1.00 \end{bmatrix}$, $\beta_{11} = \begin{bmatrix} 0.25 \\ 0.00 \\ 0.00 \end{bmatrix}$, $\beta_{21} = \begin{bmatrix} 0.00 \\ 0.25 \\ 0.00 \end{bmatrix}$, $\beta_{31} = \begin{bmatrix} 0.00 \\ 0.00 \\ 0.25 \end{bmatrix}$ and $\mathrm{L} = \begin{bmatrix} 2.00 \\ 0.00 \\ 2.00 \end{bmatrix}$.

Figure 6.2 shows the evolution of $U(z,t)$, while Figure 6.3 shows the manipulated input profiles and Figure 6.4 displays the closed-loop output profiles. The nonlin-

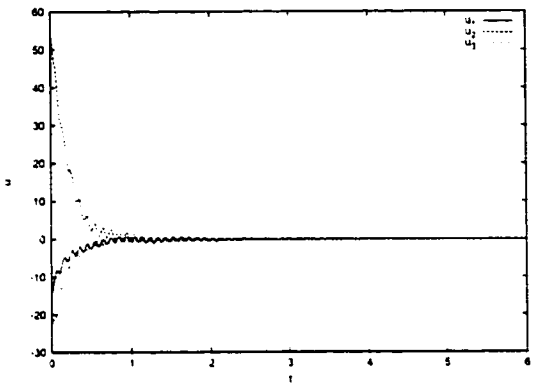

Figure 6.3: Manipulated input profiles (KdVB).

ear controller clearly enhances the convergence rate to the steady-state; this can be also seen in Figure 6.5 where the open- and closed-loop system profiles of $||U||_2$ are presented.

6.4 Kuramoto-Sivashinsky equation

We consider the one-dimensional Kuramoto-Sivashinsky equation with distributed control:

$$\frac{\partial U}{\partial t} = -\nu \frac{\partial^4 U}{\partial z^4} - \frac{\partial^2 U}{\partial z^2} - U\frac{\partial U}{\partial z} + b(z)u(t) \tag{6.30}$$

subject to the periodic boundary conditions:

$$\frac{\partial^j U}{\partial z^j}(-\pi, t) = \frac{\partial^j U}{\partial z^j}(+\pi, t), \quad j = 0, \ldots, 3 \tag{6.31}$$

and the initial condition:

$$U(z, 0) = U_0(z) \tag{6.32}$$

where $U(z,t)$ is the state of the system, $z \in [-\pi, \pi]$ is the spatial coordinate and ν is the so called instability parameter.

Introducing the Hilbert space $\mathcal{H}$ of square integrable odd functions that satisfy the boundary conditions of Eq.6.31 and have spatial zero mean (i.e., $\forall\ \omega \in \mathcal{H}$,

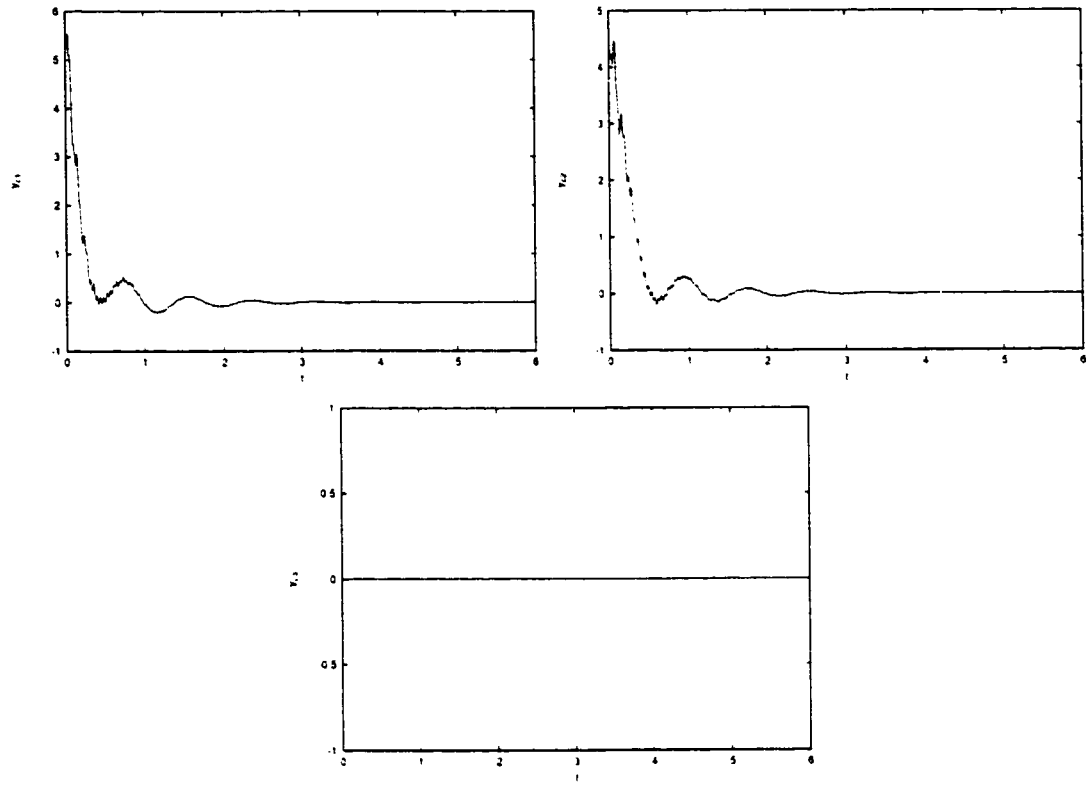

Figure 6.4: Closed-loop output profiles (KdVB).

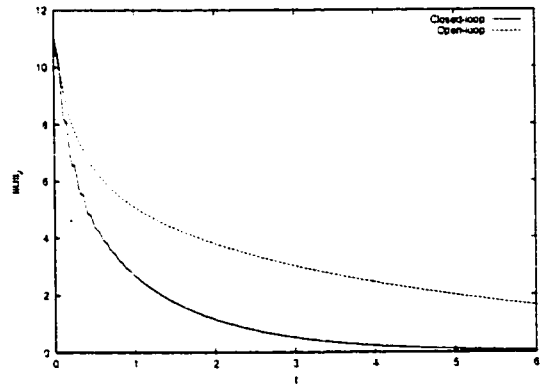

Figure 6.5: Profiles of $||U||_2$ for open-loop (dashed line) and closed-loop (solid line) systems (KdVB).

$\int_{-\pi}^{\pi} \omega(z)dz = 0$) and defining the state function $x \in \mathcal{H}$ as:

$$x(t) = U(z,t), \quad \forall\, z \in [-\pi, \pi], \tag{6.33}$$

the system of Eqs.6.30-6.32 can be written in the form of Eq.6.1, where the spatial differential operator takes the form:

$$\begin{aligned} \mathcal{A}x =& -\nu \frac{\partial^4 x}{\partial z^4} - \frac{\partial^2 x}{\partial z^2}, \\ & x \in D(\mathcal{A}) = \left\{ x \in \mathcal{H}([-\pi, \pi]; \mathbb{R});\ \frac{\partial^j x}{\partial z^j}(-\pi) = \frac{\partial^j x}{\partial z^j}(\pi), \quad j = 0, \ldots, 3 \right\} \end{aligned} \tag{6.34}$$

A direct computation of the solution of the eigenvalue problem for $\mathcal{A}$ yields $\lambda_j = -\nu j^4 + j^2$, $\phi_j(z) = \sqrt{\frac{1}{\pi}} sin(jz)$, $j = 1, \ldots, \infty$ (note that $\phi_j(z) = \sqrt{\frac{1}{2\pi}}$ and $\phi_j(z) = \sqrt{\frac{1}{\pi}} cos(jz)$, $j = 1, \ldots, \infty$ are also eigenfunctions of $\mathcal{A}$, but are not considered here since we focus on odd functions with spatial zero mean). Clearly, a real eigenvalue of the system of Eq.6.30 crosses the imaginary axis when:

$$\nu = \frac{1}{j^2}, \quad j = 1, \ldots, \infty \tag{6.35}$$

Apparently, the smallest value of j for which the $U(z,t) = 0$ solution of the system of Eq.6.30 is about to become unstable is $\nu = 1$ (the reader may refer to [36] for a detailed stability analysis; see also [33, 32]). For example, when $\nu = 0.3$, the operator of Eq.6.34 possesses one unstable eigenvalue. The spatiotemporal evolution of $U(z,t)$ for $\nu = 0.3$ is shown in Figure 6.6, for the initial condition $U_0(z) = 5.0 \sum_{j=1}^{5} [sin(j\ z)]$ (for the simulation of Eq.6.30 a 30-th order ODE system derived using Galerkin's method is used; higher order approximations led to identical numerical results). It is clear that for $\nu = 0.3$, the spatially uniform steady-state $U(z,t) = 0$ is unstable. Therefore, we use the proposed method to design a nonlinear finite-dimensional controller which uses one measurement of $U(z,t)$ at $z = \frac{\pi}{2}$ to stabilize the system at $U(z,t) = 0$, for

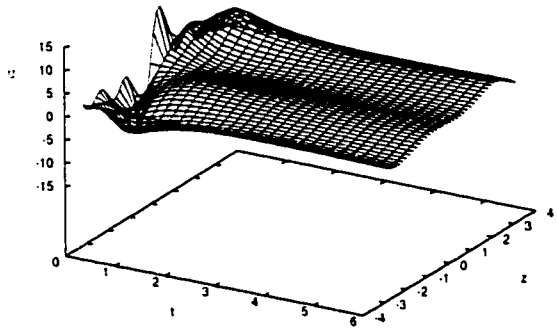

Figure 6.6: Open-loop spatiotemporal profile of $U(z,t)$ for $\nu = 0.3$ (KS).

$\nu = 0.3$. To achieve this control objective, the controlled output is defined as:

$$y_c(t) = \int_{-\pi}^{\pi} \sqrt{\frac{1}{\pi}} sin(z) U(z,t) dz \tag{6.36}$$

and the actuator distribution function is taken to be $b_1(z) = \delta(z - \frac{\pi}{2})$ (i.e., point control actuation at $z = \frac{\pi}{2}$). To show the improvement in closed-loop performance achieved when nonlinear Galerkin's method is used for model reduction, standard Galerkin's method was initially used to derive a first-order model which was employed for the synthesis of a nonlinear controller using the formula of Eq.6.21. This

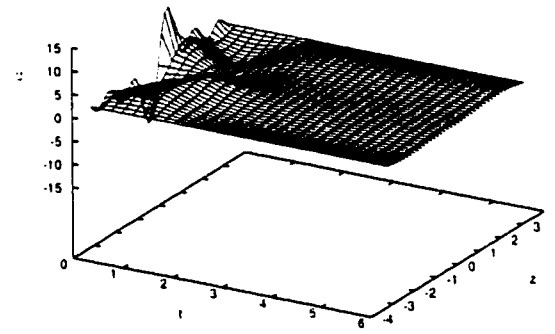

Figure 6.7: Closed-loop spatiotemporal profile of $U(z,t)$ for $\nu = 0.3$ and $(1,0)$ controller (KS).

controller is denoted as $(1,0)$ where 1 denotes the order of the controller and 0 denotes the order of the approximate inertial manifold. The controller parameters are

$\beta_{10} = 1.00$, $\beta_{11} = 0.20$ and $L = 3.80$. Figure 6.7 shows the evolution of $U(z,t)$, while Figures 6.9 and 6.10 show the corresponding manipulated input and controlled output profiles (dashed lines), respectively. Note that this controller requires more than 15

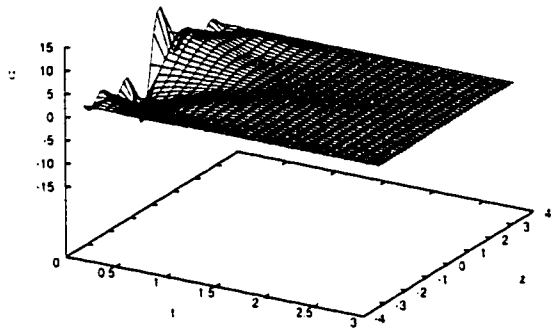

Figure 6.8: Closed-loop spatiotemporal profile of $U(z,t)$ for $\nu = 0.3$ and $(1,2)$ controller (KS).

time units to stabilize the system at $U(z,t) = 0$. To achieve stabilization with better convergence rate to the steady state, the proposed combination of Galerkin's method with approximate inertial manifolds (i.e., nonlinear Galerkin's method) was used to derive a first-order model with $\tilde{m} = 2$ (dimension of AIM), which was subsequently

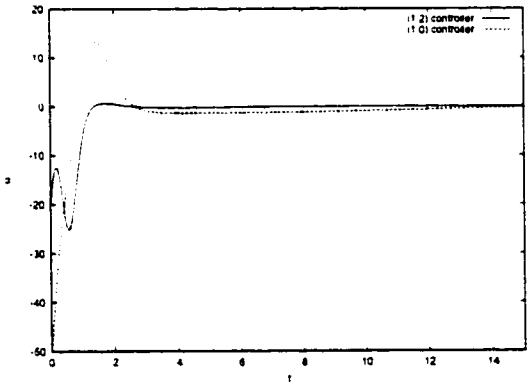

Figure 6.9: Manipulated input profiles for $(1,0)$ controller (dashed line) and $(1,2)$ (solid line) controller (KS, $\nu = 0.3$).

employed for the construction of a nonlinear controller. This controller is denoted as

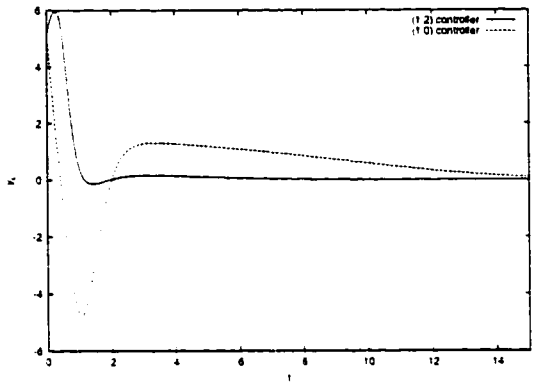

Figure 6.10: Closed-loop output profiles for $(1,0)$ controller (dashed line) and $(1,2)$ (solid line) controller (KS, $\nu = 0.3$).

$(1,2)$ and is implemented with $\beta_{10} = 1.00$, $\beta_{11} = 0.20$ and $L = 3.80$. Figure 6.8 shows the evolution of $U(z,t)$, while Figures 6.9 and 6.10 show the corresponding manipulated input and output profiles (solid lines), respectively. Note that this controller stabilizes the system at $U(z,t) = 0$ after 3 time units, while achieving a smooth transient profile. The improvement on the convergence rate to the steady state, which is

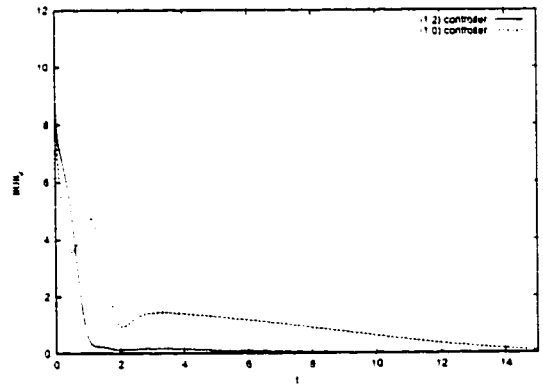

Figure 6.11: Closed-loop profiles of $||U||_2$ for $(1,0)$ controller (dashed line) and $(1,2)$ (solid line) controller (KS, $\nu = 0.3$).

achieved by using nonlinear Galerkin's method to derive the model used for controller design, is also shown in Figure 6.11, where the closed-loop profiles of $||U||_2$ under the

$(1,0)$ and $(1,2)$ controllers are presented.

Finally, in order to illustrate the value of proposed method when multiple eigenvalues are unstable, we also consider the stabilization of the KS equation with $\nu = 0.1$;

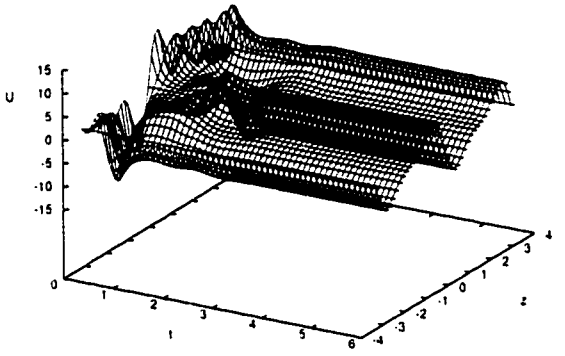

Figure 6.12: Open-loop spatiotemporal profile of $U(z,t)$ for $\nu = 0.1$ (KS).

in this case, the open-loop system possesses three positive (unstable) eigenvalues. The spatiotemporal evolution of $U(z,t)$ for $\nu = 0.1$ and $U_0(z) = 5.0\sum_{j=1}^{5}[sin(j\ z)]$ is shown in Figure 6.12. The proposed method is used to design a nonlinear multivariable finite-dimensional controller which uses three point measurements of $U(z,t)$ at $z = -\frac{\pi}{2}$, $z = -\frac{\pi}{4}$, $z = \frac{\pi}{3}$ to stabilize the system at $U(z,t) = 0$. To achieve this control objective, the three controlled outputs are defined as:

$$\begin{aligned} y_{c_1}(t) &= \int_{-\pi}^{\pi}\sqrt{\frac{1}{\pi}}sin(z)U(z,t)dz \\ y_{c_1}(t) &= \int_{-\pi}^{\pi}\sqrt{\frac{1}{\pi}}sin(2\ z)U(z,t)dz \\ y_{c_1}(t) &= \int_{-\pi}^{\pi}\sqrt{\frac{1}{\pi}}sin(3\ z)U(z,t)dz \end{aligned} \tag{6.37}$$

and three point actuators are used with the following actuator distribution functions: $b_1(z) = \delta(z+\frac{\pi}{3})$, $b_2(z) = \delta(z-\frac{\pi}{4})$ and $b_3(z) = \delta(z-\frac{\pi}{2})$ (i.e., point control actuation is used at $z = -\frac{\pi}{3}$, $z = \frac{\pi}{4}$ and $z = \frac{\pi}{2}$, respectively). Two different controllers are employed for the stabilization of the system to the spatially uniform steady state

$U(z,t) = 0.0$. Initially, a nonlinear output feedback controller was designed on the

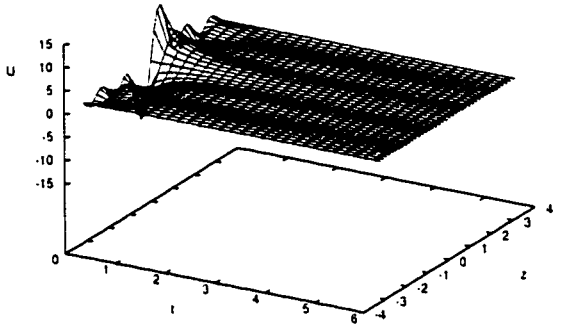

Figure 6.13: Closed-loop spatiotemporal profile of $U(z,t)$ for $\nu = 0.1$ and $(9,0)$ controller (KS).

basis of an ODE model which was derived through standard Galerkin's method. It was found that the lowest order nonlinear controller that achieves stabilization of the zero solution with a reasonable convergence rate is nine (a controller of order eight achieves stabilization with a very slow convergence rate, and controllers of order seven and lower can not stabilize the closed-loop system, for the chosen initial conditions, controller parameters and $\nu = 0.1$). Based on this ninth-order model, a nonlinear controller was synthesized using the formula of Eq.6.21 and is denoted as (9,0). The controller parameters are as follows: $\beta_{10} = \begin{bmatrix} 1.0 \\ 0.0 \\ 0.0 \\ 0.0 \\ \vdots \\ 0.0 \end{bmatrix}$, $\beta_{20} = \begin{bmatrix} 0.0 \\ 1.0 \\ 0.0 \\ 0.0 \\ \vdots \\ 0.0 \end{bmatrix}$, $\beta_{30} = \begin{bmatrix} 0.0 \\ 0.0 \\ 1.0 \\ 0.0 \\ \vdots \\ 0.0 \end{bmatrix}$, $\beta_{11} = \begin{bmatrix} 0.5 \\ 0.0 \\ 0.0 \\ 0.0 \\ \vdots \\ 0.0 \end{bmatrix}$, $\beta_{21} = \begin{bmatrix} 0.0 \\ 0.5 \\ 0.0 \\ 0.0 \\ \vdots \\ 0.0 \end{bmatrix}$, $\beta_{31} = \begin{bmatrix} 0.0 \\ 0.0 \\ 0.5 \\ 0.0 \\ \vdots \\ 0.0 \end{bmatrix}$ and $\mathbf{L} = \begin{bmatrix} 13.3 & -21.8 & 4.89 \\ 18.8 & -30.8 & 16.7 \\ 21.7 & -50.3 & 19.3 \\ 0.00 & 0.00 & 0.00 \\ \vdots & \vdots & \vdots \\ 0.00 & 0.00 & 0.00 \end{bmatrix}$. Figures 6.13, 6.15 and 6.16 show the evolution of $U(z,t)$, the manipulated input profiles (dashed lines) and the corresponding controlled output profiles (dashed lines).

Clearly, this ninth-order controller achieves stabilization of the closed-loop system after 12 time units. Subsequently, we employ the proposed approach to design a stabilizing controller. Using a combination of Galerkin's method with approximate iner-

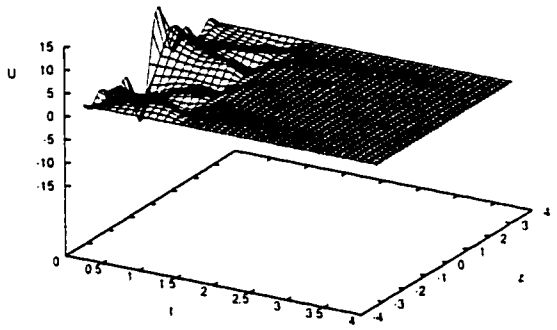

Figure 6.14: Closed-loop spatiotemporal profile of $U(z,t)$ for $\nu = 0.1$ and $(4,6)$ controller (KS).

tial manifolds (i.e., nonlinear Galerkin's method), we derived a 4th-order model with $\tilde{m} = 6$ (dimension of AIM), which was subsequently employed for the construction of a nonlinear controller (denoted as $(4,6)$). This controller was implemented with the following parameters: $\beta_{10} = \begin{bmatrix} 1.0 \\ 0.0 \\ 0.0 \\ 0.0 \end{bmatrix}$, $\beta_{20} = \begin{bmatrix} 0.0 \\ 1.0 \\ 0.0 \\ 0.0 \end{bmatrix}$, $\beta_{30} = \begin{bmatrix} 0.0 \\ 0.0 \\ 1.0 \\ 0.0 \end{bmatrix}$, $\beta_{11} = \begin{bmatrix} 0.5 \\ 0.0 \\ 0.0 \\ 0.0 \end{bmatrix}$, $\beta_{21} = \begin{bmatrix} 0.0 \\ 0.5 \\ 0.0 \\ 0.0 \end{bmatrix}$, $\beta_{31} = \begin{bmatrix} 0.0 \\ 0.0 \\ 0.5 \\ 0.0 \end{bmatrix}$ and $\mathrm{L} = \begin{bmatrix} 13.3 & -21.8 & 4.89 \\ 18.8 & -30.8 & 16.7 \\ 21.7 & -50.3 & 19.3 \\ 0.00 & 0.00 & 0.00 \end{bmatrix}$. Figures 6.14, 6.15 and 6.16 show the evolution of $U(z,t)$, the manipulated input and controlled output profiles, respectively. Clearly, this controller stabilizes the closed-loop system at $U(z,t) = 0$ after 4 time units, while achieving a smooth transient profile. Finally, Figure 6.17 shows the closed-loop profiles of the "energy" of the system $\|U\|_2$ under the $(9,0)$ and $(4,6)$ controllers. We can clearly see that the nonlinear controller based on the model obtained by nonlinear Galerkin's method outperforms the nonlinear controller based on the model obtained by standard Galerkin's method.

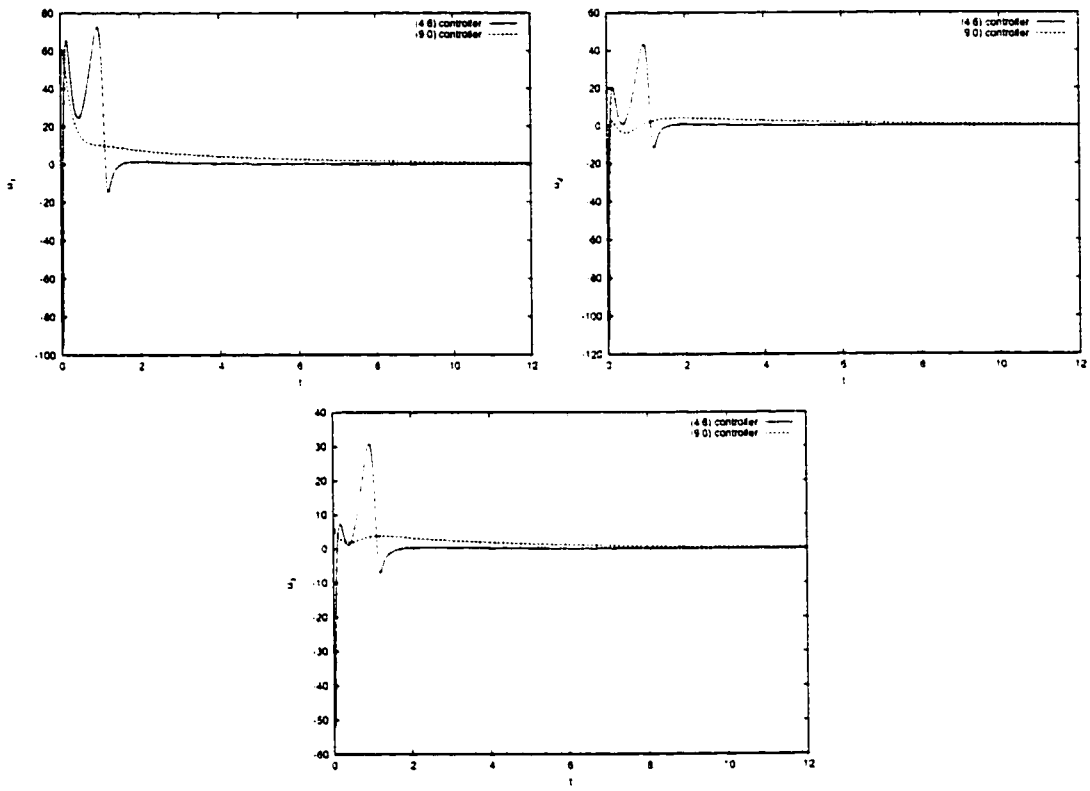

Figure 6.15: Manipulated input profiles for $(9,0)$ controller (dashed line) and $(4,6)$ (solid line) controller (KS, $\nu = 0.1$).

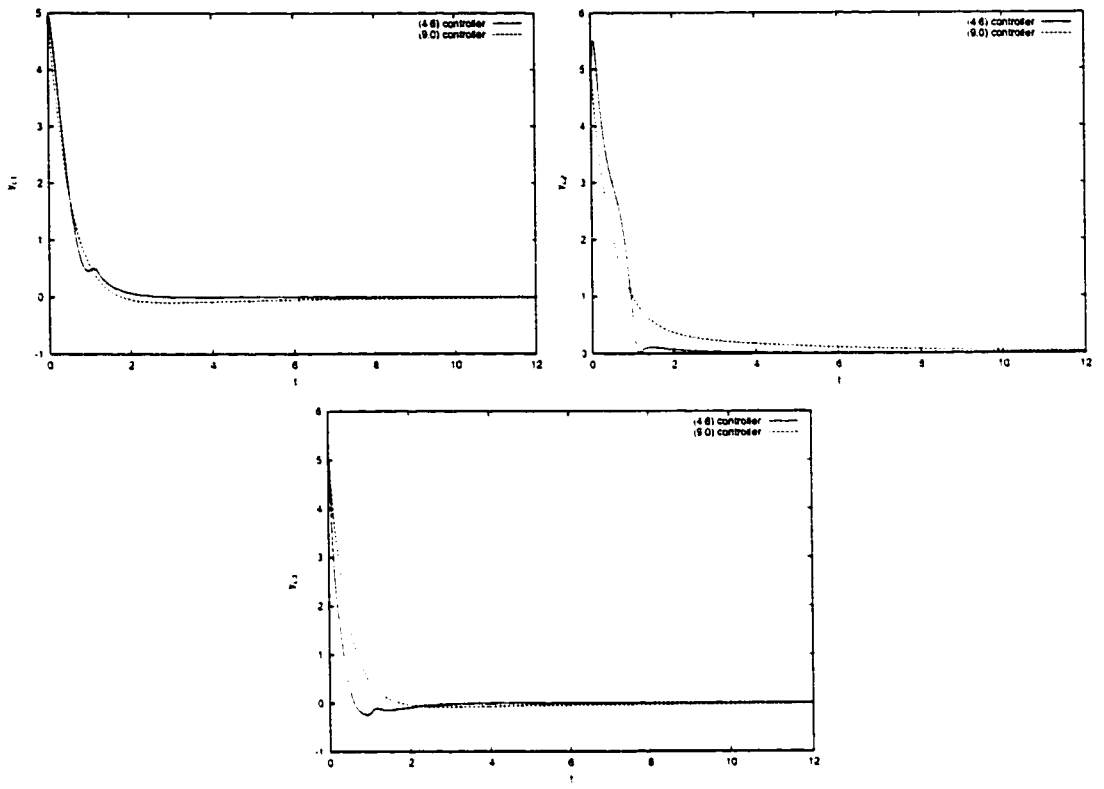

Figure 6.16: Closed-loop output profiles for $(9,0)$ controller (dashed line) and $(4,6)$ (solid line) controller (KS, $\nu = 0.1$).

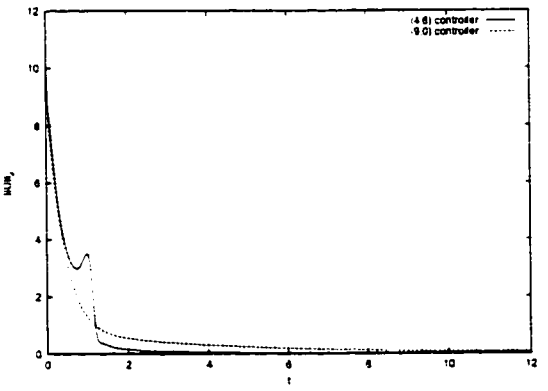

Figure 6.17: Closed-loop profiles of $||U||_2$ for $(9,0)$ controller (dashed line) and $(4,6)$ (solid line) controller (KS, $\nu = 0.1$).

Remark 6.7: We note that in the case of point actuation (sensing) which influences (measures) the system at z_0, the function $\delta(z - z_0)$ is assumed to have the finite value $\frac{1}{2\epsilon}$ in the interval $[z_0 - \epsilon, z_0 + \epsilon]$ (where ϵ is a small positive real number) and be zero elsewhere in the domain of definition of z.

Remark 6.8: We note that even though both the Korteweg-de Vries-Burgers equation and the Kuramoto-Sivashinsky equation considered in the above simulation studies are subjected to periodic boundary conditions, the proposed approach for nonlinear controller design can be also utilized when other sets of boundary conditions are used, provided that the resulting infinite-dimensional system is dissipative and contains a finite number of unstable eigenvalues. In addition, the proposed approach can be used to control PDE systems that include a finite number of unstable eigenvalues and a continuum spectrum of stable eigenvalues like diffusion-reaction processes defined in infinitely-large domains (see, for example, [128]). Finally, it is important to note that it is not possible to stabilize an infinite-dimensional system which includes infinitely many unstable eigenvalues (i.e., continuum of unstable eigenvalues) with a finite-number of control actuators and measurements sensors (i.e., the setup considered in this chapter) no matter what kind of control algorithm is employed.

6.5 Conclusions

In this chapter, we focused on nonlinear finite-dimensional control of the KdVB and KS equations. We initially proposed a nonlinear controller design method for quasi-linear evolutionary PDEs, employing a combination of nonlinear Galerkin's method with the concept of approximate inertial manifold to derive low-dimensional ODE models, which are subsequently used for the synthesis of low-order nonlinear output feedback controllers that enforce the desired stability properties in the closed-loop

system. This method was subsequently used to synthesize nonlinear low-order controllers for the KdVB and KS equations that enhance convergence rate and achieve stabilization to spatially uniform steady-states, respectively. The controllers used measurements obtained by point sensors and were implemented via point control actuators. The performance of the proposed controllers was successfully tested through simulations.

Chapter 7

Global Stabilization of the Kuramoto-Sivashinsky Equation via Distributed Output Feedback Control

7.1 Introduction

In this chapter, we consider the problem of global exponential stabilization of the zero solution, $x(z,t) = 0$, of the Kuramoto-Sivashinsky Equation (KSE) with periodic boundary conditions, for any value of the instability parameter ν, via distributed static output feedback control. Under the assumptions that the number of measurements is equal to the total number of unstable and critically stable eigenvalues of the KSE and a necessary and sufficient stability condition is satisfied, linear static output feedback controllers are designed that achieve global (i.e., for every initial condition) stabilization of the $x(z,t) = 0$ solution of Eq.7.1. The proposed output feedback controllers are designed on the basis of ODE approximations of the KSE obtained

through Galerkin's method. Numerical simulations of the closed-loop system, for different values of the instability parameter, confirm the theoretical results.

7.2 Preliminaries

The KSE is a nonlinear dissipative fourth-order partial differential equation (PDE) of the form:

$$\frac{\partial x}{\partial t} = -\nu \frac{\partial^4 x}{\partial z^4} - \frac{\partial^2 x}{\partial z^2} - x\frac{\partial x}{\partial z} \tag{7.1}$$

where $\nu > 0$ is the so-called instability parameter, which describes incipient instabilities in a variety of physical and chemical systems. Examples include falling liquid films [36], unstable flame fronts [161, 131, 162], Belouzov-Zabotinskii reaction patterns [114, 115] and interfacial instabilities between two viscous fluids [91]. Analytical and numerical studies of the dynamics of Eq.7.1 with periodic boundary conditions (e.g., [168, 36, 84, 106]) have revealed the existence of steady and periodic wave solutions, as well as chaotic behavior for very small values of ν. In addition to the existence of complex solution patterns, the above studies have revealed that the dominant dynamics of the KSE can be adequately characterized by a small number of degrees of freedom (e.g., [168]).

Motivated by this, we will address the design of linear finite-dimensional output feedback controllers for stabilization of the zero solution of the KSE on the basis of ordinary differential equation (ODE) approximations, obtained through linear/nonlinear Galerkin's method, that accurately describe the dominant dynamics.

We consider the integrated form of the *controlled* Kuramoto-Sivashinsky equation:

$$\begin{aligned} \frac{\partial x}{\partial t} &= -\nu \frac{\partial^4 x}{\partial z^4} - \frac{\partial^2 x}{\partial z^2} - x\frac{\partial x}{\partial z} + \sum_{i=1}^{m} b_i u_i(t) \\ y_\kappa^m &= \int_{-\pi}^{\pi} s_\kappa(z) x dz, \ \kappa = 1, \ldots, p \end{aligned} \tag{7.2}$$

subject to the periodic boundary conditions:

$$\frac{\partial^j x}{\partial z^j}(-\pi,t) = \frac{\partial^j x}{\partial z^j}(+\pi,t), \quad j = 0,\ldots,3 \tag{7.3}$$

and the initial condition:

$$x(z,0) = x_0(z) \tag{7.4}$$

where $x \in L_p^2(-\pi,\pi)$ is the state of the system, $L_p^2(-\pi,\pi)$ denotes the space of square integrable functions that satisfy the boundary conditions of Eq.7.3 (i.e., $L_p^2(-\pi,\pi) = \{x \in L^2(-\pi,\pi) : \frac{\partial^j x}{\partial z^j}(-\pi,t) = \frac{\partial^j x}{\partial z^j}(+\pi,t),\ j = 0,\ldots,3\}$), z is the spatial coordinate, ν is the instability parameter which is assumed to be known, t is the time and 2π is the length of the spatial domain, $x_0(z) \in L_p^2([-\pi,\pi])$ is the initial condition, m is the number of manipulated inputs (i.e., variables that can be manipulated externally to modify the dynamics of Eq.7.2 in a desired fashion), $u_i(t)$ is the $i-$th manipulated input, $b_i(z)$ is the actuator distribution function (i.e., $b_i(z)$ determines how the control action computed by the i-th control actuator, $u_i(t)$, is distributed (e.g., point or distributed actuation) in the spatial interval $[-\pi,\pi]$), $y_\kappa^m \in \mathbb{R}$ denotes a measured output, and $s_\kappa(z)$ is a known smooth function of z which is determined by the location and type of the measurement sensors (e.g., point/distributed sensing). We note that in the case of point actuation (sensing) which influences (measures) the system at z_0 (i.e., $b_i(z)$ or $s_\kappa(z)$ is equal to $\delta(z-z_0)$ where $\delta(\cdot)$ is the standard Dirac function), we approximate the function $\delta(z-z_0)$ by the finite value $\frac{1}{2\epsilon}$ in the interval $[z_0-\epsilon, z_0+\epsilon]$ (where ϵ is a small positive real number) and zero elsewhere in $[-\pi,\pi]$. Finally, in $L_p^2([-\pi,\pi])$, we define the inner product and norm: $(\omega_1,\omega_2) = \int_{-\pi}^{\pi} \omega_1(z)\omega_2(z)dz$, $||\omega_1||_2 = (\omega_1,\omega_1)^{\frac{1}{2}}$ where ω_1,ω_2 are two elements of $L_p^2([-\pi,\pi])$.

The dynamics of Eq.7.2 depend heavily on the value of ν. To make this point clear, we compute the linearization of the system of Eq.7.1 around $x(z,t) = 0$, which

takes the form:

$$\frac{\partial x}{\partial t} = -\nu \frac{\partial^4 x}{\partial z^4} - \frac{\partial^2 x}{\partial z^2} \tag{7.5}$$

and consider the corresponding eigenvalue problem:

$$\mathcal{A}\phi_n = -\nu \frac{\partial^4 \phi_n}{\partial z^4} - \frac{\partial^2 \phi_n}{\partial z^2} = \mu_n \phi_n, \quad n = 1, \ldots, \infty \tag{7.6}$$

subject to:

$$\frac{\partial^j \phi_n}{\partial z^j}(-\pi, t) = \frac{\partial^j \phi_n}{\partial z^j}(+\pi, t), \quad j = 0, \ldots, 3 \tag{7.7}$$

where μ_n denotes an eigenvalue and ϕ_n denotes an eigenfunction. A direct computation of the solution of the above eigenvalue problem yields $\mu_0 = 0$ with $\psi_0(z) = \frac{1}{\sqrt{2\pi}}$, and $\mu_n = -\nu n^4 + n^2$ (μ_n is an eigenvalue of multiplicity two) with eigenfunctions $\phi_n(z) = \frac{1}{\sqrt{\pi}}\sin(nz)$ and $\psi_n(z) = \frac{1}{\sqrt{\pi}}\cos(nz)$, $n = 1, \ldots, \infty$. Clearly, a pair of eigenvalues of the system of Eq.7.5 crosses the imaginary axis when:

$$\nu = \frac{1}{n^2}, \quad n = 1, \ldots, \infty \tag{7.8}$$

Apparently, the smallest value of ν, for which the $x(z,t) = 0$ solution of the system of Eq.7.5 is about to become unstable is $\nu = 1$. Clearly, when $\frac{1}{n^2} > \nu > \frac{1}{(n+1)^2}$, the system of Eq.7.5 has $2n$ positive eigenvalues.

The above stability analysis implies that the spatially uniform steady-state of the nonlinear system of Eqs.7.1-7.3, $x(z,t) = 0$, is locally unstable when $\nu < 1$. Instead, there is a generation of *stable* spatially non-uniform stationary solutions as well as spatially non-uniform periodic solutions, while for very small values of ν no stable solutions exist and the system of Eq.7.2 exhibits chaotic behavior (the reader may refer to [36, 106] for detailed characterizations of the solution patterns for various ranges of values of ν).

7.3 Static output feedback control

In this section, we synthesize output feedback controllers that globally stabilize the system of Eqs.7.2-7.3 at $x(z,t) = 0$. We initially use Galerkin's method to derive ODE approximations of the system of Eq.7.2 that capture the dynamics of the unstable modes. Expanding the solution of the system of Eq.7.2 in an infinite series in terms of the eigenfunctions of the operator of Eq.7.6, we obtain:

$$x(z,t) = \sum_{n=1}^{\infty} \alpha_n(t)\phi_n(z) + \sum_{n=0}^{\infty} \beta_n(t)\psi_n(z) \tag{7.9}$$

where $\alpha_n(t)$, $\beta_n(t)$ are time-varying coefficients and $\phi_n(z) = \frac{1}{\sqrt{\pi}} sin(nz)$, $\psi_0(z) = \frac{1}{\sqrt{2\pi}}$ and $\psi_n(z) = \frac{1}{\sqrt{\pi}} cos(nz)$. Substituting the above expansion for the solution, $x(z,t)$, into the system of Eq.7.2 and taking the inner product in $L_p^2([-\pi,\pi])$ with the adjoint eigenfunctions, $\phi_n^*(z) = \frac{1}{\sqrt{\pi}} sin(nz)$, $\psi_0^*(z) = \frac{1}{\sqrt{2\pi}}$ and $\psi_n^*(z) = \frac{1}{\sqrt{\pi}} cos(nz)$ of the operator of Eq.7.6 (note that the operator of Eq.7.6 subject to the boundary condition of Eq.7.7 is self-adjoint, i.e., $\phi_n(z) = \phi_n^*(z)$, $\psi_0(z) = \psi_0^*(z)$, $\psi_n(z) = \psi_n^*(z)$), the following infinite system of ODEs is obtained:

$$\begin{aligned}
\dot{\alpha}_n &= (-\nu n^4 + n^2)\alpha_n - f_{n\alpha} + \sum_{i=1}^{m} b_{i\,\alpha}^n u_i(t), \quad n = 1, \ldots, \infty \\
\dot{\beta}_n &= (-\nu n^4 + n^2)\beta_n - f_{n\beta} + \sum_{i=1}^{m} b_{i\,\beta}^n u_i(t), \quad n = 0, \ldots, \infty \\
y_\kappa^m &= \int_{-\pi}^{\pi} s_\kappa(z) \left(\sum_{n=1}^{\infty} \alpha_n(t)\phi_n(z) + \sum_{n=0}^{\infty} \beta_n(t)\psi_n(z) \right) dz, \quad \kappa = 1, \ldots, p
\end{aligned} \tag{7.10}$$

where

$$
\begin{aligned}
f_{n\alpha} &= \int_{-\pi}^{\pi} \phi_n(z)\left(\sum_{n=1}^{\infty}\alpha_n(t)\phi_n(z) + \sum_{n=0}^{\infty}\beta_n(t)\psi_n(z)\right) \\
&\qquad \times \left(\sum_{n=1}^{\infty}\alpha_n(t)\frac{d\phi_n}{dz}(z) + \sum_{n=0}^{\infty}\beta_n(t)\frac{d\psi_n}{dz}(z)\right) dz, \\
f_{n\beta} &= \int_{-\pi}^{\pi} \psi_n(z)\left(\sum_{n=1}^{\infty}\alpha_n(t)\phi_n(z) + \sum_{n=0}^{\infty}\beta_n(t)\psi_n(z)\right) \\
&\qquad \times \left(\sum_{n=1}^{\infty}\alpha_n(t)\frac{d\phi_n}{dz}(z) + \sum_{n=0}^{\infty}\beta_n(t)\frac{d\psi_n}{dz}(z)\right) dz, \\
b_{i\,\alpha}^{n} &= \int_{-\pi}^{\pi} \phi_n(z)\, b_i(z)\, dz, \quad n = 1, \ldots, \infty, \\
b_{i\,\beta}^{n} &= \int_{-\pi}^{\pi} \psi_n(z)\, b_i(z)\, dz, \quad n = 0, \ldots, \infty,
\end{aligned}
\tag{7.11}
$$

and $\frac{d\phi_n}{dz}(z) = \frac{n}{\sqrt{\pi}}\, cos(nz)$, $\frac{d\psi_n}{dz}(z) = -\frac{n}{\sqrt{\pi}}\, sin(nz)$.

Owing to its infinite-dimensional nature, the system of Eq.7.10 cannot be directly used for the design of controllers that can be implemented in practice (i.e., the practical implementation of controllers which are designed on the basis of this system will require the computation of infinite sums which cannot be done by a computer). Instead, we will base the controller design on linear finite-dimensional approximations of this system. Moreover, the maximum number of eigenvalues of $\mathcal{A}$ which are identical, for any ν, is four, and thus, the use of five control actuators is sufficient for stabilizing any stabilizable finite-dimensional approximation of the system of Eq.7.10 with linear state feedback (four control actuators are needed due to the presence of four identical unstable eigenvalues and one control actuator is needed to ensure that the conservation of mass condition, $\int_{-\pi}^{\pi} x(z,t)dz = 0$, is satisfied at steady state). We note that even though the use of five control actuators is sufficient to stabilize any stabilizable finite-dimensional approximation of the system of Eq.7.10 with linear state feedback, it is not necessary. For example, when $\nu = 0.4$, $\mathcal{A}$ possesses only three unstable eigenvalues, and thus, stabilization can be achieved with three control

actuators; see section 7.4 for a numerical demonstration of this point.

Assuming that the number of unstable eigenvalues of the system of Eq.7.5 is $2l$ (i.e., $1/l^2 > \nu > 1/(l+1)^2$) and using m control actuators (where $m \leq 5$), the infinite set of ODEs of Eq.7.11 can be written in the following form:

$$\begin{aligned} \dot{\alpha}_u &= A_u\alpha_u + B_u u - \tilde{f}_u \\ \dot{\alpha}_s &= A_s\alpha_s + B_s u - \tilde{f}_s \\ y^m &= S_u\alpha_u + S_s\alpha_s \end{aligned} \tag{7.12}$$

where $\alpha_u = [\beta_0\ \alpha_1\ \beta_1\ \alpha_2\ \beta_2\ \cdots\ \alpha_l\ \beta_l]^T$, $\tilde{f}_u = [0\ f_{1\alpha}\ f_{1\beta}\ f_{2\alpha}\ f_{2\beta}\ \cdots\ f_{l\alpha}\ f_{l\beta}]^T$, $\alpha_s = [\alpha_{l+1}\ \beta_{l+1}\ \cdots]^T$, $\tilde{f}_s = [f_{l+1\alpha}\ f_{l+1\beta}\ f_{l+2\alpha}\ f_{l+2\beta}\ \cdots]^T$, $y^m = [y_1^m\ y_2^m\ \cdots\ y_p^m]^T$, $u \in \mathbb{R}^m$ and

$$A_u = \begin{bmatrix} 0 & 0 & 0 & 0 & \cdots & 0 & 0 \\ 0 & -\nu+1 & 0 & 0 & \cdots & 0 & 0 \\ 0 & 0 & -\nu+1 & 0 & \cdots & 0 & 0 \\ \vdots & \vdots & \vdots & \vdots & \cdots & \vdots & \vdots \\ 0 & 0 & 0 & 0 & \cdots & -l^4\nu + l^2 & 0 \\ 0 & 0 & 0 & 0 & \cdots & 0 & -l^4\nu + l^2 \end{bmatrix}, \tag{7.13}$$

$$A_s = \begin{bmatrix} -(l+1)^4\nu + (l+1)^2 & 0 & 0 & 0 & \cdots & 0 & 0 \\ 0 & -(l+1)^4\nu + (l+1)^2 & 0 & 0 & \cdots & 0 & 0 \\ \vdots & \vdots & \vdots & \vdots & \cdots & \vdots & \vdots \end{bmatrix}, \tag{7.14}$$

$$B_u = \begin{bmatrix} b_{1\beta}^0 & b_{2\beta}^0 & \cdots & b_{m\beta}^0 \\ b_{1\alpha}^1 & b_{2\alpha}^1 & \cdots & b_{m\alpha}^1 \\ b_{1\beta}^1 & b_{2\beta}^1 & \cdots & b_{m\beta}^1 \\ \vdots & \vdots & \cdots & \vdots \\ b_{1\alpha}^l & b_{2\alpha}^l & \cdots & b_{m\alpha}^l \\ b_{1\beta}^l & b_{2\beta}^l & \cdots & b_{m\beta}^l \end{bmatrix}, \quad S_u = \begin{bmatrix} s_{1\beta}^0 & s_{1\alpha}^1 & s_{1\beta}^1 & \cdots & s_{1\alpha}^l & s_{1\beta}^l \\ \vdots & \vdots & \cdots & \vdots & \vdots & \vdots \\ s_{p\beta}^0 & s_{p\alpha}^1 & s_{p\beta}^1 & \cdots & s_{p\alpha}^l & s_{p\beta}^l \end{bmatrix} \tag{7.15}$$

$$B_s = \begin{bmatrix} b_1^{l+1}{}_\beta & b_2^{l+1}{}_\beta & \cdots & b_m^{l+1}{}_\beta \\ b_1^{l+2}{}_\beta & b_2^{l+2}{}_\beta & \cdots & b_m^{l+2}{}_\beta \\ \vdots & \vdots & \cdots & \vdots \end{bmatrix}, \quad S_s = \begin{bmatrix} s_1^{l+1}{}_\alpha & s_1^{l+1}{}_\beta & \cdots \\ \vdots & \vdots & \cdots \\ s_p^{l+1}{}_\alpha & s_p^{l+1}{}_\beta & \cdots \end{bmatrix} \tag{7.16}$$

The following assumption is needed in order to obtain estimates of the states α_u of the system of Eq.7.12 from the measurements y_κ^m, $\kappa = 1, \ldots, p$.

Assumption 7.1: $p = 2l + 1$ *(i.e., the number of measurements is equal to the number of eigenvalues which are in the closed right-half of the complex plane), and*

the inverse of the operator S_u exists so that $\hat{\alpha}_u = S_u^{-1} y^m$, where $\hat{\alpha}_u$ is an estimate of α_u.

Theorem 7.1 that follows provides a necessary and sufficient condition under which, for a given value of ν, there exists a linear static output feedback controller that uses five control actuators and $2l+1$ measurements to globally exponentially stabilize the zero solution of the Kuramoto-Sivashinsky equation. The proof of Theorem 7.1 is presented in section G.1.

Theorem 7.1: *Let the number of unstable eigenvalues of the system of Eq.7.5 be $2l$ (i.e., $1/l^2 > \nu > 1/(l+1)^2$), $m = 5$ and assumption 7.1 hold. Then, the existence of a matrix K so that the following infinite range matrix:*

$$A_{cl} = \begin{bmatrix} A_u + B_u K & B_u K S_u^{-1} S_s \\ B_s K & A_s + B_s K S_u^{-1} S_s \end{bmatrix} \tag{7.17}$$

is Hurwitz (i.e., it possesses eigenvalues with strictly negative real part), is necessary and sufficient for the following output feedback controller:

$$u = K S_u^{-1} y^m \tag{7.18}$$

to ensure that the $x(z,t) = 0$ solution of the closed-loop system (Eqs.7.2-7.17) is exponentially stable, for any initial condition in $L_p^2([-\pi,\pi])$ and any $1/l^2 > \nu > 1/(l+1)^2$.

Remark 7.1: The requirement on matrix A_{cl} depends on the structure of the matrices B_u, S_u, and therefore, on the shape of the actuator distribution functions b_i and the measurement sensor shape functions s_κ which, in most practical applications, cannot be chosen by the control designer. Whenever the requirement on matrix A_{cl} is not satisfied, one can use more than five control actuators to ensure that the system of Eq.7.12 is stabilizable via output feedback. Furthermore, the requirement of

assumption 7.1 that the inverse of the operator S_u is necessary for the solution of the output feedback control problem, and clearly depends on the shape and location of the measurement sensors. However, this requirement does not appear to be restrictive from a practical standpoint (see numerical results in the next section). Finally, we note that the requirement $m = 5$ in theorem 7.1 is imposed to ensure stabilization of the closed-loop system even for values of ν for which $\mathcal{A}$ possesses four identical unstable eigenvalues; clearly, it is possible to achieve stabilization of the KSE with a smaller number of control actuators as long as the matrix A_{cl} is stable (see section 7.4 for such an example).

Remark 7.2: Even though the matrix A_{cl} of Eq.7.17 has infinite range, the fact that the eigenvalues of the matrix A_s grow in a fourth-order fashion in the left-half of the complex plane implies that there exists an N sufficiently large so that the verification of the stability of A_{cl} can be done on the basis of a finite-dimensional approximation obtained by keeping the first $(2l + 1 + 2N)$ rows and columns of A_{cl} (this fact is numerically verified in section 7.4). This means that the design of the gain matrix K which stabilizes the closed-loop system (Eqs.7.2-7.18) can be done on the basis of a $(2l + 1 + 2N)$-dimensional system utilizing standard pole-placement methods for static output feedback of finite-dimensional systems (see, for example, [20, Section 13.5] for details). This fact can be also rigorously established by using a singular perturbation formulation of the closed-loop system similar to the one employed in [42] to show stability of a parabolic PDE system under robust output feedback control. The details of this analysis are given in section G.2.

Remark 7.3: When the measurement sensor shape functions are chosen so that $S_u^{-1}S_s = 0$ (which implies that $\hat{\alpha}_u = \alpha_u$; state feedback case), the matrix A_{cl} of

Eq.7.17 simplifies to:

$$A_{cl} = \begin{bmatrix} A_u + B_u K & 0 \\ B_s K & A_s \end{bmatrix} \tag{7.19}$$

and the infinite-dimensional stabilizability requirement of theorem 7.1 reduces to the one of stability of the finite-dimensional matrix $A_u + B_u K$ (i.e., the pair $[A_u \ B_u]$ should be controllable).

Remark 7.4: On the other hand, when the distribution functions of the control actuators are chosen so that $B_s = 0$ (which implies that no spill-over [11] effect is present in the closed-loop system), the matrix A_{cl} of Eq.7.17 simplifies to:

$$A_{cl} = \begin{bmatrix} A_u + B_u K & B_u K S_u^{-1} S_s \\ 0 & A_s \end{bmatrix} \tag{7.20}$$

and the stabilizability requirement of theorem 7.1 again reduces to the one of stability of $A_u + B_u K$.

Remark 7.5: Even though static output feedback control requires a larger number of measurements ($2l+1$ versus m, with $m \leq 5$) for small values of ν and is more sensitive to measurement noise than dynamic output feedback, we prefer to use static feedback of y^m in the controller of Eq.7.18 because it allows us to globally exponentially stabilize the zero solution; this is not possible when linear finite-dimensional dynamic output feedback control is used [38].

Remark 7.6: The exponential stability of the closed-loop system ensures a certain degree of robustness with respect to sufficiently small disturbances and uncertainty in process parameters (i.e., ν, $b^n_{i\alpha}, b^n_{i\beta}, s_\kappa$), as well as robustness of the closed-loop system with respect to fast and asymptotically stable unmodeled dynamics (for example, actuator and sensor dynamics). The problem of designing robust controllers that explicitly account and compensate for the presence of uncertainty will not be addressed in this chapter; the reader may refer to [42] for results on robust control of

parabolic PDE systems.

Remark 7.7: We note that the proposed approach can be also employed to compute necessary and sufficient conditions for the global exponential stabilization of the zero solution of the KSE subject to non-periodic boundary conditions (such as the ones studied in [124]) via distributed static output feedback control.

Remark 7.8: Even though the proposed approach allows achieving *global* stabilization of the zero solution of the KSE, improved *local* convergence rates of the state of the closed-loop system to the zero solution can be achieved by utilizing nonlinear controllers constructed on the basis of ODE models obtained from combination of Galerkin's method with approximate inertial manifolds (see [6] for details and [26, 25, 155] for other applications of inertial manifold theory to control of nonlinear distributed parameter systems). Furthermore, it is important to note that the L_p^2 exponential convergence of $x(z,t)$ to the zero solution does not necessarily lead to pointwise convergence.

Remark 7.9: We note that the approach that we followed for controller synthesis based on finite-dimensional approximations of the Kuramoto-Sivashinsky equation obtained via Galerkin's method is motivated from the fact that the dominant dynamics of the equation are characterized by a finite (small) number of degrees of freedom. This approach has been successfully used to control parabolic PDEs arising in the context of transport-reaction processes (see, for example, [11, 48, 49, 27]).

7.4 Numerical results

In this section, we evaluate, through computer simulations, the ability of the output feedback controller of Eq.7.18 to stabilize the system of Eqs.7.2-7.3 at the steady

state $x(z,t) = 0$. Two simulation runs were performed for $\nu = 0.4$ and 0.2. For the numerical simulation of the KSE, we used a 51-order nonlinear ordinary differential equation model obtained from the application of Galerkin's method to the system of Eq.7.2 (the use of higher-order Galerkin approximations in simulating the open-loop system of Eqs.7.2-7.3 as well as the closed-loop system led to identical numerical results). In all the simulation runs, the system is assumed to be at a spatially non-uniform initial condition, $x_0 = \frac{1.0}{\sqrt{2\pi}} + \frac{2.5}{\sqrt{\pi}}\sum_{n=1}^{5}(sin(n\,z) + cos(n\,z)) \in L_p^2([-\pi,\pi])$.

In the first simulation run, we set $\nu = 0.4$ which implies that the linearized system of Eq.7.5 possesses two identical eigenvalues in the right half of the complex plane. Therefore, the use of three control actuators and three measurement sensors is necessary and sufficient for achieving stabilization of the closed-loop system. One distributed control actuator with $b_1(z) = \frac{1}{\sqrt{2\pi}}$, two point control actuators placed at $z = -\frac{\pi}{2}$ and $z = \frac{\pi}{6}$ (i.e., $b_2(z) = \delta(z+\frac{\pi}{2})$ and $b_3(z) = \delta(z-\frac{\pi}{6})$), one distributed sensor with $s_1(z) = \frac{1}{\sqrt{2\pi}}$ and two point measurement sensors placed at $z = 0.0$ and $z = -\frac{\pi}{4}$ (i.e., sensor shape functions $s_2(z) = \delta(z-0.0)$, $s_3(z) = \delta(z+\frac{\pi}{4})$) are used to stabilize the system of Eqs.7.2-7.3 at $x(z,t) = 0$. The control actions, $u_1(t), u_2(t), u_3(t)$, were computed from the formula of Eq.7.18 with:

$$K = \begin{bmatrix} -4.000 & -2.404 & 4.163 \\ 0.000 & 6.026 & -3.478 \\ 0.000 & 0.000 & -6.958 \end{bmatrix} \tag{7.21}$$

to ensure that the matrix A_{cl} is stable. Figure 7.1 shows the closed-loop spatio-temporal profile of $x(z,t)$ and the profiles of the three manipulated inputs. It is clear that the controller stabilizes the state of the system at $x(z,t) = 0$, indicating that the use of three control control actuators suffices to stabilize the system for $\nu = 0.4$.

In the second simulation run, we used $\nu = 0.2$ which implies that the linearized system of Eq.7.5 possesses four identical unstable eigenvalues (i.e., $\mu_1 = \mu_2 = 0.8$; both μ_1, μ_2 are eigenvalues of multiplicity 2), thus requiring five control actuators

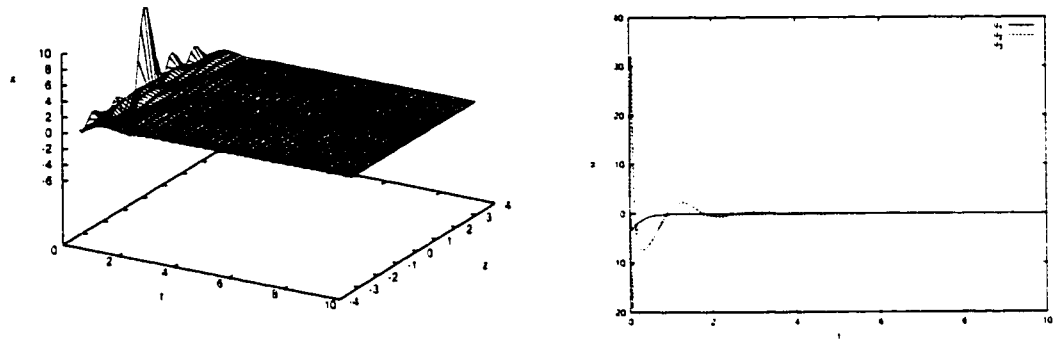

Figure 7.1: Closed-loop spatio-temporal profile of $x(z,t)$ (left figure) and manipulated input profiles (right figure), for $\nu = 0.4$.

and five measurement sensors of $x(z,t)$ to stabilize the system at $x(z,t) = 0$. One distributed control actuator with $b_1(z) = \frac{1}{\sqrt{2\pi}}$, four point control actuators placed at $z = \frac{\pi}{2}$, $z = \frac{\pi}{6}$, $z = -\frac{\pi}{4}$ and $z = -\frac{\pi}{2}$, (i.e., $b_2(z) = \delta(z - \frac{\pi}{2})$, $b_3(z) = \delta(z - \frac{\pi}{6})$, $b_4(z) = \delta(z + \frac{\pi}{4})$ and $b_5(z) = \delta(z + \frac{\pi}{2})$), one distributed measurement sensor with $s_1(z) = \frac{1}{\sqrt{2\pi}}$ and four point measurement sensors placed at $z = \frac{\pi}{6}$, $z = \frac{\pi}{4}$, $z = -\frac{\pi}{4}$ and $z = -\frac{\pi}{2}$, (i.e., $s_2(z) = \delta(z - \frac{\pi}{6})$, $s_3(z) = \delta(z - \frac{\pi}{4})$, $s_4(z) = \delta(z + \frac{\pi}{4})$ and $s_5(z) = \delta(z + \frac{\pi}{2})$) are used to stabilize the system at $x(z,t) = 0$. The control actions, $u_1(t), u_2(t), u_3(t), u_4(t), u_5(t)$, were computed from the formula of Eq.7.18 with:

$$K = \begin{bmatrix} -4.000 & 0.000 & 3.621 & 0.298 & -2.263 \\ 0.000 & -2.836 & -1.175 & 1.175 & 2.836 \\ 0.000 & 0.000 & -3.836 & -2.713 & 0.000 \\ 0.000 & 0.000 & -3.322 & 3.323 & 0.000 \\ 0.000 & 2.836 & -0.744 & -2.531 & 2.836 \end{bmatrix} \tag{7.22}$$

to ensure that the matrix A_{cl} is stable. The closed-loop profile of $x(z,t)$ and the profiles of the five manipulated inputs are displayed in Figure 7.2. The stabilization of the state of the system at $x(z,t) = 0$, for $\nu = 0.2$, has been accomplished.

From the results of the simulation study, it is evident that the proposed control algorithm achieves stabilization of the Kuramoto-Sivashinsky equation at $x(z,t) = 0$

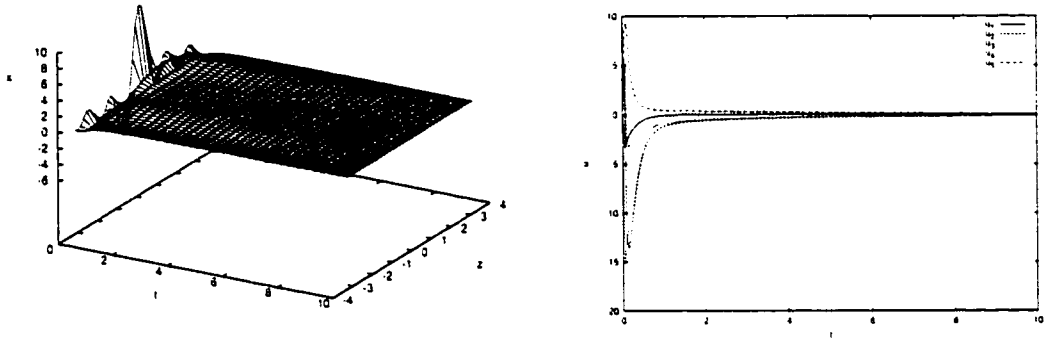

Figure 7.2: Closed-loop spatio-temporal profile of $x(z,t)$ (left figure) and manipulated input profiles (right figure), for $\nu = 0.2$.

for values of ν for which the zero solution is unstable.

7.5 Conclusions

In this chapter, we have considered the problem of global exponential stabilization of the zero solution, $x(z,t) = 0$, of the Kuramoto-Sivashinsky Equation (KSE) with periodic boundary conditions, for any value of the instability parameter ν, via distributed static output feedback control. Under the assumptions that the number of measurements is equal to the total number of unstable and critically stable eigenvalues of the KSE and a necessary and sufficient stability condition is satisfied, linear static output feedback controllers are designed that achieve global (i.e., for every initial condition) stabilization of the $x(z,t) = 0$ solution of Eq.7.1. The proposed output feedback controllers are designed on the basis of ODE approximations of the KSE obtained through Galerkin's method. The theoretical results were confirmed by computer simulations of the closed-loop system for different values of the instability parameter.

Chapter 8

Bounded Output Feedback Control of the Kuramoto-Sivashinsky Equation with Input Constraints

8.1 Introduction

In Chapter 6 we presented a method for the synthesis of nonlinear finite-dimensional output feedback controllers that locally stabilize the zero solution of the Kuramoto-Sivashinsky Equation (KSE) on the basis of ordinary differential equation (ODE) approximations, obtained through and nonlinear [6] Galerkin's method. The global stabilization of the KSE was subsequently addressed in Chapter 7 via distributed static output feedback control.

Even though the above designs allow the systematic design of practically implementable nonlinear controllers for the KS, they do not deal with the problem of constraints in the capacity of the control actuators. Input constraints may restrict

our ability to freely modify the dynamic behavior of a dynamical system and may lead to sluggishness of response, oscillations, and loss of stability if they are not accounted for in the controller design. Results on control of systems with input constraints include controller design and stability analysis within the model predictive control framework (e.g., [145]), constrained nonlinear optimal control (e.g., [67]), and the design of "anti-windup" schemes (e.g., [110, 105]).

In this chapter, we consider the problem of stabilization of the zero solution, $U(z,t) = 0$, of the KSE with periodic boundary conditions using constrained control action. Initially, finite-dimensional Galerkin approximations of the KSE which capture the dominant dynamics of the equation for a given value of the instability parameter are derived. These finite-dimensional systems are used for the synthesis of bounded nonlinear stabilizing controllers which explicitly account for the input constraints. An explicit characterization of the limitations imposed by the input constraints on the allowable control actuator locations is provided. The theoretical results are successfully illustrated through computer simulations of the closed-loop system using a high-order discretization of the KSE.

8.2 Preliminaries

We consider the one-dimensional KSE with distributed control:

$$\begin{aligned} \frac{\partial U}{\partial t} &= -\nu\frac{\partial^4 U}{\partial z^4} - \frac{\partial^2 U}{\partial z^2} - U\frac{\partial U}{\partial z} + \sum_{i=1}^{l} b_i u_i(t) \\ y_c^i &= \int_{-\pi}^{\pi} c_i(z) U dz, \; i = 1, \ldots, l \\ y_m^\kappa &= \int_{-\pi}^{\pi} s_\kappa(z) U dz, \; \kappa = 1, \ldots, p \end{aligned} \tag{8.1}$$

subject to the periodic boundary conditions:

$$\frac{\partial^j U}{\partial z^j}(-\pi, t) = \frac{\partial^j U}{\partial z^j}(+\pi, t), \quad j = 0, \ldots, 3 \tag{8.2}$$

and the initial condition:

$$U(z,0) = U_0(z) \tag{8.3}$$

where $U(z,t)$ is the state of the system, $z \in [-\pi, \pi]$ is the spatial coordinate, t is the time and 2π is the length of the spatial domain, $\nu > 0$ is the instability parameter, and $U_0(z)$ is the initial condition. $u_i \in [u_{i,min}, u_{i,max}] \subset \mathbb{R}$ denotes the i-th constrained manipulated input, l is the total number of manipulated inputs, $b_i(z)$ is the i-th actuator distribution function (i.e., $b_i(z)$ determines how the control action computed by the i-th control actuator, $u_i(t)$, is distributed (e.g., point or distributed actuation) in the spatial interval $[-\pi, \pi]$), y_c^i denotes a controlled output, $c_i(z)$ is a known smooth function of z which is determined by the desired stability/performance specifications, $y_m^\kappa \in \mathbb{R}$ denotes a measured output, and $s_\kappa(z)$ is a known smooth function of z which is determined by the location and type of the measurement sensors (e.g., point/distributed sensing). We note that whenever the control action enters the system at a single point z_0, with $z_0 \in [-\pi, \pi]$ (i.e. point actuation), the function $b_i(z)$ is taken to be nonzero in a finite spatial interval of the form $[z_0 - \epsilon, z_0 + \epsilon]$, where ϵ is a small positive real number, and zero elsewhere in $[-\pi, \pi]$. We will use the order of magnitude notation $O(\epsilon)$. In particular, $\delta(\epsilon) = O(\epsilon)$ if there exist positive real numbers k_1 and k_2 such that: $|\delta(\epsilon)| \leq k_1|\epsilon|$, $\forall\, |\epsilon| < k_2$.

To present our theoretical results, we formulate the system of Eq.8.1 as an infinite dimensional system in the Hilbert space $\mathcal{H}([-\pi, \pi]; \mathbb{R})$, with $\mathcal{H}$ being the space of vector functions defined on $[-\pi, \pi]$ that satisfy the boundary condition of Eq.8.2, with inner product and norm:

$$(\omega_1, \omega_2) = \int_{-\pi}^{\pi} (\omega_1(z), \omega_2(z))_{\mathbb{R}} dz, \; ||\omega_1||_2 = (\omega_1, \omega_1)^{\frac{1}{2}} \tag{8.4}$$

where ω_1, ω_2 are two elements of $\mathcal{H}([-\pi, \pi]; \mathbb{R})$ and the notation $(\cdot, \cdot)_{\mathbb{R}}$ denotes the

standard inner product in $\mathbb{R}$. Defining the state function x on $\mathcal{H}([-\pi,\pi];\mathbb{R})$ as:

$$x(t) = U(z,t), \quad t > 0, \quad z \in [-\pi,\pi], \tag{8.5}$$

the operator $\mathcal{A}$ in $\mathcal{H}([-\pi,\pi];\mathbb{R})$ as:

$$\begin{aligned} &\mathcal{A}x = -\nu\frac{\partial^4 U}{\partial z^4} - \frac{\partial^2 U}{\partial z^2} \\ &x \in D(\mathcal{A}) = \{x \in \mathcal{H}([-\pi,\pi];\mathbb{R}) : \\ &\left.\frac{\partial^j U}{\partial z^j}(-\pi,t) = \frac{\partial^j U}{\partial z^j}(+\pi,t), \quad j = 0,\ldots,3\right\} \end{aligned} \tag{8.6}$$

and the input, controlled output, and measured output operators as:

$$\mathcal{B}u = \sum_{i=1}^{m} b_i u_i, \quad \mathcal{C}x = (c, kx), \quad \mathcal{S}x = (s, \omega x) \tag{8.7}$$

the system of Eqs.8.1-8.2-8.3 takes the form:

$$\begin{aligned} \dot{x} &= \mathcal{A}x + \mathcal{B}u + f(x), \quad x(0) = x_0 \\ y_c &= \mathcal{C}x, \quad y_m = \mathcal{S}x \end{aligned} \tag{8.8}$$

where $f(x(t)) = -U\dfrac{\partial U}{\partial z}$ and $x_0 = U_0(z)$.

To formulate our assumptions on the properties of $\mathcal{A}$, we consider the following eigenvalue problem:

$$\mathcal{A}\phi_n = -\nu\frac{\partial^4 \phi_n}{\partial z^4} - \frac{\partial^2 \phi_n}{\partial z^2} = \lambda_n \phi_n, \quad n = 1,\ldots,\infty \tag{8.9}$$

subject to:

$$\frac{\partial^j \phi_n}{\partial z^j}(-\pi) = \frac{\partial^j \phi_n}{\partial z^j}(+\pi), \quad j = 0,\ldots,3 \tag{8.10}$$

where λ_n denotes an eigenvalue and ϕ_n denotes an eigenfunction. A direct computation of the solution of the above eigenvalue problem yields $\lambda_0 = 0$ with $\psi_0(z) = \dfrac{1}{\sqrt{2\pi}}$, and $\lambda_n = -\nu n^4 + n^2$ (λ_n is an eigenvalue of multiplicity two) with eigenfunctions $\phi_n(z) = \dfrac{1}{\sqrt{\pi}}\sin(nz)$ and $\psi_n(z) = \dfrac{1}{\sqrt{\pi}}\cos(nz)$ for $n = 1,\ldots,\infty$. We also define the eigenspectrum of $\mathcal{A}$, $\sigma(\mathcal{A})$, as the set of all eigenvalues of $\mathcal{A}$, i.e. $\sigma(\mathcal{A}) = \{\lambda_1, \lambda_2, \ldots,\}$. From the expression for the eigenvalues, it follows that for a fixed value of $\nu > 0$ the

number of unstable eigenvalues of $\mathcal{A}$ is finite and the distance between two consecutive eigenvalues increases as n increases. This implies that for a fixed value of ν, the dominant dynamics of the KSE can be described by a finite-dimensional system and motivates considering infinite-dimensional systems of the form of Eq.8.8 for which $\mathcal{A}$ satisfies the following assumption.

Assumption 8.1:

1. $Re\{\lambda_1\} \geq Re\{\lambda_2\} \geq \cdots \geq Re\{\lambda_j\} \geq \cdots$, *where* $Re\{\lambda_j\}$ *denotes the real part of* λ_j.

2. $\sigma(\mathcal{A})$ *can be partitioned as* $\sigma(\mathcal{A}) = \sigma_1(\mathcal{A}) + \sigma_2(\mathcal{A})$, *where* $\sigma_1(\mathcal{A})$ *consists of the first* m *(with* m *finite) eigenvalues, i.e.* $\sigma_1(\mathcal{A}) = \{\lambda_1, \ldots, \lambda_m\}$, *and* $\dfrac{|Re\{\lambda_1\}|}{|Re\{\lambda_m\}|} = O(1)$.

3. $Re\{\lambda_{m+1}\} < 0$ *and* $\dfrac{|Re\{\lambda_m\}|}{|Re\{\lambda_{m+1}\}|} = O(\epsilon)$ *where* $\epsilon < 1$ *is a small positive number.*

Remark 8.1: Referring to Eq.8.1, we note that the value of the parameter ν determines the stability of the zero solution and significantly affects the overall dynamic behavior of the KSE. To make this point clear, we compute the linearization of the system of Eq.8.8 around $x(t) = 0$, which takes the form:

$$\dot{x} = \mathcal{A}x \tag{8.11}$$

Clearly, a pair of eigenvalues of the system of Eq.8.11 crosses the imaginary axis when:

$$\nu = \frac{1}{n^2}, \quad n = 1, \ldots, \infty \tag{8.12}$$

Apparently, the smallest value of ν, for which the $x(z,t) = 0$ solution of the system of Eq.8.11 is about to become unstable is $\nu = 1$. This implies that the spatially uniform steady-state, $U(z,t) = 0$, of the nonlinear system of Eqs.8.1-8.2 is locally

unstable when $\nu < 1$. Instead, there is a generation of *stable* spatially non-uniform stationary solutions as well as spatially non-uniform periodic solutions, while for very small values of ν no stable solutions exist and the system of Eq.8.1 exhibits chaotic behavior (the reader may refer to [36, 106] for detailed characterizations of the solution patterns for various ranges of values of ν).

8.3 Galerkin's method

In this section, we apply standard Galerkin's method to the system of Eq.8.8 to derive an approximate finite-dimensional system. Let $\mathcal{H}_s$, $\mathcal{H}_f$ be modal subspaces of $\mathcal{A}$, defined as $\mathcal{H}_s = span\{\phi_1, \phi_2, \ldots, \phi_m\}$ and $\mathcal{H}_f = span\{\phi_{m+1}, \phi_{m+2}, \ldots,\}$ (the existence of $\mathcal{H}_s$, $\mathcal{H}_f$ follows from assumption 8.1). Defining the orthogonal projection operators P_s and P_f such that $x_s = P_s x$, $x_f = P_f x$, the state x of the system of Eq.8.8 can be decomposed as:

$$x = x_s + x_f = P_s x + P_f x \tag{8.13}$$

Applying P_s and P_f to the system of Eq.8.8 and using the above decomposition for x, the system of Eq.8.8 can be equivalently written in the following form:

$$\begin{aligned}
\frac{dx_s}{dt} &= \mathcal{A}_s x_s + \mathcal{B}_s u + f_s(x_s, x_f) \\
\frac{\partial x_f}{\partial t} &= \mathcal{A}_f x_f + \mathcal{B}_f u + f_f(x_s, x_f) \\
y_c &= \mathcal{C} x_s + \mathcal{C} x_f, \qquad y_m = \mathcal{S} x_s + \mathcal{S} x_f, \\
x_s(0) &= P_s x(0) = P_s x_0, \\
x_f(0) &= P_f x(0) = P_f x_0
\end{aligned} \tag{8.14}$$

where $\mathcal{A}_s = P_s\mathcal{A}$, $\mathcal{B}_s = P_s\mathcal{B}$, $f_s = P_s f$, $\mathcal{A}_f = P_f\mathcal{A}$, $\mathcal{B}_f = P_f\mathcal{B}$ and $f_f = P_f f$ and the notation $\frac{\partial x_f}{\partial t}$ is used to denote that the state x_f belongs in an infinite-dimensional space. In the above system, $\mathcal{A}_s$ is a diagonal matrix of dimension $m \times m$ of the form $\mathcal{A}_s = diag\{\lambda_j\}$, $f_s(x_s, x_f)$ and $f_f(x_s, x_f)$ are Lipschitz vector functions, and $\mathcal{A}_f$ is an unbounded differential operator which is exponentially stable (following from part 3

of assumption 8.1 and the selection of $\mathcal{H}_s, \mathcal{H}_f$). Neglecting the fast and stable infinite-dimensional x_f-subsystem in the system of Eq.8.14, the following m-dimensional slow system is obtained:

$$\begin{aligned} \frac{d\bar{x}_s}{dt} &= \mathcal{A}_s\bar{x}_s + \mathcal{B}_s u + f_s(\bar{x}_s, 0) \\ \bar{y}_c &= \mathcal{C}\bar{x}_s, \qquad \bar{y}_m = \mathcal{S}\bar{x}_s \end{aligned} \tag{8.15}$$

where the bar symbol in $\bar{x}_s$, $\bar{y}_c$ and $\bar{y}_m$ denotes that these variables are associated with a finite-dimensional system.

Remark 8.2: We note that the above model reduction procedure which led to the approximate ODE system of Eq.8.14 can also be used, when empirical eigenfunctions of the system of Eq.8.8 computed through Karhunen-Loéve expansion (see [40] for details) are used as basis functions in $\mathcal{H}_s$ and $\mathcal{H}_f$ instead of the eigenfunctions of $\mathcal{A}$.

8.4 Bounded output feedback control

In this section, we use the m-dimensional slow system of Eq.8.15 as a basis for the synthesis of bounded output feedback controllers that stabilize the system of Eqs.8.8 at $x(z,t) = 0$.

To achieve our objective, we initially synthesize, using Lyapunov-based techniques (see [67] for details), bounded nonlinear state feedback controllers of the general form

$$u = p(\bar{x}_s, \bar{v}, u_{max}) \tag{8.16}$$

where $p(\bar{x}_s, \bar{v}, u_{max})$ is a bounded vector function (i.e., $|u| \leq u_{max}$ where $|\cdot|$ is the Euclidean norm) and $\bar{v}$ is a vector of the form $\bar{v} = \mathcal{V}(v_i, v_i^{(1)}, \ldots, v_i^{(r_i)})$ where $\mathcal{V}(v_i, v_i^{(1)}, \ldots, v_i^{(r_i)})$ is a smooth vector function, $v_i^{(k)}$ is the k^{th} time derivative of the external reference input v_i (which is assumed to be a smooth function of time) and r_i is the relative order of the output y_{ci} with respect to the vector of manipulated inputs.

The controller enforces asymptotic (and locally exponential) stability and reference input tracking in the infinite-dimensional closed-loop system in the presence of active input constraints. We also provide an explicit characterization of the region in state-space where the aforementioned properties are guaranteed to hold. To implement the bounded nonlinear controller using output measurements only, we need to impose the following assumption needed to obtain estimates of the states $\bar{x}_s$ of the system of Eq.8.8 from the measurements y_m^κ, $\kappa = 1, \ldots, p$.

Assumption 8.2: *p=m (i.e., the number of measurements is equal to the number of eigenvalues which belong to $\sigma_1(\mathcal{A})$), and the inverse of the operator S exists so that $\hat{x}_s = S^{-1} y_m$, where $\hat{x}_s$ is an estimate of x_s.*

To present the controller formula in theorem 8.1 below, we will need to transform the system of Eq.8.15 into the following partially linear form

$$\begin{aligned} \dot{e} &= Fe + K\left[l(\bar{x}_s) + C(\bar{x}_s)u\right] \\ \dot{\eta}_1 &= \Psi_1(e, \eta, \bar{v}) \\ &\vdots \\ \dot{\eta}_{n-\sum_i r_i} &= \Psi_{n-\sum_i r_i}(e, \eta, \bar{v}) \\ \bar{y}_{ci} &= e_1^{(i)} + v_i, \quad i = 1, \ldots, m \end{aligned} \tag{8.17}$$

where e is an $\sum_i r_i \times 1$ vector of the tracking error, F, K are constant matrices, $l(\bar{x}_s)$ is a vector function whose specific form is omitted for brevity, and $C(\bar{x}_s)$ is the characteristic matrix of the system of Eq.8.15. To simplify notation, we further define $\bar{f}(e, \eta, \bar{v}) = Fe + Kl(\bar{x}_s)$ and $\bar{G}(\bar{x}_s) = KC(\bar{x}_s)$.

Theorem 8.1 below provides an explicit synthesis formula of the output feedback control law and conditions that guarantee closed-loop stability and asymptotic output tracking. The proof is presented in Appendix H.

Theorem 8.1: *Consider the system of Eq.8.15 and assume that:* 1) *its characteristic matrix, $C(\bar{x}_s)$, is nonsingular $\forall\ \bar{x}_s \in D \subset \mathbb{R}^m$, and* 2) *the η-subsystem of Eq.8.17*

is input-to-state stable with respect to e and $\bar{v}$ and locally exponentially stable when $e = 0$. Finally, consider the dissipative PDE system of Eq.8.1, for which assumptions 8.1 and 8.2 hold, under the nonlinear output feedback controller

$$\begin{aligned} u &= -\frac{1}{2}R^{-1}(\hat{x}_s)\left(L_{\bar{g}}V\right)^T \\ \hat{x}_s &= S^{-1}y_m, \end{aligned} \tag{8.18}$$

where

$$R^{-1}(\hat{x}_s) = \frac{L_{\bar{f}}^* V + \sqrt{(L_{\bar{f}}^* V)^2 + \left(u_{max}^2 (L_{\bar{g}}V)(L_{\bar{g}}V)^T\right)^2}}{(L_{\bar{g}}V)(L_{\bar{g}}V)^T\left[1 + \sqrt{1 + u_{max}^2 (L_{\bar{g}}V)(L_{\bar{g}}V)^T}\right]}$$

$L_{\bar{f}}^* V = L_{\bar{f}}V + \rho|e|^2$, $\rho > 0$, $L_{\bar{g}}V = [L_{\bar{g}_1}V \cdots L_{\bar{g}_m}V]$, $\bar{g}_i$ is the i-the column of $\bar{G}$, $V = e^T\Phi e$, Φ is a positive definite matrix that satisfies the Riccati inequality $F^T\Phi + \Phi F - \Phi K K^T \Phi < 0$. Then given any positive real number δ_s such that

$$L_{\bar{f}}^* V \leq u_{max}|L_{\bar{g}}V| \tag{8.19}$$

for $|x_s| \leq \delta_s$ and given any positive real numbers δ_f, δ_v there exists $\epsilon^* > 0$ such that if $\epsilon \in (0, \epsilon^*]$, $|x_s(0)| < \delta_s$, $||x_f(0)||_2 < \delta_f$, $||v||_2 < \delta_v$, then the infinite-dimensional closed-loop system is asymptotically stable and locally exponentially stable and $\limsup_{t\to\infty} |y_c^i - v_i| = O(\epsilon)$.

Remark 8.3: For constrained nonlinear systems of the form of Eq.8.15, it was shown in [67] that Eq.8.19 describes the region of feasible initial states, starting from which, the desired closed-loop ODE system properties are guaranteed in the presence of input constraints. Owing to the dependence of $\mathcal{B}_s$ on the actuator location, however, this region becomes now parameterized by the actuator locations and can be used to explicitly identify the admissible locations that can be used to guarantee stability in the presence of constraints. Finally, note that, according to theorem 1, this region is practically preserved for the full PDE system in the sense that given *any* compact subset of the region described by Eq.8.19, one can always find an ϵ sufficiently small

such that the statements of theorem 1 hold.

Remark 8.4: We note that the controller of Eq.8.18 uses static feedback of the measured outputs y_m^κ, $\kappa = 1, \ldots, p$, and thus, it feeds back both x_s and x_f (this is in contrast to the bounded state feedback control [66] which only uses feedback of the slow state x_s). However, even though the use of x_f feedback could lead to destabilization of the stable fast subsystem, the large separation of the slow and fast modes of the spatial differential operator (i.e., assumption that ϵ is sufficiently small) and the fact that the controller does not include terms of the form $O(1/\epsilon)$ do not allow such a destabilization to occur.

8.5 Numerical results

In this section, we present through computer simulations, the ability of the output feedback controller of Eq.8.18 to stabilize the system of Eqs.8.1-8.2 at the steady state $x(z,t) = 0$ using constrained control action and compute an explicit characterization of the region in state-space where the stability is guaranteed to hold. In order to better present our theoretical results, we will consider the KSE in the space of odd functions with spatial zero mean. Introducing the Hilbert space $\mathcal{H}$ of square integrable odd functions that satisfy the boundary conditions of Eq.8.2 and have spatial zero mean (i.e., $\forall\, \omega \in \mathcal{H}$, $\int_{-\pi}^{\pi} \omega(z)dz = 0$) and defining the state function $x \in \mathcal{H}$ as:

$$x(t) = U(z,t), \quad \forall\, z \in [-\pi, \pi], \tag{8.20}$$

the system of Eqs.8.1-8.3 can be written in the form of Eq.8.8, where the domain of definition of the spatial differential operator $\mathcal{A}$ now takes the form:

$$\begin{aligned} x \in D(\mathcal{A}) = \Big\{ & x \in \mathcal{H}([-\pi, \pi]; \mathbb{R}); \\ & \frac{\partial^j x}{\partial z^j}(-\pi) = \frac{\partial^j x}{\partial z^j}(\pi), \quad j = 0, \ldots, 3 \Big\} \end{aligned} \tag{8.21}$$

and the eigenvalue problem for $\mathcal{A}$ yields $\lambda_j = -\nu j^4 + j^2$, $\phi_j(z) = \sqrt{\frac{1}{\pi}} sin(jz)$, $j = 1, \ldots, \infty$ (note that $\phi_j(z) = \sqrt{\frac{1}{2\pi}}$ and $\phi_j(z) = \sqrt{\frac{1}{\pi}} cos(jz)$, $j = 1, \ldots, \infty$ are not considered here since we focus only on odd functions with spatial zero mean).

All the simulation runs shown below were performed for $\nu = 0.3$ and for initial conditions of the form

$$U_0(z) = E_0 \sum_{j=1}^{4} [sin(j\ z)], \tag{8.22}$$

where E_0 is a positive constant to be defined below, using a 20-order nonlinear ordinary differential equation model obtained from the application of Galerkin's method to the system of Eq.8.1 (the use of higher-order Galerkin approximations led to identical numerical results, thereby implying that the following simulation runs are independent of the discretization).

Linearizing the system around the spatially uniform steady-state for $\nu = 0.3$, we observe that the system of Eq.8.8 possesses one unstable eigenvalue. The spatiotemporal evolution of $U(z,t)$ for $\nu = 0.3$ is shown in Figure 8.1, for the initial condition $U_0(z) = 1.35 \sum_{j=1}^{4} [sin(j\ z)]$. It is clear that for $\nu = 0.3$, the spatially uniform steady-

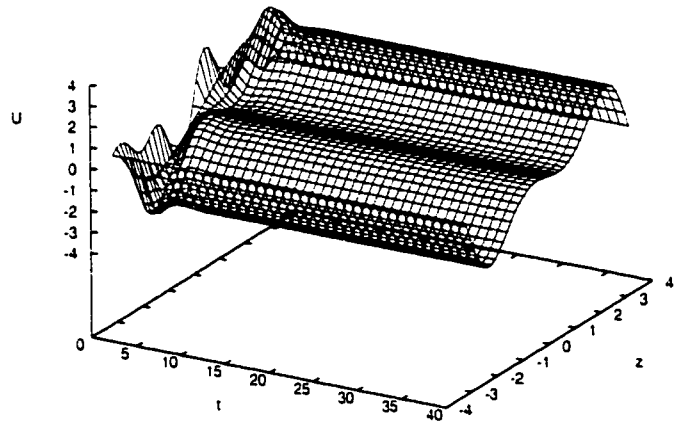

Figure 8.1: Open-loop spatiotemporal profile of $U(z,t)$ for $\nu = 0.3$ and $E_0 = 1.35$.

state $U(z,t) = 0$ is unstable. Therefore, we use the proposed method to design a nonlinear finite-dimensional controller which uses one measurement of $U(z,t)$ at $z_c = -\pi/2$ to stabilize the system at $U(z,t) = 0$, for $\nu = 0.3$ and maximum available control action of $u_{max} = 1.3$ (i.e., $|u| \leq 1.3$). To achieve this control objective, the controlled output is defined as:

$$y_c(t) = \int_{-\pi}^{\pi} \sqrt{\frac{1}{\pi}} sin(z) U(z,t) dz \tag{8.23}$$

and the actuator distribution function is taken to be $b_1(z) = \delta(z - z_c)$ (i.e., point control actuation at $z = z_c$). Standard Galerkin's method was initially used to derive the following first-order model,

$$\dot{x} = (-\nu + 1)x + \phi_1(z_c)u, \tag{8.24}$$

which was employed for the synthesis of a nonlinear controller using the formula of Eq.8.18.

Initially, we use the inequality of Eq.8.19 to explicitly characterize the limitations imposed by input constraints on the allowable control actuator locations that can be used to achieve stabilization starting from a given initial condition. The region of

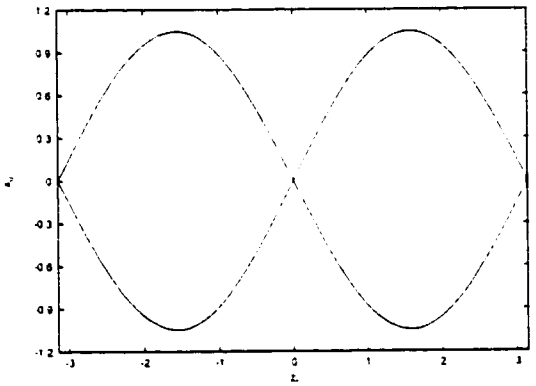

Figure 8.2: Region of guaranteed stability for $\nu = 0.3$ and $u_{max} = 1.3$.

guaranteed closed-loop stability can be computed analytically for this example and

Figure 8.2 depicts how the set of feasible initial conditions for the first eigenmode (ordinate) varies as a function of actuator location when $u_{max} = 1.3$. In this plot, the set of values between the two curves at a given location represent the set of feasible initial conditions at that location. We observe that the size of this set increases at the controller actuator locations $-\pi/2$ and $\pi/2$ and diminishes at $-\pi$, 0 and π, as expected owing to the shape of the first eigenfunction. Alternatively, Figure 8.2 can be used to determine, for a fixed initial condition, where the actuator can be placed to guarantee the closed-loop stability in the presence of the input constraints. Figure 8.3 shows the evolution of U and Figure 8.4 shows the manipulated input profile under the controller of Eq.8.18 when the actuator is placed at $z_c = 0.5\pi$ and the initial state is at $E_0 = 0.75$. For this initial condition, the location $z_c = 0.5\pi$ is an admissible one

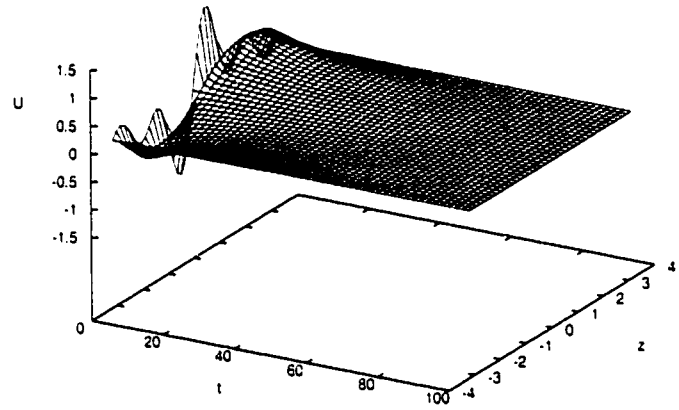

Figure 8.3: Closed-loop spatio-temporal profile of $U(z,t)$ for $E_0 = 0.75$ and $z_c = 0.5\pi$.

when $u_{max} = 1.3$ (see Figure 8.2). Clearly, the controller successfully stabilizes the KSE at $U(z,t) = 0$, as can also be seen by the controlled output profile (shown in Figure 8.7 with a dashed line).

We also tested the ability of the controller to stabilize the KSE when the initial condition, for a given actuator location, falls outside the region of guaranteed closed-

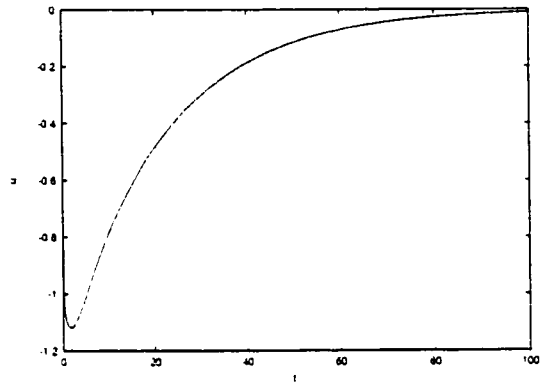

Figure 8.4: Manipulated input profile for $E_0 = 0.75$ and $z_c = 0.5\pi$.

loop stability. Figure 8.5 shows the evolution of U when the actuator is placed at $z_c = 0.5\pi$ and the initial state is at $E_0 = 1.35$, while Figure 8.6 shows the evolution of U when the actuator is placed at $z_c = 0.1\pi$ and the initial state is at $E_0 = 0.75$. We observe that in both cases the controller is unable to stabilize the system at the

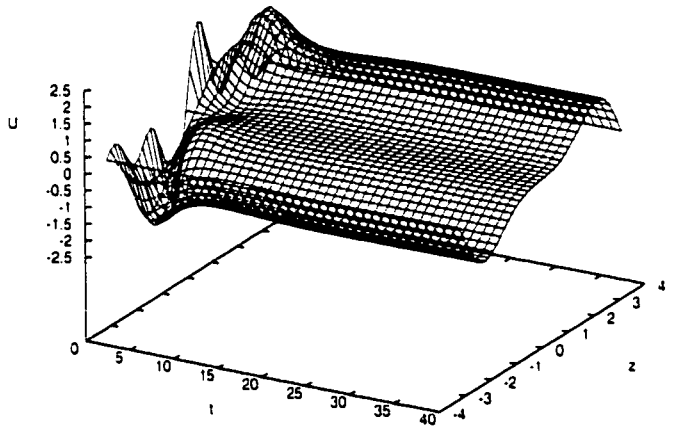

Figure 8.5: Closed-loop spatio-temporal profile of $U(z,t)$ for $E_0 = 1.35$ and $z_c = 0.5\pi$.

desired steady-state and the system moves to a spatially non-uniform steady-state. This can also be seen in Figure 8.7 which presents the controlled output profiles when the actuator is placed at $z_c = 0.5\pi$ and the initial state is at $E_0 = 1.35$ (solid line) and when the actuator is placed at $z_c = 0.1\pi$ and the initial state is at $E_0 = 0.75$

(dotted line).

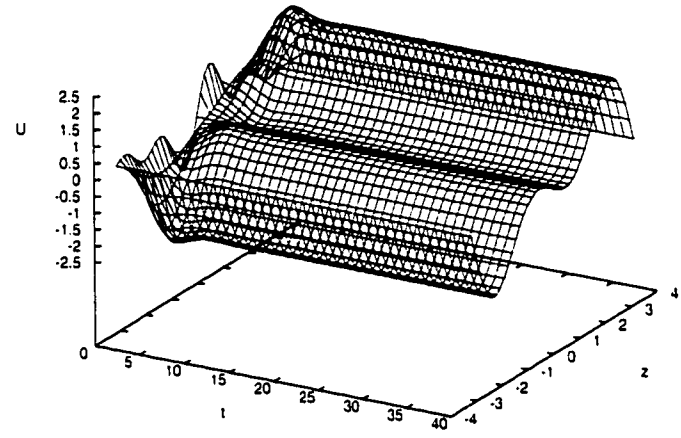

Figure 8.6: Closed-loop spatio-temporal profile of $U(z,t)$ for $E_0 = 0.75$ and $z_c = 0.1\pi$.

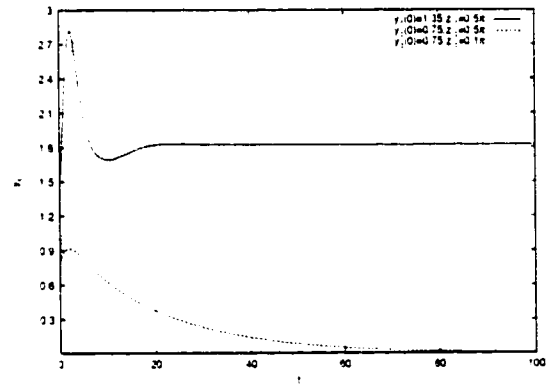

Figure 8.7: Controlled variable for $E_0 = 1.35$ and $z_c = 0.5\pi$ (solid line), $E_0 = 0.75$ and $z_c = 0.5\pi$ (dashed line), $E_0 = 0.75$ and $z_c = 0.1\pi$ (dotted line).

8.6 Conclusions

In this chapter, we developed a method for the synthesis of bounded nonlinear controllers that address the issue of stabilization of the zero solution, $U(z,t) = 0$, of the KSE with periodic boundary conditions in the presence of limitations in the capacity of the control actuators Initially, finite-dimensional Galerkin approximations of the

KSE which capture the dominant dynamics of the KSE for a given value of the instability parameter were derived. These finite-dimensional systems were subsequently used for the synthesis of bounded nonlinear stabilizing controllers which explicitly account for the input constraints. The developed method also provided with an explicit characterization of the limitations imposed by the input constraints on the allowable control actuator locations.

Chapter 9

Plasma Enhanced Chemical Vapor Deposition: Modeling and Control

9.1 Introduction

Single-wafer plasma-enhanced chemical vapor deposition (PECVD) is an emerging technology used in microelectronics industry to deposit thin films of compounds (e.g. amorphous silicon, silicon nitride, etc.) on substrates. In a PECVD process, the activation of the reacting gases is achieved through impact with electrons. This is in contrast to conventional chemical vapor deposition where the reacting gases are activated thermally. The main advantage of plasma assisted activation of the reacting gases is that low operational temperatures (compared to the ones required in conventional chemical vapor deposition processes) are achieved, thereby allowing the deposition of high-temperature sensitive films. An additional advantage of PECVD processes is the relatively high deposition rate which results in a significant reduction in the processing time; a very important benefit for single wafer processing. The ability to treat devices that are sensitive to heating and the high deposition rate make PECVD an attractive alternative over conventional furnace-based chemical vapor de-

position processes employed in the fabrication of devices with submicron dimensional constraints. However, at this stage, the widespread use of PECVD is seriously limited by the significant spatial nonuniformity of the deposition rate which, in many cases, violates the tight requirements set by the industry.

The design and operation of PECVD processes that achieve the desired performance specifications requires the derivation of accurate mathematical models that can be used to design optimal reactor and flow arrangements and test the performance of different control systems. The key issue in the development of high-fidelity models for PECVD processes is the understanding and characterization of the physico-chemical phenomena taking place in such processes including glow discharge chemistry, electron density and energy distribution, ion transport, diffusive and convective mass transfer, bulk and deposition reaction kinetics. Fortunately, significant research has been carried out in this direction including the characterization of plasma chemistry (e.g. [116, 8, 63]), the experimental measurement of electron density profiles in plasma reactors (e.g. [15, 19]), and the identification of bulk and deposition reactions and their mechanisms (e.g. [140, 76, 141, 62]).

The improved understanding of plasma physics and chemistry has led to the development of fundamental mathematical models for various plasma-assisted etching and deposition processes. In this area, important contributions include the development of comprehensive models for plasma etching processes [64, 137, 138], and more recently, for PECVD reactors used to deposit silicon nitride thin films [119, 121, 29]. These models were used in the design of reactor configurations that reduce the radial etching rate and deposition rate nonuniformity. For example, it was established that the use of a showerhead arrangement instead of the conventional single opening one, to enter the precursor gas into the reaction chamber, reduces significantly the radial

etching and film thickness nonuniformity. Despite the recent advances on modeling of PECVD processes, there are still many PECVD processes for which detailed mathematical models are not available including the one used to deposit amorphous silicon thin films. Furthermore, available results on control of plasma-assisted processes are mainly limited to plasma etching (e.g. [129, 130, 132]), thereby motivating further the study of modeling and control of PECVD processes.

In this chapter, we consider a single-wafer parallel electrode PECVD process with showerhead arrangement used to deposit a 500 A amorphous silicon thin film on a 8 cm wafer. The objective is to develop a detailed fundamental model for this process, able to predict the deposition rate profile across the radius of the wafer, and a feedback control strategy that can substantially reduce deposition rate radial nonuniformity. Initially, a two-dimensional unsteady-state model is developed that accounts for diffusive and convective mass transfer, bulk and deposition reactions, and nonuniform fluid flow and plasma electron density profiles. The model predicts that the radial film thickness nonuniformity is almost 19%. Then, a feedback control system is designed and implemented on the process to reduce the film thickness nonuniformity. The control system consists of three spatially-distributed proportional integral controllers that use measurements of the deposition rate at several locations across the wafer, to manipulate the inlet concentration of silane in the showerhead and achieve a uniform deposition rate across the wafer. The implementation of the proposed control system is shown to reduce the film thickness nonuniformity to 3.8%. The robustness properties of the control system with respect to disturbances are also tested.

9.2 Process description and modeling

We consider a single-wafer parallel electrode PECVD process with showerhead arrangement shown in Figure 9.1. The objective of the process is to deposit a 500 A amorphous silicon thin film on a 8 cm wafer, which is placed on the top of the lower electrode. The reactor is fed through the showerhead by a gas stream consisting of silane, SiH_4, and inert gases (typically H_2 or He). The flow rate and composition

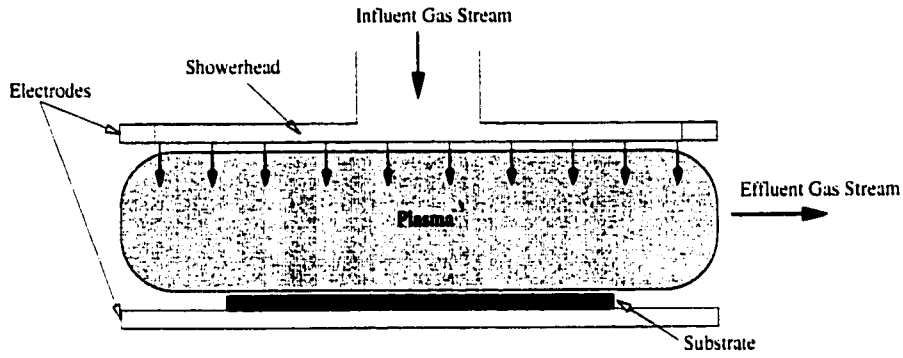

Figure 9.1: Cylindrical showerhead electrode plasma enhanced CVD reactor.

of the influent gas stream is assumed to be uniform throughout the showerhead. An RF (radio frequency) power source is used to generate the plasma (i.e. chemically reactive mixture of ions, electrons and radicals) from silane. The radicals are then transported via convection and diffusion to the surface of the wafer where they react and deposit amorphous silicon. Plasma species that do not deposit and unreacted silane are pumped radially outwards. The reactor is assumed to be at 1 $Torr$ pressure and 500 K temperature, while a 13.56 MHz frequency alternate voltage is applied to the electrodes generating a glow discharge. In the remainder of this section, we develop a fundamental model for the PECVD reactor of Figure 9.1.

Flow field. The gas flow inside the PECVD reactor of Figure 9.1 resembles the three-dimensional axisymmetric stagnation flow. Under the standard assumptions: a)

treating plasma as a continuum medium, b) constant physical properties of the gas, c) negligible volume change of the reacting gases, and d) azimuthal reactor symmetry, the evolution of the velocity profile inside the PECVD reactor can be computed from the Navier-Stokes and continuity equations:

$$\begin{aligned}
\frac{\partial v_r}{\partial t} + v_r\frac{\partial v_r}{\partial r} + v_z\frac{\partial v_r}{\partial z} &= -\frac{1}{\rho}\frac{\partial P}{\partial r} + \nu\left(\frac{\partial^2 v_r}{\partial r^2} + \frac{1}{r}\frac{\partial v_r}{\partial r} - \frac{v_r}{r^2} + \frac{\partial^2 v_r}{\partial z^2}\right) \\
\frac{\partial v_z}{\partial t} + v_r\frac{\partial v_z}{\partial r} + v_z\frac{\partial v_z}{\partial z} &= -\frac{1}{\rho}\frac{\partial P}{\partial z} + \nu\left(\frac{\partial^2 v_z}{\partial r^2} + \frac{1}{r}\frac{\partial v_z}{\partial r} + \frac{\partial^2 v_z}{\partial z^2}\right) \\
\frac{\partial v_r}{\partial r} + \frac{v_r}{r} + \frac{\partial v_z}{\partial z} &= 0
\end{aligned} \tag{9.1}$$

subject to the boundary conditions:

$$\begin{aligned}
v_r(r,0) &= 0, \quad v_z(r,0) = 0, \\
v_r(r,L) &= 0, \quad v_z(r,L) = -v_w
\end{aligned} \tag{9.2}$$

where v_r is the velocity in the r-direction, v_z is the velocity in the z-direction, $r \in [0, r_t]$ is the radial coordinate, r_t is the radius of the reactor, $z \in [0, L]$ is the axial coordinate, L is the height of the reactor (i.e. distance between the two electrodes), ρ is the (constant) density of the plasma, P is the pressure, ν is the (constant) kinematic viscosity defined as $\nu = \frac{\mu}{\rho}$, μ is the (constant) viscosity of the plasma, and v_w is the velocity of the feed gas entering the chamber. The velocity of the feed gas at the upper electrode is assumed to be uniform and is calculated from the equation: $v_w = \frac{Q(T,P)}{N_h \pi r_h^2}$, where $Q(T,P)$ is the volumetric rate of the precursor gas at the operating conditions of the reactor, N_h is the number of holes on the top electrode, and r_h is the radius of each hole.

Defining the wall Reynolds number as $Re_w = \frac{v_w L}{4\nu}$, using that for the reactor of Figure 9.1, $Re_w = 0.49 < 1$ (the computation of Re_w was made by using the values of Table 9.1) and assuming that v_z is only a function of z, the following steady-state approximate analytic solution of the Navier-Stokes and continuity equations of Eq.9.1

can be computed (see also [64]):

$$\begin{aligned} v_r(z,r) &= \frac{v_w}{L} r \left[\frac{3}{4} - \frac{3}{4}\psi^2 + Re_w(-\frac{1}{160}\psi^6 + \frac{3}{32}\psi^4 + \frac{1}{4}\psi^3 - \frac{117}{1120}\psi^2 - \frac{1}{4}\psi + \frac{19}{1120}) \right] \\ v_z(z) &= -v_w \left[\frac{1}{2} + \frac{3}{4}\psi - \frac{1}{4}\psi^3 \right. \\ &\quad \left. + Re_w(-\frac{1}{1120}\psi^7 + \frac{3}{160}\psi^5 + \frac{1}{16}\psi^4 - \frac{39}{1120}\psi^3 - \frac{1}{8}\psi^2 + \frac{19}{1120}\psi + \frac{1}{16}) \right] \end{aligned} \tag{9.3}$$

where $\psi = 2\frac{z}{L} - 1$. The above analytic expressions for $v_r(z,r)$ and $v_z(z)$ were employed in the simulations of sections 9.3 and 9.4.

Table 9.1: Process parameters

P	=	1.0	$Torr$
T	=	500	K
L	=	3.6	cm
r_t	=	8.0	cm
r_w	=	4.0	cm
Q	=	50.0	$scm^3\ min^{-1}$
N_h	=	350	
r_h	=	0.1	cm
n_{eo}	=	2.0×10^{10}	cm^{-3}
μ	=	1.832×10^{-7}	$kg\ s^{-1}\ cm^{-1}$
ρ	=	1.030×10^{-9}	$kg\ cm^{-3}$
ρ_{Si}	=	8.292×10^{-10}	$mol\ A^{-1}\ cm^{-2}$

Electron density profile. For 1 $Torr$ pressure and 13.56 MHz frequency alternate voltage, the secondary electron emission is negligible and the glow is mainly sustained by bulk ionization. Therefore, the steady-state electron density profile is computed by assuming diffusion-controlled discharge in a cylindrical container and is given by the following formula [138]:

$$n_e(r,z) = n_{eo} J_0(2.405\frac{r}{r_t}) sin(\frac{\pi z}{L}) \tag{9.4}$$

where $n_e(r,z)$ is the electron density, n_{eo} is the maximum electron density in the reactor (n_{eo} depends on the power dissipated in the plasma, the plasma volume and

the effective electric field; the value of n_{e_o} used in our calculations was computed in [19] from experimental data), J_0 is the zero order Bessel function of the first kind and r_t is the radius of the reactor. From Eq.9.4, it is clear that the electron density profile attains its maximum value in the center of the reactor (i.e. $r = 0,\ z = L/2$).

Reactions and mass transport. Regarding the reactions that take place on the bulk of the plasma, we assume that SiH_4 enters the reactor and dissociates according to the following reaction scheme:

$$\begin{aligned} e^- + SiH_4 &\rightarrow SiH_2 + 2H + e^- \\ e^- + SiH_4 &\rightarrow SiH_3 + H + e^- \\ H + SiH_4 &\rightarrow SiH_3 + H_2 \\ SiH_3 + SiH_3 &\rightarrow SiH_4 + SiH_2 \\ SiH_4 + SiH_2 &\rightarrow Si_2H_6 \end{aligned} \tag{9.5}$$

where e^- is the electron, SiH_2 is the silylene radical, SiH_3 is the silyl radical, Si_2H_6 is the disilane and H is the atomic hydrogen. The reaction scheme of Eq.9.5 was proposed in [85, 120] to represent various sets of experimental data. According to this reaction scheme, SiH_4 initially dissociates due to electron impact forming silylene, silyl radicals and atomic hydrogen; this stage is described by the following reactions:

$$\begin{aligned} e^- + SiH_4 &\rightarrow SiH_2 + 2H + e^- \\ e^- + SiH_4 &\rightarrow SiH_3 + H + e^- \end{aligned} \tag{9.6}$$

The hydrogen radical H then reacts with SiH_4 according to the following abstraction reaction forming SiH_3:

$$H + SiH_4 \rightarrow SiH_3 + H_2 \tag{9.7}$$

SiH_3 diffuses towards the surface of the wafer where the following recombination reaction occurs:

$$SiH_3 + SiH_3 \rightarrow SiH_4 + SiH_2 \tag{9.8}$$

The following insertion reaction forming disilane also takes place:

$$SiH_4 + SiH_2 \rightarrow Si_2H_6 \tag{9.9}$$

Assuming that the effective reaction rates of the reactions of Eq.9.5 can be expressed as a product of the dissociation constants, electron density and reactant species concentrations [116], the following expressions can be written for the rate of change of the concentration, $r_{x,i}$, of the species SiH_4, SiH_2, SiH_3, H due to consumption and production according to the reactions of Eq.9.5:

$$\begin{aligned} r_{x,1} &= -k_1 n_e c_1 - k_2 n_e c_1 - k_3 c_1 c_4 + k_4 c_3 c_3 - k_5 c_1 c_2 \\ r_{x,2} &= k_1 n_e c_1 + k_4 c_3 c_3 - k_5 c_1 c_2 \\ r_{x,3} &= k_2 n_e c_1 + k_3 c_1 c_4 - 2k_4 c_3 c_3 \\ r_{x,4} &= 2k_1 n_e c_1 + k_2 n_e c_1 - k_3 c_1 c_4 \end{aligned} \tag{9.10}$$

where the subscripts $i = 1, 2, 3, 4$ correspond to silane SiH_4, silylene radical SiH_2, silyl radical SiH_3, and atomic hydrogen H, respectively, c_i is the concentration of each species, and k_j, $j = 1, 2, 3, 4, 5$ is the reaction rate constant for each reaction in the scheme of Eq.9.5.

Owing to the complex and poorly-understood nature of the deposition reactions, we assume that SiH_3 and SiH_2 approach the wafer surface and instantaneously react towards SiH_4 and $a-Si$, and $a-Si$ and H_2, respectively. To determine the amount of SiH_4 and $a-Si$ being produced by the deposition reactions, we use the concepts of sticking and recombination probabilities (see also [141, 63, 8]). Specifically, we compute the amount of $a-Si$ and SiH_4 produced by the deposition reactions of SiH_3 by multiplying the flux of SiH_3 on the wafer surface by s_3 (sticking probability) and γ_3 (recombination probability), respectively. The amount of $a-Si$ which is produced by the deposition reactions of SiH_2 is computed by multiplying the flux of SiH_2 on the wafer surface by s_2 (sticking probability). We note that the contribution of disilane Si_2H_6 in $a-Si$ deposition at 500 K is negligible [119], and thus, it is not included in our calculations.

Applying dynamic material balances to the process and accounting for diffusive

and convective mass transfer, and bulk and surface reactions, a mathematical model that describes the spatio-temporal evolution of the concentration of the species, SiH_4, SiH_2, SiH_3 and H, throughout the reactor is obtained. The model consists of four nonlinear parabolic partial differential equations and can be written in the following compact form:

$$\frac{\partial c_i}{\partial t} = D_i\left(\frac{\partial^2 c_i}{\partial r^2}+\frac{1}{r}\frac{\partial c_i}{\partial r}+\frac{\partial^2 c_i}{\partial z^2}\right)-v_r\frac{\partial c_i}{\partial r}-v_z\frac{\partial c_i}{\partial z}+r_{x,i}(n_e, c_1, c_2, c_3, c_4),\ i = 1, ..., 4 \quad (9.11)$$

subject to the boundary conditions:

$$\frac{\partial c_i}{\partial r}(t, 0, z) = 0,\ \ \frac{\partial c_i}{\partial r}(t, r_t, z) = 0,\quad i = 1, ..., 4 \quad (9.12)$$

$$c_i(t, r, L) = c_{w,i}(t, r),\quad i = 1, ..., 4 \quad (9.13)$$

$$\frac{\partial c_1}{\partial z}(t, r, 0) = -\gamma_3\frac{D_3}{D_1}\frac{\partial c_3}{\partial z}(t, r, 0),\ \ c_2(t, r, 0) = 0,$$
$$c_3(t, r, 0) = 0,\ \ \frac{\partial c_4}{\partial z}(t, r, 0) = 0,\quad 0 \le r \le r_w \quad (9.14)$$

$$\frac{\partial c_i}{\partial z}(t, r, 0) = 0,\ \ r_w < r \le r_t,\quad i = 1, ..., 4 \quad (9.15)$$

and the initial conditions:

$$c(0, r, z) = c_i^o(r, z),\quad i = 1, ..., 4 \quad (9.16)$$

where D_i is the diffusion coefficient of the i-th species, r_w is the radius of the wafer, $c_{w,i}(t)$ is the concentration of the specific species at the feed, $c_i^o(r, z)$ is the concentration of the species initially in the chamber, and γ_3 represents the percentage of SiH_3 surface reaction leading to SiH_4 (recombination probability). The boundary condition $\frac{\partial c_1}{\partial z}(t, r, 0) = -\gamma_3\frac{D_3}{D_1}\frac{\partial c_3}{\partial z}(t, r, 0)$ accounts for the production of SiH_4 by SiH_3 consumption on the wafer surface, the boundary conditions $c_2(t, r, 0) = 0,\ c_3(t, r, 0) = 0$ express the instantaneous consumption of SiH_2 and SiH_3 on the wafer surface, and the boundary condition $\frac{\partial c_4}{\partial z}(t, r, 0) = 0$ accounts for non-flux of H on the wafer. The boundary conditions outside of the wafer surface (Eq.9.15) result from the fact that

SiH_4, SiH_2, SiH_3, H do not react with the walls of the reactor. The deposition rate of amorphous silicon on the wafer is calculated from the following equation:

$$R_{dep}(t,r) = \frac{1}{\rho_{Si}}[\sum_{i=1}^{4} s_i D_i \frac{\partial c_i}{\partial z}(t,r,0)], \tag{9.17}$$

where ρ_{Si} is the density of $a-Si$ and s_i represents the percentage of the flux of the i-th species towards the surface leading to deposition of amorphous silicon (sticking probability).

The values of the operating conditions and the reactor parameters are given in Table 9.1, the values of the reaction rate constants are presented in Table 9.2, and finally, the values of physico-chemical properties of the species are tabulated in Table 9.3. We note that: a) the physical properties of the plasma (e.g. viscosity) were

Table 9.2: Reaction rate constants

Reaction	Rate Constant	units
$e^- + SiH_4 \rightarrow SiH_2 + 2H$	$k_1 = 1.870 \times 10^{-11}$	$s^{-1}\ cm^3$
$e^- + SiH_4 \rightarrow SiH_3 + H$	$k_2 = 1.590 \times 10^{-10}$	$s^{-1}\ cm^3$
$H + SiH_4 \rightarrow SiH_3 + H_2$	$k_3 = 1.325 \times 10^{12}$	$s^{-1}\ mol^{-1}\ cm^3$
$SiH_3 + SiH_3 \rightarrow SiH_4 + SiH_2$	$k_4 = 9.033 \times 10^{13}$	$s^{-1}\ mol^{-1}\ cm^3$
$SiH_4 + SiH_2 \rightarrow Si_2H_6$	$k_5 = 2.830 \times 10^{13}$	$s^{-1}\ mol^{-1}\ cm^3$

computed by assuming that the plasma consists of pure silane, b) the density of the mixture was calculated from the ideal gas law, and c) the diffusion coefficients of the radicals and the silane were calculated from equations based on Lennard-Jones potential under the assumption that all the species diffuse through pure silane (see also [149, 89]).

9.3 Open-loop simulation results

The mathematical model of the PECVD reactor of Figure 9.1 consisting of the four unsteady-state two-dimensional diffusion-reaction equations (Eq.9.11), the velocity (Eq.9.3) and electron density (Eq.9.4) profiles, was solved using numerical techniques. Specifically, the finite-difference method was initially used to discretize the spatial

Table 9.3: Physico-chemical properties of plasma species

Properties	SiH_4	SiH_2	SiH_3	H	units
D_i	285.05	321.86	319.16	2107.75	$cm^2\ s^{-1}$
c_i^o/c_t	1.0	0.0	0.0	0.0	
$c_{w,i}/c_t$	1.0	0.0	0.0	0.0	
γ_i	0.0	0.0	0.6	0.0	
s_i	0.0	1.0	0.4	0.0	

derivatives of Eq.9.11 in the r and z directions (75 and 75 discretization points were used in the r and z direction, respectively; it was verified that further increase in the number of discretization points in both r and z directions results in insignificant improvements in the accuracy of the computed solution). Then, the time-integration of the resulting large (75×75) set of ordinary differential equations was performed by utilizing the alternate direction implicit (ADI) method. In all the simulation runs, the reactor is initially assumed to be filled with pure silane.

Figure 9.2 shows the profile of the steady-state dimensionless concentration of silane, SiH_4, inside the reactor (in the r-axis: 0 cm is the center of the wafer, 4.0 cm is the edge of the wafer and 8.0 cm is the edge of the reactor; in the z-axis: 0 cm is the wafer surface and 3.6 cm is the showerhead). We observe that the concentration of silane is lower towards the center of the reactor. This is because silane is mainly consumed by the dissociation reactions, $e^- + SiH_4 \rightarrow SiH_2 + 2H$, $e^- + SiH_4 \rightarrow SiH_3 + H$, whose rate is larger at the center of the reactor owing to the maximum of the

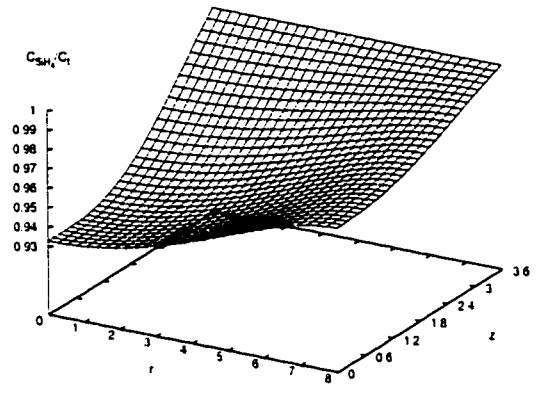

Figure 9.2: Open-loop steady-state concentration profile of SiH_4 as a function of radius and height.

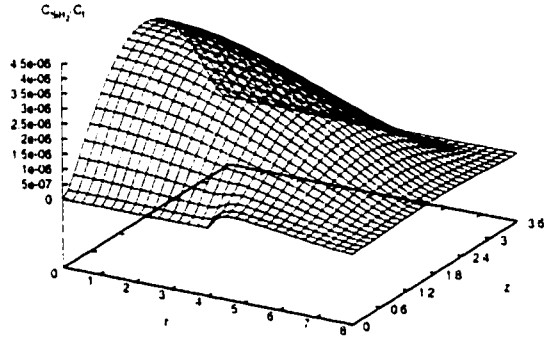

Figure 9.3: Open-loop steady-state concentration profile of SiH_2 as a function of radius and height.

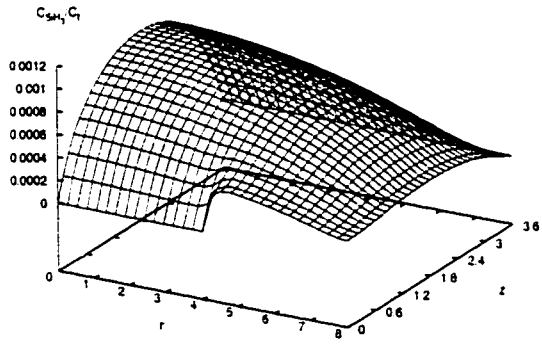

Figure 9.4: Open-loop steady-state concentration profile of SiH_3 as a function of radius and height.

electron density profile there. Figures 9.3 and 9.4 show the profiles of the steady-state

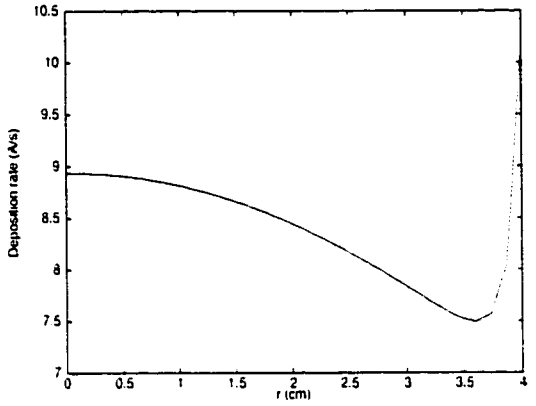

Figure 9.5: Open-loop steady-state deposition rate of $a-Si$ as a function of wafer radius.

concentration of silylene, SiH_2, and silyl, SiH_3, respectively. The concentration of SiH_3 is much higher than the concentration of SiH_2 due to the higher reactivity of SiH_2 in the bulk of the plasma (see also [76, 63] for similar observations). The low concentration of SiH_2 decreases the role of the reactions of this species that lead to $a-Si$ deposition, and suggests that amorphous silicon is mainly produced by SiH_3 consumption. As expected, the maximum steady-state concentration for both SiH_2 and SiH_3 is located at the center of the reactor due to the maximum of the electron density in this location.

The nonuniform concentration of SiH_3 on the wafer surface, together with the fact that the deposition rate is mainly determined by the deposition reaction of SiH_3, create a nonuniform deposition rate profile for amorphous silicon along the radius of the wafer (Figure 9.5). This results in a radially nonuniform final film thickness profile which is shown in Figure 9.6. A measure of the spatial nonuniformity, say M_N, can be defined as $M_N = \frac{H_{max} - H_{min}}{H_{min}}$, where H_{max}, H_{min} are the maximum and minimum height of the film for $0\ cm \leq r \leq 3.6\ cm$. The large film thickness nonuniformity appeared for $3.6\ cm \leq r \leq 4.0\ cm$ is due to the large gradient on the

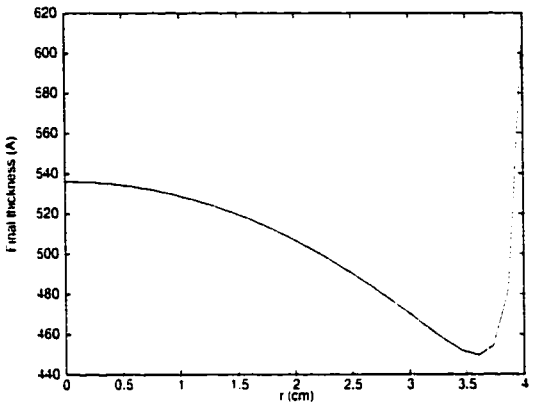

Figure 9.6: Open-loop final thickness of $a - Si$ film as a function of radius.

concentration of SiH_2 and SiH_3 at the wafer edge (Figure 9.3; this is a result of the fact that SiH_2 and SiH_3 do not react with the walls of the reactor), and it will not be accounted for in M_N because it occurs in a region which is not utilized for the placement of an integrated circuit. Using the values for H_{max}, H_{min} from Figure 9.6, the nonuniformity measure for the open-loop process is computed to be $M_N = 19.2\%$. This is a very large value, according to any industrial standard, which suggests the implementation of a feedback control system on the PECVD process to reduce radial film thickness nonuniformity.

9.4 Controller design - closed-loop simulations

We now design and implement a feedback control system on the PECVD process in order to reduce the radial nonuniformity of the deposition rate and final film thickness. The proposed control system utilizes point measurements of the deposition rate at several locations across the radius of the wafer to manipulate the inlet concentration of silane in the showerhead and achieve spatially uniform deposition of the 500 A amorphous silicon thin film. The concentration of silane at the showerhead was chosen as the manipulated variable because of its strong effect on the deposition rate

(this was verified with several open-loop simulation runs for different inlet silane concentrations; the effect of the inlet flow rate on the deposition rate was also examined and found to be negligible). Furthermore, the choice of the inlet silane concentration

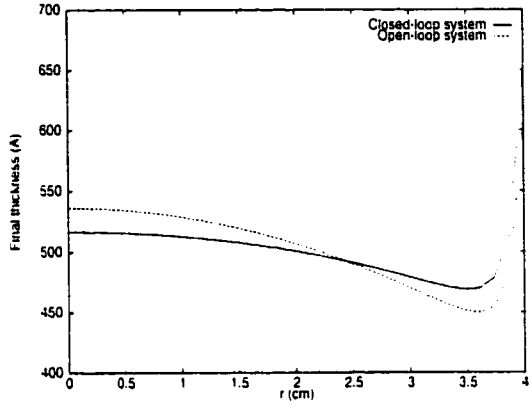

Figure 9.7: Controlled final thickness of $a-Si$ film across the radius of the wafer (single PI controller).

as manipulated variable was motivated by the realization that the suppression of radial deposition rate nonuniformity requires the use of a manipulated variable that is distributed across the radius of the wafer. We note that in practice, the inlet silane concentration is manipulated by adjusting the composition of an inert gas such as H_2 or He [125] in the feed to the showerhead (the use of such a diluent does not effect the velocity profile inside the reactor, i.e. v_w remains constant). Owing to the mildly nonlinear nature of the process model of Eq.9.11 (it only includes bilinear nonlinearities since the assumption of isothermal operation allows considering the reaction rate parameters independent of temperature), a linear proportional integral (PI) controller with the following state-space description:

$$\begin{aligned} \dot{\xi} &= y_{sp} - y, \ \xi(0) = 0 \\ u &= K(y_{sp} - y) + \frac{1}{\tau}\xi \end{aligned} \tag{9.18}$$

was initially used to manipulate the inlet concentration of silane throughout the showerhead to achieve offsetless set-point tracking. In the controller of Eq. 9.18, ξ is the

controller state variable, y_{sp} denotes the set-point value of the deposition rate, y denotes the *on-line measurement* of the deposition rate, K is the proportional controller gain and τ is the integral time constant. The manipulated input u was defined as $u = \frac{c_{w,1}}{c_t}$, where $c_{w,1}$ represents the concentration of silane at the showerhead, and the controlled output was defined as $y(t) = \frac{1}{\rho_{Si}} \int_0^{r_w} [\sum_{i=1}^{4} s_i D_i \frac{\partial c_i}{\partial z}(t, r, 0)] dr$, where r_w is the radius of the wafer, and was computed by using 30 measurements of the deposition rate across the wafer. In practice, a variety of on-line measurement techniques can be employed to determine the thickness of the deposited film in situ (and thus, the deposition rate), such as ellipsometry [125] and transient photoconductivity [133]. y_{sp} was set equal to 6.9 A/s which means that the time required for the growth of a 500 A thin film is approximately 73 s (the corresponding time for the open-loop process is 60 s). Figure 9.7 shows the closed-loop final film thickness as a function of wafer radius, while figure 9.8 shows the corresponding manipulated input profile (note that

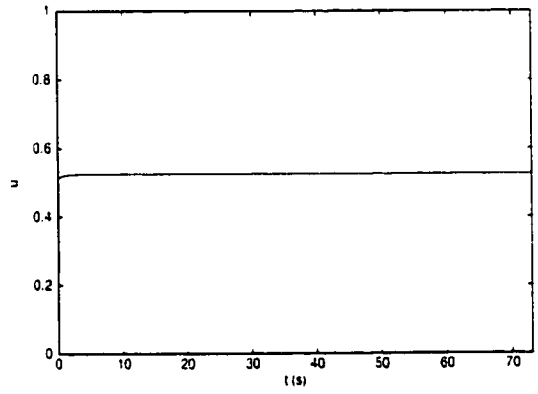

Figure 9.8: Manipulated input profile for a single PI controller.

$u = 0.0$ means that no silane enters the reactor, while $u = 1.0$ means that the feed consists of pure silane). The controller decreases the radial nonuniformity of the final thickness to $M_N = 10.2$ % (note that in the open-loop system the nonuniformity is $M_N = 19.2$ %). Even though the use of a single PI controller reduces the film

thickness nonuniformity compared to the one of the open-loop process, the reduction obtained is not significant enough, thereby motivating the design of a new feedback control system.

To further reduce the film thickness nonuniformity, we divide the showerhead area into three concentric regions (Figure 9.9) and use three PI controllers to adjust the inlet silane concentration in each one of these regions. We note that no controller was used in the showerhead region which is outside of the wafer. The idea for dividing

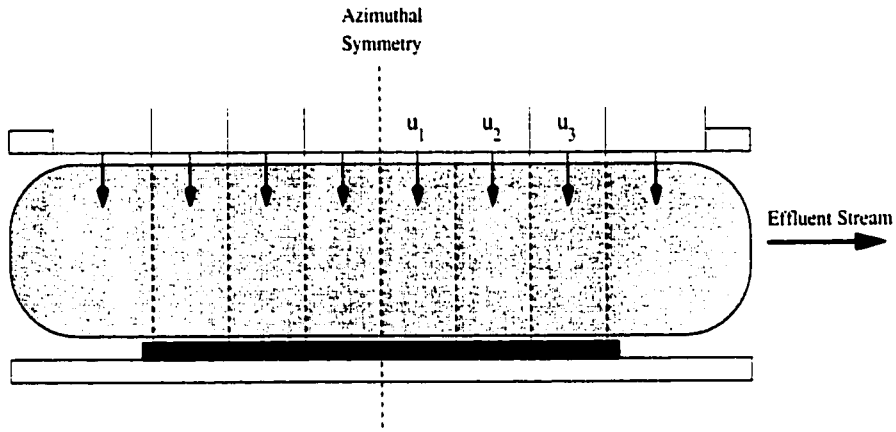

Figure 9.9: Control configuration for PECVD reactor.

the showerhead region into three concentric subregions is based on the realization that the effective control of a variable that is distributed in space (as is the case with the deposition rate in this problem) should be achieved by independently-controlled manipulated inputs that are also distributed in space. The state-space representation of the feedback control system takes then the form:

$$\begin{aligned} \dot{\xi}_\kappa &= y_{sp,\kappa} - y_\kappa,\ \xi_\kappa(0) = 0,\ \ \kappa = 1,2,3 \\ u_\kappa &= K_\kappa(y_{sp,\kappa} - y_\kappa) + \frac{1}{\tau_\kappa}\xi_\kappa \end{aligned} \tag{9.19}$$

where the κ-th controlled output is defined as $y_\kappa(t) = \frac{1}{\rho_{Si}}\int_{r_{s,\kappa}}^{r_{f,\kappa}}[\sum_{i=1}^{4} s_i D_i \frac{\partial c_i}{\partial z}(t,r,0)]dr$, where $r_{s,\kappa}, r_{f,\kappa}$ are the internal and external radii of the region where the $\kappa-$th control

action is applied, and $y_{sp,\kappa}$ is the set-point for the κ-th region. Table 9.4 below provides the parameters and set-point values for the three PI controllers, and the radii of the regions where they are applied.

Table 9.4: Parameters for the 3 PI controllers

κ	K_κ	τ_κ (s)	$r_{s,\kappa}$ (cm)	$r_{f,\kappa}$ (cm)	$y_{sp,\kappa}$ (A/s)
1	0.5	1.25	0.0	2.0	6.9
2	0.5	1.25	2.0	3.0	6.9
3	0.5	1.25	3.0	4.0	6.9

Figure 9.10 shows the closed-loop final thickness in the case of using three PI controllers, while Figure 9.11 displays the corresponding manipulated input profiles. It is clear that the use of three spatially-distributed PI controllers has substantially reduced the film thickness nonuniformity; the nonuniformity measure for the profile of Figure 9.10 is $M_N = 3.8$ % which is much less than 19.2 % (uncontrolled process) and 10.2 % (single PI controller). We also tested the robustness properties of the

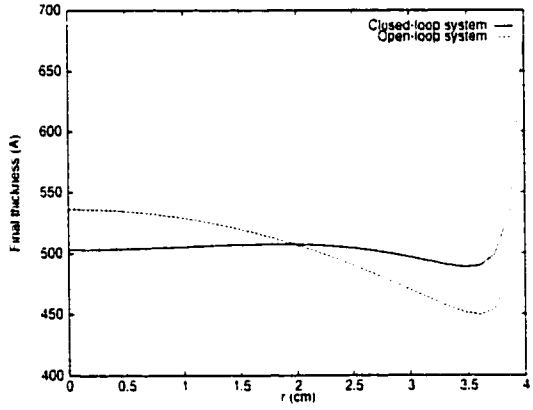

Figure 9.10: Controlled final thickness of $a - Si$ film across the radius of the wafer (three PI controllers).

proposed PI control system in the presence of modeling errors. Specifically, the value of n_{eo} was assumed to vary, in a sinusoidal fashion, 20 % around the nominal value of Table 9.1 with a period of 4.0 s, for the first 20 s of operation of the process. Figure

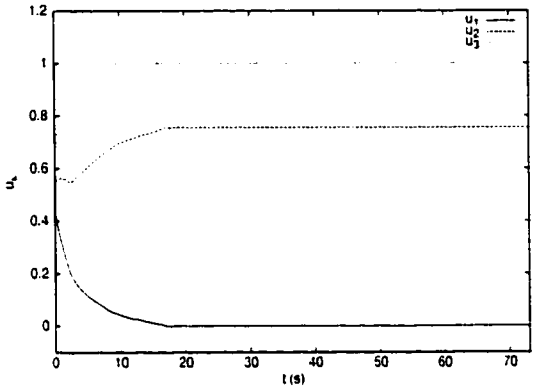

Figure 9.11: Manipulated input profiles for the three PI controllers.

9.12 displays the final film thickness profile for this simulation run. The thickness nonuniformity measure is again $M_N = 3.8$ %, thereby indicating that the proposed control system possesses excellent robustness properties with respect to significant modeling errors.

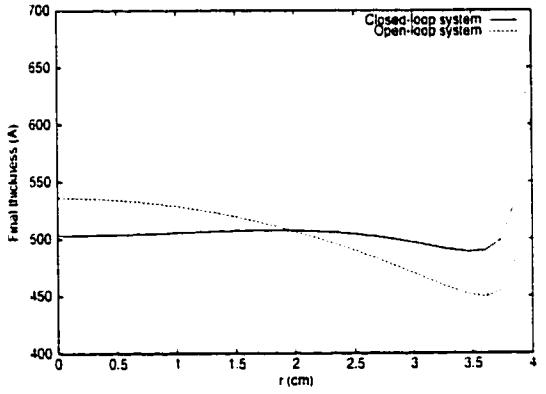

Figure 9.12: Controlled final thickness of $a - Si$ film across the radius of the wafer in the presence of model uncertainty (three PI controllers).

Remark 9.1: From the above closed-loop system simulation results, it is evident that the division of the showerhead region into three concentric subregions is the main reason for the significant reduction in film thickness nonuniformity. To further establish this observation, we carried out several simulation runs using more than

three concentric regions and PI controllers, and found that further reduction on the film thickness nonuniformity was achieved (i.e. the resulting M_N was less than 3.8 %). Even though the use of more than three concentric subregions is not particularly meaningful for the deposition problem studied in this chapter (since $M_N = 3.8$ % is already very small), it should be definitely examined in the case of film deposition on larger wafers (e.g. 4.0 *in* wafer instead of 8.0 *cm* one), where the open-loop film thickness nonuniformity is going to be considerably higher than 19.2%.

9.5 Conclusions

In this chapter, we studied the modeling and control of a single-wafer parallel electrode PECVD process with showerhead arrangement used to deposit a 500 A amorphous silicon thin film on a 8 *cm* wafer. Initially, a two-dimensional unsteady-state model was developed for the process that accounts for diffusive and convective mass transfer, bulk and deposition reactions, and nonuniform fluid flow and plasma electron density profiles. The model was solved using finite-difference techniques and the radial film thickness nonuniformity was found to be 19.2%. Then, a feedback control system was designed and implemented on the process to reduce the film thickness nonuniformity. The control system consists of three spatially-distributed proportional integral controllers that use measurements of the deposition rate at several locations across the wafer, to manipulate the inlet concentration of silane in the showerhead and achieve a uniform deposition rate across the wafer. The implementation of the proposed control system was shown to reduce the film thickness nonuniformity to 3.8%. The proposed control system was also found to be robust with respect to modeling errors. We finally note that even though this study focused on the deposition of an amorphous silicon thin film, the developed numerical model and control strategy can be readily applied

to other plasma-assisted processes (e.g. plasma etching) and chemistries.

Chapter 10

Feedback Control of Plasma Etching Reactors for Improved Etching Uniformity

10.1 Introduction

Single-wafer plasma etching (PE) is an important process used in semiconductor manufacturing to selectively remove areas of thin films of compounds (e.g., amorphous silicon, silicon nitride, etc.) which are placed on substrates. In a PE process, the activation of the gases is achieved through impact with electrons and leads to the reacting species. The main advantages of plasma-assisted etching include directional selectivity of the reactions that take place on the surface of the wafer (etch anisotropy), reduced processing time and elimination of wet chemicals used in traditional etching processes. Even though the advantages of plasma etching are well known, a major issue which limits the widespread use of the PE process is the significant spatial nonuniformity of the etching rate. Radially nonuniform etching rates result in nonuniform film thickness, which adversely affects the subsequent processing

steps, and ultimately, product yield. This problem is usually addressed with over-etching, leading to: a) higher than necessary times for the specific process step, and b) degradation of the structures, resulting also in lower product yield. The design and operation of PE processes that achieve the desired performance specifications requires the derivation of accurate mathematical models that can be used to design optimal reactor and flow arrangements and test the performance of different control systems.

The key issue in the development of high-fidelity models is the understanding and characterization of the physico-chemical phenomena taking place in PE processes. In this direction, research efforts have focused on the characterization of plasma chemistry (e.g., [68, 142]), the experimental measurement of electron density profiles in plasma reactors (e.g., [15]), and the identification of surface reactions and their mechanisms (e.g., [69, 142]). The improved understanding of plasma properties has led to the development of accurate mathematical models for various plasma etching processes which can be used to compute reactor configurations that reduce the etching nonuniformity (e.g., [137, 138, 24, 175]). Such studies have revealed that the use of a showerhead arrangement to introduce the precursor gas into the reaction chamber, significantly reduces the radial etching nonuniformity. Previous work on control of plasma etching processes include radical concentration control [129, 130, 132], and nonuniformity control using feedback control schemes [87, 171].

In this chapter, we consider a parallel electrode PE process with showerhead arrangement used to etch a 500 A amorphous silicon film on a 4 in wafer. The objective is to develop a detailed fundamental model for this process, able to predict the etching rate profile across the radius of the wafer, and a feedback control strategy that can substantially reduce the etching rate radial nonuniformity. Initially, a two-dimensional

dynamic model is developed that accounts for diffusive and convective mass transfer, bulk and etching reactions, and nonuniform fluid flow and plasma electron density profiles. The model predicts that the radial etching rate nonuniformity is 30.2%. Then, a feedback control system is designed and implemented on the process to reduce this nonuniformity. The control system consists of three spatially-distributed proportional integral controllers that use measurements of the etching rate at three locations across the wafer, to manipulate the inlet concentration of carbon tetrafluoride in the showerhead and achieve a uniform etching rate across the radius of the wafer. The implementation of the proposed control system is shown to reduce the etching rate nonuniformity to 3.8%.

10.2 Process description and modeling

We consider a parallel electrode PE process with showerhead arrangement [138] shown in Figure 10.1. The objective of the process is to etch a 500 A amorphous silicon thin

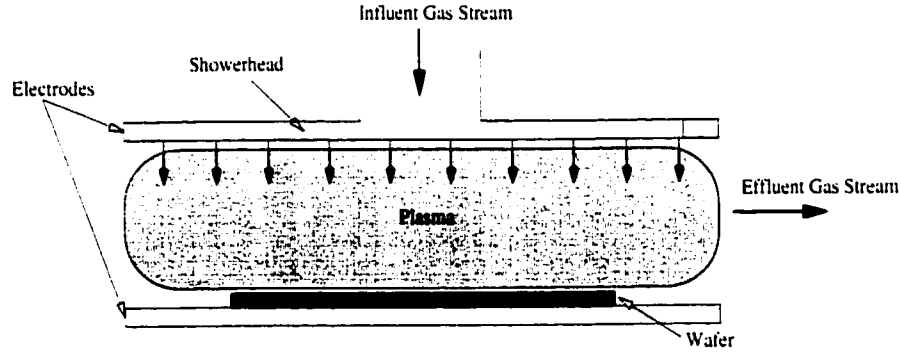

Figure 10.1: Cylindrical parallel electrode plasma etch reactor with showerhead configuration.

film placed on a 4 in wafer, which is located on the top of the lower electrode. The reactor is fed through the showerhead by a gas stream including carbon tetrafluoride, CF_4, and inert gases (typically He or Ar). The flow rate and composition of the influent gas stream is assumed to be uniform throughout the showerhead. An RF

(radio frequency) power source is used to generate the plasma (i.e., chemically reactive mixture of ions, electrons and radicals) from CF_4. The radicals are then transported via convection and diffusion to the surface of the wafer where they react towards SiF_4, etching the amorphous silicon. The plasma species that do not react with silicon, the etching products, and unreacted CF_4 are pumped radially outwards. The reactor is assumed to be at 0.5 $Torr$ pressure and 325 K temperature, while a 13.56 MHz frequency alternate voltage is applied to the electrodes generating a glow discharge. The wafer is assumed to be at a constant temperature of 400 K which is accomplished by a heating coil situated underneath the lower electrode. In the remainder of this section, we develop a fundamental model for the PE reactor of Figure 10.1.

Flow field. The gas flow inside the reactor resembles the three-dimensional axisymmetric stagnation flow. Under the standard assumptions: a) treating plasma as a continuum medium, b) constant physical properties of the gas, c) negligible volume change of the reacting gases, and d) azimuthal reactor symmetry, the flow field can be described by using the Navier-Stokes and continuity equations. The feed enters the chamber through the showerhead upper electrode at a constant velocity, v_w, which is assumed to be radially uniform and is calculated from the equation: $v_w = \dfrac{Q(T_r, P)}{N_h \pi r_h^2}$, where $Q(T_r, P)$ is the volumetric rate of the precursor gas at the operating conditions of the reactor, T_r is the reactor temperature, P is the pressure, N_h is the number of holes on the top electrode, and r_h is the radius of each hole. Defining the wall Reynolds number as $Re_w = \dfrac{v_w L \rho}{4\mu}$, where L is the height of the reactor (i.e., distance between the two electrodes), ρ is the (constant) density of the plasma, and μ is the (constant) viscosity of the plasma, the operating conditions of Table 10.1 correspond to $Re_w = 0.61 < 1$. For this value of Reynold's number, the following steady-state approximate analytic solution of the Navier-Stokes and continuity equations can be

Table 10.1: Process parameters

L	=	3.6	cm	P	=	0.5	$Torr$
r_t	=	8.0	cm	T_r	=	325	K
r_w	=	5.08	cm	T_w	=	400	K
Q	=	50.0	$scm^3\ min^{-1}$	ne_o	=	1.5×10^{10}	cm^{-3}
N_h	=	350		μ	=	1.7756×10^{-7}	$Kg\ s^{-1}\ cm^{-1}$
r_h	=	0.15	cm	ρ	=	2.171×10^{-9}	$Kg\ cm^{-3}$
				ρ_{Si}	=	8.292×10^{-10}	$mole\ A^{-1}\ cm^{-2}$

computed (for a more detailed analysis the reader may refer to [4] and [64]), under the assumption that the velocity in the z-direction, v_z, is only a function of z:

$$\begin{aligned} v_r(z,r) &= \frac{v_w}{L} r \left[\frac{3}{4} - \frac{3}{4}\psi^2 + Re_w(-\frac{1}{160}\psi^6 + \frac{3}{32}\psi^4 + \frac{1}{4}\psi^3 - \frac{117}{1120}\psi^2 - \frac{1}{4}\psi + \frac{19}{1120})\right] \\ v_z(z) &= -v_w \left[\frac{1}{2} + \frac{3}{4}\psi - \frac{1}{4}\psi^3 \right. \\ &\quad \left. + Re_w(-\frac{1}{1120}\psi^7 + \frac{3}{160}\psi^5 + \frac{1}{16}\psi^4 - \frac{39}{1120}\psi^3 - \frac{1}{8}\psi^2 + \frac{19}{1120}\psi + \frac{1}{16})\right] \end{aligned} \tag{10.1}$$

where $\psi = 2\frac{z}{L} - 1$, v_r is the velocity in the r-direction, v_z is the velocity in the z-direction, $r \in [0, r_t]$ is the radial coordinate, r_t is the radius of the reactor, and $z \in [0, L]$ is the axial coordinate. The above analytic expressions for $v_r(z,r)$ and $v_z(z)$ were employed in the simulations of sections 10.3 and 10.4. Referring to the flow field, we also note that the axisymmetric stagnation flow inside the reactor implies that the Reynolds number computed with respect to all the values of the velocity vector throughout the entire flow field does not vary significantly and is everywhere close to 1. This in turn means that there are no sharp velocity gradients in the flow field close to the showerhead which could lead to jetting effects and flow instabilities (this is also the case for the closed-loop system as discussed in section 10.4 below).

Electron density profile. For 0.5 $Torr$ pressure and 13.56 MHz frequency alternate voltage, the secondary electron emission is negligible and the glow is mainly sustained by bulk ionization. Therefore, the steady-state electron density profile is

computed by assuming diffusion-controlled discharge in a cylindrical container and is given by the following formula [138]:

$$n_e(r,z) = n_{eo} J_0(2.405\frac{r}{r_t}) sin(\frac{\pi z}{L}) \tag{10.2}$$

where $n_e(r,z)$ is the electron density, n_{eo} is the maximum electron density in the reactor (n_{eo} depends on the power dissipated in the plasma, the plasma volume and the effective electric field; the value of n_{eo} used in our calculations was computed in [153] based on experimental data), J_0 is the zero order Bessel function of the first kind and r_t is the radius of the reactor. From Eq.10.2, it is clear that the electron density profile attains its maximum value in the center of the reactor (i.e., $r = 0,\ z = L/2$).

Reactions and mass transport. Regarding the reactions that take place on the bulk of the plasma, we assume that CF_4 enters the reactor and dissociates according to the following reaction scheme [68, 65]:

$$\begin{aligned} e^- + CF_4 &\rightarrow CF_3 + F + e^- \\ e^- + CF_4 &\rightarrow CF_2 + 2\,F + e^- \\ F + CF_2 &\rightarrow CF_3 \\ F + CF_3 &\rightarrow CF_4 \\ CF_3 + CF_3 &\rightarrow C_2F_6 \end{aligned} \tag{10.3}$$

where e^- is the electron, CF_3 is trifluoromethyl radical, CF_2 is difluoromethylene, F is the fluorine radical and C_2F_6 is hexafluoroethane. According to this reaction scheme, CF_4 initially dissociates due to impact with electrons forming difluoromethylene, trifluoromethyl radical and atomic fluorine; this stage is described by the reactions: $e^- + CF_4 \rightarrow CF_3 + F + e^-$, $e^- + CF_4 \rightarrow CF_2 + 2\ F + e^-$. The fluorine radical F then reacts with CF_2 and subsequently with CF_3 according to the recombination reactions $F + CF_2 \rightarrow CF_3$, $F + CF_3 \rightarrow CF_4$ forming CF_4. CF_3 also recombines to form C_2F_6, according to the reaction $CF_3 + CF_3 \rightarrow C_2F_6$. Assuming that the effective reaction rates of the reactions of Eq.10.3 can be expressed as a product of the

dissociation constants, electron density and reactant species concentrations [65, 138], the following expressions can be written for the rate of change of the concentration, $r_{x,i}$, of the species CF_4, CF_2, CF_3, F due to consumption and production according to the reactions of Eq.10.3:

$$\begin{aligned} r_{x,1} &= -k_1 n_e c_1 - k_2 n_e c_1 + k_4 c_3 c_4 \\ r_{x,2} &= k_2 n_e c_1 - k_3 c_2 c_4 \\ r_{x,3} &= k_1 n_e c_1 + k_3 c_2 c_4 - k_4 c_3 c_4 - k_5 c_3 c_3 \\ r_{x,4} &= k_1 n_e c_1 + 2k_2 n_e c_1 - k_3 c_2 c_4 - k_4 c_3 c_4 \end{aligned} \tag{10.4}$$

where the subscripts $i = 1, 2, 3, 4$ correspond to carbon tetrafluoride CF_4, trifluoromethyl radical CF_3 , difluoromethylene CF_2 and fluorine radical F respectively, c_i is the concentration of each species, and k_j, $j = 1, 2, 3, 4, 5$ is the reaction rate constant for each reaction in the scheme of Eq.10.3.

The radicals CF_3 and F that are produced in the bulk of the plasma are transported to the wafer surface where they react with amorphous silicon Si according to [69, 153]:

$$\begin{aligned} CF_3(g) + Si(s) &\rightarrow CF_3(s) \\ F(g) + CF_3(s) &\rightarrow CF_4(g) \\ CF_3(g) + CF_3(s) &\rightarrow C_2F_6(g) \\ 4\,F(g) + Si(s) &\rightarrow SiF_4(g) \end{aligned} \tag{10.5}$$

where SiF_4 is tetrafluorosilane, (g) denotes the gas phase and (s) denotes the surface bound species. Referring to the above scheme, note that only the last reaction leads to the etching of amorphous silicon. Based on this reaction scheme, the rate of change of the concentration on the wafer surface, $r_{s,i}$, of the species CF_4, CF_2, CF_3, F can be expressed as:

$$\begin{aligned} r_{s,1} &= k_{s2} c_4 \theta \\ r_{s,2} &= 0 \\ r_{s,3} &= -k_{s3} c_3 \theta - k_{s1} c_3 (1 - \theta) \\ r_{s,4} &= -k_{etch}(1 - \theta) - k_{s2} c_4 \theta \end{aligned} \tag{10.6}$$

where c_i is the concentration of each species in the gas phase, k_{sj}, $j = 1, 2, 3$ is the

reaction rate constant for the first three reactions in the scheme of Eq.10.5 respectively, and k_{etch} is the reaction rate constant of the etching reaction (fourth reaction). θ denotes the surface coverage of CF_3 and is given from the following expression

$$\theta = \frac{k_{s1} c_{3(g)}}{(k_{s3} + k_{s1}) c_{3(g)} + k_{s2} c_{4(g)}} \tag{10.7}$$

under the assumption of equilibrium for the surface reactions. Since we assume isothermal operation, the reaction rate constants of the bulk and surface reactions are taken to be constant.

Applying dynamic material balances to the process and accounting for diffusive and convective mass transfer, and bulk and surface reactions, a mathematical model that describes the spatio-temporal evolution of the concentration of the species, CF_4, CF_2, CF_3 and F, throughout the reactor is obtained. The model consists of four nonlinear parabolic partial differential equations and can be written in the following compact form:

$$\frac{\partial c_i}{\partial t} = D_i\left(\frac{\partial^2 c_i}{\partial r^2} + \frac{1}{r}\frac{\partial c_i}{\partial r} + \frac{\partial^2 c_i}{\partial z^2}\right) - v_r \frac{\partial c_i}{\partial r} - v_z \frac{\partial c_i}{\partial z} + r_{x,i}(n_e, c_1, c_2, c_3, c_4),\ i = 1, ..., 4 \tag{10.8}$$

subject to the boundary conditions:

$$\frac{\partial c_i}{\partial r}(t, 0, z) = 0, \quad \frac{\partial c_i}{\partial r}(t, r_t, z) = 0, \quad i = 1, ..., 4 \tag{10.9}$$

$$D_i \frac{\partial c_i}{\partial z}(t, r, 0) = r_{s,i},\ 0 \le r \le r_w \quad , \quad \frac{\partial c_i}{\partial z}(t, r, 0) = 0,\ r_w < r \le r_t \quad , \quad c_i(t, r, L) = c_{w,i}(t, r), \quad i = 1, ..., 4 \tag{10.10}$$

and the initial conditions:

$$c(0, r, z) = c_i^o(r, z),\ i = 1, ..., 4 \tag{10.11}$$

where D_i is the diffusion coefficient of the i-th species, r_w is the radius of the wafer, $c_{w,i}(t)$ is the concentration of the specific species at the feed and $c_i^o(r, z)$ is the concentration of the species initially in the chamber. The boundary conditions outside of

the wafer surface (Eq.10.10) result from the fact that CF_4, CF_2, CF_3, F do not react with the walls of the reactor. The etching rate of amorphous silicon on the wafer is calculated from the following equation [138]:

$$R_{etch}(t,r) = \rho_{Si}\frac{1}{4}k_{etch}c_4(t,r,0)(1-\theta(t,r)) \tag{10.12}$$

where ρ_{Si} is the density of $a-Si$ and θ is given from Eq.10.7.

The values of the operating conditions and the reactor parameters are given in Table 10.1, the values of the reaction rate constants are presented in Tables 10.2 and 10.3, and finally, the values of physico-chemical properties of the species are tabulated in Table 10.4. We note that: a) the physical properties of the plasma (e.g., viscosity) were computed by assuming that the plasma consists of pure carbon tetrafluoride (see also [149]), and b) the density of the mixture was calculated from the ideal gas law.

Table 10.2: Bulk reaction rate constants

Reaction	Rate Constant	units
$e^- + CF_4 \rightarrow CF_3 + F + e^-$	6.00×10^{-10}	$s^{-1}\ cm^3$
$e^- + CF_4 \rightarrow CF_2 + 2\ F + e^-$	1.40×10^{-9}	$s^{-1}\ cm^3$
$F + CF_2 \rightarrow CF_3$	2.53×10^{11}	$s^{-1}\ mole^{-1}\ cm^3$
$F + CF_3 \rightarrow CF_4$	7.83×10^{12}	$s^{-1}\ mole^{-1}\ cm^3$
$CF_3 + CF_3 \rightarrow C_2F_6$	4.82×10^{12}	$s^{-1}\ mole^{-1}\ cm^3$

Table 10.3: Surface reaction rate constants

Reaction	Rate Constant	units
$CF_3(g) + Si(s) \rightarrow CF_3(s)$	17.52	$s^{-1}\ cm^3$
$F(g) + CF_3(s) \rightarrow CF_4(g)$	85.80	$s^{-1}\ cm^3$
$CF_3(g) + CF_3(s) \rightarrow C_2F_6(g)$	08.76	$s^{-1}\ cm^3$
$4\ F(g) + Si(s) \rightarrow SiF_4(g)$	85.24	$s^{-1}\ cm^3$

Table 10.4: Physico-chemical properties of plasma species

Properties	CF_4	CF_2	CF_3	F	units
D_i	110.85	183.97	125.38	405.44	$cm^2\ s^{-1}$
c_i^o/c_t	1.0	0.0	0.0	0.0	
$c_{w,i}/c_t$	1.0	0.0	0.0	0.0	

10.3 Open-loop simulation results

The mathematical model of the PE reactor consisting of the four unsteady-state two-dimensional diffusion-convection-reaction equations (Eq.10.8), the velocity (Eq.10.1) and electron density (Eq.10.2) profiles, was solved by using numerical techniques. Following [4], the finite-difference method was initially used to discretize the spatial derivatives of Eq.10.8 in the r and z directions (75 and 75 discretization points were used in the r and z direction, respectively; it was verified that further increase in the number of discretization points in both r and z directions results in insignificant improvements in the accuracy of the computed solution). The time-integration of the resulting large (75 $\times$ 75) set of ordinary differential equations was performed by utilizing the alternate direction implicit (ADI) method. In all the simulation runs, the reactor is initially assumed to be filled with pure carbon tetrafluoride. Figure 10.2a shows the profile of the steady-state dimensionless concentration of carbon tetrafluoride, CF_4, inside the reactor (in the r-axis: 0 cm is the center of the wafer, 5.08 cm is the edge of the wafer and 8.0 cm is the edge of the reactor; in the z-axis: 0 cm is the wafer surface and 3.6 cm is the showerhead). We observe that the concentration of CF_4 is lower towards the center of the reactor. This is because CF_4 is mainly consumed by the dissociation reactions, whose rate is larger at the center of the reactor owing to the maximum of the electron density profile there. Figures 10.2b and 10.2c show the profiles of the steady-state concentration of difluoromethylene,

CF_2, and trifluoromethyl radical, CF_3, respectively. The concentration of CF_2 is

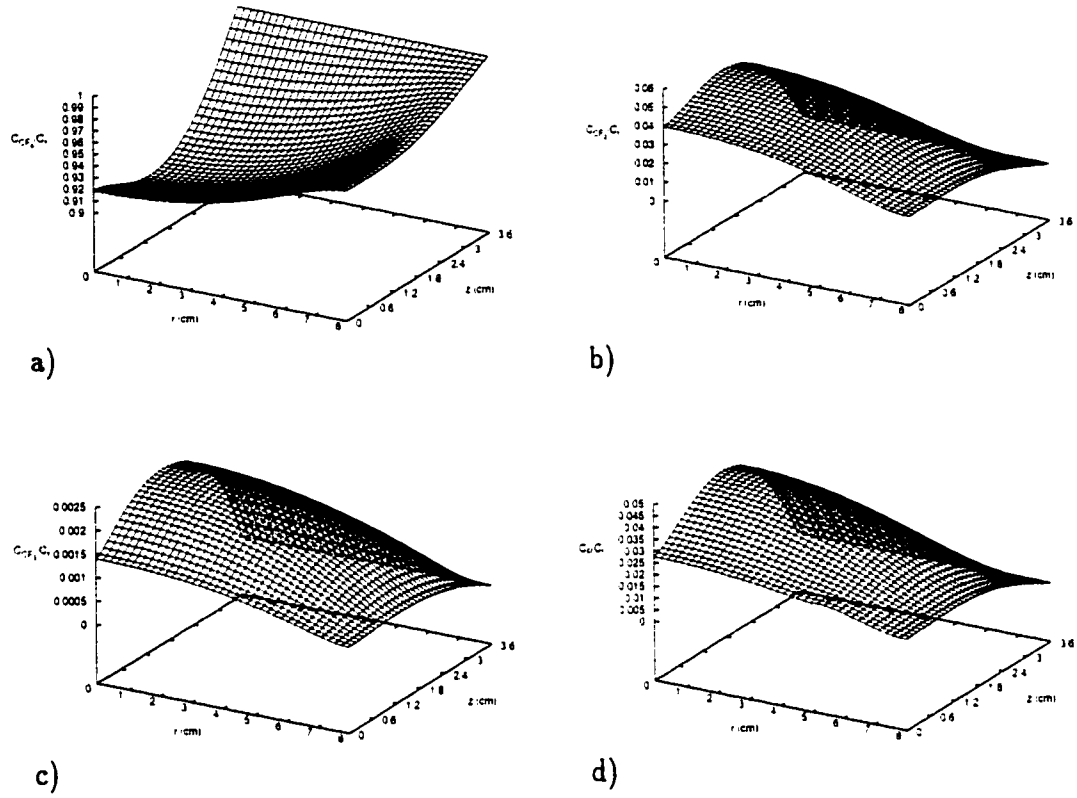

Figure 10.2: Open-loop steady-state concentration profile of CF_4 (a), CF_2 (b), CF_3 (c), F (d).

much higher than the concentration of CF_3 due to the higher reactivity of CF_3 in the bulk of the plasma and wafer surface and higher dissociation rate of CF_4 towards CF_2. As expected, the maximum steady-state concentration for both CF_2 and CF_3 is located at the center of the reactor due to the maximum of the electron density in this location.

The nonuniform concentration of CF_3 and F on the wafer surface, together with the fact that the etching rate is mainly determined by the coverage of the surface by the adsorbed CF_3 and the concentration of F (which reacts towards SiF_4), result in a nonuniform etching rate of the amorphous silicon profile along the radius of the wafer (Figure 10.3a). We observe that the etching rate exhibits a maximum at the center of

the wafer and decreases as the radius increases, matching the concentration profile of F (Figure 10.2d). The small increase in the etching rate appearing close to the edge of the wafer is due to the gradient of the concentration of F in this location (Figure 10.2d); this is a result of the fact that F does not react with the walls of the reactor (see also [138] for similar observations). A measure of the spatial nonuniformity, say R_M, can be defined as $R_M = \frac{R_{max} - R_{min}}{R_{min}}$, where R_{max}, R_{min} are the maximum and minimum etching rate for $0\ cm \leq r \leq 5.08\ cm$. Using the values for R_{max}, R_{min} from Figure 10.3a, the nonuniformity measure for the open-loop process is computed to be $R_M = 30.2\%$.This is a very large value, according to any industrial standard, which suggests the implementation of a feedback control system on the PE process to reduce radial film thickness nonuniformity.

10.4 Controller design - closed-loop simulations

In this section, we focus on the design and implementation of a feedback control system on the PE process in order to reduce the radial nonuniformity of the etching rate. The proposed control system utilizes point measurements of the etching rate at

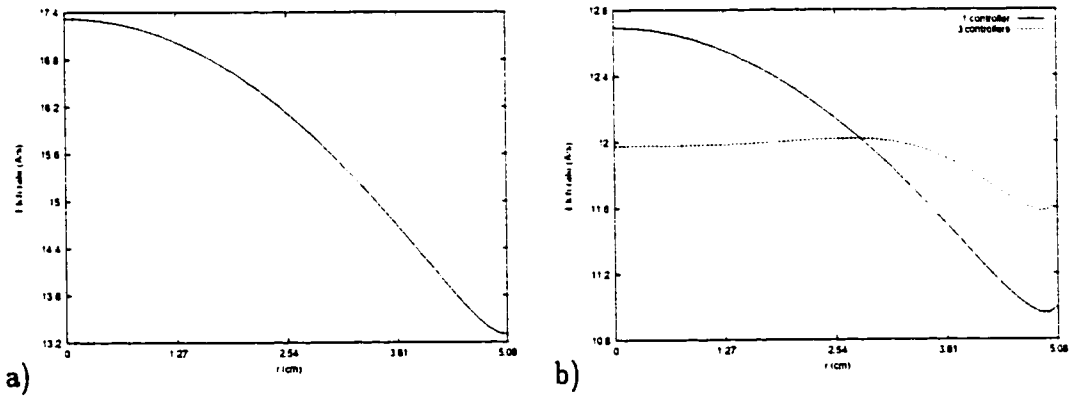

Figure 10.3: Etching rate of $a-Si$ as a function of wafer radius at final time for open-loop (a), closed-loop (b) process.

three locations across the radius of the wafer to manipulate the inlet concentration of CF_4 in the showerhead and achieve uniform etching of a 500 A amorphous silicon thin film. In practice, a variety of on-line measurement techniques can be employed to determine the thickness of the $a-Si$ film in situ (and thus, the etching rate), such as ellipsometry [75] and microwave conductivity [133]. The concentration of CF_4 at the showerhead was chosen as the manipulated variable because of its strong effect on the etching rate (this was verified with several open-loop simulation runs for different inlet CF_4 concentrations; the effect of the inlet flow rate on the etching rate was also examined and found to be less effective (see [138] for results on flow rate and etching rate dependency). Furthermore, the choice of the inlet CF_4 concentration as manipulated variable was motivated by the realization that the suppression of the radial variation of the etching rate requires the use of a manipulated variable that is distributed across the radius of the reactor. We note that in practice, the inlet carbon tetrafluoride concentration is manipulated by adjusting the composition of an inert gas such as He or Ar in the feed to the showerhead (the use of such a diluent does not effect the velocity profile inside the reactor, i.e., v_w remains constant). Finally, the manipulation of the inlet CF_4 concentration does not lead to perturbations (and possible jetting effects and instabilities) of the flow field when the controller is active, as it could happen in the case of using the flow rate in the showerhead as the manipulated variable.

Owing to the mildly nonlinear nature of the process model of Eq.10.8 (it only includes bilinear nonlinearities since the assumption of isothermal operation allows considering the reaction rate parameters independent of temperature), a proportional

integral (PI) controller with the following state-space description:

$$\begin{aligned} \dot{\xi} &= y_{sp} - y,\ \xi(0) = 0 \\ u &= K(y_{sp} - y) + \frac{1}{\tau}\xi \end{aligned} \tag{10.13}$$

was initially used to manipulate the inlet concentration of CF_4 at the showerhead to achieve offsetless set-point tracking. The area of the showerhead in which the inlet concentration of CF_4 is manipulated was assumed to be the circular area over the wafer, while in the region of the showerhead outside the wafer the feed was taken to be pure CF_4 for all times. In the controller of Eq.10.13, ξ is the controller state variable, y_{sp} denotes the set-point value of the etching rate, y denotes the *on-line measurement* of the etching rate, K is the proportional controller gain and τ is the integral time constant. The manipulated input, u, was defined as $u = \frac{c_{w,1}}{c_t}$, where $c_{w,1}$ represents the concentration of CF_4 at the showerhead, and the controlled output was defined as $y(t) = \rho_{Si}\frac{k_{etch}}{4}c_4(t, \frac{r_w}{2}, 0)(1 - \theta(t, \frac{r_w}{2}))$, where r_w is the radius of the wafer, and was computed by using 1 measurement of the etching rate at radius $r = \frac{r_w}{2}$. Note that since the etching rate setpoint y_{sp} was set equal to 12.0 A/sec, the time required for the etching of a 500 A thin film is approximately 42 sec (the corresponding time for the open-loop process is 36 sec). Figure 10.3b shows the closed-loop etching rate as a function of wafer radius, while figure 10.5a shows the corresponding manipulated input profile (note that $u = 0.0$ means that no CF_4 enters the reactor, while $u = 1.0$ means that the feed consists of pure CF_4). The controller decreases the radial nonuniformity of the etching rate to $R_M = 15.8$ % (note that in the open-loop system the nonuniformity is $R_M = 30.2$ %). Even though the use of a single PI controller reduces the film thickness nonuniformity compared to the one of the open-loop process, the reduction obtained is not significant enough, thereby motivating the design of a new feedback control system.

To further reduce the film thickness nonuniformity, we divide the showerhead area

into three concentric regions (Figure 10.4) and use three PI controllers to adjust the inlet CF_4 concentration in each one of these regions. We note that no controller was used in the showerhead region outside of the wafer, and the feed was pure CF_4. The

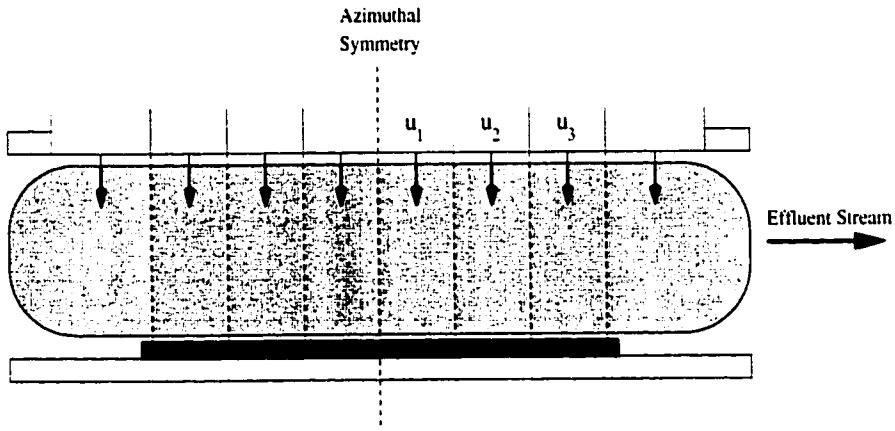

Figure 10.4: Control configuration for PE reactor.

idea for dividing the showerhead region into three concentric subregions is based on the realization that the effective control of a variable that is distributed in space (as is the case with the etching rate in this problem) should be achieved by independently-controlled manipulated inputs that are also distributed in space. The state-space representation of the feedback control system takes then the form:

$$\begin{aligned} \dot{\xi}_\kappa &= y_{sp,\kappa} - y_\kappa, \ \xi_\kappa(0) = 0, \ \ \kappa = 1,2,3 \\ u_\kappa &= K_\kappa(y_{sp,\kappa} - y_\kappa) + \frac{1}{\tau_\kappa}\xi_\kappa \end{aligned} \tag{10.14}$$

where $u_\kappa(t)$ is the $\kappa-$th control action and $r_{i,\kappa}$ and $r_{f,\kappa}$ are the internal and external radii of the region where the $\kappa-$th control action is applied. The κ-th controlled output for this region is defined as $y_\kappa(t) = \rho_{Si}\frac{k_{etch}}{4}c_4(t, r_{c,\kappa}, 0)(1 - \theta(t, r_{c,\kappa}))$, where $r_{c,\kappa}$ is the position of the κ-th $on-line$ measurement. Table 10.5 below provides the parameters and set-point values for the three PI controllers, and the radii of the regions where they are applied. Figure 10.3b shows the closed-loop etching rate in the case of using three PI controllers, while Figure 10.5b displays the corresponding

Table 10.5: Parameters for the 3 PI controllers

κ	K_κ	τ_κ (sec)	$r_{s,\kappa}$ (cm)	$r_{f,\kappa}$ (cm)	$r_{c,\kappa}$ (cm)	$y_{sp,\kappa}$ (A/sec)
1	0.1	5.0	0.00	2.00	1.00	12.0
2	0.1	5.0	2.00	3.50	2.75	12.0
3	0.1	5.0	3.50	5.08	4.00	12.0

manipulated input profiles. It is clear that the use of three spatially-distributed PI controllers has substantially reduced the film thickness nonuniformity; the nonuniformity measure for the profile of Figure 10.5 is R_M = 3.8 % which is much less than 30.2 % (uncontrolled process) and 15.8 % (single PI controller). From the above closed-loop system simulation results, it is evident that the division of the showerhead region into three concentric subregions is the main reason for the significant reduction in etching rate nonuniformity.

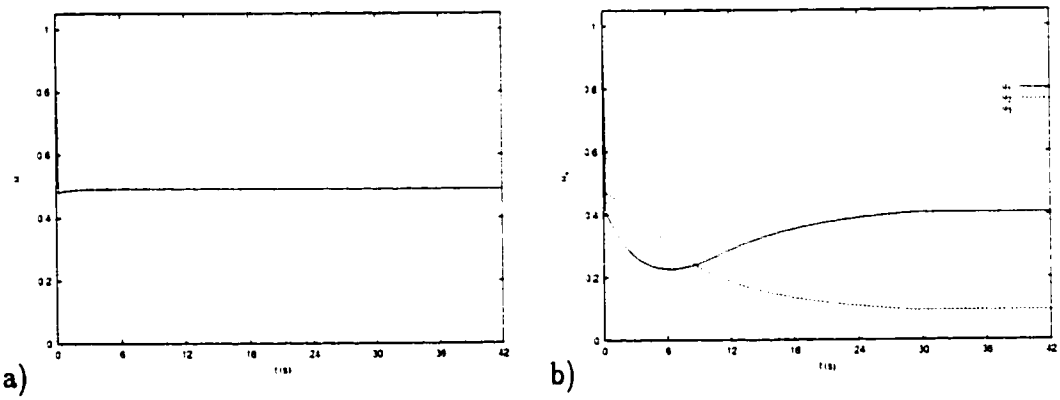

Figure 10.5: Manipulated input profiles for the case of using one PI controller (a) and three PI controllers (b).

10.5 Conclusions

This chapter focused on the implementation of a feedback control system on a parallel electrode PE process with showerhead arrangement used to etch a 500 A amorphous

silicon thin film on a 4 *in* wafer. The feedback control system consists of three spatially-distributed proportional integral controllers that use measurements of the etching rate at three locations across the wafer, to manipulate the inlet concentration of carbon tetrafluoride in the showerhead and achieve a uniform etching rate across the wafer. The controller was implemented on a detailed fundamental model of the process which accounts for diffusive and convective mass transfer, bulk and surface reactions, and nonuniform fluid flow and plasma electron density profiles. The implementation of the proposed control system was shown to reduce the etching rate nonuniformity from 30.2% to 3.8%.

Chapter 11

Conclusions

The present doctoral thesis has focused on the development of a general and practical methodology for the nonlinear model reduction and control of a general class of process models, mathematically described by dissipative partial differential equation (PDE) systems, which arise in the modeling of diffusion-convection-reaction processes with fixed and time-varying spatial domains and fluid flows. Combination of Galerkin's method with approximate inertial manifolds was used to derive low-dimensional approximations of the distributed process model, which were subsequently employed for the selection of the control configuration and the synthesis of high-performance nonlinear feedback controllers using geometric control methods and Lyapunov techniques. A rigorous analysis of the closed-loop system (distributed process model and controller) is performed to derive precise conditions which guarantee that the desired stability and performance properties are achieved in the presence of uncertainty in the values of the parameters of the process model. The developed methods are subsequently applied, via computer simulations, to industrially important transport-reaction processes such as the Czochralski crystal growth, plasma-enhanced chemical vapor deposition (PECVD) and plasma etching (PE) processes

and towards the suppression of instabilities exhibited by falling and shallow liquid films (described by the Kuramoto-Sivashinsky (KS) and Korteweg-de-Vries Burgers (KdVB) equations respectively). Specifically, the main contributions of this dissertation can be summarized as follows:

Control of quasi-linear parabolic PDE systems. A methodology was developed for the synthesis of nonlinear finite-dimensional time-varying output feedback controllers for systems of quasi-linear PDEs with time-dependent spatial domains, whose dynamics can be partitioned into slow and fast ones. Initially, a nonlinear model reduction scheme based on combination of Galerkin's method with the concept of approximate inertial manifold was employed for the derivation of low-order ordinary differential equation (ODE) systems that yield solutions which are close, up to a desired accuracy, to the ones of the PDE system, for almost all times. Then, these ODE systems were used as the basis for the explicit construction of nonlinear time-varying output feedback controllers via geometric control methods. The controllers guarantee stability and enforce the output of the closed-loop parabolic PDE system to follow, up to a desired accuracy, a prespecified response for almost all times, provided that the separation of the slow and fast dynamics is sufficiently large.

Control of quasi-linear parabolic PDE systems with uncertainty. Utilizing nonlinear order-reduction methods and a combination of geometric control concepts with Lyapunov's direct method, robust nonlinear static output feedback controllers for the systems of quasi-linear parabolic partial differential equations with time-dependent spatial domains and uncertain variables were synthesized that guarantee boundedness of the state and achieve asymptotic output tracking with arbitrary degree of asymptotic attenuation of the effect of the uncertain variables on the output of the closed-loop system.

Control of nonlinear parabolic PDE systems. A methodology was proposed for the synthesis of finite-dimensional nonlinear output feedback controllers for nonlinear parabolic partial differential equation (PDE) systems with time-dependent spatial domains. Initially, the nonlinear parabolic PDE system is expressed with respect to an appropriate time-invariant spatial coordinate and a representative (with respect to different initial conditions and input perturbations) ensemble of solutions of the resulting time-varying PDE system was constructed by computing and solving a high-order discretization of the PDE. Subsequently, Karhunen-Loève expansion was applied to the ensemble of solutions to derive a small set of empirical eigenfunctions (dominant spatial patterns) that capture almost all the energy of the ensemble of solutions. The empirical eigenfunctions were subsequently used as basis functions within a Galerkin's model reduction framework to derive low-order ordinary differential equation (ODE) systems that accurately describe the dominant dynamics of the PDE system. The ODE systems were then used for the synthesis of nonlinear output feedback controllers using geometric control methods.

Suppression of wavy behavior through feedback control. A novel approach was proposed for the suppression of wavy behavior for fluid flows that are mathematically described by dissipative partial differential systems, which employs nonlinear/linear Galerkin's method to derive low-dimensional approximations of the flow models, which are subsequently used for controller synthesis via geometric control methods. The proposed approach was applied to the KdVB and KS equations, two high-order nonlinear PDEs which describe motion of waves in a variety of fluid flow processes, to synthesize nonlinear low-dimensional output feedback controllers for the KdVB and KS equations that enhance convergence rate and achieve stabilization to spatially uniform steady-states, respectively. Furthermore, linear and bounded non-

linear stabilizing controllers were synthesized on the basis of the developed low-order approximations of the KS that address the problem of global exponential stabilization and stabilization in the presence of input constraints, respectively. It is worth noting that in the case of bounded control an explicit characterization of the limitations imposed by the input constraints on the allowable control actuator locations is provided.

Control of microelectronics manufacturing processes. The methodology developed in chapter 2 was successfully applied to design control configurations and nonlinear multivariable model-based controllers, when needed, for a variety of important microelectronic manufacturing processes. Specifically, a novel control configuration was designed and a multivariable fourth-order model-based feedback controller was synthesized for the reduction of thermal gradients inside the growing crystal in the Czochralski crystal growth process after the crystal radius has reached its final value. Also, two-dimensional dynamic models were developed for the PECVD and PE process that account for diffusive and convective mass transfer, bulk and surface reactions, and nonuniform fluid flow and plasma electron density profiles. Based on results from these models, a novel control configuration was designed and a feedback control system consisting of three spatially-distributed proportional integral controllers was synthesized and implemented to reduce the film thickness nonuniformity. In all these applications, the proposed control scheme was successfully implemented on the process and the robustness of the proposed control configuration with respect to parametric model uncertainty, exogenous disturbances and unmodeled actuator and sensor dynamics was demonstrated through simulations.

Appendix A

Basic Concepts in Process Control

Concepts of relative order and characteristic matrix

First, the Lie derivative of the scalar function $h_{0i}(t, x_s)$ with respect to the vector function $f_0(t, x_s)$ is defined as $L_{f_0} h_{0i}(t, x_s) = \frac{\partial h_{0i}}{\partial x_s} f_0(t, x_s) + \frac{\partial h_{0i}}{\partial t}$ (this definition of Lie derivative was introduced in [134] and is different than the standard one used in [98] for the case of time-invariant h_{0i}, f_0), $L^k_{f_0} h_{0i}(t, x_s)$ denotes the k-th order Lie derivative and $L_{g_{0l}} L^k_{f_0} h_{0l}(t, x_s)$ denotes the mixed Lie derivative. Now, referring to the system of Eq.2.24, we set $\mathcal{A}_s(t)x_s + f_s(t, x_s, 0) = f_0(t, x_s)$, $\mathcal{B}_s(t) = g_0(t, x_s)$, $\mathcal{C}_i(t)x_s = h_{0i}(t, x_s)$ to obtain:

$$\begin{aligned} \frac{dx_s}{dt} &= f_0(t, x_s) + g_0(t, x_s)u \\ y_{cs_i} &= h_{0i}(t, x_s) \end{aligned} \tag{A.1}$$

For the above system, the relative order of the output y_{cs_i} with respect to the vector of manipulated inputs u is defined as the smallest integer r_i for which:

$$\left[L_{g_{0_1}} L^{r_i-1}_{f_0} h_{0i}(t, x_s) \cdots L_{g_{0_l}} L^{r_i-1}_{f_0} h_{0i}(t, x_s)\right] \not\equiv [0 \cdots 0] \tag{A.2}$$

or $r_i = \infty$ if such an integer does not exist. Furthermore, the matrix:

$$C_0(t, x_s) = \begin{bmatrix} L_{g_{0_1}} L_{f_0}^{r_1-1} h_{01}(t, x_s) & \cdots & L_{g_{0_l}} L_{f_0}^{r_1-1} h_{01}(t, x_s) \\ L_{g_{0_1}} L_{f_0}^{r_1-1} h_{01}(t, x_s) & & \\ L_{g_{0_1}} L_{f_0}^{r_2-1} h_{02}(t, x_s) & \cdots & L_{g_{0_l}} L_{f_0}^{r_2-1} h_{02}(t, x_s) \\ \vdots & & \\ L_{g_{0_1}} L_{f_0}^{r_l-1} h_{0l}(t, x_s) & \cdots & L_{g_{0_l}} L_{f_0}^{r_l-1} h_{0l}(t, x_s) \end{bmatrix} \tag{A.3}$$

is the characteristic matrix of the system of Eq.A.1.

Appendix B

Proofs of chapter 2

B.1 Proof of proposition 2.1

The proof of the proposition will be obtained by following a two-step approach. In the first step, we will show that the system of Eq.2.14 is exponentially stable, provided that the initial conditions and ϵ are sufficiently small. The exponential stability property will be used in the second step to prove closeness of solutions as given in Eq.2.23.

Exponential stability: The system of Eq.2.14 can be equivalently written as:

$$\begin{aligned} \frac{dx_s}{dt} &= \mathcal{A}_s(t)x_s + f_s(t, x_s, 0) + [f_s(t, x_s, x_f) - f_s(t, x_s, 0)] \\ \epsilon\frac{\partial x_f}{\partial t} &= \mathcal{A}_{f\epsilon}(t)x_f + \epsilon f_f(t, x_s, x_f) \end{aligned} \tag{B.1}$$

Let μ_1^*, μ_2^* with $\mu_1^* \geq a_5$ and $\mu_2^* \geq b_5$ be two positive real numbers such that if $|x_s| \leq \mu_1^*$ and $\|x_f\|_2 \leq \mu_2^*$, then there exist positive real numbers (k_1, k_2, k_3) such that

$$\begin{aligned} |f_s(t, x_s, x_f) - f_s(t, x_s, 0)| &\leq k_1\|x_f\|_2 \\ \|f_f(t, x_s, x_f)\|_2 &\leq k_2|x_s| + k_3\|x_f\|_2 \end{aligned} \tag{B.2}$$

Pick $\mu_1 < a_5 < \mu_1^*$ and $\mu_2 < b_6 < \mu_2^*$.

Consider the smooth time-varying function $L : \mathcal{H}_s(t) \times \mathcal{H}_f(t) \rightarrow \mathbb{R}_{\geq 0}$:

$$L(t, x_s, x_f) = V(t, x_s) + W(t, x_f) \tag{B.3}$$

where $V(t, x_s)$ and $W(t, x_f)$ were defined in assumptions 2.3 and 2.4, respectively, as a Lyapunov function candidate for the system of Eq.B.1. From Eq.2.20 and Eq.2.22, we have that $L(t, x_s, x_f)$ is positive definite, proper (tends to $+\infty$ as $|x_s| \rightarrow \infty$, or $\|x_f\|_2 \rightarrow \infty$) and decrescent, with respect to its arguments. Computing the time-derivative of L along the trajectories of the system of Eq.B.1, and using the bounds of Eq.2.20 and Eq.2.22 and the estimates of Eq.B.2, the following expressions can be obtained:

$$\begin{aligned}
\dot{L}(t, x_s, x_f) &= \frac{\partial V}{\partial t} + \frac{\partial V}{\partial x_s}\dot{x}_s + \frac{\partial W}{\partial t} + \frac{\partial W}{\partial x_f}\dot{x}_f \\
&= \frac{\partial V}{\partial t} + \frac{\partial V}{\partial x_s}[\mathcal{A}_s(t)x_s + f_s(t, x_s, 0)] + \frac{\partial V}{\partial x_s}[f_s(t, x_s, x_f) - f_s(t, x_s, 0)] \\
&\quad + \frac{\partial W}{\partial t} + \frac{1}{\epsilon}\frac{\partial W}{\partial x_f}\mathcal{A}_{f\epsilon}(t)x_f + \frac{\partial W}{\partial x_f}f_f(t, x_s, x_f) \\
&\leq -a_3|x_s|^2 + a_4k_1|x_s|\|x_f\|_2 + b_5\|x_f\|_2^2 \\
&\quad - \frac{b_3}{\epsilon}\|x_f\|_2^2 + b_4\|x_f\|_2(k_2|x_s| + k_3\|x_f\|_2) \\
&\leq -a_3|x_s|^2 + (a_4k_1 + b_4k_2)|x_s|\|x_f\|_2 - (\frac{b_3}{\epsilon} - b_4k_3 - b_5)\|x_f\|_2^2 \\
&\leq -\begin{bmatrix} |x_s| & \|x_f\|_2 \end{bmatrix} \begin{bmatrix} a_3 & -\frac{a_4k_1 + b_4k_2}{2} \\ -\frac{a_4k_1 + b_4k_2}{2} & \frac{b_3}{\epsilon} - b_4k_3 - b_5 \end{bmatrix} \begin{bmatrix} |x_s| \\ \|x_f\|_2 \end{bmatrix}
\end{aligned} \tag{B.4}$$

Defining $\epsilon_1 = \dfrac{(a_3 - \sqrt{\delta})b_3}{(a_3 - \sqrt{\delta})(b_5 + b_4k_3 + \sqrt{\delta}) + \left(\dfrac{a_4k_1 + b_4k_2}{2}\right)^2}$, where $\delta \in \mathbb{R}_{>0}$, we have that if $\epsilon \in (0, \epsilon_1]$ then $\dot{L}(x_s, x_f) \leq -\delta(|x_s|^2 + \|x_f\|_2^2)$, which from the properties of L directly implies that the state of the system of Eq.B.1 is exponentially stable, i.e. there exists a positive real number σ such that:

$$\begin{bmatrix} |x_s| \\ \|x_f\|_2 \end{bmatrix} \leq e^{-\sigma t} \begin{bmatrix} |x_s(0)| \\ \|x_f(0)\|_2 \end{bmatrix} \tag{B.5}$$

Closeness of solutions:

We will initially show the closeness of solution result for the x_f-states, and then for the x_s-states (note that from the first part of the proof $\epsilon \in (0, \epsilon_1]$). To establish the estimate for the x_f-states, we initially prove that the off manifold transients decay quickly (the decay rate will be precisely given below) to the manifold. To this end, we define the error vector $e_f(t) = x_f(t) - \Sigma(t, x_s, 0, \epsilon)$, differentiate $e_f(t)$ with respect to time and multiply the resulting system with ϵ, to obtain the following dynamical system:

$$\frac{\partial e_f}{\partial \tau} = \mathcal{A}_{f\epsilon}(t)e_f + \epsilon f_f(t, x_s, e_f + \Sigma(t, x_s, 0, \epsilon)) - \epsilon f_f(t, x_s, \Sigma(t, x_s, 0, \epsilon)) \quad \text{(B.6)}$$

Referring to the above system with $\epsilon = 0$, we have from assumption 2.4 that there exists a Lyapunov functional $\bar{W} : \mathcal{H}_f(t) \to \mathbb{R}_{\geq 0}$ and a set of positive real numbers $(\bar{b}_1, \bar{b}_2, \bar{b}_3, \bar{b}_4, \bar{b}_5, \bar{b}_6)$, such that for all $e_f \in \mathcal{H}_f(t)$ that satisfy $\|e_f\|_2 \leq \bar{b}_6$, the following conditions hold:

$$\begin{aligned} \bar{b}_1\|e_f(\tau)\|_2^2 &\leq \bar{W}(t, e_f(\tau)) \leq \bar{b}_2\|e_f(\tau)\|_2^2 \\ \frac{\partial \bar{W}}{\partial e_f}\mathcal{A}_{f\epsilon}(t)e_f &\leq -\bar{b}_3\|e_f(\tau)\|_2^2 \\ \|\frac{\partial \bar{W}}{\partial e_f}\|_2 &\leq \bar{b}_4\|e_f(\tau)\|_2 \\ \|\frac{\partial \bar{W}}{\partial t}\|_2 &\leq \bar{b}_5\|e_f(\tau)\|_2^2 \end{aligned} \quad \text{(B.7)}$$

Computing the time-derivative of $\bar{W}(t, e_f)$ along the trajectories of the system of Eq.B.6 and using that $\|f_f(t, x_s, e_f + \Sigma(t, x_s, 0, \epsilon)) - f_f(t, x_s, \Sigma(t, x_s, 0, \epsilon))\|_2 \leq k_5\|e_f\|_2$, where k_5 is a positive real number (which follows from the fact that the states (x_s, e_f) are bounded), we have:

$$\begin{aligned} \frac{\partial \bar{W}}{\partial \tau} &\leq -\bar{b}_3\|e_f\|_2^2 + \epsilon\bar{b}_5\|e_f\|_2^2 + \epsilon\bar{b}_4\|e_f\|_2 k_5\|e_f\|_2 \\ &\leq -(\bar{b}_3 - \epsilon(\bar{b}_4 k_5 + \bar{b}_5)\|e_f\|_2^2 \end{aligned} \quad \text{(B.8)}$$

Set $\epsilon_2 = \dfrac{\bar{b}_3 - \bar{\delta}}{\bar{b}_4 k_5 + \bar{b}_5}$ and $\epsilon^* = min\{\epsilon_1, \epsilon_2\}$, where $\bar{\delta} \in \mathbb{R}_{>0}$. From the above inequality

we have that if $\epsilon \in (0, \epsilon^*]$, the following bound holds for $\|e_f(\tau)\|_2$ for all $t \in [0, \infty)$:

$$\|e_f(\tau)\|_2 \leq K_3 \|e_f(0)\|_2 e^{-\gamma \frac{t}{\epsilon}} \tag{B.9}$$

where K_3, γ are positive real numbers. From the series expansion of $\Sigma(t, x_s, 0, \epsilon)$ and the definition of the $O(\epsilon^{k+1})$, we also have that:

$$\|\Sigma(t, x_s, 0, \epsilon) - \tilde{x}_f\|_2 \leq \tilde{k}_1 \epsilon^{k+1} \tag{B.10}$$

where $\tilde{x}_f = \Sigma_0(t, \tilde{x}_s, 0) + \epsilon \Sigma_1(t, \tilde{x}_s, 0) + \epsilon^2 \Sigma_2(t, \tilde{x}_s, 0) + \cdots + \epsilon^k \Sigma_k(t, \tilde{x}_s, 0)$ and $\tilde{k}_1$ is a positive number. Combining the bounds of Eqs.B.9-B.10, the following bound can be written:

$$\|x_f - \tilde{x}_f\|_2 \leq \tilde{k}_1 \epsilon^{k+1} + \tilde{k}_2 e^{-\gamma \frac{t}{\epsilon}}, \quad \forall\, t \in [0, \infty) \tag{B.11}$$

where $\tilde{k}_2$ is a positive number. It follows directly that $x_f = \tilde{x}_f + O(\epsilon^{k+1}), \quad \forall\, t \in [t_b, \infty)$, where t_b is the time required for x_f to approach the inertial manifold (i.e. $\tilde{k}_2 e^{-\gamma \frac{t}{\epsilon}} = 0$ for $t \geq t_b$).

Defining the error coordinate $e_s(t) = x_s(t) - \tilde{x}_s(t)$ and differentiating $e_s(t)$ with respect to time, the following system can be obtained:

$$\frac{de_s}{dt} = \mathcal{A}_s(t) e_s + f_s(t, \tilde{x}_s + e_s, x_f) - f_s(t, \tilde{x}_s, \tilde{x}_f) \tag{B.12}$$

The representation of the system of Eq.B.12 in the fast time-scale τ takes the form:

$$\frac{de_s}{d\tau} = \epsilon [\mathcal{A}_s(t) e_s + f_s(t, \tilde{x}_s + e_s, x_f) - f_s(t, \tilde{x}_s, \tilde{x}_f)] \tag{B.13}$$

where $(e_s, \tilde{x}_s, t)$ can be considered approximately constant, and thus based on $|e_s(0)| = 0$ and the continuity of solutions for $e_s(\tau)$, the following bound holds:

$$|e_s(\tau)| \leq \epsilon k_7 \tau_b, \quad \forall\, \tau \in [0, \tau_b) \tag{B.14}$$

where k_7 is a positive real number and $\tau_b = \frac{t_b}{\epsilon} = O(1)$. Based on the fact that $\tilde{x}_s(t)$, $\tilde{x}_f(t)$ decay exponentially to zero, and from assumption 2.3, we have that the system:

$$\frac{de_s}{dt} = \mathcal{A}_s(t) e_s + f_s(t, \tilde{x}_s + e_s, \tilde{x}_f) - f_s(t, \tilde{x}_s, \tilde{x}_f) \tag{B.15}$$

is exponentially stable, which implies that there exists a smooth Lyapunov function $\tilde{V} : \mathcal{H}_s \to \mathbb{R}_{\geq 0}$ and a set of positive real numbers $(\tilde{a}_1, \tilde{a}_2, \tilde{a}_3, \tilde{a}_4, \tilde{a}_5)$, such that for all $e_s \in \mathcal{H}_s$ that satisfy $|e_s| \leq \tilde{a}_5$, the following conditions hold:

$$\begin{aligned} &\tilde{a}_1|e_s|^2 \leq \tilde{V}(t, e_s) \leq \tilde{a}_2|e_s|^2 \\ &\dot{\tilde{V}}(e_s) = \frac{\partial \tilde{V}}{\partial t} + \frac{\partial \tilde{V}}{\partial e_s}[\mathcal{A}_s(t)e_s + f_s(t, \tilde{x}_s + e_s, \tilde{x}_f) - f_s(t, \tilde{x}_s, \tilde{x}_f)] \leq -\tilde{a}_3|e_s|^2 \\ &|\frac{\partial \tilde{V}}{\partial e_s}| \leq \tilde{a}_4|e_s| \end{aligned} \tag{B.16}$$

From the assumption that $f_s(t, x_s, x_f)$ is Lipschitz continuous with respect to x_s and x_f :

$$|f_s(t, \tilde{x}_s + e_s, x_f) - f_s(t, \tilde{x}_s + e_s, \tilde{x}_f)| \leq \tilde{k}\|x_f - \tilde{x}_f\|_2 \tag{B.17}$$

where $\tilde{k}$ is a positive number. Substituting the inequality of Eq.B.11 to Eq.B.17 the following bound is obtained:

$$|f_s(t, \tilde{x}_s + e_s, x_f) - f_s(t, \tilde{x}_s + e_s, \tilde{x}_f)| \leq \tilde{k}\tilde{k}_1\epsilon^{k+1} + \tilde{k}\tilde{k}_2 e^{-\gamma\frac{t}{\epsilon}} \tag{B.18}$$

Computing the time-derivative of $\tilde{V}(t, e_s)$ along the trajectories of the system of Eq.B.12 and using that for $t \in [0, \infty)$ the bound described in Eq. B.18 holds, we have for all $t \in [0, \infty)$:

$$\dot{\tilde{V}}(t, e_s) \leq -\tilde{a}_3|e_s|^2 + (\tilde{k}_1\epsilon^{k+1} + \tilde{k}_2 e^{-\gamma\frac{t}{\epsilon}})\tilde{a}_4|e_s| \tag{B.19}$$

From the above inequality, using corollary 5.3 in [107] and the fact that $|e_s(0)| = 0$, we have that the following bound holds for $|e_s(t)|$ for all $t \in [0, \infty)$:

$$|e_s(t)| \leq \bar{K}e^{-\gamma\frac{t}{\epsilon}} + \bar{K}\epsilon^{k+1} \tag{B.20}$$

where $\bar{K}, \bar{K}$ are positive real numbers. Since the term $\bar{K}e^{-\gamma\frac{t}{\epsilon}}$ vanishes outside the interval $[0, t_b)$, it follows from Eq.B.20 that for all $t \in [t_b, \infty)$:

$$|e_s(t)| \leq \bar{K}\epsilon^{k+1} \tag{B.21}$$

From the above inequality, the estimate $x_s(t) = \tilde{x}_s(t) + O(\epsilon^{k+1})$, for $t \geq t_b$, follows directly. $\triangle$

B.2 Proof of theorem 2.1

Substituting the output feedback controller of Eq.2.29 into the system of Eq.2.14, we get:

$$\begin{aligned}
\frac{d\eta}{dt} &= \mathcal{A}_s(t)\eta + \mathcal{B}_s(t)\left(p_0(t,\eta) + Q_0(t,\eta)v + \epsilon[p_1(t,\eta) + Q_1(t,\eta)v]\right) \\
&\quad + f_s(t,\eta,\epsilon\Sigma_1(t,\eta,\bar{u}_0)) + LS(t)(x_s + x_f - \eta - \epsilon\Sigma_1(t,\eta,\bar{u}_0)) \\
\frac{dx_s}{dt} &= \mathcal{A}_s(t)x_s + \mathcal{B}_s(t)\left(p_0(t,\eta) + Q_0(t,\eta)v + \epsilon[p_1(t,\eta) + Q_1(t,\eta)v]\right) \\
&\quad + f_s(t,x_s,x_f) \\
\epsilon\frac{\partial x_f}{\partial t} &= \mathcal{A}_{f\epsilon}(t)x_f + \epsilon\mathcal{B}_f(t)\left(p_0(t,\eta) + Q_0(t,\eta)v + \epsilon[p_1(t,\eta) + Q_1(t,\eta)v]\right) \\
&\quad + \epsilon f_f(t,x_s,x_f) \\
y_{ci} &= C_i(t)x_s + C_i(t)x_f, \quad i = 1,\ldots,l
\end{aligned} \tag{B.22}$$

Performing a two-time-scale decomposition in the above system, the fast subsystem takes the form:

$$\frac{\partial x_f}{\partial \tau} = \mathcal{A}_{f\epsilon}(t)x_f \tag{B.23}$$

which is assumed to be exponentially stable (assumption 2.4). The $O(\epsilon^2)$ approximation of the closed-loop inertial form is:

$$\begin{aligned}
\frac{d\eta}{dt} &= \mathcal{A}_s(t)\eta + \mathcal{B}_s(t)\left(p_0(t,\eta) + Q_0(t,\eta)v + \epsilon[p_1(t,\eta) + Q_1(t,\eta)v]\right) \\
&\quad + f_s(t,\eta,\epsilon\Sigma_1(t,\eta,\bar{u}_0)) + LS(t)(x_s + \epsilon\Sigma_1(t,x_s,\bar{u}_0) - \eta - \epsilon\Sigma_1(t,\eta,\bar{u}_0)) \\
\frac{dx_s}{dt} &= \mathcal{A}_s(t)x_s + \mathcal{B}_s(t)\left(p_0(t,\eta) + Q_0(t,\eta)v + \epsilon[p_1(t,\eta) + Q_1(t,\eta)v]\right) \\
&\quad + f_s(t,x_s,\epsilon\Sigma_1(t,x_s,\bar{u}_0)) \\
y_{csi} &= C_i(t)x_s + \epsilon C_i(t)\Sigma_1(t,x_s,\bar{u}_0), \quad i = 1,\ldots,l
\end{aligned} \tag{B.24}$$

Using the hypothesis $\eta(0) = x_s(0)$, the above system can be written as:

$$\begin{aligned}
\frac{dx_s}{dt} &= \mathcal{A}_s(t)x_s + \mathcal{B}_s(t)\left(p_0(t,\eta) + Q_0(t,\eta)v + \epsilon[p_1(t,x_s) + Q_1(t,x_s)v]\right) \\
&\quad + f_s(t, x_s, \epsilon\Sigma_1(t, x_s, \bar{u}_0)) \\
y_{cs_i} &= C_i(t)x_s + \epsilon C_i(t)\Sigma_1(t, x_s, \bar{u}_0), \quad i = 1, \ldots, l
\end{aligned} \tag{B.25}$$

Computing the time-derivatives of the controlled output y_{cs_i} up to order r_i and substituting into Eq.2.31, one can show that the input/output response of Eq.2.31 is enforced in the above closed-loop system. Furthermore, an approach, similar to the one in [134], can be followed to establish that assumptions 2.1 and 2.2 of the theorem guarantee that the system of Eq.B.25 is locally exponentially stable. Therefore, we have that system of Eq.B.24 is locally exponentially stable and its outputs y_{cs_i}, $i = 1, \ldots, l$, change according to Eq.2.31. A direct application of the result of proposition 2.1 then yields that there exist positive real numbers $\tilde{\mu}_1, \tilde{\mu}_2, \tilde{\epsilon}^*$ such that if $|x_s(0)| \leq \tilde{\mu}_1$, $\|x_f(0)\|_2 \leq \tilde{\mu}_2$ and $\epsilon \in (0, \tilde{\epsilon}^*]$, the closed-loop infinite-dimensional system is exponentially stable and the relation of Eq.2.30 holds. $\triangle$

Appendix C

Proofs of chapter 3

Proof of Theorem 3.1

Substituting the controller of Eq.3.17 into the parabolic PDE system of Eq.3.8, we obtain:

$$\begin{aligned} \dot{x} &= \mathcal{A}(t)x + \mathcal{B}(t)a_0(t, x_s, x_f, \bar{v}) + f(t, x) + \mathcal{W}(t, x, \theta) \\ y_c &= \mathcal{C}(t)x, \;\; y_m = \mathcal{S}(t)x \end{aligned} \tag{C.1}$$

One can easily verify that assumption 3.2 holds for the above system, and thus, it can be written in the following form:

$$\frac{dx_s}{dt} = \mathcal{A}_s(t)x_s + \mathcal{B}_s(t)a_0(t, x_s, x_f, \bar{v}) + f_s(t, x_s, x_f) + \mathcal{W}_s(t, x_s, x_f, \theta) \tag{C.2}$$

$$\epsilon\frac{dx_f}{dt} = \mathcal{A}_{f\epsilon}(t)x_f + \epsilon\mathcal{B}_f(t)a_0(t, x_s, x_f, \bar{v}) + \epsilon f_f(t, x_s, x_f) + \epsilon\mathcal{W}_f(t, x_s, x_f, \theta)$$

Rewriting the above system in the fast time-scale $\tau = \frac{t}{\epsilon}$ and setting $\epsilon = 0$, we obtain the following infinite-dimensional fast subsystem from the system of Eq.C.2:

$$\frac{\partial x_f}{\partial \tau} = \mathcal{A}_{f\epsilon}(t)x_f \tag{C.3}$$

which is globally exponentially stable. Setting $\epsilon = 0$ in the system of Eq.C.2, we have that $x_f = 0$ and thus, the finite-dimensional slow system takes the form:

$$\begin{aligned} \frac{dx_s}{dt} &= F_0(t, x_s) + \sum_{i=1}^{l} \mathcal{B}_0^i(t) a_0^i(t, x_s, 0, \bar{v}) + \mathcal{W}_0(t, x_s, 0, \theta) \\ y_{c_i} &= C_i(t) x_s =: h_{i0}(t, x_s) \end{aligned} \tag{C.4}$$

For the above system, there exists a $\phi \in (0, \phi^*]$ such that if the following bound $\max\{|x_s(0)|, ||\theta||, ||\dot{\theta}||, ||\bar{v}||\} \leq \delta$ holds, then its state is bounded and its outputs satisfy $\limsup_{t \to \infty} |y_{c_i} - v_i| \leq O(\phi)$, $i = 1, \ldots, l$. Finally, since the infinite-dimensional fast subsystem of Eq.3.11 is exponentially stable, we can use standard singular perturbation arguments to obtain that there exists an $\epsilon^*(\phi)$, such that if $\epsilon \in (0, \epsilon^*(\phi)]$, $\max\{|x_s(0)|, ||x_f(0)||_2, ||\theta||, ||\dot{\theta}||, ||\bar{v}||\} \leq \delta$, then the state of the closed-loop parabolic PDE system of Eq.C.1 is bounded and that its outputs satisfy the relation of Eq.3.18.

$\triangle$

Appendix D

Proofs of chapter 4

Proof of Theorem 4.1

Substituting the controller of Eq.4.37 into the infinite-dimensional system of Eq.4.9, we obtain:

$$\begin{aligned} \frac{d\eta}{dt} &= \mathcal{L}_s(t,\eta) + \mathcal{B}_s(t)u(t,\eta) + f_s(t,\eta) + L\,(y_m - \mathcal{S}(t)\eta) \\ \dot{x} &= \mathcal{L}(t,x) + \mathcal{B}(t)[p(t,\eta) + Q(t,\eta)v] + f(t,x), \;\; x(0) = x_0 \\ y_c &= \mathcal{C}(t)x, \;\; y_m = \mathcal{S}(t)x \end{aligned} \tag{D.1}$$

A direct application of Galerkin's method to the above system with the Hilbert spaces $\mathcal{H}_s = span\{\phi_1, \phi_2, \ldots, \phi_m\}$ and $\mathcal{H}_f = span\{\phi_{m+1}, \phi_{m+2}, \ldots\}$, and the orthogonal projection operators P_s and P_f such that $x_s = P_s x$, $x_f = P_f x$, yields:

$$\begin{aligned} \frac{d\eta}{dt} &= \mathcal{L}_s(t,\eta) + \mathcal{B}_s(t)u(t,\eta) + f_s(t,\eta) + L\,(y_m - \mathcal{S}(t)\eta) \\ \frac{dx_s}{dt} &= \mathcal{L}_s(t,x_s,x_f) + \mathcal{B}_s(t)[p(t,\eta) + Q(t,\eta)v] + f_s(t,x_s,x_f) \\ \frac{\partial x_f}{\partial t} &= \mathcal{L}_f(t,x_s,x_f) + \mathcal{B}_f(t)[p(t,\eta) + Q(t,\eta)v] + f_f(t,x_s,x_f) \end{aligned} \tag{D.2}$$

or

$$\begin{aligned}
\frac{d\eta}{dt} &= \mathcal{L}_s(t,\eta) + \mathcal{B}_s(t)[p(t,\eta) + Q(t,\eta)v] + f_s(t,\eta) + L\,(y_m - S(t)\eta) \\
\frac{dx_s}{dt} &= \mathcal{L}_s(t,x_s,x_f) + \mathcal{B}_s(t)[p(t,\eta) + Q(t,\eta)v] + f_s(t,x_s,x_f) \\
\epsilon\frac{\partial x_f}{\partial t} &= \epsilon L_{fs}(t)x_s + L_f(t)x_f + \epsilon\bar{f}_f(t,x_s,x_f) + \epsilon\mathcal{B}_f(t)[p(t,\eta) + Q(t,\eta)v] \\
&\quad + \epsilon f_f(t,x_s,x_f)
\end{aligned} \tag{D.3}$$

The system of Eq.D.3 is in the standard singularly perturbed form (see [109] for a precise definition of standard form), with x_s being the slow states and x_f being the fast states. Introducing the fast time-scale $\tau = \frac{t}{\epsilon}$ and setting $\epsilon = 0$, we obtain the following infinite-dimensional fast subsystem from the system of Eq.D.3:

$$\frac{\partial x_f}{\partial \tau} = L_f(t)x_f \tag{D.4}$$

Since $L_f(t)$ is a stable matrix, we have that the above system is globally exponentially stable. Setting $\epsilon = 0$ in the system of Eq.D.3, we have that $x_f = 0$ and thus, the finite-dimensional slow system takes the form:

$$\begin{aligned}
\frac{d\eta}{dt} &= \mathcal{L}_s(t,\eta) + \mathcal{B}_s(t)[p(t,\eta) + Q(t,\eta)v] + f_s(t,\eta) + L\,(y_m - S(t)\eta) \\
\frac{dx_s}{dt} &= \mathcal{L}_s(t,x_s,0) + f_s(t,x_s,0) + \mathcal{B}_s(t)[p(t,\eta) + Q(t,\eta)v] \\
&=: f(t,x_s) + g(t,x_s)[p(t,\eta) + Q(t,\eta)v] \\
y_{cs_i} &= C_i(t)x_s =: h_i(t,x_s)
\end{aligned} \tag{D.5}$$

For the above system, one can show (see [134, 98] for details) that it is locally exponentially stable provided that assumptions 1 and 2 of the theorem hold and that the output follows the reference input. Finally, since the infinite-dimensional fast subsystem of Eq.D.4 is exponentially stable, an application of proposition 1 in Chapter 2 (singular perturbation stability result for infinite dimensional systems) yields that there exists an ϵ^*, such that if $\epsilon \in (0,\epsilon^*]$, $\max\{|x_s(0)|, ||x_f(0)||_2\} \leq \delta$, then the state of the closed-loop parabolic PDE system is exponentially stable and that its outputs satisfy the relation of Eq.4.38. $\triangle$

Appendix E

View Factors and Crystal Radius Control for the Cz Process

E.1 View factors

In order to calculate the radiative heat transfer between the crystal, the surfaces of the chamber, and the surface of the melt we need to take into account the geometric relations between the corresponding surfaces. These relations are expressed by utilizing the concept of view factor. In particular, the differential view factor $dF_{1\to 2}$ is defined as the fraction of the energy which arrives at a differential black element dA_2 over the energy that leaves a differential black surface element dA_1 [157]. From this definition, it follows that the view factor $dF_{1\to 2}$ depends exclusively on the size of dA_2 and its orientation with respect to dA_1. The view factor definition can be extended to cover the full surfaces A_1 and A_2 and is given from the equation:

$$F_{1\to 2} = \frac{1}{A_1}\int_{A_1}\int_{A_2^{vis}} \frac{cos\beta_1\, cos\beta_2}{\pi s^2} dA_2\, dA_1 \qquad \text{(E.1)}$$

where A_1 and A_2 are the areas of the surfaces, A_2^{vis} is the area of the surface 2 which is *visible* to surface 1, β_1 and β_2 are the angles between the unit normal vectors to the

corresponding surfaces and the line connecting the two points, and s is the length of this line. Based on the above definitions the following properties hold:

I) Reciprocity:

$$A_1 F_{1\to 2} = A_2 F_{2\to 1} \tag{E.2}$$

where A_i is the surface area and $F_{i\to j}$ is the view factor of j with respect to i.

II) The view factors of surfaces that form a complete enclosure satisfy:

$$\sum_{i=1}^{n} F_{k\to i} = 1, \quad k = 1, \ldots, n \tag{E.3}$$

where n is the total number of surfaces that form the enclosure.

In the process model of Eq.5.1, the view factors $F_{cr\to m}(\cdot,\cdot)$, $F_{cr\to ch}(\cdot,\cdot)$, $F_{cr\to amb}(\cdot,\cdot)$ and $F_{cr\to i}(\cdot,\cdot)$ were separately computed by decomposing the corresponding complex geometries into simple geometries for which analytical computation of the view factors is possible. The reader may refer to [166] for more results on the computation of view factors for the Czochralski crystal growth process. Specifically, the following simple geometries were utilized:

Directly opposed parallel annuli (Figure E.1a) [122]:

$$F_{1\to4} = \frac{1}{2}\left[\frac{R_4^2 - r_3^2}{r_1^2} - \sqrt{\left(1 + \frac{R_4^2 + L^2}{r_1^2}\right)^2 - 4\frac{R_4^2}{r_1^2}} - \sqrt{\left(1 + \frac{r_3^2 + L^2}{r_1^2}\right)^2 - 4\frac{r_3^2}{r_1^2}}\right] \quad \text{(E.4)}$$

$$F_{2\to4} = \frac{1}{2(R_2^2 - r_1^2)}\left[\sqrt{(R_2^2 + r_3^2 + L^2)^2 - (2r_3^2R_2^2)^2} - \sqrt{(R_2^2 + R_4^2 + L^2)^2 - (2R_2^2R_4^2)^2} + \sqrt{(r_1^2 + R_4^2 + L^2)^2 - (2r_1^2R_4^2)^2} - \sqrt{(r_1^2 + r_3^2 + L^2)^2 - (2r_1^2r_3^2)^2}\right] \quad \text{(E.5)}$$

Directly opposed parallel disks (Figure E.1b) [122]:

$$F_{1\to2} = \frac{1}{2}\left[1 + \frac{R_2^2 - L^2}{R_1^2} - \sqrt{\left(1 + \frac{R_2^2 + L^2}{R_1^2}\right)^2 - 4\frac{R_2^2}{R_1^2}}\right] \quad \text{(E.6)}$$

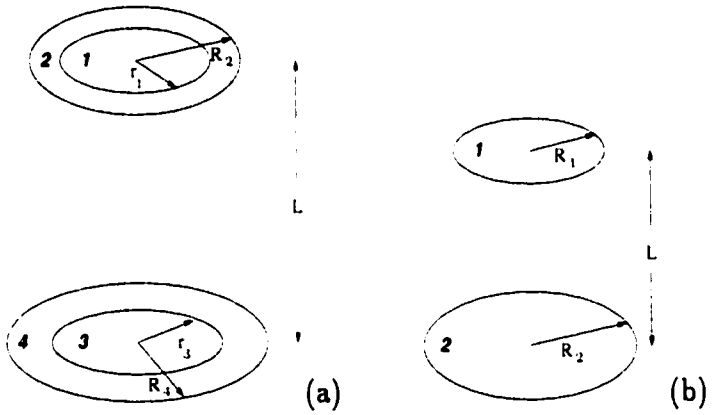

Figure E.1: View factors: a) annulus to annulus, b) disk to disk.

Annulus to cylinder (annulus is on the top of the cylinder) (Figure E.2a) [122]:

$$F_{2\to4} = \frac{1}{2}\left[1 + \frac{1}{2(R^2 - r^2)}\left(L\sqrt{4R^2 + L^2} - \sqrt{(r^2 + R^2 + L^2)^2 - (2r^2R^2)^2}\right)\right] \quad \text{(E.7)}$$

$$F_{1\to4} = \frac{1}{2}\left[1 - \frac{R^2 + L^2}{r^2} + \sqrt{\left(1 + \frac{R^2 + L^2}{r^2}\right)^2 - 4\frac{R^2}{r^2}}\right] \quad \text{(E.8)}$$

Cylinder to disk (Figure E.2b) [148]:

$$F_{1\to2} = \frac{1}{2\pi}\left\{cos^{-1}\left(\frac{l^2 - R^2 + r^2}{l^2 + R^2 - r^2}\right) - \frac{r}{2l}\left[sin^{-1}\left(\frac{r}{R}\right)\left(\frac{l^2 - R^2 + r^2}{r^2}\right)\right.\right.$$
$$\left.\left. + cos^{-1}\left(\frac{r(l^2 - R^2 + r^2)}{R(l^2 + R^2 - r^2)}\right)\sqrt{\left(\frac{r^2 + R^2 + L^2}{r^2}\right)^2 - 4\frac{R^2}{r^2}} - \frac{\pi(l^2 + R^2 - r^2)}{2r^2}\right]\right\} \quad \text{(E.9)}$$

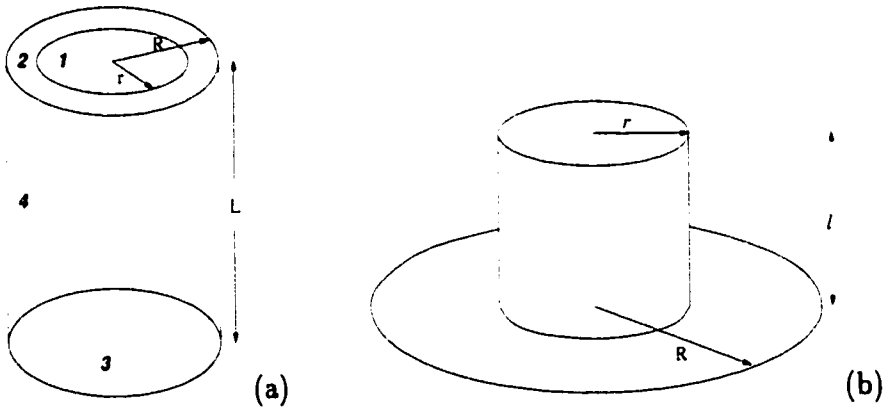

Figure E.2: View factors: a) annulus to cylinder, b) cylinder to disk.

Based on the above view factors, it is possible to find the view factors between cylinders for the following two configurations.

Cylinder to cylinder (configuration I; Figure E.3a) [148]:

$$F_{1\to 2} = 1 + \frac{b}{L}F_b + \frac{c}{L}F_c - \frac{L+b}{L}F_{L+b} - \frac{L+c}{L}F_{L+c} \tag{E.10}$$

Cylinder to cylinder (configuration II; Figure E.3b) [148]:

$$F_{1\to 2} = \frac{L+D}{L}F_{L+D} + \frac{Y+D}{L}F_{Y+D} - \frac{D}{L}F_D - \frac{L+Y+D}{L}F_{L+Y+D} \tag{E.11}$$

where F_l denotes the view factor of Eq.E.9 with the length of the cylinder being l.

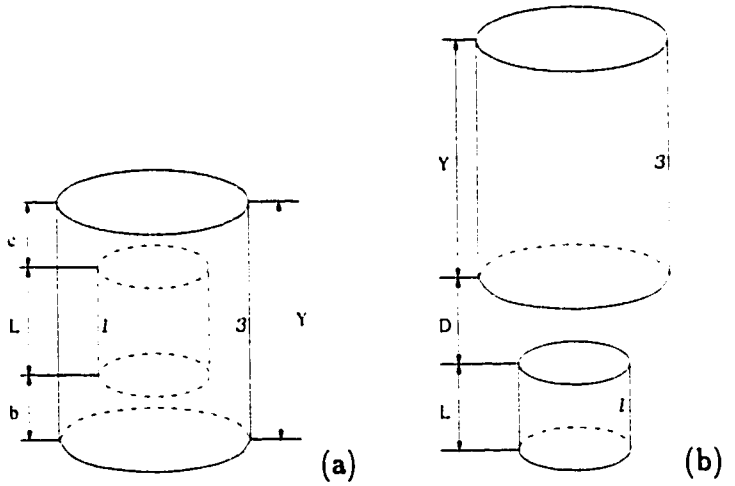

Figure E.3: Cylinder to cylinder view factors a) configuration I, b) configuration II.

E.2 Feedback control of crystal radius:

The shape of the melt-crystal interface in the Czochralski crystal growth is a complex system that varies with time and can be described by a thermal equilibrium at the interface condition, called the Stefan condition [47]. Analyzing this condition at the crystal-melt-air trijunction point and assuming an almost planar crystal-melt interface [95], one can predict the difference of height between the trijunction point and the melt surface away form the melt-crystal interface, $h(t, R)$, by using the following equation [95]:

$$k_c \frac{\partial T_c}{\partial z}(R) - k_m \frac{\partial T_m}{\partial z}(R) = \Delta_m H(v_p - \frac{\partial h}{\partial t}) \tag{E.12}$$

where k_c is the crystal thermal conductivity, k_m is the melt thermal conductivity, $\Delta_m H$ is the latent heat of melting, T_c and T_m are the crystal and melt temperature respectively and R is the crystal radius.

Approximating the heat transfer at the crystal-melt interface from the melt side in Eq.E.12 with a linear temperature drop [95], we obtain the following equation:

$$k_m \frac{\partial T_m}{\partial z} \approx k_m \frac{T_m^b - T_{mp}}{h} \tag{E.13}$$

where T_m^b is the temperature at the bulk of the melt. The heat transfer at the crystal-melt interface from the crystal side in Eq.E.12 can be approximated by differentiating the solution of the thermal model of the process Eq.5.1 (or similarly the model used for controller design) in the axial direction at position $(z, r) = (0, R)$.

The dynamics of the crystal radius are governed by to the following ODE [47]:

$$\frac{dR}{dt} = (v_p - \frac{\partial h}{\partial t}) tan(\theta_l - \theta_l^0) \tag{E.14}$$

where r is the radius, θ_l is the contact angle between the melt and the crystal at the trijunction point, θ_l^0 is the contact angle between the melt and the crystal at the trijunction point at steady-state.

For a holm geometry of the meniscus shape, which applies to our system, the Laplace-Young equation has been solved approximately by Boucher and Jones [21] (see [93] for a relevant analysis) and is of the form:

$$h = \left[\frac{\beta(1 - sin\theta_l)}{1 + \frac{1}{R}\sqrt{\frac{\beta}{2}}} \right]^{1/2} \tag{E.15}$$

where $\beta = \frac{2\sigma_s}{\rho_m g}$, σ_s is the surface tension of the melt, ρ_m is the density of the melt and g is the acceleration of free fall.

Based on Eqs.E.12-E.14-E.15-E.13 we can derive the following ODE system which describes the crystal radius dynamics as a function of the heat transfer mechanisms at the trijunction point and the pulling rate:

$$\begin{aligned}
\Delta_m H \frac{d^2R}{dt^2} &= \left[(k_c \frac{\partial T_c}{\partial z}(R) - k_m \frac{T_m^b - T_{mp}}{h})(tan^2(\theta_l - \theta_l^0) + 1) \frac{\partial \theta_l}{\partial R} \right. \\
&\left. + k_c tan(\theta_l - \theta_l^0) \frac{\partial^2 T_c}{\partial R \partial z}(R) \right] \frac{dR}{dt} \\
&+ \left[(k_c \frac{\partial T_c}{\partial z}(R) - k_m \frac{T_m^b - T_{mp}}{h})(tan^2(\theta_l - \theta_l^0) + 1) \frac{\partial \theta_l}{\partial h} \right. \\
&\left. + k_m \frac{T_m^b - T_{mp}}{h^2} tan(\theta_l - \theta_l^0) \right] \times \\
&\times \left(v_p - \frac{1}{\Delta_m H} (k_c \frac{\partial T_c}{\partial z}(R) - k_m \frac{T_m^b - T_{mp}}{h}) \right)
\end{aligned} \tag{E.16}$$

where $\frac{\partial T_c}{\partial z}(R)$, $\frac{\partial^2 T_c}{\partial R \partial z}(R)$ are given from the solution of the thermal model of Eq.5.1 and θ_l is given from the solution of Eq.E.15:

$$\theta_l = sin^{-1} \left(1 - \frac{h^2}{\beta} \left[1 + \frac{1}{R}\sqrt{\frac{\beta}{2}} \right] \right) \tag{E.17}$$

with $\frac{\partial \theta_l}{\partial h}$ and $\frac{\partial \theta_l}{\partial R}$ given from:

$$\begin{aligned}
\frac{\partial \theta_l}{\partial h} &= -\frac{2h(1+\frac{1}{R}\sqrt{\frac{\beta}{2}})}{\beta^2\sqrt{1-\left(1-\frac{h^2}{\beta^2}(1+\frac{1}{R}\sqrt{\frac{\beta}{2}})\right)^2}}, \\
\frac{\partial \theta_l}{\partial R} &= \frac{h^2\sqrt{2}}{2\beta R\sqrt{1-\left(1-\frac{h^2}{\beta^2}(1+\frac{1}{R}\sqrt{\frac{\beta}{2}})\right)^2}}
\end{aligned} \tag{E.18}$$

Using geometric control methods [98], we design a nonlinear controller which manipulates the pulling rate to stabilize the radius of the crystal at a specified value R_{set} and is of the form:

$$\begin{aligned}
v_p &= \frac{1}{\Delta_m H}(k_c\frac{\partial T_c}{\partial z}(R) - k_m\frac{T_m^b - T_{mp}}{h})\left\{1+\left[\Delta_m H\frac{R_{set}-R}{\gamma_2}\right.\right. \\
&-tan(\theta_l-\theta_l^0)\left((k_c\frac{\partial T_c}{\partial z}(R) - k_m\frac{T_m^b-T_{mp}}{h})(tan^2(\theta_l-\theta_l^0)+1)\frac{\partial \theta_l}{\partial R}\right. \\
&\left.\left.+k_c tan(\theta_l-\theta_l^0)\frac{\partial^2 T_c}{\partial R\partial z}(R) + \Delta_m H\frac{\gamma_1}{\gamma_2}\right)\right]\times \\
&\times\left[(k_c\frac{\partial T_c}{\partial z}(R) - k_m\frac{T_m^b-T_{mp}}{h})(tan^2(\theta_l-\theta_l^0)+1)\frac{\partial \theta_l}{\partial h}\right. \\
&\left.\left.+k_m\frac{T_m^b-T_{mp}}{h^2}tan(\theta_l-\theta_l^0)\right]^{-1}\right\}
\end{aligned} \tag{E.19}$$

where the terms $\frac{\partial T_c}{\partial z}(R)$, $\frac{\partial^2 T_c}{\partial R\partial z}(R)$ are given from the solution of the reduced-order thermal model used for the design of the controller Eq.5.6, θ_l is given from Eq.E.17 and $\frac{\partial \theta_l}{\partial h}$, $\frac{\partial \theta_l}{\partial R}$ from Eq.E.18 and γ_1, γ_2 are controller parameters. The above controller ensures that the crystal radius reaches a constant value in a very small time-interval compared to the time needed to grow the entire crystal, thereby allowing to assume a constant crystal radius in the problem of regulating the thermal gradients inside the

body of the crystal.

Finally, we note that the change of the melt level inside the crucible (which is much slower than the dynamics of the crystal radius) may result in a change of the position of the crystal-melt interface relative to the crucible, which in turn may lead to pulling rates which are outside prespecified limits in order to achieve a constant crystal radius. To deal with this problem, the chamber temperature T_{ch} can be used as a second manipulated variable to keep the window of operation of the pulling rate v_p within prespecified limits. The chamber temperature affects the crystal radius dynamics of Eq.E.16 through the terms $\frac{\partial T_c}{\partial z}(R)$ and $\frac{\partial^2 T_c}{\partial R \partial z}(R)$ that describe the heat transfer between the crystal surface and its surroundings due to conduction and radiation at the trijunction point.

Appendix F

Proofs of chapter 6

Proof of Theorem 6.1

Under the controller of Eq.6.21, the closed-loop system takes the form:

$$\begin{aligned}
\frac{d\eta}{dt} &= f(\eta) + L(y_m - h_m(\eta)) + g(\eta)\left\{[\beta_{1r_1}\cdots\beta_{lr_l}]C(\eta)\right\}^{-1}\left\{v - \sum_{i=1}^{l}\sum_{k=0}^{r_i}\beta_{ik}L_f^k h_{ci}(\eta)\right\} \\
\frac{d\xi}{dt} &= \left\{[\beta_{1r_1}\cdots\beta_{lr_l}]C(\eta)\right\}^{-1}\left\{v - \sum_{i=1}^{l}\sum_{k=0}^{r_i}\beta_{ik}L_f^k h_{ci}(\eta)\right\} \\
\dot{x} &= \mathcal{A}x + \mathcal{B}\xi + \mathcal{R}(x)
\end{aligned} \tag{F.1}$$

Applying Galerkin's method to the above system, we obtain:

$$\begin{aligned}
\frac{d\eta}{dt} &= f(\eta) + L(y_m - h_m(\eta)) + g(\eta)\left\{[\beta_{1r_1}\cdots\beta_{lr_l}]C(\eta)\right\}^{-1}\left\{v - \sum_{i=1}^{l}\sum_{k=0}^{r_i}\beta_{ik}L_f^k h_{ci}(\eta)\right\} \\
\frac{d\xi}{dt} &= \left\{[\beta_{1r_1}\cdots\beta_{lr_l}]C(\eta)\right\}^{-1}\left\{v - \sum_{i=1}^{l}\sum_{k=0}^{r_i}\beta_{ik}L_f^k h_{ci}(\eta)\right\} \\
\frac{dx_s}{dt} &= \mathcal{A}_s x_s + \mathcal{B}_s\xi + \mathcal{R}_s(x_s, x_f) \\
\frac{\partial x_f}{\partial t} &= \mathcal{A}_f x_f + \mathcal{B}_f\xi + \mathcal{R}_f(x_s, x_f)
\end{aligned} \tag{F.2}$$

Performing a linearization of the above system around the zero solution, defining the variable $e_o = \eta - \hat{x}_s$, introducing the fast time-scale $\tau = t/\epsilon$ and setting $\epsilon = 0$, the

fast dynamics of the above system are described by the system:

$$\frac{de_o}{d\tau} = Ae_o \tag{F.3}$$

which is clearly exponentially stable. Computing the system that describes the dynamics of the system of Eq.F.2 included in the model used for controller design, we obtain:

$$\begin{aligned}
\frac{d\xi}{dt} &= \{[\beta_{1r_1} \cdots \beta_{lr_l}]C(\hat{x}_s)\}^{-1} \left\{ v - \sum_{i=1}^{l} \sum_{k=0}^{r_i} \beta_{ik} L_f^k h_{ci}(\hat{x}_s) \right\} \\
\frac{dx_s}{dt} &= \mathcal{A}_s x_s + \mathcal{B}_s \xi + \mathcal{R}_s(x_s, x_f) \\
\frac{\partial x_f}{\partial t} &= \mathcal{A}_f x_f + \mathcal{B}_f \xi + \mathcal{R}_f(x_s, x_f)
\end{aligned} \tag{F.4}$$

From assumptions 2 and 3 and the fact that β_{ik} are chosen so that the roots of the equation $det(B(s)) = 0$ are in the open left-half of the complex plane, we have that the linearization of the above system around the zero solution is also exponentially stable. Therefore, there exists [109] a real positive number ϵ^* such that $\forall\, \epsilon \in (0, \epsilon^*]$, the linearization of Eq.F.2 is exponentially stable. Using Theorem 5.1.1 in [88], we then have that there exists a real positive number μ such that if $||x_0||_2 \leq \mu$, the zero solution of the closed-loop system of Eq.F.2 (and thus of Eq.F.1) is exponentially stable.

Appendix G

Proofs of Chapter 7

G.1 Proof of Theorem 7.1

Part 1: We initially show that if the condition of Eq.7.17 holds, then the controller of Eq.7.18 exponentially stabilizes the Kuramoto-Sivashinsky equation without the term $-x\frac{\partial x}{\partial z}$. Under the controller of Eq.7.18, the closed-loop system without the term $-x\frac{\partial x}{\partial z}$ takes the form:

$$\frac{\partial x}{\partial t} = -\nu\frac{\partial^4 x}{\partial z^4} - \frac{\partial^2 x}{\partial z^2} + bKS_u^{-1}y^m \tag{G.1}$$

where $b = [b_1\ b_2\ \cdots\ b_m]$. Applying Galerkin's method to the above system, the following infinite set of ordinary differential equations is obtained:

$$\begin{aligned} \dot{\alpha}_u &= A_u\alpha_u + B_uKS_u^{-1}(S_u\alpha_u + S_s\alpha_s) \\ \dot{\alpha}_s &= A_s\alpha_s + B_sKS_u^{-1}(S_u\alpha_u + S_s\alpha_s) \end{aligned} \tag{G.2}$$

or

$$\begin{bmatrix} \dot{\alpha}_u \\ \dot{\alpha}_s \end{bmatrix} = \begin{bmatrix} A_u + B_uK & B_uKS_u^{-1}S_s \\ B_sK & A_s + B_sKS_u^{-1}S_s \end{bmatrix} \begin{bmatrix} \alpha_u \\ \alpha_s \end{bmatrix} \tag{G.3}$$

From the above system, it is clear that the existence of a matrix K so that the matrix of Eq.7.17 is Hurwitz is necessary and sufficient for the local exponential stability of the zero solution of the closed-loop system of Eq.G.1 for $1/l^2 > \nu > 1/(l+1)^2$.

Part 2: In this part of the proof, we use a Lyapunov argument to show that a linear static output feedback controller of the form of Eq.7.18 that exponentially stabilizes the closed-loop system of Eq.G.1, ensures also global exponential stability of the zero solution of the Kuramoto-Sivashinsky equation with the term $-x\frac{\partial x}{\partial z}$. To this end, we first use the fact that exponential stability of the system of Eq.G.3 implies that there exists a positive constant c such that the linear self-adjoint closed-loop operator:

$$\bar{A}x = -\nu\frac{\partial^4 x}{\partial z^4} - \frac{\partial^2 x}{\partial z^2} + bK \begin{bmatrix} \int_{-\pi}^{\pi} s_1(z)\, x(z,t)\, dz \\ \int_{-\pi}^{\pi} s_2(z)\, x(z,t)\, dz \\ \int_{-\pi}^{\pi} s_3(z)\, x(z,t)\, dz \\ \cdots \\ \int_{-\pi}^{\pi} s_{2l}(z)\, x(z,t)\, dz \\ \int_{-\pi}^{\pi} s_{2l+1}(z)\, x(z,t)\, dz \end{bmatrix} \tag{G.4}$$

satisfies $(x, \bar{A}x) \leq -c||x||_2^2$. Now, multiplying the nonlinear closed-loop system:

$$\frac{\partial x}{\partial t} = -\nu\frac{\partial^4 x}{\partial z^4} - \frac{\partial^2 x}{\partial z^2} - x\frac{\partial x}{\partial z} + bKS_u^{-1}y^m \tag{G.5}$$

by x and integrating from $[-\pi, \pi]$ and using the notation of Eq.G.4, we obtain:

$$\int_{-\pi}^{\pi} x\frac{\partial x}{\partial t}dz = \int_{-\pi}^{\pi} x\bar{A}x dz - \int_{-\pi}^{\pi} x^2\frac{\partial x}{\partial z}dz \tag{G.6}$$

Using the boundary conditions of Eq.7.3, one can show that (see [168] for details):

$$\int_{-\pi}^{\pi} x^2\frac{\partial x}{\partial z}dz = 0 \tag{G.7}$$

which implies that Eq.G.6 can be written as:

$$\begin{aligned} \frac{1}{2}\frac{d}{dt}||x||_2^2 &= (x, \bar{A}x) \\ &\leq -c||x||_2^2 \end{aligned} \tag{G.8}$$

From the above inequality, the exponential stability of the solution, $x(z,t) = 0$, of the closed-loop system (Eq.G.1), for any initial condition in $L_p^2([-\pi, \pi])$, follows.

G.2 Stability Analysis for the infinite-dimensional linear system

We show that given the value of the instability parameter ν, if there exists a gain matrix K so that the condition of Eq.7.17 is satisfied for a $(2l+1+2N)$-dimensional approximation of the closed-loop system of Eq.G.1 without the term $-x\frac{\partial x}{\partial z}$, then the infinite dimensional closed-loop system of Eqs.7.2-7.18 without the term $-x\frac{\partial x}{\partial z}$ is also globally exponentially stable. Note that the nonlinear term $-x\frac{\partial x}{\partial z}$ is neglected because in the previous section G.1 we have shown that a linear static output feedback controller that exponentially stabilizes the Kuramoto-Sivashinsky equation without the term $-x\frac{\partial x}{\partial z}$, enforces also global exponential stability of the zero solution of the Kuramoto-Sivashinsky equation when this term is present.

Given ν, we fix l, and apply Galerkin's method to the closed-loop system of Eq.G.1 without the term $-x\frac{\partial x}{\partial z}$ to obtain the following infinite set of ODEs:

$$\begin{aligned} \dot{\alpha}_{sl} &= A_{sl}\alpha_{sl} + B_{sl}KS_u^{-1}y^m \\ \dot{\alpha}_f &= A_f\alpha_f + B_fKS_u^{-1}y^m \\ y^m &= S_{sl}\alpha_{sl} + S_s\alpha_f \end{aligned} \tag{G.9}$$

where $\alpha_{sl} = [\beta_0\ \alpha_1\ \beta_1\ \alpha_2\ \beta_2\ \cdots\ \alpha_{l+N}\ \beta_{l+N}]^T$, $\alpha_f = [\alpha_{l+N+1}\ \beta_{l+N+1}\ \cdots]^T$, and the explicit structure of the matrices $A_{sl}, B_{sl}, A_f, B_f, S_{sl}, S_s$ is similar to the structure of the corresponding matrices in the system of Eq.7.12 and will be omitted for brevity.

Now, defining the parameter $\epsilon = \frac{|\mu_1|}{|\mu_{l+N+1}|} < 1$ and multiplying the α_f-subsystem of Eq.G.9 by ϵ, we obtain:

$$\begin{aligned} \dot{\alpha}_{sl} &= A_{sl}\alpha_{sl} + B_{sl}KS_u^{-1}y^m \\ \epsilon\dot{\alpha}_f &= A_{f\epsilon}\alpha_f + \epsilon B_fKS_u^{-1}y^m \\ y^m &= S_{sl}\alpha_{sl} + S_s\alpha_f \end{aligned} \tag{G.10}$$

where $A_{f\epsilon} = \epsilon A_f$. In the above system, the operators A_{sl} and $A_{f\epsilon}$ generate semigroups with growth rates which are of the same order of magnitude, i.e., the solutions α_{sl}

and α_f of the systems $\dot{\alpha}_{sl} = A_{sl}\alpha_{sl}$ and $\dot{\alpha}_f = A_{f\epsilon}\alpha_f$, respectively, satisfy: $|\alpha_{sl}(t)| \leq K|\alpha_{sl}(0)|e^{k_1 t}$, $|\alpha_f(t)| \leq K|\alpha_f(0)|e^{k_2 t}$, where K, k_1, k_2 are real numbers, and $O(k_1) = O(k_2)$ ($O(\cdot)$ denotes the standard order of magnitude notation). This means that the system of Eq.G.10 is in the standard singularly perturbed form with α_{sl} being the slow states and α_f being the fast states. The stability properties of this system can be analyzed within the singular perturbation framework by decomposing it into reduced-order subsystems describing its behavior in the fast and slow time scales. Specifically, the slow subsystem can be obtained by setting $\epsilon = 0$ in the system of Eq.G.10 that yields $\alpha_f = 0$ and:

$$\dot{\alpha}_{sl} = A_{sl}\alpha_{sl} + B_{sl}KS_u^{-1}S_{sl}\alpha_{sl} \tag{G.11}$$

Under the assumption that there exists a gain matrix K so that the condition of Eq.7.17 is satisfied for a $(2l + 1 + 2N)$-dimensional approximation of the closed-loop system, we have that the above finite-dimensional system is exponentially stable. Furthermore, rewriting the system of Eq.G.10 in the fast time-scale $\tau = t/\epsilon$ and setting $\epsilon = 0$, the following system which describes the fast dynamics of the system of Eq.G.10 is obtained:

$$\frac{d\alpha_f}{d\tau} = A_{f\epsilon}\alpha_f \tag{G.12}$$

which is also exponentially stable. Finally, utilizing results from singular perturbation theory for systems of the form of Eq.G.10 in which the fast subsystem is an infinite-dimensional system [45], we have that the exponential stability of the slow and fast subsystems implies that there exists an ϵ^* such that if $\epsilon \in (0, \epsilon^*]$, the system of Eq.G.10 is exponentially stable. From the definition of ϵ, it follows directly that ϵ decreases as N increases, thereby implying that given $\nu > 0$, there exists an N^* sufficiently large (i.e., ϵ^* sufficiently small) so that the design of the gain matrix K which stabilizes the infinite dimensional closed-loop system (Eqs.7.2-7.18) can be done on the basis of a

$(2l+1+2N)$-dimensional approximation of this system, provided $N \geq N^*$. Note that ϵ^* (and thus, N^*) depends on all the matrices of the system of Eq.G.10, and thus, in turn, it depends on ν, and the distribution functions of the measurement sensors and control actuators.

Appendix H

Proofs of Chapter 8

Proof of Theorem 8.1

Under the controller of Eq.8.18, the closed-loop system takes the form:

$$\dot{x} = \mathcal{A}x + \frac{1}{2}R^{-1}(S_m^{-1}Sx)\mathcal{B}(L_{\tilde{g}}V)^T + f(x), \tag{H.1}$$

Applying Galerkin's method to the above system and owing to the time scale separation between the two subsystems (following from part 3 of assumption 8.1) the following infinite set of ordinary differential equations expressed in singularly perturbed form can be obtained:

$$\begin{aligned} \frac{dx_s}{dt} &= \mathcal{A}_s x_s + f_s(x_s, x_f) \\ &\quad + \frac{1}{2}R^{-1}(S_m^{-1}[Sx_s + Sx_f])\mathcal{B}_s(L_{\tilde{g}}V)^T \\ \epsilon\frac{\partial x_f}{\partial t} &= \mathcal{A}_{f\epsilon}x_f + \epsilon f_f(x_s, x_f) \\ &\quad + \epsilon\frac{1}{2}R^{-1}(S_m^{-1}[Sx_s + Sx_f])\mathcal{B}_f(L_{\tilde{g}}V)^T \end{aligned} \tag{H.2}$$

where $\mathcal{A}_{f\epsilon} = \epsilon\mathcal{A}_f$ is a Hurwitz matrix with the same magnitude of eigenvalues as $\mathcal{A}_s$.

Performing a two-time-scale decomposition in the above system, the fast subsystem takes the form:

$$\frac{\partial x_f}{\partial \tau} = \mathcal{A}_{f\epsilon}x_f, \tag{H.3}$$

which is exponentially stable. As a result, the slow closed-loop system is given by:

$$\begin{aligned}\frac{dx_s}{dt} &= \mathcal{A}_s x_s + f_s(x_s, 0) \\ &\quad + \frac{1}{2} R^{-1}(S_m^{-1}[S x_s])\mathcal{B}_s(L_{\bar{g}} V)^T\end{aligned} \tag{H.4}$$

Referring to the above closed-loop ODE system, the proposed bounded nonlinear output feedback control has been shown to lead to an exponentially stable system (the details on the bounded nonlinear controller synthesis can be found in [67] and is omitted for brevity).

Bibliography

[1] H. Aling, S. Benerjee, A. K. Bangia, V. Cole, J. Ebert, A. Emani-Naeini, K. F. Jensen, I. G. Kevrekidis, and S. Shvartsman. Nonlinear model reduction for simulation and control of rapid thermal processing. In *Proceedings of American Control Conference*, pages 2233–2238, Albuquerque, NM, 1997.

[2] A. Armaou and P. D. Christofides. Nonlinear feedback control of parabolic PDE systems with time-dependent spatial domains. *J. Math. Anal. Appl.*, 239:124–157, 1999.

[3] A. Armaou and P. D. Christofides. Nonlinear model reduction of processes with moving domains: Computation of empirical eigenfunctions. In *AIChE Annual Meeting, paper 231c, Dallas, TX*, 1999.

[4] A. Armaou and P. D. Christofides. Plasma-enhanced chemical vapor deposition: Modeling and control. *Chem. Eng. Sci.*, 54:3305–3314, 1999.

[5] A. Armaou and P. D. Christofides. Robust control of parabolic PDE systems with time-dependent spatial domains. *Automatica*, 37:61–69, 2000.

[6] A. Armaou and P. D. Christofides. Wave suppression by nonlinear finite-dimensional control. *Chem. Eng. Sci.*, 55:2627–2640, 2000.

[7] L. J. Atherton, J. J. Derby, and R. A. Brown. Radiative heat exchange in Czochralski crystal growth. *J. Crystal Growth*, 84:57–78, 1987.

[8] E. R. Austin and F. W. Lampe. Hydrogen-atom initiated decomposition of monosilane. *J. Phys. Chem.*, 80:2811–2817, 1976.

[9] J. Baker and P. D. Christofides. Finite dimensional approximation and control of nonlinear parabolic PDE systems. *Int. J. Contr.*, 73:439–456, 2000.

[10] P. Bakewell and J. L. Lumley. Viscous sublayer and adjacent wall region in turbulent pipe flow. *Phys. Fluids*, 10:1880–1889, 1967.

[11] M. J. Balas. Feedback control of linear diffusion processes. *Int. J. Contr.*, 29:523–533, 1979.

[12] M. J. Balas. Trends in large scale structure control theory: Fondest hopes, wildest dreams. *IEEE Trans. Automat. Contr.*, 27:522–535, 1982.

[13] M. J. Balas. Nonlinear finite-dimensional control of a class of nonlinear distributed parameter systems using residual mode filters: A proof of local exponential stability. *J. Math. Anal. Appl.*, 162:63–70, 1991.

[14] A. K. Bangia, P. F. Batcho, I. G. Kevrekidis, and G. E. Karniadakis. Unsteady 2-D flows in complex geometries: Comparative bifurcation studies with global eigenfunction expansion. *SIAM J. Sci. Comp.*, 18:775–805, 1997.

[15] P. Belenguer and J. P. Boeuf. Transition between different regimes of RF glow discharges. *Phys. Rev. A*, 41:4447–4459, 1990.

[16] A. Bensoussan, G. da Prato, M. C. Delfour, and S. K. Mitter. *Representation and Control of Infinite Dimensional Systems, Volume I.* Birkhäuser, Boston, 1992.

[17] A. Bensoussan, G. da Prato, M.C. Delfour, and S. K. Mitter. *Representation and Control of Infinite Dimensional Systems, Volume II.* Birkhäuser, Boston, 1993.

[18] S. Beringen. Active control of transition by periodic suction and blowing. *Phys. Fluids*, 27:1345–1348, 1984.

[19] C. Bohm and J. Perrin. Spatially resolved optical emission and electrical properties of SiH_4 RF discharges at $13.56MHz$ in a symmetric parallel-plate configuration. *J. Phys. D: Appl. Phys.*, 24:865–881, 1991.

[20] W. L. Brogan. *Modern Control Theory.* Prentice-Hall, New Jersey, 1991.

[21] E. A. Buchner and T. G. J. Jones. Capillary phenomena part 11. approximate treatment of the shape and properties of fluid interface of infinite extent meeting solids ans graviational field. *J.C.S. Faraday*, 76:1419–1432, 1980.

[22] J. A. Burns and B. B. King. Optimal sensor location for robust control of distributed parameter systems. In *Proceedings of 33rd IEEE Conference on Decision and Control*, pages 3965–3970, Orlando, FL, 1994.

[23] J. A. Burns and Y.-R. Ou. Feedback control of the driven cavity problem using LQR designs. In *Proceedings of 33rd IEEE Conference on Decision and Control*, pages 289–294, Orlando, FL, 1994.

[24] S. Bushman, T.F. Edgar, and I. Trachtenberg. Modeling of plasma etch systems using ordinary least squares, recurrent neural network, and projection to latent structure models. *J. Electrochem. Soc.*, 144:1379–1389, 1997.

[25] C. A. Byrnes, D. S. Gilliam, and V. I. Shubov. Global lyapunov stabilization of a nonlinear distributed parameter system. In *Proc. of 33rd IEEE Conference on Decision and Control*, pages 1769–1774, Orlando, FL, 1994.

[26] C. A. Byrnes, D. S. Gilliam, and V. I. Shubov. On the dynamics of boundary controlled nonlinear distributed parameter systems. In *Proc. of Symposium on Nonlinear Control Systems Design'95*, pages 913–918, Tahoe City, CA, 1995.

[27] C. I. Byrnes. Adaptive stabilization of infinite dimensional linear systems. In *Proceedings of 26th IEEE Conference on Decision and Control*, pages 1435–1440, Los Angeles, CA, 1987.

[28] B. J. Cantwell. Organized motion in turbulent flow. *Ann. Rev. Fluid Mech.*, 13:457–515, 1981.

[29] H. Caquineau and B. Despax. Influence of the reactor design in the case of silicon nitride PECVD. *Chem. Eng. Sci.*, 52:2901–2914, 1997.

[30] H. A. Carlson and J. L. Lumley. Active control in the turbulent wall layer of a minimal flow unit. *J. Fluid Mech.*, 329:341–371, 1996.

[31] H. C. Chang. Nonlinear waves on liquid film surfaces-I. Flooding in vertical tube. *Chem. Eng. Sci.*, 41:2463–2476, 1986.

[32] H. C. Chang, E. A. Demekhin, and D. I. Kopelevich. Local stability theory of solitary pulses in an active medium. *Physica D*, 97:353–375, 1996.

[33] H. C. Chang, E. A. Demekhin, D. I. Kopelevich, and Y. Ye. Nonlinear wave-number selection in gradient-flow systems. *Phys. Rev. E*, 55:2818–2834, 1997.

[34] C. C. Chen and H. C. Chang. Accelerated disturbance damping of an unknown distributed system by nonlinear feedback. *AIChE J.*, 38:1461–1476, 1992.

[35] C. C. Chen, E. E. Wolf, and H. C. Chang. Low-dimensional spatiotemporal thermal dynamics on nonuniform catalytic surfaces. *J. Phys. Chem.*, 97:1055–1064, 1993.

[36] L. H. Chen and H. C. Chang. Nonlinear waves on liquid film surfaces-II. Bifurcation analyses of the long-wave equation. *Chem. Eng. Sci.*, 41:2477–2486, 1986.

[37] H. Choi, R. Temam, P. Moin, and J. Kim. Feedback control for unsteady flow and its application to the stochastic burger's equation. *J. Fluid Mech.*, 253:509–543, 1993.

[38] P. D. Christofides. Feedback control of the Kuramoto-Sivashinsky equation. In *Proceedings of the 37th IEEE Conference on Decision and Control*, pages 4646–4651, Tampa, FL, 1998.

[39] P. D. Christofides. Robust control of parabolic PDE systems. *Chem. Eng. Sci.*, 53:2949–2965, 1998.

[40] P. D. Christofides. *Nonlinear and Robust Control of PDE Systems: Methods and Applications to Transport-Reaction Processes.* Birkhäuser, Boston, 2001.

[41] P. D. Christofides and A. Armaou. Nonlinear control of Navier-Stokes equations. In *Proceedings of American Control Conference*, pages 1355–1359, Philadelphia, PA, 1998.

[42] P. D. Christofides and J. Baker. Robust output feedback control of quasi-linear parabolic PDE systems. *Syst. & Contr. Lett.*, 36:307–316, 1999.

[43] P. D. Christofides and P. Daoutidis. Nonlinear control of diffusion-convection-reaction processes. *Comp. & Chem. Engng.*, 20(s):1071–1076, 1996.

[44] P. D. Christofides and P. Daoutidis. Control of nonlinear distributed parameter systems: Recent results and future research directions. In *Proceedings of 5th International Conference on Chemical Process Control.*, pages 302–306, Tahoe City, CA, 1997.

[45] P. D. Christofides and P. Daoutidis. Finite-dimensional control of parabolic PDE systems using approximate inertial manifolds. *J. Math. Anal. Appl.*, 216:398–420, 1997.

[46] P. D. Christofides and P. Daoutidis. Robust control of hyperbolic PDE systems. *Chem. Eng. Sci.*, 53:85–105, 1998.

[47] A. B. Crowley. Mathematical modelling of heat flow in Czochralski crystal pulling. *IMA J. Appl. Math.*, 30:173–189, 1983.

[48] R. F. Curtain. Finite-dimensional compensator design for parabolic distributed systems with point sensors and boundary input. *IEEE Trans. Automat. Contr.*, 27:98–104, 1982.

[49] R. F. Curtain. Disturbance decoupling for distributed systems by boundary control. In *Proceedings of 2nd International Conference on Control Theory for Distributed Parameter Systems and Applications*, pages 109–123, Vorau, Austria, 1984.

[50] R. F. Curtain. Invariance concepts in infinite dimensions. *SIAM J. Contr. & Optim.*, 24:1009–1030, 1986.

[51] R. F. Curtain and K. Glover. Robust stabilization of infinite dimensional systems by finite dimensional controllers. *Syst. & Contr. Lett.*, 7:41–47, 1986.

[52] R. F. Curtain and H. J. Zwart. *An Introduction to Infinite Dimensional Linear Systems*. Springer-Verlag, New York, 1995.

[53] R. D'Andrea, R. L. Behnken, and R. M. Murray. Rotating stall control of an axial flow compressor using pulsed air injection. *J. Turbomachinery*, 1997.

[54] A. E. Deane, I. G. Kevrekidis, G. E. Karniadakis, and S. A. Orszag. Low-dimensional models for complex geometry flows: Application to grooved channels and circular cylinders. *Phys. Fluids A*, 3:2337–2354, 1991.

[55] M. A. Demetriou. Model reference adaptive control of slowly time-varying parabolic systems. In *Proceedings of 33rd IEEE Conference on Decision and Control*, pages 775–780, Orlando, FL, 1994.

[56] J. J. Derby, L. J. Atherton, P. D. Thomas, and R. A. Brown. Finite-element methods for analysis of the dynamics and control of Czochralski crystal growth. *J. Sci. Comp.*, 2:297–343, 1987.

[57] J. J. Derby and R. A. Brown. Thermal-capillary analysis of Czochralski and liquid encapsulated Czochralski crystal growth II. simulation. *J. Crystal Growth*, 74:605–624, 1986.

[58] J. J. Derby and R. A. Brown. Thermal-capillary analysis of Czochralski and liquid encapsulated Czochralski crystal growth II. processing strategies. *J. Crystal Growth*, 75:227–240, 1986.

[59] J. J. Derby and R. A. Brown. On the dynamics of Czochralski crystal growth. *J. Crystal Growth*, 83:137–151, 1987.

[60] J. J. Derby and R. A. Brown. On the quasi-steady state assumption in modeling Czochralski crystal growth. *J. Crystal Growth*, 87:251–260, 1988.

[61] M. Desai and K. Ito. Optimal controls of Navier-Stokes equations. *SIAM J. Contr. & Optim.*, 32:1428–1446, 1994.

[62] D. A. Doughty, J. R. Doyle, G. H. Lin, and A. Gallagher. Surface reaction probability of film-producing radicals in silane glow discharges. *J. Appl. Phys.*, 67:6220–6228, 1990.

[63] J. R. Doyle, D. A. Doughty, and A. Gallagher. Silane dissociation products in deposition discharges. *J. Appl. Phys.*, 68:4375–4384, 1990.

[64] D. J. Economou, S. Park, and G. D. Williams. Uniformity of etching in parallel plate plasma reactors. *J. Electrochem. Soc.*, 136:188–198, 1989.

[65] D. Edelson and D.L. Flamm. Computer simulation of a CF_4 plasma etching silicon. *J. Appl. Phys.*, 56:1522–1531, 1984.

[66] N. H. El-Farra, A. Armaou, and P. D. Christofides. Analysis and control of parabolic PDE systems with input constraints. *Automatica*, submitted, 2001.

[67] N. H. El-Farra and P. D. Christofides. Integrating robustness, optimality, and constraints in control of nonlinear processes. *Chem. Eng. Sci.*, 56:1841–1868, 2001.

[68] D.L. Flamm, V.M. Donnelly, and D.E. Ibbotson. Basic chemistry and mechanisms of plasma etching. *Semicon. Int.*, 6:136–143, 1983.

[69] D.L. Flamm, V.M. Donnelly, and J.A. Mucha. The reaction of fluorine atoms with silicon. *J. Appl. Phys.*, 52:3633–3639, 1981.

[70] C. Foias, M.S. Jolly, I.G. Kevrekidis, G.R. Sell, and E.S. Titi. On the computation of inertial manifolds. *Phys. Lett. A*, 131:433–437, 1989.

[71] C. Foias, G.R. Sell, and E.S. Titi. Exponential tracking and approximation of inertial manifolds for dissipative equations. *J. Dynamics and Differential Equations*, 1:199–244, 1989.

[72] C. Foias and R. Témam. Algebraic approximation of attractors: The finite dimensional case. *Physica D*, 32:163–182, 1988.

[73] A. Friedman. *Partial Differential Equations.* Holt, Rinehart & Winston, New York, 1976.

[74] K. Fukunaga. *Introduction to statistical pattern recognition.* Academic Press, New York, 1990.

[75] C.G. Galarza, P.P. Khargonekar, and F.L. Jr. Terry. Real-time estimation of patterned wafer parameters using in situ spectroscopic ellipsometry. In *Proceedings of the IEEE International Conference on Control Applications*, pages 773–778, Kohala Coast, HI, 1999.

[76] A. Gallagher. Neutral radical deposition from silane discharges. *J. Appl. Phys.*, 63:2406–2413, 1988.

[77] J. P. Gauthier and C. Z. Xu. H^{∞}-control of a distributed parameter system with non-minimum phase. *Int. J. Contr.*, 53:45–79, 1989.

[78] M. A. Gevelber. Dynamics and control of the Czochralski process III. interface dynamics and control requirements. *J. Crystal Growth*, 139:271–285, 1994.

[79] M. A. Gevelber. Dynamics and control of the Czochralski process IV. control structure design for interface shape control and perfomance evaluation. *J. Crystal Growth*, 139:286–301, 1994.

[80] M. A. Gevelber and G. Stephanopoulos. Dynamics and control of the Czochralski process I. modelling and dynamic characterization. *J. Crystal Growth*, 84:647–668, 1987.

[81] M. A. Gevelber, G. Stephanopoulos, and M. J. Wargo. Dynamics and control of the Czochralski process II. objectives and control structure design. *J. Crystal Growth*, 91:199–217, 1988.

[82] M. A. Gevelber, M. J. Wargo, and G. Stephanopoulos. Advanced control design considerations for the Czochralski process. *J. Crystal Growth*, 85:256–263, 1987.

[83] M. D. Graham and I. G. Kevrekidis. Alternative approaches to the karhunen-loeve decomposition for model reduction and data analysis. *Comp. & Chem. Eng.*, 20:495–506, 1996.

[84] J. M. Greene and J. S. Kim. The steady-states of the Kuramoto-Sivashinsky equation. *Physica D.*, 33:99–120, 1988.

[85] E. S. Hamby, P. T. Kabamba, and S. M. Meerkov. A system-theoretic approach to modeling and analysis of deposition rate uniformity in PECVD. In *Proceedings of 33rd IEEE Conference on Decision & Control*, pages 86–90, Orlando, FL, 1994.

[86] E. M. Hanczyc and A. Palazoglu. Sliding mode control of nonlinear distributed parameter chemical processes. *I & EC Res.*, 34:557–566, 1995.

[87] M. Hankinson, T.L. Vincent, K. Irani, and P.P. Khargonekar. Combined real-time and run-to-run control of etch depth and spatial uniformity in plasma etching. *J. Electrochem. Soc.*, 144:2473–2479, 1997.

[88] D. Henry. *Geometric Theory of Semilinear Parabolic Equations.* Springer-Verlag, Berlin Heidelberg, Germany, 1981.

[89] J. O. Hirschfelder, C. F. Curtiss, and R. B. Bird. *Molecular Theory of Gases and Liquids.* Wiley, New York, 1954.

[90] P. Holmes, J. L. Lumley, and G. Berkooz. *Turbulence, Coherent Structures, Dynamical Systems and Symmetry.* Cambridge University Press, New York, 1996.

[91] A. P. Hooper and R. Grimshaw. Nonlinear instability at the interface between two viscous fluids. *Phys. Fluids*, 28:37–45, 1985.

[92] L. S. Hou and Y. Yan. Dynamics for controlled navier-stokes systems with distributed controls. *SIAM J. Contr. & Optim.*, 35:654–677, 1997.

[93] D. T. J. Hurle. Analytical represntation of the shape of the meniscus in Czochralski growth. *J. Crystal Growth*, 63:13–17, 1983.

[94] D. T. J. Hurle. *Handbook of Crystal Growth Vol. 2: Bulk Crystal Growth. Part B: Growth Mechanisms and Dynamics.* Elsevier Science B.V., Amsterdam, 1994.

[95] D. T. J. Hurle, G. C. Joyce, M. Ghassempoory, A. B. Crowley, and E. J. Stern. The dynamics of Czochralski growth. *J. Crystal Growth*, 100:11–25, 1990.

[96] R. Irizarry-Rivera and W. D. Seider. Model-predictive control of the Czochralski crystallization process. part I: Conduction-dominated melt. *J. Crystal Growth*, 178:593–611, 1997.

[97] R. Irizarry-Rivera and W. D. Seider. Model-predictive control of the Czochralski crystallization process. part II:. *J. Crystal Growth*, 178:612–633, 1997.

[98] A. Isidori. *Nonlinear Control Systems: An Introduction.* Springer-Verlag, Berlin-Heidelberg, second edition, 1989.

[99] K. Ito and S. S. Ravindran. Reduced order methods for nonlinear infinite dimensional control systems. In *Proceedings of 36th IEEE Conference on Decision and Control*, pages 2213–2218, San Diego, California, 1997.

[100] Hurle D. T. J. *Handbook of Crystal Growth. Vol. 2: Bulk Crystal Growth. Part A: Basic Techniques.* Elsevier Science B.V., Amsterdam, 1994.

[101] C. A. Jacobson and C. N. Nett. Linear state-space systems in infinite-dimensional space: The role and characterization of joint stabilizability/detectability. *IEEE Trans. Autom. Contr.*, 33:541–551, 1988.

[102] D. A. Jones and E. S. Titi. A remark on quasi-stationary approximate inertial manifolds for the Navier-Stokes equations. *SIAM J. Math. Anal.*, 25:894–914, 1994.

[103] S. S. Joshi, J. L. Speyer, and J. Kim. Modeling and control of two dimensional poiseuille flow. In *Proceedings of 34th IEEE Conference on Decision and Control*, pages 921–927, New Orleans, LA, 1995.

[104] S. Kang and K. Ito. A feedback control law for systems arising in fluid dynamics. In *Proceedings of 30th IEEE Conference on Decision and Control*, pages 384–385, Tampa, AZ, 1992.

[105] N. Kapoor, A. R. Teel, and P. Daoutidis. An anti-windup design for linear systems with input saturation. *Automatica*, 34:559–574, 1998.

[106] I. G. Kevrekidis, B. Nicolaenko, and J. C. Scovel. Back in the saddle again: A computer assisted study of the Kuramoto-Sivashinsky equation. *SIAM J. Appl. Math.*, 50:760–790, 1990.

[107] H. K. Khalil. *Nonlinear Systems.* Prentice Hall, New Jersey, second edition, 1996.

[108] B. B. King and Y. Qu. Nonlinear dynamic compensator design for flow control in a driven cavity. In *Proceedings of 34th IEEE Conference on Decision and Control*, pages 3741–3746, New Orleans, LA, 1995.

[109] P. V. Kokotovic, H. K. Khalil, and J. O'Reilly. *Singular Perturbations in Control: Analysis and Design.* Academic Press, London, 1986.

[110] M. V. Kothare, P. J. Campo, M. Morari, and C. N. Nett. A unified framework for the study of anti-windup designs. *Automatica*, 30:1869–1883, 1994.

[111] A. Kowalewski. Optimal control of a distributed hyperbolic system with multiple time-varying lags. *Inter. J. Contr.*, 71:419–435, 1998.

[112] A. Kowalewski. Optimal control of distributed hyperbolic systems with deviating arguments. *Inter. J. Contr.*, 73:1026–1041, 2000.

[113] N. Kunimatsu and H. Sano. Compensator design of semilinear parabolic systems. *Int. J. Contr.*, 60:243–263, 1994.

[114] Y. Kuramoto and T. Tsuzuki. On the formation of dissipative structures in reaction-diffusion systems. *Prog. Theor. Phys.*, 54:687–699, 1975.

[115] Y. Kuramoto and T. Tsuzuki. Persistent propagation of concentration waves in dissipative media far from thermal equilibrium. *Prog. Theor. Phys.*, 55:356–369, 1976.

[116] M. J. Kushner. A model for the discharge kinetics and plasma chemistry during plasma enhanced chemical vapor deposition of amorphous silicon. *J. Appl. Phys.*, 63:2532–2551, 1988.

[117] I. Lasiecka. Control of systems governed by partial differential equations: A historical perspective. In *Proceedings of 34th IEEE Conference on Decision and Control*, pages 2792–2797, New Orleans, LA, 1995.

[118] L. Lasiecka and R. Triggiani. *Differential and Algebraic Riccati Equations with Applications to Boundary Point Control Problems: Continuous Theory and Approximation Theory.* Lecture Notes in Control and Information Sciences, Vol. 164, Springer-Verlag, Berlin, 1991.

[119] L. Layeillon, A. Dollet, J. P. Couderc, and B. Despax. Analysis and modeling of plasma enhanced CVD reactors. part I: Two-dimensional treatment of $a - Si$: H deposition. *Plasma Sources Sci. Technol.*, 3:61–71, 1994.

[120] L. Layeillon, A. Dollet, J. P. Couderc, and B. Despax. Analysis and modeling of plasma enhanced CVD reactors. part II: Model improvement and systematic use. *Plasma Sources Sci. Technol.*, 3:72–79, 1994.

[121] L. Layeillon, A. Dollet, and B. Despax. Plasma enhanced deposition of $a - Si$: Comparison of two reactor arrangements. *Chem. Eng. J.*, 58:1–5, 1995.

[122] H. Leuenberger and R. A. Person. Compilation of radiation shape factors for cylindrical assemblies. *ASME A Paper*, 56-A-144, 1956.

[123] W.-J. Liu and M. Krstić. Controlling nonlinear water waves: boundary stabilization of the korteweg-de vries-burgers equation. In *Proceedings of the 1999 American Control Conference*, pages 1637–1641, San Diego, CA, 1999.

[124] W.-J. Liu and M. Krstić. Stability enhancement by boundary control in the kuramoto-sivashinsky equation. *Nonlin. anal.-theory meth. & appl.*, 43:485–507, 2001.

[125] W. Luft and Y. S. Tsuo. *Hydrogenated Amorphous Silicon Alloy Deposition Processes.* Marcel Dekker, Inc, USA, 1993.

[126] J. L. Lumley. Drag reduction in turbulent flow by polymer additives. *J. Polymer Sci. D: Macromol. Rev.*, 7:263–290, 1973.

[127] J. L. Lumley. Coherent structures in turbulence. In *Transition and Turbulence*, pages 215–242, Academic Press, New York, 1981.

[128] W. Marquardt. Traveling waves in chemical processes. *Int. Chem. Engng.*, 4:585–606, 1990.

[129] K. J. McLaughlin, S. W. Butler, T. F. Edgar, and I. Trachtenberg. Development of techniques for real-time monitoring and control in plasma etching i. response surface modeling of CF_4/O_2 and CF_4/H_2 etching of silicon and silicon dioxide. *J. Electrochem. Soc.*, 138:789–799, 1991.

[130] K. J. McLaughlin, S. W. Butler, T. F. Edgar, and I. Trachtenberg. Development of techniques for real-time monitoring and control in plasma etching i. multivariable control system analysis of manipulated, measured and performance variables. *J. Electrochem. Soc.*, 138:2727–2735, 1991.

[131] D. M. Michelson and G. I. Sivashinsky. Nonlinear analysis of hydrodynamic instability in laminar flames- II numerical experiments. *Acta Astronautica*, 4:1207–1221, 1977.

[132] P. K. Mozumder, S. Saxena, and D. J. Collins. A monitor wafer based controller for semiconductor processes. *IEEE Trans. on Semic. Man.*, 7:400–411, 1994.

[133] H. C. Neitzert, W. Hirsch, M. Kunst, and M. E. A. Nell. *In situ* thickness control during plasma deposition of hydrogenated amorphous silicon films by time-resolved microwave conductivity measurements. *Applied Optics*, 34:676–680, 1995.

[134] S. Palanki and C. Kravaris. Controller synthesis for time-varying systems by input/output linearization. *Comp. & Chem. Engng.*, 21:891–903, 1997.

[135] A. Palazoglu and S. E. Owens. Robustness analysis of a fixed-bed tubular reactor: Impact of modeling decisions. *Chem. Eng. Comm.*, 47:213–227, 1987.

[136] H. M. Park and D.H. Cho. The use of the Karhunen-Loeve decomposition for the modeling of distributed parameter systems. *Chem. Eng. Sci.*, 51:81–98, 1996.

[137] S. Park and D. J. Economou. Numerical simulation of a single-wafer isothermal plasma etching reactor. *J. Electrochem. Soc.*, 137:2624–2634, 1990.

[138] S. Park and D. J. Economou. A mathematical model for etching of silicon using CF_4 in a radial flow plasma reactor. *J. Electrochem. Soc.*, 138:1499–1508, 1991.

[139] A. Pazy. *Semigroups of Linear Operators and Applications to Partial Differential Equations.* Springer-Verlag, New York, 1983.

[140] J. Perrin and T. Broekhuizen. Surface reaction and recombination of the SiH_3 radical on hydrogenated amorphous silicon. *Appl. Phys. Lett.*, 50:433–435, 1987.

[141] J. Perrin, Y. Takeda, N. Hirano, Y. Takeuchi, and A. Matsuda. Sticking and recombination of the SiH_3 radical on the hydrogenated amorphous silicon: The catalytic effect of diborane. *Surf. Sci.*, 210:114–128, 1989.

[142] I.C. Plumb and K.R. Ryan. A model of the chemical processes occurring in CF_4/O_2 discharges used in plasma etching. *Plasma Chem. Plasma Proc.*, 6:205–230, 1986.

[143] A. J. Pritchard and D. Salamon. The linear quadratic control problem for infinite-dimensional systems with unbounded input and output operators. *SIAM Journal of Control and Optimization*, 25:121–144, 1987.

[144] F. Qin, E. E. Wolf, and H. C. Chang. Controlling spatiotemporal patterns on a catalytic wafer. *Phys. Rev. Lett.*, 72:1459–1462, 1994.

[145] C. V. Rao and J. B. Rawlings. Steady states and constraints in model predictive control. *AIChE J.*, 45:1266–1278, 1999.

[146] W. H. Ray. *Advanced Process Control.* McGraw-Hill, New York, 1981.

[147] W. H. Ray and J. H. Seinfeld. Filtering in distributed parameter systems with moving boundaries. *Automatica*, 11:509–515, 1975.

[148] S. N. Rea. Rapid method for determining concentric cylinder radiation view factors. *AIAA J.*, 13:1122–1123, 1975.

[149] R. C. Reid, J. M. Prausnitz, and B. E. Poling. *The Properties of Gases and Liquids, 4th ed.* McGraw-Hill, New York, 1987.

[150] C. W. Rowley and J. E. Marsden. Reconstruction equations and the Karhunen-Loève expansion for systems with symmetry. *Physica D*, 142:1–19, 2000.

[151] D. L. Russell and B.Y. Zhang. Smoothing and decay properties of solutions of the Korteweg-de Vries equation on a periodic domain with point dissipation. *J. Math. Anal. Appl.*, 190:449–489, 1995.

[152] D. L. Russell and B.Y. Zhang. Exact controllability and stabilizability of the Korteweg-de Vries equation. *Trans. Amer. Math. Soc.*, 348:3643–3672, 1996.

[153] K.R. Ryan and I.C. Plumb. A model for the etching of Si in CF_4 plasmas: comparison with experimental measurements. *Plasma Chem. Plasma Proc.*, 6:231–246, 1986.

[154] H. Sano and N. Kunimatsu. Feedback control of semilinear diffusion systems: Inertial manifolds for closed-loop systems. *IMA J. Math. Contr. Inform.*, 11:75–92, 1994.

[155] H. Sano and N. Kunimatsu. An application of inertial manifold theory to boundary stabilization of semilinear diffusion systems. *J. Math. Anal. Appl.*, 196:18–42, 1995.

[156] S. Y. Shvartsman and I. G. Kevrekidis. Nonlinear model reduction for control of distributed parameter systems: A computer assisted study. *AIChE J.*, 44:1579–1595, 1998.

[157] R. Siegel and J. R. Howell. *Thermal Radiation Heat transfer.* Hemisphere Publishing, U.S.A., second edition, 1981.

[158] L. Sirovich. Turbulence and the dynamics of coherent structures: I-III. *Quart. Appl. Math.*, XLV:561–590, 1987.

[159] L. Sirovich. Turbulence and the dynamics of coherent structures: part I: Coherent structures. *Quart. Appl. Math.*, XLV:561–571, 1987.

[160] L. Sirovich, B. W. Knight, and J. D. Rodriguez. Optimal low-dimensional dynamical approximations. *Quart. Appl. Math.*, XLVIII:535–548, 1990.

[161] G. I. Sivashinsky. Nonlinear analysis of hydrodynamic instability in laminar flames- I derivation of basic equations. *Acta Astronautica*, 4:1177–1206, 1977.

[162] G. I. Sivashinsky. On flame propagation under conditions of stoichiometry. *SIAM J. Appl. Math*, 39:67–82, 1980.

[163] M. W. Smiley. Global attractors and approximate inertial manifolds for nonautonomous dissipative equations. *Applicable Analysis*, 50:217–241, 1993.

[164] T. Smith and D. Boning. Artificial neural network exponentially weighted moving average control for semiconductor processes. *J. Vac. Sci. Tech. A*, 15:1377–1384, 1997.

[165] J. Smoller. *Shock Waves and Reaction-Diffusion Equations.* Springer-Verlag, Berlin-Heidelberg, 1983.

[166] R. K. Srivastava, P. A. Ramachandran, and M. P. Duduković. Radiation view factors in Czochralski crystal growth apparatus for short crystals. *J. Crystal Growth*, 74:281–291, 1986.

[167] G. Szabó. Thermal strain during Czochralski growth. *J. Crystal Growth*, 73:131–141, 1985.

[168] R. Temam. *Infinite-Dimensional Dynamical Systems in Mechanics and Physics.* Springer-Verlag, New York, 1988.

[169] A. Theodoropoulou, R. A. Adomaitis, and E. Zafiriou. Inverse model based real-time control for temperature uniformity of rtcvd. *IEEE Trans. Sem. Manuf.*, 12:87–101, 1999.

[170] E. S. Titi. On approximate inertial manifolds to the Navier-Stokes equations. *J. Math. Anal. Appl.*, 149:540–557, 1990.

[171] J.G. Van Antwerp, R.D. Braatz, and N.V. Sahinidis. Robust nonlinear control of plasma etching. In *Proceedings of the Symposium on Silicon Nitride and Silicon Dioxide Thin Insulating Films*, pages 454–462, Montreal, Canada, 1997.

[172] N. Van den Bogaert and F. Dupret. Dynamic global simulation of the Czochralski process I. principles of the method. *J. Crystal Growth*, 171:65–76, 1997.

[173] N. Van den Bogaert and F. Dupret. Dynamic global simulation of the Czochralski process II. analysis of the growth of a germanium crystal. *J. Crystal Growth*, 171:77–93, 1997.

[174] B. van Keulen. *H_∞-Control for Distributed Parameter Systems: A State-Space Approach.* Birkhauser, Boston, 1993.

[175] S.P. Venkatesan, I. Trachtenberg, and T.F. Edgar. Effect of flow direction on etch uniformity in parallel-plate (radial flow) isothermal plasma reactors. *J. Electrochem. Soc.*, 134:3194–3197, 1987.

[176] P. K. C. Wang. Control of a distributed parameter system with a free boundary. *Int. J. Contr.*, 5:317–329, 1967.

[177] P. K. C. Wang. Stabilization and control of distributed systems with time-dependent spatial domains. *J. Optim. Theor. & Appl.*, 65:331–362, 1990.

[178] P. K. C. Wang. Feedback control of a heat diffusion system with time-dependent spatial domains. *Optim. Contr. Appl. & Meth.*, 16:305–320, 1995.

[179] J. T. Wen and M. J. Balas. Robust adaptive control in hilbert space. *J. Math. Anal. Appl.*, 143:1–26, 1989.

[180] E. B. Ydstie and A. A. Alonso. Process systems and passivity via the Clausius-Planck inequality. *Syst. & Contr. Lett.*, 30:253–264, 1997.

[181] J. Zabczyk. *Mathematical Control Theory: An Introduction.* Birkhäuser, Boston, 1995.

[182] W. Zhou, D. E. Bornside, and R. A. Brown. Dynamic simulation of Czochralski crystal growth using an integrated thermal-capillary model. *J. Crystal Growth*, 137:26–31, 1994.